Investigation into PtNi Nanoparticles as Electrocatalyst for the Methanol Oxidation Reaction

Dissertation
to receive the degree

Dr. rer. nat.
at the Faculty of Mathematics, Informatics and Natural Sciences
of the University of Hamburg

submitted to the
Department of Chemistry
of the University of Hamburg

Hanna Lena Wittern

born in Hamburg

Hamburg, June 2015

The experimental work described in this thesis has been carried out between October 2010 and February 2015 at the Institute of Physical Chemistry at the University of Hamburg in the research group of Prof. Dr. Weller.

1. Reviewer: Prof. Dr. Horst Weller
2. Reviewer: Prof. Dr. Alf Mews

Date of thesis defense: 17.07.2015

Für meinen Sascha

Abstract

Bimetallic Pt alloy nanoparticles with first row transition metals as catalyst materials for the direct methanol fuel cell have generated much research activity in recent years. In this work PtNi nanoparticles are investigated in regard to their electrocatalytic properties for the methanol oxidation reaction. PtNi particles of various sizes and compositions are synthesized following the hot and continuous injection method and applied to a glassy carbon substrate via spin coating under formation of a mono-layered particle film. Electrochemical investigations carried out with this simple, two-component electrodes exhibit strong agglomeration of the individual nanoparticles as can be shown via scanning electron microscopy. Coating the electrodes with a thin layer of Nafion results in a substantial stabilization of the particle film. The phenomenon of particle agglomeration is further investigated with respect to different treatments for ligand removal applied to the oleylamine and oleic acid stabilized PtNi nanoparticles. Treatments examined in this work are ligand exchange with tetrabutylammonium hydroxide in methanol, treatment in a muffle furnace, plasma treatment, UV/ozone treatment, and treatment in a vacuum furnace. As a reference untreated nanoparticles are investigated. The observed agglomeration is strongly treatment-dependent, as is the resulting catalytic activity for the methanol oxidation reaction. A pronounced treatment-dependency is also found in regard to catalyst stability, where the plasma treatment and other strongly oxidizing influences lead to the best long-term performance as shown by subjecting the respective electrodes to $10\,000$ potential cycles and simultaneously determining their electrochemically active surface area. In regard to size and composition the investigated PtNi particles show surprisingly small differences in their catalytic activity for the methanol oxidation reaction, indicating that the influence of these parameters is not a crucial factor. Experiments conducted with differently shaped nanoparticles seem to have a greater influence in this regard. However, a clear trend for the catalytic activity with respect to the methanol oxidation reaction is found for the investigated PtNi nanoparticles with the best results observed for rather large (approx. $7\,$nm) alloy (1:1, Pt:Ni) particles, which exhibit a catalytic activity twice as high as compared to smaller Pt-rich nanoparticles.

Kurzfassung

Bimetallische Nanopartikel aus Platin und 3d-Übergangsmetallen sind in den letzten Jahren verstärkt als Katalysatormaterial für die Direktmethanolbrennstoffzelle in den Fokus der Forschung gerückt. Im Rahmen der hier vorliegenden Arbeit wurden die elektrokatalytischen Eigenschaften von PtNi-Nanopartikeln in Bezug auf die Methanol-Oxidation untersucht. Zu diesem Zweck wurden Partikel unterschiedlicher Größe und Zusammensetzung nach der *Hot-Injection*-Methode synthetisiert und mittels Rotationsbeschichtung in einer Monolage auf ein *Glassy-Carbon*-Substrat aufgebracht. Mithilfe der Rasterelektronenmikroskopie konnte anschließend gezeigt werden, dass mit diesen einfachen Zwei-Komponenten-Elektroden durchgeführte elektrochemische Analysen zu einer starken Agglomeration der einzelnen Partikel führen. Eine Stabilisierung des Partikelfilms konnte durch Aufbringen einer dünnen Nafion-Schicht erreicht werden. Weiterhin wurde das Agglomerationsverhalten in Abhängigkeit von verschiedenen Methoden zur Entfernung der stabilisierenden Liganden von der Partikeloberfläche untersucht. Hierzu wurden die Proben entweder im Muffelofen, im Plasma, mit UV/Ozon oder im Vakuum behandelt oder ein Ligandenaustausch mit Tetrabutylammoniumhydroxid in Methanol durchgeführt. Als Referenz wurden unbehandelte Nanopartikel untersucht. In den sich anschließenden elektrochemischen Messungen konnte gezeigt werden, dass sowohl die Agglomeration als auch die katalytische Aktivität für die Methanol-Oxidation stark von der jeweiligen Vorbehandlung abhängig sind. Gleiches gilt für die Stabilität des Katalysators, wobei die besten Ergebnisse in Langzeituntersuchungen für die Plasmabehandlung und andere oxidierende Behandlungen gefunden wurden. Dies konnte anhand der Entwicklung der elektrochemisch aktiven OberflÃ¤che über 10 000 Potentialzyklen nachgewiesen werden. Größe und Zusammensetzung der untersuchten Nanopartikel haben hingegen nur einen vergleichsweise geringen Einfluß auf die katalytische Aktivität für die Methanol-Oxidation. Messungen mit Nanopartikeln unterschiedlicher Form zeigten im Vergleich einen größeren Einfluss auf die katalytische Aktivität. Hinsichtlich Größe und Zusammensetzung lässt sich dennoch ein deutlicher Trend für die untersuchten PtNi-Nanopartikel erkennen, wobei die besten Ergebnisse für eher große (ca. 7 nm) Legierungspartikel (1:1, Pt:Ni) gefunden wurden. Im Vergleich zu kleineren Pt-reichen Nanopartikeln zeigten diese eine etwa doppelt so große katalytische Aktivität.

Contents

CONTENTS

CONTENTS

List of Abbreviations

AAS Atomic absorption spectroscopy

ac Acetat

acac Acetylacetonate

AFM Atomic force microscopy

APT Amperometric pretreatment

CA Chronoamperometry

CAv Current averaging

CI Continuous injection

CV Cyclic voltammetry

DCB 1,2-Dichlorobenzene

DEMS Differential electrochemical mass spectrometry

DMFC Direct methanol fuel cell

DPE Diphenyl ether

ECC Electrochemical cleaning

ECSA Electrochemically active surface area

EDX Energy dispersive X-ray spectroscopy

emf Electromotive force

FTIR Fourier transform infrared spectroscopy

List of Abbreviations

FWHM Full width at half maximum

GC Glassy carbon

GCE Glassy carbon electrode

GHS Globally Harmonized System

HDD 1,2-Hexadecanediol

HER Hydrogen evolution reaction

HI Hot injection

LEx Ligand exchange

LSV Linear sweep voltammetry

MOR Methanol oxidation reaction

NHE Normal hydrogen electrode

NP Nanoparticle

NPs Nanoparticles

OA Oleic acid

OAm Oleylamine

ORR Oxygen reduction reaction

RHE Reversible hydrogen electrode

SCE Saturated calomel electrode

SEM Scanning electron microscopy

SHE Standard hydrogen electrode

STEM Scanning transmission electron microscopy

TBAOH Tetrabutylammonium hydroxide

TEM Transmission electron microscopy

TG Thermogravimetric

TGA Thermogravimetric analysis

UHV Ultra high vacuum

WDX Wavelength dispersive X-ray spectroscopy

XPS X-ray photoelectron spectroscopy

XRD X-ray diffraction

1

Introduction

" 'Yes, my friends, I believe that water will one day be employed as fuel, that hydrogen and oxygen which constitute it, used singly or together, will furnish an inexhaustible source of heat and light, (...) Water will be the coal of the future.' "(1) Such are the words Jules Verne bestowed upon one of his characters, the engineer Captain Cyrus Harding, in his famous novel "The Mysterious Island" from 1874. The 19th century saw the development of the first fuel cell by Sir William Grove, a set-up that consisted of a hydrogen anode and an oxygen cathode, which he called a "gaseous voltaic battery".(2) Since then the dream of generating energy by means of the electrochemical conversion of a fuel, be it hydrogen, methanol, ethanol, or any other suitable substance, has mostly been realized as is evidenced by examples such as the use of fuel cells in the space shuttle program by NASA, their employment by the military, as well as their use in the public transportation sector.(3) Nowadays, fuel cell research is mainly driven by the need to develop renewable energy technologies in order to satisfy rising energy demands while fossil fuel reserves diminish and to reduce the emission of environmental pollutants(4) However, for a broad commercialization of fuel cell technologies some scientific challenges still have to be met.

For the direct methanol fuel cell (DMFC), which is at the center of this work, the oxygen reduction reaction (ORR) commencing at the cathode and the methanol oxidation reaction (MOR) at the anode pose different challenging problems. For the MOR these are the high costs caused by the requirement of platinum as electrocatalyst, the relatively slow electrode kinetics of the six electron transfer reaction, and the poisoning of the electrocatalyst due to intermediately formed carbon monoxide.(5)(6) Improving the performance of the electrocatalyst with respect to its activity, selectivity and stability is thus the key to its optimization.(7) Due to its high activity for the dissociative adsorption of methanol almost all electrocatalyst for the MOR are platinum-based. In order

to reduce the costs associated with the employment of platinum its utilization has to be optimized. With their high surface-to-volume ratio nanoparticles are perfectly suited for this task. Moreover, nanoparticles present the possibility of finely tuning their size, composition, and shape during synthesis, thus additionally resulting in different surface morphologies, all factors that have a strong effect on catalytic activity.(8) Due to their lower costs compared to pure platinum catalysts, their enhanced electrocatalytic activity, and their better resistance to CO poisoning, binary alloy systems in particular have gained increasing attention in the last decade.(9)

In order to investigate the suitability of a batch of nanoparticles for the electrochemical conversion of different fuels, certain requirements must be met, e.g., a narrow size distribution, a homogeneous composition and morphology throughout the particle batch, and a defined surface structure. Nanoparticles from solution synthesis have been shown to possess these properties.(10) They are, however, usually capped by organic ligands, which block active sites on the particle surface and need to be removed in order to exploit the full catalytic potential. Different treatments for ligand removal have been proposed, including chemical washing, heat, and oxidation treatment.(11)

A promising catalyst for the MOR, next to the chiefly employed PtRu particles,(5) are PtNi nanoparticles, which have been shown to enhance catalytic activity with respect to pure platinum particles.(12) However, investigations concerning the dependency of catalytic activity for the MOR not only on the composition but also on the size of PtNi nanoparticles are still missing to the best of the authors' knowledge. So are studies giving detailed insight into the impact of different treatments (e.g., thermal, chemical, oxidative) on PtNi particles, especially in respect to their agglomeration under electrochemical conditions. The agglomeration of nanoparticles employed as electrocatalysts is a well-known phenomenon,(13) but scarcely examined when studies with respect to catalytic activity are performed. Gaining a better understanding of the evolution of size, composition, and shape under various treatments and (electro)chemical conditions has, however, been called "a focal point of future research" in the field of nanostructured electrocatalysis.(14)

In this work, PtNi nanoparticles synthesized following an advanced hot injection approach were investigated via cyclic voltammetry (CV) in regard to the influence their size and composition had on the catalytic activity for the MOR. Furthermore, changes in the size, composition, shape, and structure of the electrocatalyst occurring due to the application of different treatments for ligand removal as well as under exposure to electrochemical conditions were examined via scanning electron microscopy (SEM) and other suitable methods at different stages of their development.

2

Theoretical Background

2.1   Electrochemistry - Basic Concepts

"Electrochemistry is the science of electron transfer across the solution-electrode interface."(15) This simple sentence may satisfy the need for a definition of the term "electrochemistry". It does not, however, do justice to the extensive scope of theories, methods, and applications assembled under its banner. Electrochemistry is concerned not only with the description of thermodynamic and kinetic phenomena taking place at the electrode surface but mainly with their manifestation as the conversion of chemical into electrical energy (or vice versa). In this context the potential dependency of the conversion, its temperature, concentration, and pH dependencies as well as its dependency on diffusional mass transport, convection, and dissolution are of interest. Furthermore, electrochemical models cover phenomena like interfacial charge transfer, charge separation, adsorption, and some of the solid electrodes surface properties. This chapter intends to give a brief overview of the interdisciplinary and broad field of electrochemistry while covering some important concepts along the way.

For an electrochemical investigation scientists can choose between a multitude of different techniques. It is useful to discern between two general types of measurement techniques, namely static and dynamic methods.(16) Static methods are those for which the system is not disturbed and Nernstian equilibrium is maintained throughout the measurement meaning that no current flow occurs. Potentiometric measurements, e.g., pH determination, belong to this category. Dynamic methods entail the application of an excitation signal, thus generating non-equilibrium conditions and a flow of current. This excitation signal can be any potential or current program and determines the kind of experiment that is carried out, e.g., chronoamperometry (CA), which consists of measuring the current as a function of time while applying a constant potential or

cyclic voltammetry (CV), where the current is measured while the potential is ramped linearly versus time in a see-saw fashion, thus generating a cyclic voltammogram per completed potential cycle.

Its wide variety of methods makes electrochemistry a useful tool for researching an array of reactions and chemical phenomena. Additionally, electrochemical techniques are the basis of many economic applications, some of them important industrial processes, e.g., chlor-alkali electrolysis, electrolytic refining, and electroplating. In recent years, the importance of devices that directly convert chemical into electrical energy has increased greatly and applications such as batteries and fuel cells will play a major role for the energy industry in the future, especially in regard to zero emission vehicles.(17) Electrochemical processes comprise a great many underlying theories and principles which go beyond the scope of this thesis. In this section some of the most basic electrochemical laws will be introduced, followed by a discussion of faradaic and capacitive current, the electrical double layer, overpotential and polarization, mass transport and the Cottrell equation. The knowledge of these concepts is essential for understanding the following sections on cyclic voltammetry and electrocatalysis. For a more comprehensive overview of the topic the reader is referred to standard textbooks dealing with electrochemistry.(18)(19)

2.1.1 Fundamental Equations

Ohm's Law Ohm's law represents the most basic concept for understanding the relationship of current i and voltage V. It states that the current between two points of a conductor is directly proportional to the applied potential difference and introduces the electrical resistance R as constant of proportionality.

$$V = R \cdot i \tag{2.1}$$

Ohm's law is an empirical law and not always obeyed, but it conveys a simple relation of the most important electrical dimensions. When obeyed the respective objects and materials are called *ohmic*, as opposed to *non-ohmic* matter.

Faraday's Laws Faraday's laws, published in 1834, give a quantitative correlation between the "quantity of electricity passed" and that "of matter decomposed".(20) The measured faradaic current i is giving the amount of charge q that is transferred per unit time t

$$i = \frac{\mathrm{d}q}{\mathrm{d}t} \tag{2.2}$$

resulting in a transformation of a molar amount n of a substance needing z electrons for the reduction of each molecule of that substance. This correlation is known as Faraday's first law.

$$n = \frac{q}{zF} \tag{2.3}$$

The proportionality constant between q and n is the reciprocal of Faraday constant F multiplied with the stoichiometric factor z of the respective reaction. F is defined as the charge transferred for the reduction or oxidation one mole of substance for which $z = 1$

$$F = e\, N_A \tag{2.4}$$

with e being the elementary charge and N_A the Avogadro constant. Faraday's second law states that the mass m of an element transformed by a charge q is directly proportional to the element's equivalent weight. Combined, this results in the term

$$m = \frac{qM}{zF} \tag{2.5}$$

with M being the molar mass of the redox species. The correlation between equivalent weight and M is given by

$$\text{Equivalent weight} = \frac{M}{z}\, 1\,\text{mol} \tag{2.6}$$

With the formulation of his laws Faraday was the first to recognize the connection between charge transferred and matter transformed during electrolysis. An excellent review explaining Faraday's discoveries in their historical context was published by Ehl and Ihde.(21)

The Nernst Equation This basic equation relates the electrode potential E of a half-cell reaction of the kind $\text{Ox} + z\text{e}^- \rightleftharpoons \text{Red}$ to the concentrations c or, more accurately, to the activities a of the reaction participants Ox (oxidized species) and Red (reduced species). The Nernst equation

$$E = E^\ominus - \frac{RT}{zF} \ln Q \tag{2.7}$$

moreover contains the standard electrode potential $E^\ominus$, the ideal gas constant R, the temperature T and the factor zF, which we know from eq. 2.3. For the reaction quotient Q per definition reagents (oxidized species) are negative whereas products (reduced species) are positive with ν_i being the stoichiometric factor of each component i.

$$\ln Q = \sum \nu_i \ln a_i \tag{2.8}$$

The Nernst equation can be extended to determine the electromotive force (emf) of a cell (comprised of two half-cells, see eq. 2.12). The emf is the maximum voltage a given cell can supply and is connected to the free reaction enthalpy ($\Delta_R G$) via the exchanged charge. $\Delta_R G$ describes the maximum non-expansion work a system can generate and can be defined

$$\Delta_R G = \Delta_R G^{\ominus} + RT \ln Q \tag{2.9}$$

as a function of its reaction quotient. With $\Delta_R G^{\ominus}$ being the standard free reaction enthalpy and under consideration of the law of conservation of energy one directly obtains the Nernst equation for a cell

$$\Delta E = \Delta E^{\ominus} - \frac{RT}{zF} \ln Q \tag{2.10}$$

via

$$\Delta_R G = -zF\Delta E \quad \text{and} \quad \Delta_R G^{\ominus} = -zF\Delta E^{\ominus} \tag{2.11}$$

These two forms of the Nernst equation (eqs. 2.7 and 2.10) only apply for equilibrium reactions without kinetic hindrance (i.e. they obey thermodynamic principles) and such electrode processes are therefore said to exhibit *Nernstian* behavior. Furthermore, both forms are logically connected and by solving the Nernst equation 2.7 for both half-cells of a setup (e.g., a galvanic element) its emf can be determined via

$$\text{emf [V]} = \Delta E = E_2 - E_1 \tag{2.12}$$

with E_1 being the half-cell potential of the anode and E_2 that of the cathode. By further defining the potential of the standard hydrogen electrode (SHE)

$$H^+ + e^- \longrightarrow 1/2 \, H_2 \tag{2.1}$$

as zero, the standard electrode potential of every other half-reaction under standard conditions can be determined as the difference to the potential of the SHE when it is operated as the anode. Standard electrode potentials are thus always given for the cathode reaction (reduction).

2.1.2 Faradaic and Capacitive Currents

When a potential is applied to an electrode two fundamentally different processes can take place, namely *faradaic* and *capacitive* processes. Faradaic processes occur when charge is transferred across the interface of an electrode as the result of a reaction taking place at the electrode surface and oxidation or reduction proceed following Faraday's laws (see above). Capacitive currents (also called *non-faradaic, double layer* or *charging*
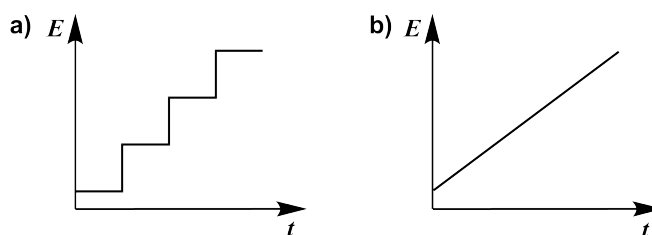
Figure 2.1: Excitation signal of a potential ramp for a) a digital and b) an analog device. The electrode potential E is plotted vs. the time t. Note that most digital potentiostats can be upgraded with a "true linear scan" option that applies a smooth analog ramp instead of a staircase sweep.

currents) are due to a charging of the interface without any additional charge transfer. The charge separation resulting from capacitive currents is the basis of the electrical double layer, which in turn can be regarded as a capacitor (see 2.1.3).

An electrochemical system under steady state conditions shows no variation of parameters like concentration profile, current, etc. with time. When the steady state is disturbed (for example through the application of a potential different to the one the system was in before) transitory processes take place to adjust all parameters to the new state. The time this transition takes can vary significantly for different systems. Under potentiostatic conditions, for example, capacitive currents usually diminish much faster than faradaic currents. As a rule the transient time of a faradaic current is larger than 1 s, whereas capacitive currents have transition times between 1 ms and 1 s. In contrast to other transient processes, faradaic currents can be described in a quantitative way (see 2.1.5).(22) This difference should always be kept in mind when choosing the appropriate measurement conditions. This is especially important when a potentiostat with digital potential output is used since measurements with a device of this type will always be potentiostatic in nature, as any potential ramp will be modeled as a sequence of very small potential steps (see figure 2.1).

2.1.3   The Electrical Double Layer

Electrochemistry describes the processes associated with charge separation and charge transfer taking place at the interface between an electrode, usually an electronic conductor, and the surrounding electrolyte, an ionic conductor. To understand them it is necessary to understand the nature of this barrier. For the sake of simplicity this discussion will be limited to the processes at a single electrode, although an electrochemical

cell normally consists of at least two electrode-solution components, called half-cells. In the interfacial region of an electrochemical half-cell charge distribution differs from that in the bulk phases of the electrode and the electrolyte respectively. It is therefore sensible to focus the description of the electrical double layer on the actual region of this phase boundary. Charge separation of positive $+q$ and negative $-q$ charges (generating a total charge q) across such a phase boundary is specified as capacitance C while the difficulty of charge transfer is described by the electrical resistance R (see also eq. 2.1).

$$C = \frac{q}{V} \tag{2.13}$$

$$R = \rho \, \frac{l}{A} \tag{2.14}$$

The electrical resistance of a conductor is thus dependent on its length l and its cross-section area A as well as the specific electrical resistance ρ of the material it is made of. The reciprocal of ρ is the electrical conductivity σ.

$$\sigma = \frac{1}{\rho} \tag{2.15}$$

Several models describing the composition and characteristics of the electrical double layer have been developed over the years. The most commonly known is the Helmholtz model(23) from 1879, which was the first to state that at the phase boundary between a charged electrode and an electrolyte two layers of opposite polarity are formed.
Depending on the charge of the electrode (negative or positive) oppositely charged ions from the electrolyte are drawn toward the electrode surface and accumulate, separated by a layer of polarized solvent molecules (see figure 2.2). Combined with the charged layer at the surface of the electrode the electrical double layer is thus formed. The Gouy-Chapman model(25)(26) (1910 - 1913) additionally takes the influence of the electrolyte concentration, the applied potential, and the Brownian motion of ions and molecules of the electrolyte into account and thus postulates, in contrast to the quite rigid double layer of the Helmholtz model, a diffuse double layer on the electrolyte's side. The Stern model(27) (1924) finally combines both approaches and postulates a rigid layer of ions close to the electrode surface, followed by a diffuse distribution of ions as described by Gouy-Chapman.
Grahame(28) extended this model in 1947 by including the possibility of specific adsorption, i.e. adsorption of non-solvated ions with strong bonding to the electrode surface. In 1963 Bockris, Devanathan, and Müller(29) recognized the importance of the nature of the electrolyte as the predominant species. Their model considers the
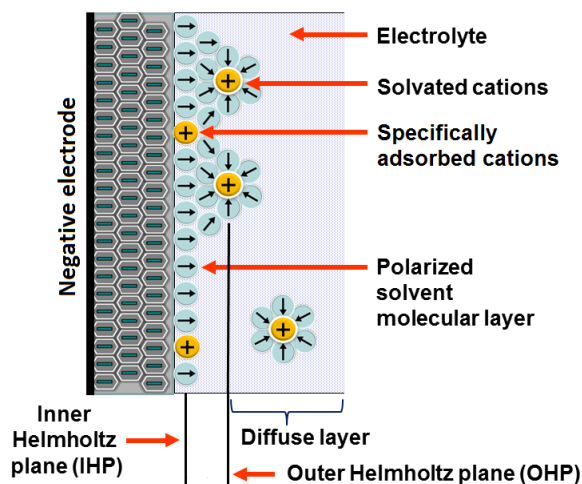
Figure 2.2: Schematic of the electrical double layer as proposed by Bockris, Devanathan, and Müller, with inner and outer Helmholtz plane as well as the diffuse double layer suggested by Gouy-Chapman.(24)

interaction of solvent dipoles and the electrode in case of using dipolar solvents, such as water, as electrolyte (see figure 2.2).

Even more comprehensive "chemical" models of the electrical double layer were developed by Damaskin and Frumkin(30)(31)(32), Trasatti(33), and Parsons(34). Chemical models consider the electronic distribution of the atoms in the electrode, which is related to the electrodes' surface work function, instead of focusing on electrostatic interactions as the above mentioned models.(35)

The capacitance of the Helmholtz double layer C_{dl} can be described in terms of a parallel-plate capacitor for which the dielectric consists of the molecules (solvent) adhered to the surface of the electrode. It is proportional to the area A of the electrode and the permittivity ε of the dielectric and inversely proportional to the distance d the latter generates between the charges.

$$C_{dl} = \varepsilon \, \frac{A}{d} \tag{2.16}$$

For a more realistic description of the system non-linear effects have to be taken into account. This gives rise to the introduction of the differential capacitance (C_d) for characterizing the electrical double layer as the correlation of the surface charge q_s of the solid electrode to the electrode potential E.

$$C_d = \frac{\partial q_s}{\partial E} \tag{2.17}$$

9

(a) Ideal polarizable electrode   (b) Ideal nonpolarizable electrode
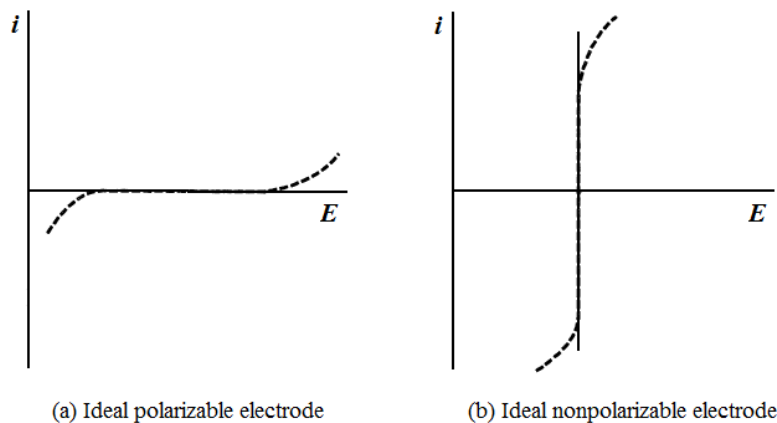
Figure 2.3: Polarization curves for (a) polarizable and (b) non-polarizable electrodes. The dashed line shows the behavior a real electrode might adopt when approaching the ideal case. For reference electrodes a constant potential is desirable and therefore a polarization behavior close to that of an ideally non-polarizable electrode.(18)

2.1.4 Overpotential and Polarization

The values predicted by thermodynamics for the equilibrium potential of a half-reaction via the Nernst equation can not always be obtained under experimental conditions. The reason for this is the existence of an overpotential η, which is described as the difference of the potential E of an electrode reaction occurring with a measurable rate, to the equilibrium potential E_{eq} predicted by thermodynamics.

$$\eta = E - E_{\mathrm{eq}} \tag{2.18}$$

The rate of an electrode reaction is *heterogeneous* in nature and its description is thus more complex than that of a *homogenous* reaction taking place in solution or in the gas phase. The rate of a reaction at the electrode-electrolyte interface, for example, depends on various surface effects of the electrode and mass transport to it in addition to the usual kinetic factors. The heterogeneous reaction rate is thus defined as the molar amount of reactant transformed per unit area A of electrode surface

$$\text{rate} \left[\mathrm{mol\,s^{-1}\,cm^{-2}}\right] = \frac{i}{zFA} = \frac{j}{zF} \tag{2.19}$$

with i being the observed current and j the current density. The hydrogen evolution reaction (HER), e.g., is inhibited at mercury electrodes in aqueous solution at the potential predicted from thermodynamics. The overpotential of the HER at a mercury electrode demands a considerably higher negative potential to be applied in order for

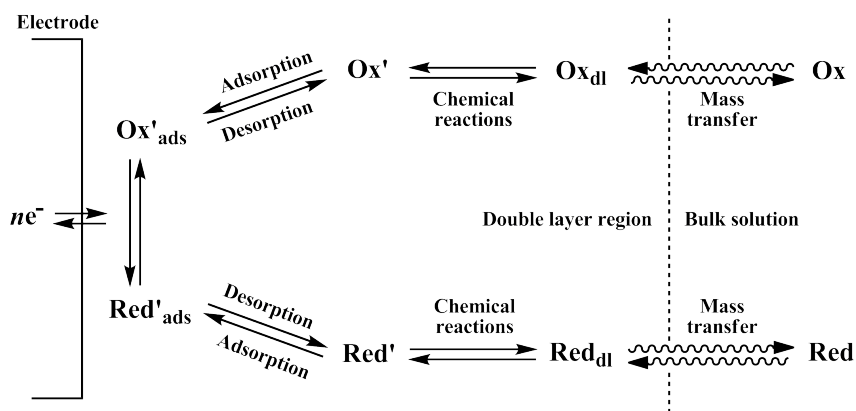**Figure 2.4:** General pathway of an electrode reaction of the kind $Ox + ne^- \rightleftharpoons Red$.(18)

the reaction to occur than it would on a platinum electrode, where the overpotential for the HER is much lower.(18) The phenomenon which is quantified by the value of overpotential is called *polarization* of an electrode. Usually *i-E* curves that are obtained under steady state conditions are called polarization curves. They show important characteristics of an electrode. Two contrary examples of polarization curves approaching ideal behavior are shown in figure 2.3. *i-E* curves obtained under non-steady state conditions, as in CV or linear sweep voltammetry (LSV), follow different principles. The "factors affecting the shape of current-potential curves" are discussed by Maloy in his paper by the same name.(36)

Electrochemical reactions are often investigated by recording the current as a function of potential, as the overpotential can easily be determined from the obtained *i-E* curve provided the investigated cell has a defined equilibrium potential E_{eq}. This is the case if a *redox couple* (for example H^+ and H_2) exists for each electrode of the cell setup, which is, for instance, true for the cell $Pt/H_2/H^+,Cl^-/AgCl/Ag$ but not for the cell $Pt/H^+,Br^-/AgBr/Ag$ (for an explanation of the nomenclature used to describe electrochemical cells the reader is referred to standard textbooks about electrochemistry(18)(19)).

There are different factors that can affect the rate of an electrode reaction and thus contribute to its overpotential. Each of these proceeds within different time spans, giving rise to the fact that under steady state conditions every step is bound to the timing of the slowest, the so called *rate-determining step*. The main steps in a typical electrode reaction are(37):

- Heterogeneous charge transfer reactions at the electrode

- Other surface reactions like adsorption, desorption or crystallization

- Coupled homogeneous reactions in solution

- Mass transport of reactant to the electrode or of product away from it

A schematic of these processes is shown in figure 2.4. The resulting current density j is an expression of the reaction rate and is influenced by the reactions overpotential η. The latter in turn is the sum of the overpotentials of the different reaction steps

$$\eta = \eta_{ct} + \eta_{ad} + \eta_{rs} + \eta_{mt} + \eta_{x} \tag{2.20}$$

with η_{ct} being the charge transfer overpotential, η_{ad} the overpotential associated with adsorption/desorption processes, η_{rs} the overpotential caused by reactions in solution preceding/following the charge transfer reaction, η_{mt} the mass transfer overpotential, and η_{x} a place holder for any kind of other overpotential occurring in the respective electrode process.

2.1.5 Mass transport and the Cottrell Equation

As described in the previous sections the double layer region near the electrode surface differs from the bulk solution. In this section the focus will lie on the concentration profile within the electrolyte and on the effects of mass transport on the resulting current. For the sake of simplicity the consideration of the concentration profile is carried out for a Nernstian reaction (i.e. an equilibrium reaction of a *redox couple* such as $Fe(CN)_6^{2-}$ and $Fe(CN)_6^{3-}$) in a stationary double layer (i.e. a double layer found in a stirred solution or at a *rotating disk electrode*). Under those conditions a concentration profile as described by the Helmholtz model of the electrical double layer (see above) will develop (see figure 2.5). The linear form of the concentration gradients is a valid approximation for many systems.

The mass transport J in the interfacial region under the assumption of steady state conditions can be described by Fick's first law of diffusion

$$J = -D\frac{\partial c}{\partial x} \tag{2.21}$$

with D being the diffusion coefficient, c the concentration and x the distance from the electrode surface. For a reaction in which mass transport occurs due to diffusion and at the same time is the rate-determining step, a so called *diffusion-controlled* reaction, Faraday's laws can be expanded to include the proportionality to mass transport.

$$i = \frac{dq}{dt} \quad \Rightarrow \quad i \propto \frac{m}{t} \propto J \propto \frac{dc}{dx} \tag{2.22}$$
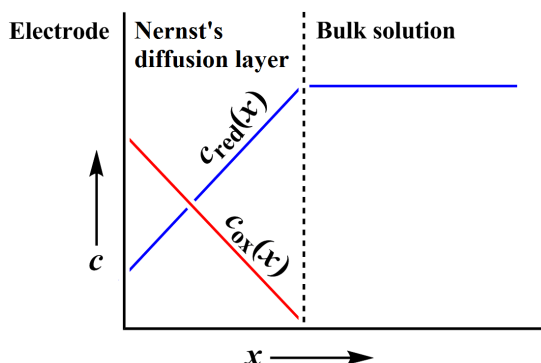
Figure 2.5: Concentration profile in front of a rotating disk electrode. Here, $c_{\text{red}}(x)$ is the concentration of the reduced species (reactant), which is the only one present at the beginning of the process. Furthermore, its concentration in bulk solution is so high that the amount of product produced is negligible. $c_{\text{ox}}(x)$ is the concentration of the oxidized species (product).(38)

The concentration of a species present at a certain moment in time t is described by Fick's second law

$$\frac{\partial c}{\partial t} = D \frac{\partial^2 c}{\partial x^2} \tag{2.23}$$

The concentration of a species is thus dependent on the distance from the electrode surface as well as time elapsed, assuming other factors like temperature and pressure are constant. With Fick's laws the concentration profile and therefore the mass transport and its dependency on time, which is equivalent to the resulting current, can be obtained considering the characteristic boundary conditions of the experiment. If it is not possible to obtain a closed-form solution numerical integration can be used to solve the equation.

Solving the diffusion equation for the simple case where the potential of a planar electrode is stepped from a potential at which no reaction occurs to a potential where the investigated reaction occurs instantaneously and completely (i.e. all reactant located at the electrode is transformed at once) yields the following expression known as the Cottrell equation

$$i = zFA\, c_{\text{j},0} \left(\frac{D_{\text{j}}}{\pi\, t} \right)^{1/2} \tag{2.24}$$

It gives the current i as a function of the number z of electrons transferred to reduce/oxidize one molecule of j, the Faraday constant F, the area of the planar electrode A, the initial concentration of j $c_{\text{j},0}$, the diffusion coefficient for species j D_{j}, and the time t. Depletion of the electroactive species thus leads to a decline in current following an inverse $t^{1/2}$ function. This type of function is typical for many kinds of experiments in
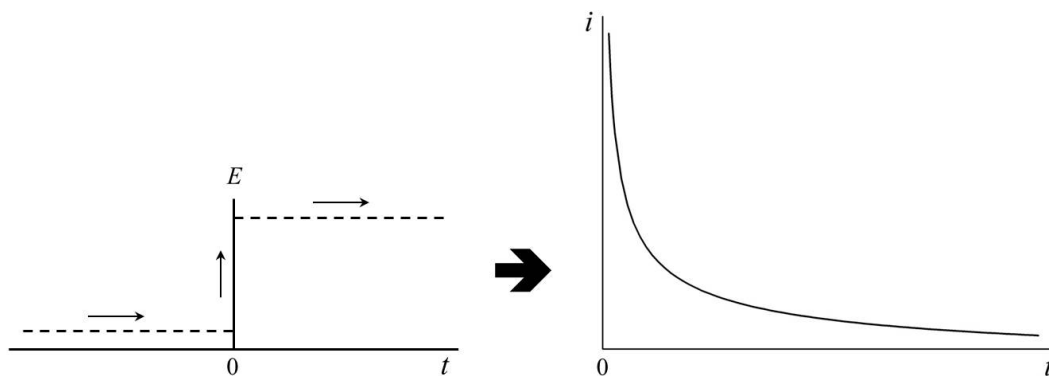
Figure 2.6: Excitation signal of a chronoamperometric experiment (left) and the resulting current response as a function of time (right) following the Cottrell equation.(38)

which diffusion is the rate-determining step. As an example the time dependency of a chronoamperometric experiment is shown in figure 2.6. It is important to note that the high currents predicted for small times in equation 2.24 are often not displayed due to limitations of the employed devices.(18)

2.2 Cyclic Voltammetry

Cyclic voltammetry is a frequently used dynamic electrochemical method and has much in common with linear sweep voltammetry. Both are based on the application of a continuous potential as a function of time. In the case of cyclic voltammetry the sweep direction is inverted at a certain potential until a second chosen potential is reached at which the sweep direction is inverted again and so forth (see figure 2.7). The response to this excitation signal is a current flow consisting of faradaic and capacitive contributions. The faradaic current (I_f) appears as a consequence of the conversion of electroactive species at the working electrode in the potential region where this reaction occurs (peak formation). The capacitive current (I_C) arises due to changes in the double layer charging. The total current is

$$I = I_\mathrm{C} + I_\mathrm{f} = C_\mathrm{d}\frac{\mathrm{d}E}{\mathrm{d}t} + I_\mathrm{f} = \nu C_\mathrm{d} + I_\mathrm{f} \tag{2.25}$$

with the scan rate ν (slope of the excitation signal, see figure 2.7) being directly proportional to the capacitive current.

$$I_\mathrm{C} \propto \nu \tag{2.26}$$

Figure 2.7: Excitation signal of a CV experiment, showing the maximal (E_{max}) and minimal (E_{min}) potential limits, as well as the initial (E_{i}) and final (E_{f}) potential. The scan rate ν is given by $|dE/dt|$. The excitation signal of a LSV experiment consists of only one gradient between the potential limits.(35)
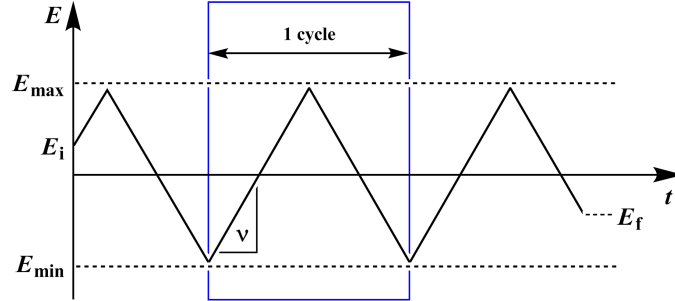
The faradaic current on the other hand is proportional to the square root of the scan rate

$$I_{\text{f}} \propto \nu^{1/2} \tag{2.27}$$

as can be seen by solving the diffusion equations for the investigated reversible, irreversible or quasi-reversible system by numerical inversion (see 2.2.1). At a planar electrode for a reaction of the kind $\text{Ox} + n e^- \to \text{Red}$ that means solving

$$\frac{\partial [\text{Ox}]}{\partial t} = D_{\text{Ox}} \frac{\partial^2 [\text{Ox}]}{\partial x^2} \tag{2.28}$$

$$\frac{\partial [\text{Red}]}{\partial t} = D_{\text{Red}} \frac{\partial^2 [\text{Red}]}{\partial x^2} \tag{2.29}$$

with D_{Ox} and D_{Red} being the diffusion coefficients for the species Ox and Red with the concentrations [Ox] and [Red], respectively. The appropriate boundary conditions are

$$t = 0 \qquad x = 0 \qquad [\text{Ox}]^* = [\text{Ox}]^\infty \quad [\text{Red}]^* = 0 \tag{2.30a}$$

$$t > 0 \qquad x \to \infty \qquad [\text{Ox}] \to [\text{Ox}]^\infty \quad [\text{Red}] \to 0 \tag{2.30b}$$

$$t > 0 \qquad x = 0 \qquad D_{\text{Ox}} \left(\frac{\partial [\text{Ox}]}{\partial x} \right) + D_{\text{Red}} \left(\frac{\partial [\text{Red}]}{\partial x} \right) = 0 \tag{2.30c}$$

$$0 < t \leq \lambda \qquad\qquad E = E_{\text{i}} - \nu t$$

$$t > \lambda \qquad\qquad E = E_{\text{i}} - \nu t + \nu(t - \lambda) \tag{2.30d}$$

with t being the time, x the distance from the electrode surface, $[\text{Ox}]^*$ and $[\text{Red}]^*$ the concentration of Ox and Red close to the electrode surface, respectively, $[\text{Ox}]^\infty$ the concentration of Ox in the bulk phase and λ the value of t when the potential is inverted.(35)

15

2. THEORETICAL BACKGROUND

2.2.1 Solution of the Boundary Value Problem

Reversible Systems   Solution of the diffusion equations 2.28 and 2.29 for a reversible (Nernstian) electrode reaction ($Ox + ne^- \rightleftharpoons Red$) requires the definition of a fifth, kinetic boundary condition. Assuming that only Ox is present in the solution at the beginning of the experiment, the electrode reaction is rapid (i.e. the respective concentrations [Ox] and [Red] instantly follow Nernstian predictions), and the excitation ramp is started in negative direction at a potential E_i where no electrode reaction occurs, this is the Nernst equation

$$\frac{[\text{Ox}]^*}{[\text{Red}]^*} = \exp\left[\frac{zF}{RT}(E - \nu t - E^{\ominus\prime})\right] \tag{2.31}$$

solved for the ratio of the concentrations of Ox and Red and reorganized in a way that it assumes a time-dependent form.(18) $E^{\ominus\prime}$ is a formal potential that is dependent on the reaction medium and includes the respective logarithmic activity coefficient terms as well as the standard electrode potential $E^{\ominus}$ so that it can be used if the Nernst equation contains concentrations instead of activities.(35) Randles(39) and Sevcik(40) were the first to provide a solution for this mathematical problem. The final result of solving the diffusion equations can be obtained by numerical inversion and written as

$$i = -zFA\,[\text{Ox}]^{\infty}\,(\pi D_{\text{Ox}}\sigma)^{1/2}\,\chi(\sigma t) \tag{2.32}$$

with

$$\sigma = \left(\frac{zF}{RT}\right)\nu \tag{2.33}$$

and

$$\sigma t = \frac{zF}{RT}(E_i - E) \tag{2.34}$$

The function $\chi(\sigma t)$ is a pure number at any given point with a maximum for $\pi^{1/2}\chi(\sigma t)$ of 0.4463. Eq. 2.32 thus gives the relation of the current and the remaining variables. In this equation the proportionality between current i and the square root of the scan rate $\nu^{1/2}$ as well as the bulk concentration $[\text{Ox}]^{\infty}$ can easily be seen. It can further be deduced that the peak potential E_p is independent of ν and that the difference between the anodic peak potential $E_{p,a}$ and the cathodic peak potential $E_{p,c}$ is $57.0\,\text{mV}/z$.

Irreversible Systems   In the case of a totally irreversible reaction ($Ox + ne^- \rightarrow Red$) elapsing in one step and with the transference of one electron the fifth, kinetic boundary condition for the solution of the diffusion equations 2.28 and 2.29 for a reduction is

$$D_{\text{Ox}}\frac{\partial[\text{Ox}]^*}{\partial x} = k_c\,[\text{Ox}]^* = k_c'\exp(bt)\,[\text{Ox}]^* \tag{2.35}$$

where

$$k'_c = k_0 \exp\left[\left(\frac{-z'F\alpha_c}{RT}\right)(E_i - E^{\ominus'})\right] \tag{2.36}$$

and

$$b = \frac{z'F\alpha_c\nu}{RT} \tag{2.37}$$

In this equations k_c is the rate constant for the cathodic reaction, α_c its activation energy, and k_0 the standard rate constant for which the cathodic is equal to the anodic rate constant ($k_c = k_a = k_0$).The number of electrons transferred in the rate-determining step is given by z'.

As for the reversible system a closed-form solution of the diffusion equations is not possible. Numerical inversion leads to

$$i_c = -zFA\,[\text{Ox}]^\infty\,(\pi D_{\text{Ox}}\nu)^{1/2}\left(\frac{z'F\alpha_c}{RT}\right)^{1/2}\chi(bt) \tag{2.38}$$

with i_c being the current of a cathodic process. If the reaction is irreversible with a reaction occurring in the anodic scan the anodic current i_a can be determined in an analogous fashion. The function $\pi^{1/2}\chi(bt)$ has its maximum at 0.4958. From eq. 2.38 one can see that the proportionality between i and the square root of the scan rate $\nu^{1/2}$ as well as the bulk concentration $[\text{Ox}]^\infty$ is still given. However, in contrast to the reversible case, the peak potential E_p is now dependent on the scan rate and peaks are shifted to more negative potentials (reduction), and are lower and broader.(35)

Quasi-reversible Systems Quasi-reversible systems are systems for which the electrode reaction shows kinetic electron-transfer limitations in one of the sweep directions. Matsuda and Ayabe(41) were the first ones to describe such behavior as *quasi-reversible* and provide a mathematical treatment of the problem. In general the irreversibility of a system increases with increasing scan rate (see figure 2.8) while the peak current decreases. Simultaneously the separation between anodic and cathodic peak potential increases compared to the reversible case.(35)

Solving the diffusion equations 2.28 and 2.29 for a quasi-reversible system includes solving the anodic and cathodic reaction concurrently and is thus more complex than for the reversible or irreversible case alone. Therefore a parameter Λ is introduced that describes peak form and position

$$\Lambda = \frac{k_0}{\left(D_{\text{Ox}}^{\alpha_c}D_{\text{Red}}^{\alpha_c}\sigma\right)^{1/2}} \tag{2.39}$$

and when $D_{\text{Ox}} = D_{\text{Red}} = D$

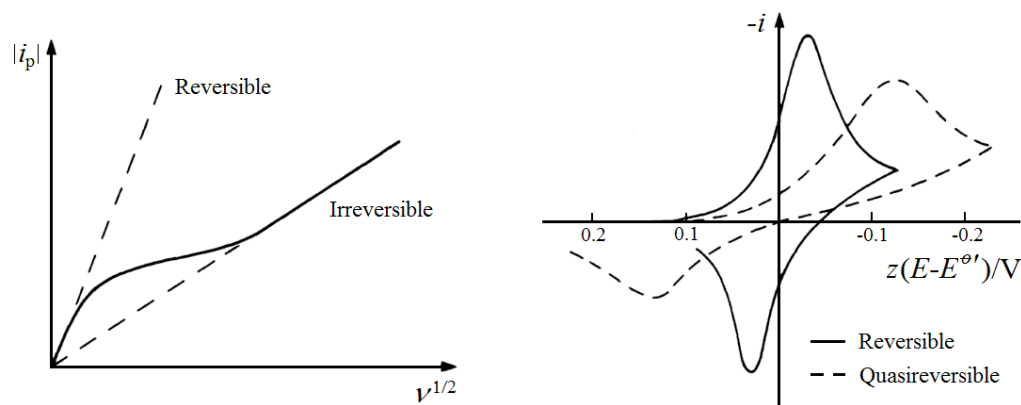$$\Lambda = k_0\left(D\sigma\right)^{-1/2} \tag{2.40}$$

Figure 2.8: Transition from reversible to irreversible behavior with increasing scan rate (left) and the effect this transition has on the course of a cyclic voltammogram (right).(35)

This factor, Λ, basically expresses the extend of a reaction's reversibility by giving the ratio kinetics/transport.(35) Typical values of Λ for reversible, quasi-reversible and irreversible reactions can be found in standard textbooks of electrochemistry.(18)(35)

2.2.2 Adsorption on Platinum Electrodes

The surface of a platinum electrode is very stable, reproducible and behaves like an ideal polarizable electrode (see fig. 2.3) in inert solutions in a potential range of 0.0 - 1.7 V vs. the reversible hydrogen electrode (RHE).(22) At an ideal polarizable electrode no charge transfer across the metal-solution interface takes place, reducing the system to the capacitive currents occurring due to charging of the electrical double layer and adsorption processes (see 2.1.3).

Adsorption of different species on its surface is the basis for platinum's catalytic properties and the determination of its *electrochemically active surface area* (ECSA). In contrast to an electrode's *geometric area*, which corresponds solely to its macroscopic dimensions, the ECSA is also often referred to as the catalyst's *real* surface area. In figure 2.9 the cyclic voltammogram of a bright, polycrystalline Pt surface in 0.5 M H_2SO_4 is shown. In it one can easily distinguish three discrete regions: the hydrogen region, the electrical double layer region and the oxygen region (see 2.2.3).

However, specific adsorption on platinum electrodes is not limited to hydrogen and oxygen species but has also been shown to occur with ions from the supporting electrolyte. For the investigation of the methanol oxidation reaction (MOR) hydrochloric acid and sulfuric acid are most commonly used as supporting electrolyte. It has been established for some decades now that the MOR on platinum electrodes is sensitive to

the choice of electrolyte(42)(43)(44) and that the effect depends strongly on the crystal face exposed. Bagotzky *et al.* investigated the blocking of platinum sites by supporting electrolyte for the (111) and (100) plane as early as 1971,(45) but it was only after Clavilier *et al.* found a way to prepare monocrystalline platinum electrodes of high quality (Clavilier method) in 1980(46) that the influence of different crystal faces on specific adsorption was resolved.

For the MOR to occur on a platinum electrode methanol must first be adsorbed (see 2.2.3). Additionally to the specific adsorption of this *electroactive* species, other *electroinactive* ions are adsorbed from the electrolyte. Thus, in case of sulfuric acid the blocking species has been identified to be sulfate ions, leading to much lower currents in the cyclic voltammogram of the MOR in sulfuric acid than in hydrochloric acid.(43) The difference is especially pronounced for the Pt(111) plane, on which the metal-ion interaction is strongest.(47)

2.2.3   Cyclic Voltammogram of Platinum in Acidic Solution

The Hydrogen Region   The hydrogen region extends from about 0 to 350 mV. In it the adsorption (negative scan) and desorption (positive scan) of hydrogen on the platinum surface take place following the reaction

$$Pt + H^+ + e^- \longrightarrow Pt-H \qquad \{2.2\}$$

The adsorption of hydrogen on platinum is denoted *hydrogen underpotential deposition* (H_{upd}) since it takes place at potentials less negative than the equilibrium potential predicted by the Nernst equation. It can be described by the Temkin isotherm, an isotherm for which the heat of adsorption q_θ is linearly dependent on surface coverage θ.(22) The two clearly discernible peaks in the anodic and cathodic sweep of this reversible hydrogen region of the cyclic voltammogram correspond to a weakly and a strongly bound form of hydrogen.(49)

Starting in the double layer region at 400 mV, where the platinum surface is free of adsorbed hydrogen, and following a cathodic scan direction the adsorption of hydrogen begins at about 350 mV on the platinum sites with the highest heat of adsorption, giving rise to the first peak in this region corresponding to strongly bound hydrogen. When the scan is continued towards more negative potentials the heat of adsorption decreases due to the increasing surface coverage and we observe a second peak, corresponding to a weakly bound form of hydrogen. At potentials lower than 0 mV the bulk formation of gaseous hydrogen begins. Upon inversion of the scan direction at this point the desorption of the two forms of hydrogen takes place in a reversible fashion
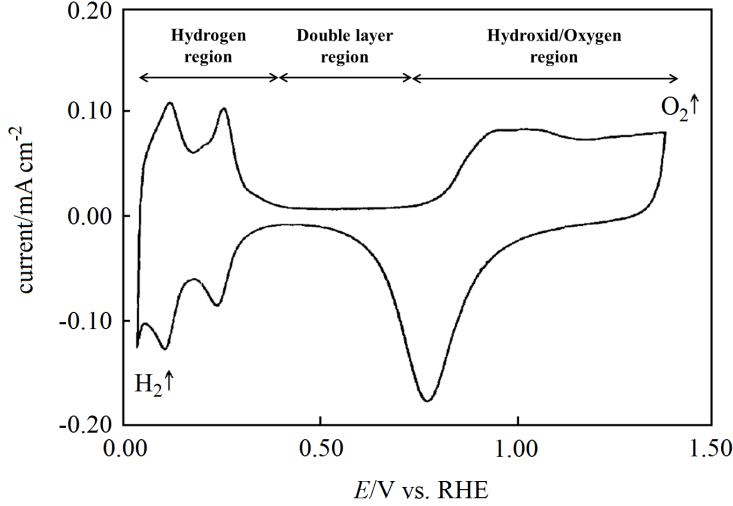
Figure 2.9: Cyclic voltammogram of a bright, polycrystalline Pt surface in $0.5\,\text{M}\ H_2SO_4$ recorded at a scan rate of $0.050\,\text{V}\,\text{s}^{-1}$.(48)

that allows us to interpret this region of the voltammogram thermodynamically.

It has been shown that a monolayer of hydrogen is adsorbed or desorbed on a platinum surface in solution in the potential region between 0 - $350\,\text{mV}$, where each platinum surface atom binds to one hydrogen atom. The charge Q_H associated with this process is slightly different for platinum's main low-index faces, so for polycrystalline platinum an average value corresponding to an atom surface density of $1.31 \times 10^{15}\,\text{cm}^{-2}$ is used. After correction for double layer charging an overall charge per unit area of $210\,\text{mC}\,\text{cm}^{-2}$ for the adsorption or desorption of hydrogen on a polycrystalline platinum surface is obtained from this.(50) The electrochemically active surface area of a platinum electrode can thus easily be determined by integration of the hydrogen region of a cyclic voltammogram via

$$\text{ECSA} = \frac{Q_H}{210\,\text{mC}\,\text{cm}^{-2}} \tag{2.41}$$

The Double Layer Region   The region following the hydrogen region in anodic direction is the double layer region (approx. 350 - $650\,\text{mV}$) in which the only occurring process is the charging of the electrical double layer.

The Hydroxide/Oxygen Region   Beginning at $650\,\text{mV}$ the hydroxide/oxygen region then follows. In it, the formation of platinum hydroxide and, beginning at a

potential of approx. $800\,mV$, the formation of platinum oxide, commence

$$Pt + H_2O \longrightarrow Pt{-}OH + H^+ + e^- \qquad\qquad \{2.3\}$$

$$2\,Pt{-}OH \longrightarrow Pt{-}O + Pt + H_2O \qquad\qquad \{2.4\}$$
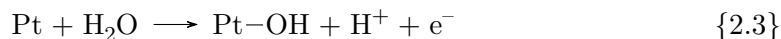
In contrast to the hydrogen region, the hydroxide/oxygen region is not reversible (at least not if an upper potential vertex of over $950\,mV$ is chosen).(51) At approx. $1600\,mV$ bulk oxygen formation takes place. After inversion of the scan direction the beginning desorption of oxide from platinum can be observed at a potential of approx. $1000\,mV$. This generates a cathodic current that increases until the oxide coverage becomes the limiting factor, thus forming a platinum oxide reduction peak at approx. $800\,mV$. This peak is followed by a short cathodic double layer region that passes on to the hydrogen region at approx. $350\,mV$ again, thus completing the cycle.(49)

2.2.4   The Methanol Oxidation Reaction

The oxidation of methanol on platinum is an example for a multi-step, non-reversible electrochemical reaction. The corresponding cyclic voltammogram is shown in figure 2.10 for two different potential ranges. The overall reaction

$$CH_3OH + H_2O \longrightarrow CO_2 + 6\,H^+ + 6\,e^- \qquad\qquad \{2.5\}$$

follows a stepwise six-electron transfer mechanism. The thermodynamic equilibrium potential of this reaction ($\Delta E^{\ominus} = 0.02\,V$) lies close to that of hydrogen, but since six electrons are needed for the complete oxidation of methanol the kinetic of this process is several orders of magnitude slower.(52)

Adsorption and dehydrogenation of methanol requires several free neighboring sites on the catalyst surface. Since methanol is not able to displace hydrogen from the surface, methanol adsorption starts as soon as the potential is positive enough for hydrogen to desorb ($200\,mV$ on polycrystalline platinum).(52) Once methanol has been adsorbed it decomposes via successive $C{-}H$ and $O{-}H$ bond activation steps via a dual path mechanism as was shown by Cao *et al.* employing a combination of chronoamperometry, cyclic voltammetry and theoretical methods.(54) Below $350\,mV$ the predominant path is governed by $C{-}H$ bond activation and subsequently leads to the formation of hydroxyl methylene, which above $350\,mV$ reacts via $O{-}H$ bond activation to give formaldehyde

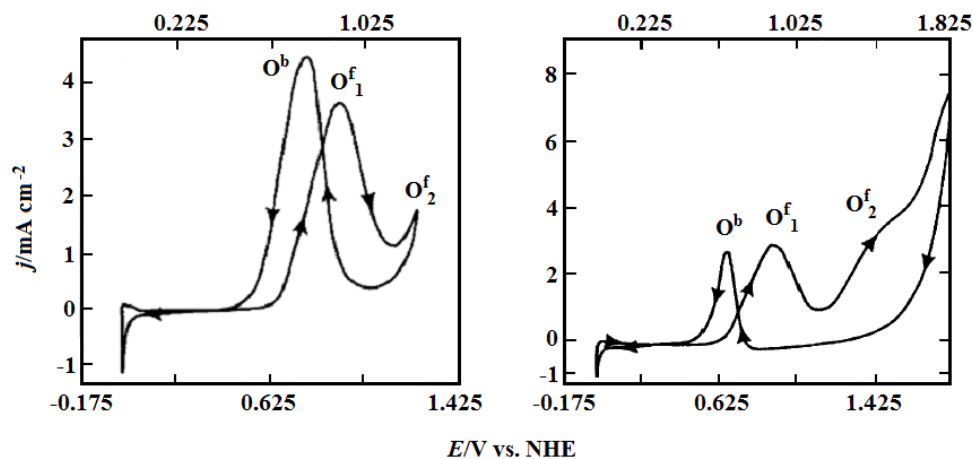**Figure 2.10:** Cyclic voltammogram of Pt in $1.0\,M$ MeOH in $2.5\,M$ H_2SO_4 recorded at a scan rate of $0.025\,V\,s^{-1}$ for a potential range from 0 - $1.250\,V$ (left) and from 0 - $1.825\,V$ (right).(53)

and finally carbon monoxide.

$$CH_3OH + Pt \longrightarrow Pt{-}CH_2OH + H^+ + e^- \qquad \{2.6\}$$

$$Pt{-}CH_2OH + Pt \longrightarrow Pt_2{-}CHOH + H^+ + e^- \qquad \{2.7\}$$

$$Pt_2{-}CHOH + Pt \longrightarrow Pt_3{-}CHO + H^+ + e^- \qquad \{2.8\}$$

$$Pt_3{-}CHO \longrightarrow Pt{-}CO + 2\,Pt + H^+ + e^- \qquad \{2.9\}$$
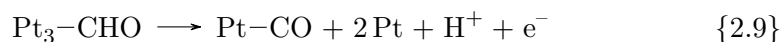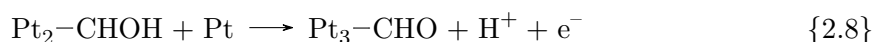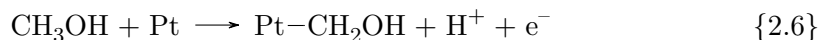
Additionally to this path alternative routes with more endothermic reaction energies are feasible (see figure 2.11). The hydration of solvated formaldehyde leads to the formation of methanediol in an equilibrium process.(55) Methanediol can then dehydrogenate to give formic acid, which in turn can dissociatively adsorb on the platinum surface under the formation of formate,(56) which has been observed experimentally and was found to be an active intermediate in the oxidation of methanol to carbon dioxide,(57) especially at lower potentials. At more positive potentials the formation of carbon dioxide via adsorbed carbon monoxide is promoted additionally and hence current efficiencies in this region are higher.(58)

The question whether the dehydrogenation steps commence *heterolytic*, i.e. via the formation of a solvated H_3O^+ species while the released electron is donated to the metal surface, or *homolytic*, i.e. by formation of an intermediate $Pt{-}H$ species which in turn protonates a water molecule while the metal retains the electron, has been

Figure 2.11: Schematics of the pathways found for the dehydrogenation of methanol on platinum according to Cao *et al.* with the predominant pathway at a potential of $500\,\mathrm{mV}$ vs. the normal hydrogen electrode (NHE) indicated by plain arrows.(53)

discussed at length and it's the heterolytic pathway that has been confirmed to control dehydrogenation.(59)(60)(61)

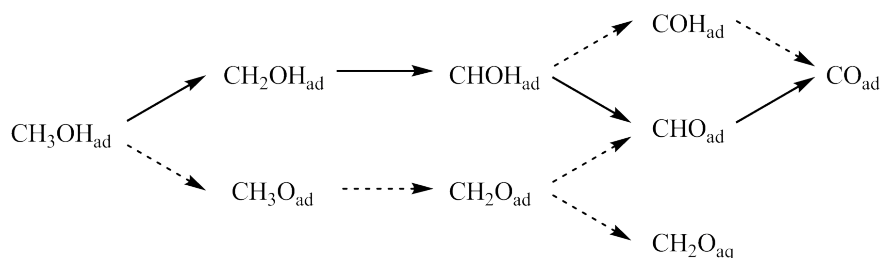In equation 2.9 the adsorbed carbon monoxide species has been depicted as a singularly bonded form. However, different CO_{ad} bonding modifications have been observed via IR measurements, namely linearly (CO_L) and bridge (CO_B) bonded carbon monoxide with bands at approx. 2060 and $1850\,\mathrm{cm}^{-1}$, respectively.(52) This adsorbed carbon monoxide is a very stable intermediate and has been found to be the species responsible for the gradual poisoning of the catalyst,(49) at least in so far as CO_{ad} is the species that accumulates on the surface at low potentials because not enough water is dissociated by platinum in those potential region to oxidize all present CO_{ad}.(52)

$$H_2O + Pt \longrightarrow Pt{-}OH + H^+ + e^- \qquad \{2.10\}$$

$$Pt{-}OH + Pt{-}CO \longrightarrow CO_2 + 2\,Pt + H^+ + e^- \qquad \{2.11\}$$
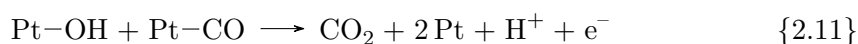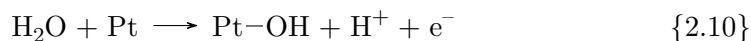
Adsorption of water on platinum slowly sets in at potentials higher than $400\,\mathrm{mV}$ and seriously begins at potentials of approx. $800\,\mathrm{mV}$ (see section 2.2.2). It leads to an increasing oxidation and thus an increasing current of the adsorbed carbon monoxide. At even higher potentials the adsorption of water becomes dominant over methanol adsorption leading to a decreasing formation of carbon dioxide and thus to the occurrence of a current peak (O_1^f) in this region. At even more positive potentials the formation of oxygen sets in, freeing platinum sites for the adsorption of fresh methanol which is then oxidized giving rise to a second peak (O_2^f) in the forward going sweep.(62) Upon inversion of the scan direction the coverage of the platinum surface with oxygen and hydroxide decreases steadily, allowing the increasing adsorption of fresh methanol which is then oxidized to carbon dioxide forming a peak (O^b) when adsorbed oxygen species at the platinum surface become rare again due to the decreasing potential.
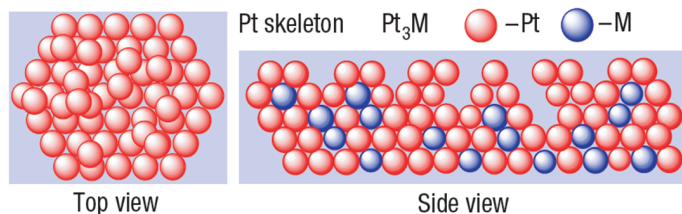
Figure 2.12: Schematic model of the platinum surface skeleton developing under potential cycling of a platinum alloy with a 3d metal.(67)

The methanol oxidation reaction thus entails the following intermediate steps: dehydrogenation, chemisorption of CO-like species, specific adsorption of oxygen-containing species (OH or H_2O), chemical interaction between OH and CO on the surface and finally the formation of CO_2.(63) Exactly which step is the rate determining step in this sequence depends on operation temperature and on the particular catalyst surface (crystallographic face, presence of defects, etc.).(64)(65)

2.2.5 Behavior of Platinum Alloys under Electrochemical Conditions

Surface segregation In electrocatalysis the use of alloys instead of pure platinum has proven to yield beneficial results (see section 2.3.1). For this reason the effect of an electrochemical environment on platinum alloys, among them the ones alloyed with 3d transition metals (Pt-M, with M = Fe, Co, Ni, etc.) which show enhanced catalytic activity for the oxygen reduction reaction as well as the methanol oxidation reaction, has been extensively studied.(66)(6) In this context it was repeatedly reported that upon potential cycling under acidic conditions a dissolution or leaching of the 3d metal takes place, leading to a so called *platinum skeleton surface* (see figure 2.12).(67) The platinum skeleton surface is usually distinguished from the *platinum skin surface*, a smooth structure that forms under annealing at elevated temperature (e.g., 600 K(68) or 1000 K(66)) in ultra high vacuum (UHV).

The platinum skin surface structure features an outer layer that is enriched in platinum atoms compared to the overall composition. This layer is followed by a subsurface second atomic layer that is richer in the alloying metal M as compared to the overall composition and finally a third layer with slightly higher platinum content before bulk composition is observed again, thus earning this structure the name "sandwich structure".(67)(69)(68) However, this sandwich-like structure is not found for the platinum skeleton surface, where the bulk composition is observed for the atomic layers following the outer platinum skeleton structure.(66)
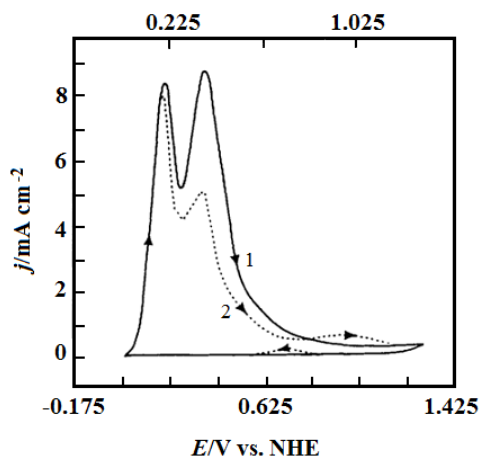
Figure 2.13: Cyclic Voltammogram of nickel in (1) 2.5 M H_2SO_4 and (2) 1 M MeOH in 2.5 M H_2SO_4. Both voltammograms were recorded at a scan rate of 0.020 V s^{-1}.(53)

Since it is the effects governing catalytic properties that are of paramount interest in the context of all these investigations, the activity and stability of above mentioned surfaces were thoroughly investigated using cyclic voltammetry and an array of spectroscopic methods. It was found that platinum skin surfaces presented both a higher activity for the ORR and a better stability than platinum skeleton surfaces, at least in so far as that their structure does not change further under potential cycling.(66) Compared to polycrystalline platinum, however, both the platinum skeleton and skin surfaces showed elevated catalytic activity for the ORR.(67) The reason for this will be further elucidated in section 2.3.1.

Cyclic Voltammetry of Nickel in Acidic Solution   In fig. 2.13 a cyclic voltammogram of bulk nickel in sulfuric acid solution (bold curve) and another one after the addition of methanol to the solution (dotted line) is shown. As can clearly be seen by the two peaks between 0 and 600 mV in both curves, dissolution of nickel takes place in this potential region. It is further noteworthy that even in the absence of platinum or another designated MOR catalyst a slight MOR activity can be observed for pure nickel as indicated by the presence of the typical $I(O_1^f)$ and $I(O^b)$ peaks.(53)

When nickel or nickel oxide are exposed to air or aqueous solutions, a passive film of several atomic layers thickness forms, consisting of two distinct layers. A nickel hydroxide layer forms at the interface to the air and a nickel oxide layer forms between this outer layer and the metal substrate.(70) The mechanism for this process can be

summarized as

$$Ni + H_2O \longrightarrow NiOH + H^+ + e^- \qquad \{2.12\}$$

$$NiOH + H_2O \longrightarrow NiOH \cdot H_2O \qquad \{2.13\}$$

$$NiOH \cdot H_2O \longrightarrow Ni(OH)_2 + H^+ + e^- \qquad \{2.14\}$$

for a Ni surface or as

$$NiO + H_2O \,(physisorbed) \longrightarrow NiO \cdot H_2O \longrightarrow Ni(OH)_2 \qquad \{2.15\}$$
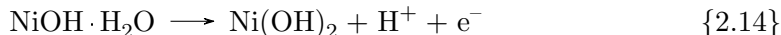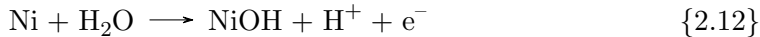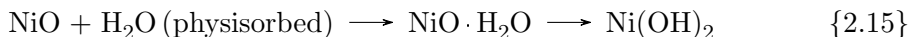
for a NiO surface.(71) Following this mechanism nickel nanoparticles (NPs) form a core-shell structure with a metallic core and a $NiO + Ni(OH)_2$ shell, as could be shown via X-ray photoelectron spectroscopy (XPS).(72) According to Manoharan and Goodenough a very similar mechanism to the one shown above is proposed for the dissolution of Ni in acidic solution, with the addition that at more anodic potentials the Ni^{2+} ion dissolution is replaced by the formation of a stable Ni^{3+} oxyhydroxide.(53) This process can be represented by

$$NiOH + H_2O \longrightarrow NiOOH + 2\,H^+ + 2\,e^- \qquad \{2.16\}$$
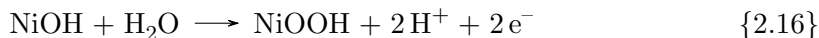
The forming Ni^{2+}/Ni^{3+} redox couple has a standard electrode potential of $0.49\,V$ vs. SHE(73) and follows the reaction equation

$$NiOOH + H_2O + e^- \longrightarrow Ni(OH)_2 + OH^- \qquad \{2.17\}$$

2.3   Electrocatalysis

In their excellent paper on electrocatalysis Guerrini and Trasatti distinguish between "real" and "apparent" electrocatalytic behavior.(74) According to their definition "real" electrocatalysis takes place if *electronic factors*, i.e. surface structure or composition, are responsible for the lowering of the activation energy commencing and/or the change of reaction mechanism that are the very core of every catalytic process. "Apparent" electrocatalysis exists if the origin of the catalytic effect is due to a mere extension of the surface of the electrode material. Using nanoparticles instead of the same material in its bulk form for an electrochemical conversion thus is not "real" electrocatalysis, although the rate (molar amount transformed per unit area, see eq. 2.19) of the reaction will be higher in the former case due to the higher surface area of the particles as compared to the bulk surface area. However, this is not to say that the material in itself, independently of its modification, can not be an electrocatalyst.

One of the most important heterogeneous catalysts is platinum, which plays a major role in electrocatalysis as well,(49) for example in context with the hydrogen evolution reaction(75) the oxygen reduction reaction(76) as well as the methanol oxidation reaction(76)(52). Heterogeneous catalysis and electrocatalysis have much in common, however, one major difference is the fact that electrocatalytic processes depend not only on given system parameters (like temperature, concentration of reactant and surface state of the catalyst) but additionally on the applied potential. "Thus, in a given system, the potential can be varied by a few tenths of a volt, while as a result, the reaction rate will change by several orders of magnitude."(22) as Bagotsky stated it in his comprehensive and intelligible textbook "Fundamentals of electrochemistry". For a historical treatise of the topic the reader is referred to this textbook or the following publication of Bockris.(77) More detailed information on the cross-cut between electrocatalysis and heterogeneous catalysis can be found here.(78)

As mentioned above, the main concern of electrocatalysis is to determine the factors that influence the rate of electrochemical reactions. In that regard electrocatalysis is closely related to electrochemical kinetics. Whereas electrochemical kinetics is interested in the absolute rate of electrochemical reactions, however, electrocatalysis is concerned with finding out which influence the catalyst has on this rate. Electrochemical kinetics are investigated primarily from data obtained under steady state conditions. The equation most often associated with these investigations is the Tafel equation, which describes the linear regions in the the Butler-Volmer equation. The Tafel equation

$$\eta = a + b \log j \tag{2.42}$$

correlates the overpotential η (see section 2.1.4) to the current j with a and b being constants that are dependent on the exchange current density j_0 and the transfer coefficient α. The exchange current density is the current density at which anodic j_+ and cathodic j_- current density are in equilibrium ($E = E_0$) and no net current flows

$$j_0 = j_+(E_0) = j_-(E_0) \tag{2.43}$$

The transfer coefficient α can range from zero to unity and describes to what extend a change in potential influences the accompanying change in activation energy for a given reaction. It is part of the Butler-Volmer equation

$$j = j_0 \left[\exp \left(\frac{-\alpha n F \eta_{\mathrm{ct}}}{RT} \right) \right] - \left[\exp \left(\frac{(1-\alpha) n F \eta_{\mathrm{ct}}}{RT} \right) \right] \tag{2.44}$$

here given for a reaction for which charge transfer is the rate-determining step. Tafel

and Butler-Volmer equation relay on transition state theory (activated-complex theory) and the respective free activation enthalpy. Since this is the very value that changes with catalysis these equations are suitable for investigating such processes.(79)

Non-steady state methods like CV and LSV also are suitable candidates for investigating electrocatalytic phenomena.(80) One big advantage of this methods is the possibility to ascertain the active surface area of the catalyst (see section 2.2.2). CV is often used to qualitatively study catalyst activity by either comparing relative activities of different catalysts towards the same reaction or by evaluation of one catalyst for different reactions. The activity is assessed by either the onset potential or the peak current. A higher activity will lead to a lower onset potential and a higher peak current. The Methanol oxidation reaction for example is commonly studied via cyclic voltammetry in acidic media using mainly the peak current as qualitative probe.(81) This can be done because "current is an expression of rate"(37) as was already derived in eq. 2.19 as well as eq. 2.22. Nonetheless, modern approaches in electrocatalysis make use of a multitude of methods, by far not all of them electrochemical, to investigate the three most important features of any catalyst: activity, stability and selectivity.(7)

2.3.1   Enhancement of Catalytic Activity through Alloying

In the search for ways to enhance platinum's electrocatalytic properties it was found that alloying with other metals (e.g. Sn, W, Ru) yielded positive results with respect to the electrocatalytic oxidation of methanol.(76) Among the 3d transition metals especially alloys with cobalt and nickel were investigated in regard to their ability to enhance the MOR.(6)(82)(12) The reason for an enhanced catalytic activity in this context is usually attributed to a better CO-tolerance and/or a better C−H activation of such alloyed electrocatalysts. The enhancement can thus be explained by an electronic effect. However, a bifunctional mechanism and an ensemble effect have also been proposed as reason for the catalytic enhancement of such alloys.(12)(83)(84)

The *electronic effect* is based on an increased d-vacancy which in turn leads to a smaller contribution of back-donation of Pt 5d electrons to the respective orbitals of the adsorbed molecule, e.g., the CO $2\pi^*$ orbital thus resulting in a weaker Pt-CO bond strength and therefore a lower CO coverage.(85) This circumstances are depicted in figure 2.14 for the case of a platinum skin surface of a PtFe alloy (see section 2.2.5). However, a change in the electronic properties of PtNi and PtCo disks has been identified by a d-vacancy shift via XPS(86) as well as for PtRu(87) early on as well.

According to the *bifunctional mechanism*, the better CO-tolerance of platinum alloys is due to the presence of an increased number of O-type species on the alloying metal
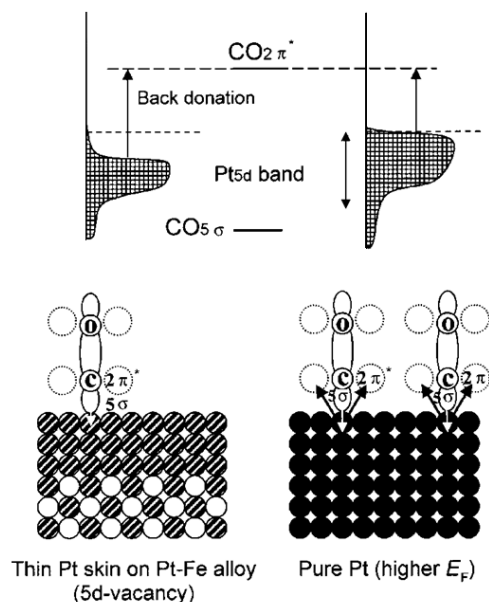
Figure 2.14: Schematic explanation of the decreased CO coverage on a Pt skin layer formed on an alloy such as PtFe.(85)

atoms, which are needed to oxidize carbon monoxide to carbon dioxide (see section 2.2.4) and thus recover active surface sites.(88) The *ensemble effect* describes a geometric arrangement of the atoms in the surface structure of a catalyst which, as a well-defined and isolated ensemble, enhances catalytic activity and selectivity.(89) However, which effect has the greatest share in the catalytic enhancement that platinum alloys generally show in comparison to pure platinum is hard to determine.

2.3.2 PtNi as Electrocatalyst for the MOR

Compared to the ORR the number of publications concerned with the MOR is rather small. Promising catalysts investigated in this context include PtRu, PtOs, PtSn, PtW and PtMo, etc.(5) Platinum alloyed with 3d metals has gained some interest as well, as these metals lower the electronic binding energy of platinum thus promoting the C–H cleavage reaction at a lower potential compared to pure platinum. In addition to this electronic effect a bifunctional mechanism provides oxygen species at the catalyst surface at low potentials, whereas an ensemble effect occurring for these alloys hinders the MOR. This is due to a dilution effect, meaning that not as many atoms of the same kind (Pt) lie adjacent to each other, a prerequisite for the dissociative chemisorption of methanol (see section 2.2.4).(6)

2. THEORETICAL BACKGROUND

The electro-oxidation of methanol is a very sensitive reaction which does not only depend on conditions such as temperature, electrolyte and alcohol concentration but also very much on the way the electrode was prepared.(90) In this context differential electrochemical mass spectrometry (DEMS) and Fourier transform infrared spectroscopy (*in situ* FTIR) studies showed that both the product distribution, and therefore the mechanism of the MOR, as well as the potential at which the reaction starts, depend strongly on experimental details.(91)(92)(93) In this regard the pH, anion adsorption characteristics of the electrolyte, the surface oxide coverage, the structure of the working electrode (e.g., catalyst loading) as well as the details of the experimental setup such as the sweep rate of CV or the applied potential in CA investigations are important factors.(90)

A discussion of the historical development of anode catalysts for the direct methanol fuel cell can be found in (63). Nowadays, the most promising catalyst for the anode in terms of bimetallic platinum alloys is believed to be PtRu.(5)(83) Nonetheless, PtNi has attracted quite some research interest as well. Park *et al.* investigated the electronic effect of Ni in PtNi nanoparticles and thin film electrodes and found the best catalytic activities for the MOR for a composition of 1:1 (Pt:Ni) as compared to compositions of 3:1 or 1:3. These findings were accompanied by a a shift in the Pt 4f peak, indicating a modification of the electronic structure of the alloy, as was shown by XPS.(84) Park *et al.* also found lower onset potentials for 1:1 PtNi and 1:1 PtRu nanoparticles in their CV investigation as compared to pure platinum and higher currents for both sets of particles in their CA experiments.(12)

Fowler *et al.* investigated the effect of surface segregation and stability on the basis of Pt_3Ni nanoparticles and $Pt_3Ni(111)$ surfaces with respect to the ORR. They found a higher stability for the $Pt_3Ni(111)$ surface exhibiting a platinum skin surface (see section 2.2.5) as compared to a pure Pt(111) surface. This difference was assigned to a modification in the electronic structure of the alloy (lower d-band center) which in turn lead to a weaker interaction with adsorbed OH, thus decreasing the amount of OH_{ad} so that there is less tendency for place exchange with the platinum surface atoms and therefore for irreversible roughening.(69)

Wang *et al.* investigated PtNi nanoparticles of different compositions also with respect to their catalytic activity for the ORR. They reported that out of Pt_3Ni, PtNi, $PtNi_2$ and $PtNi_3$ the nanoparticles with 1:1 composition showed the highest activity and that for all investigated particles a surface skeleton structure formed under electrochemical conditions.(94)

Wang *et al.* examined platinum-decorated nickel nanoparticles that were prepared by a galvanic displacement reaction between Ni nanoparticles on carbon black (denoted

Ni/C) and $PtCl_6^{2-}$ in aqueous solution and found an enhancement of methanol oxidation reaction compared to pure platinum and RuPt.(88) Liu *et al.* prepared segmented nanorods as model bifunctional catalysts for the methanol oxidation reaction(95)(96) whilst others worked with PtNi catalysts on different carbon supports, e.g. graphene(97) or carbon nanotubes.(98)(99) A detailed review covering the methanol oxidation reaction on platinum alloys with the first row transition metals Ni and Co was published by Antolini.(6) He found conflicting reports about the modification of the MOR using PtCo and PtNi as electrocatalyst, especially regarding the question weather alloying with cobalt or nickel were able to enhance the MOR. A review on anode catalysts for the DMFC focusing on different methods of catalyst preparation and supports can be found here.(5) Tiwari *et al.* published a review on recent progress in the development of both anode and cathode catalyst for the DMFC.(100)

2.4 Fuel Cells

When Swiss scientist Schönbein reported the observation of an electrical current as a consequence of combining hydrogen and oxygen in 1838 he had discovered the fuel cell principle. However, it was Sir William Grove who in 1839 probably built the first real fuel cell when he experimented with a setup that consisted of a hydrogen anode and an oxygen cathode. In 1950 Sir Francis Bacon presented the first alkaline fuel cell and shortly after NASA equipped their space shuttles with such fuel cells.(17)

Fuel cells are capable of producing energy by directly converting the chemical energy of a fuel (hydrogen, methanol, ethanol etc.) into electrical energy. The fuel is consumed in a cold combustion under the formation of water and, depending on the form of fuel used, other direct reaction products. In addition to offering an alternative to the production of energy from fossil fuels, the use of fuel cells instead of conventional power sources thus decreases waste and pollution generated from burning combustible fuels.(101) Nowadays, there are six major types of fuel cells that researchers and developers are working on.(17)

- **AFC** The alkaline fuel cell runs with an electrolyte of aqueous potassium hydroxide solution and has a working temperature of around 90 °C

- **DMFC** The direct methanol fuel cell runs with methanol and has a low working temperature between 50 and 120 °C

- **MCFC** The molten carbonate fuel cell runs with an electrolyte of alkali carbonates in a ceramic matrix and has a working temperature between 600 and 700 °C
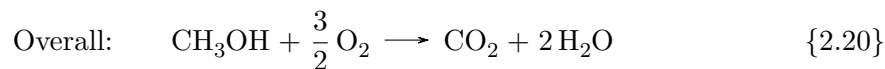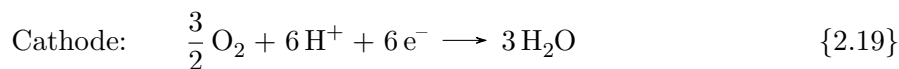
- **PAFC** The phosphoric acid fuel cell runs with phosphoric acid as electrolyte and has a working temperature between 100 and 250 °C

- **PEMFC** The polymer electrolyte membrane or proton exchange membrane fuel cell has a solid polymer membrane electrolyte and a working temperature around 80 °C

- **SOFC** The solid oxide fuel cell has a solid ceramic electrolyte and a working temperature between 700 and 1000 °C

In the following section the direct methanol fuel cell will be introduced in some greater detail, since it is the anode reaction of this cell, the methanol oxidation reaction, the investigations in this work are centered around.

2.4.1 The Direct Methanol Fuel Cell

The DMFC is basically a PEMFC that is run with liquid methanol as anode fuel. The cell is denoted "direct" methanol fuel cell because it uses methanol directly instead of reforming it first and running with the formed hydrogen. The DMFC is promising especially in respect to its use for portable power devices, because of its low operating temperature, its quick-start characteristics, the convenience, safety and sustainability of generating energy from a liquid and renewable fuel as well as low emissions of environmental pollutants.[9][102] Methanol has a high net energy density of $5.26 \, \text{kW h kg}^{-1}$[101] and a thermodynamic cell voltage of $1.21 \, \text{V}$.[14] The chemical reactions generating electrical energy in a DMFC are the oxidation of methanol at the anode and the reduction of oxygen from air at the cathode.

$$\text{Anode:} \quad CH_3OH + H_2O \longrightarrow CO_2 + 6\,H^+ + 6\,e^- \qquad \{2.18\}$$

$$\text{Cathode:} \quad \frac{3}{2}\,O_2 + 6\,H^+ + 6\,e^- \longrightarrow 3\,H_2O \qquad \{2.19\}$$

$$\text{Overall:} \quad CH_3OH + \frac{3}{2}\,O_2 \longrightarrow CO_2 + 2\,H_2O \qquad \{2.20\}$$

Despite intensive research over the past decades problems concerning the electrocatalyst for the MOR still remain. Those are mainly the high costs caused by the requirement of platinum as electrocatalyst, the relatively slow electrode kinetics of the six electron transfer reaction at the anode, and the poisoning of the electrocatalyst due to intermediately formed carbon monoxide.[5][8] Another problem in the development of the DMFC is the methanol crossover from the anode to the cathode side causing a mixed

potential and thus a performance degradation.(6) The two main challenges in the commercialization of the DMFC thus regard the electrocatalyst and the polymer electrolyte membrane.

2.4.2   Nanostructured Catalysts in Fuel Cells

Nanoparticles are ideally suited for their use in catalytic applications due to their high surface-to-volume ratio as well as their size, shape, composition, and morphology dependent properties, which in turn allow a fine tuning of their catalytic features.(8) In the field of fuel cell research binary Pt alloy systems in particular have gained increasing attention due to their lower costs compared to pure platinum catalysts, their enhanced electrocatalytic activity, and their better resistance to CO poisoning.(9)

Although many advances have been made in this context in recent years, the development of a low-cost, robust and efficient catalyst still remains the crucial factor for fuel cells to become broadly commercially available.(14) A lot of research has been done to ascertain the optimal combination of particle properties for a given reaction, e.g. the ORR or the MOR. Often, such investigations are done using a glassy carbon (GC) substrate as electrode onto which a *catalyst ink* (also called *supported catalyst*), consisting of the particles under investigation, carbon black (e.g. Vulcan XC-72, Ketjen Black, etc.) and Nafion, a proton-conducting Teflon-like polymer, is deposited. The resulting glassy carbon electrode (GCE) is then subjected to electrochemical measurements, such as cyclic voltammetry, chronoamperometry, or the recording of polarization curves in order to ascertain the particles catalytic activity for the investigated conversion.

In order to exploit the full catalytic capacity of a specific kind of nanoparticle, e.g., nanoparticles of a certain size, shape, and composition, alloyed or of the core-shell type, it is mandatory for the particle batch to exhibit a narrow size distribution and a homogeneous composition and morphology. If those requirements are not met, the properties of the particle ensemble will be inhomogeneous. This will not only prevent a sensible characterization but also lead to a lower catalytic activity. Nanoparticles from solution synthesis, which are gained via the hot injection method, have been shown to possess the desired properties.(10) They are, however, usually capped by organic ligands which block catalytically active sites on the particle surface and therefore need to be removed in order to exploit the full catalytic potential. Different treatments for ligand removal have been proposed, including chemical washing, heat, and oxidation treatment.(11)

Agglomeration   The words *agglomeration* and *aggregation* are often used interchangeably, a condition that, in the words of Nichols *et al.* is an "unacceptable situation".(103) They propose to restrict the term agglomeration to phenomena of particle assemblage, exclusively. The term aggregate in contrast is supposed to be used only in connection with "prenucleation structures that arise from the association of molecules into supramolecular structures". This work will follow their proposed terminology.

Particle agglomeration is an important issue in fuel cell development, where finely dispersed noble metal particles are used to maximize the catalytic surface area.(13) Agglomeration is a phenomenon that decreases the ECSA of a catalyst. However, due to the often simultaneous formation of surface defects, which are well-known to be particularly catalytically active in carbon monoxide oxidation,(104) during the agglomeration process, enhanced catalytic activity has been reported as well.(13)(105) As Somorjai puts it: "Rough surfaces do chemistry".(106) However, it has to be kept in mind that there is a distinction between "multi-grained" agglomerates with many step and defect sites and fully coalesced particles forming one homogenous new structure and that these forms of agglomerates may behave very differently in respect to electrocatalytic activity.

Surface segregation (see 2.2.5) and agglomeration under electrochemical conditions lead to a change of structure, size, shape, and composition of the electrocatalyst and therefore to the need to investigate the forming agglomerates in regard to their electrocatalytic properties.(14) Particle agglomeration may not only occur during electrochemical measurements, but also due to other treatments such as the aforementioned catalyst activation through treatments for ligand removal (see 2.4.2). Flat surfaces are ideal model systems for the study of agglomeration phenomena since changes of the particulate structure can easily be followed by methods such as scanning electron microscopy, transmission electron microscopy (TEM), and atomic force microscopy (AFM). Important factor determining the degree of agglomeration are particle–particle interactions and the particle–substrate interactions. A quantitative contemplation of this topic can be found here.(14)

2.5   Catalytic Nanoparticles

Metallic nanoparticles exhibit many chemical and physical properties that are markedly different from those of the respective bulk material.(107) Among those the size and shape dependent properties, including the interatomic bond distance and the melting point(108) as well as optical and electronic properties and thus chemical reactivity(104)

are especially interesting. Furthermore, the great surface-to-volume ration of nanoparticles makes them very promising candidates for their application as heterogeneous catalysts. Recently, the use of bimetallic nanoparticles as a way to improve catalytic activity and durability in addition to reducing the amount of precious metals necessary has shown great advantages in comparison to monometallic nanoparticles.(109) The most important properties determining catalytic activity of a batch of nanoparticles can thus be summarized to include their size, shape, and composition. Some other important factors influencing catalytic activity will be discussed in 3.6.

As was already mentioned in 2.4.2 nanoparticles gained via solvothermal synthesis following the hot injection approach have been shown to allow excellent control over size and composition of the synthesized nanoparticles while leading to a small size distribution and homogenous compositional distribution in the obtained particle batch.(10) This is important because the uniformity of a particle batch is directly related to the homogeneity of its physical and chemical properties(110) and thus to an optimization of factors such as catalytic activity. For that reason the hot injection approach and the nucleation and growth principles governing the size, shape, and composition of the forming nanoparticles will be introduced in the next sections.

2.5.1 Formation of Nanoparticles

The hot injection method is one of two approaches that have been extensively studied in the last decades because of their ability to produce uniform nanoparticles with distinct crystallinity, sometimes called nanocrystals. Besides the hot injection approach it is the use of heat up techniques that is most favorable in the formation of such uniform nanocrystals. However, since in this work the hot injection method was employed exclusively, the following discussion will focus on this approach. Furthermore, the term "nanoparticle" will be used instead of "nanocrystal", non the less describing a *crystalline* nanoparticle in doing so.

The hot injection method is a bottom-up approach which is based on the phenomenon of self-organization of atoms through collision and the following nucleation which is the starting point for the formation of nanoparticles. The basic concepts describing these processes and the origin of the resulting size distribution of the particle batch are burst nucleation, growth from excess monomers and Ostwald ripening.(110)

Burst Nucleation Nucleation describes a process in which the formation of a new phase is induced in another phase. For this process to commence the presence of a seed species in the initial phase is necessary. At the interface of this seed species and the ambient phase, often a solution, crystallization may set in. The process of this
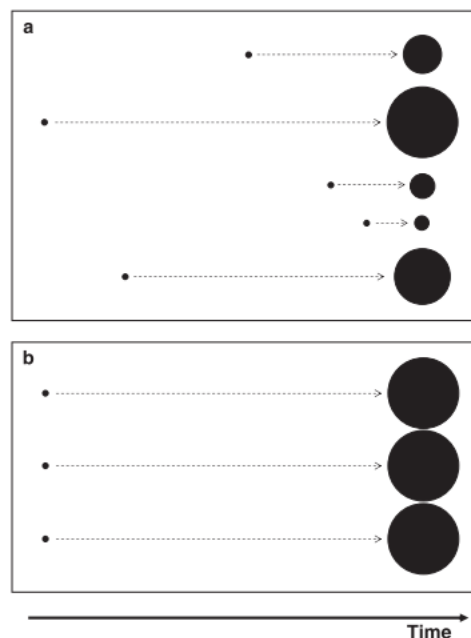
Figure 2.15: Schematic explanation of the size distribution observed in cases where the nucleation occurs (a) randomly and (b) at once. The small dots on the left symbolize forming nuclei, whereas the dots on the right symbolize nanoparticles (a) with partially different sizes and (b) of the same size.(111)

beginning crystallization is termed nucleation and the aggregated seed species is called nuclei. Depending on whether the seed species is a noncrystalline foreign species or nucleation takes place from a single homogenous liquid spontaneously, *heterogeneous* and *homogenous* nucleation are distinguished. Since it is the homogenous nucleation that is most important in questions regarding the synthesis of monodisperse nanoparticles the following discussion will be concerned with this form of nucleation, exclusively.(110)

In figure 2.15 the effects on size distribution of a homogenous nucleation occurring in a broad time interval or all at once are depicted. A monodisperse particle distribution is only gained in the latter case, where nucleation occurs at once and all particles grow under the same conditions. In order to produce a nucleation that is similar to such an ideal single nucleation event in a homogenous solution, a high level of supersaturation has to be induced in a short time span. This is achieved by the hot injection method through injection of a solution of the precursor to a hot solution of the other reaction components. The nucleation process in such a case is called burst nucleation, which inherently does not lead to the monodisperse size distribution gained by an ideal single
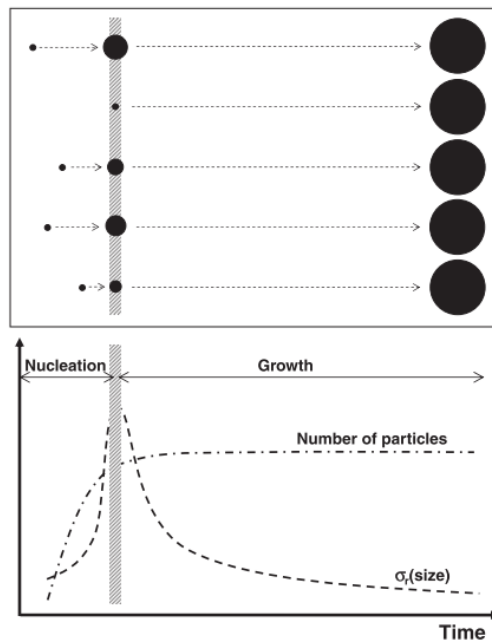
Figure 2.16: Schematic explanation of the size distribution observed in cases where a burst nucleation occurs. The shaded line symbolizes the time at which the nucleation process is terminated and the growth period begins. In the lower picture the development of the number of particles and the relative standard deviation of the size distribution, σ_r(size), with time are shown.(111)

nucleation event as the one shown in figure 2.15 b. In the case of burst nucleation both nucleation and particle growth take place in the period the supersaturation lasts, thus inevitably leading to a broad initial size distribution as depicted in figure 2.16.

However, due to the fast monomer consumption in the nucleation phase and the consequential nuclei formation and particle growth, a continued nucleation in the following growth phase is prevented because the monomer-saturation is not high enough any more. Furthermore, the nucleation phase is much shorter than the growth phase, causing the particles to grow under very similar conditions once the nucleation phase is completed. This is the reason why the relative standard deviation of the size distribution (σ_r) decreases exponentially at the end of the nucleation phase and reaches its highest value just prior to this decrease, at the end of the nucleation phase.(110) On the basis of this explanations it can be understood why classical concepts of size control in nanoparticle formation are the separation of nucleation and growth phase and the minimization of the duration of the nucleation phase.

Particle Growth   In the growth phase of nanoparticle formation the number of particles remains constant as can be seen in the lower part of figure 2.16. As was already mentioned in the paragraph above, the size distribution also becomes narrower (σ_r decreases) in this phase. The reason for this *size focusing*(112) is that smaller particles grow faster than bigger ones. The reaction taking place at the particle surface is a reversible one, which means at the one hand precipitation of monomer from the solution can occur, whilst on the other hand dissolution of the particle under formation of monomer in solution might take place. The direction this reaction takes is dependent mainly on the relationship between the concentration of monomer in the solution and the solubility of the particle, which in turn is dependent on its size. If the particle solubility has a value dominant over monomer concentration dissolution of the particle occurs. Vice versa, precipitation of monomer takes place if its concentration in solution has a higher value than the solubility of the particle.(110)

Ostwald ripening is a process by which larger particles grow at the expense of smaller particles, which in turn dissolve. This is a consequence of the Gibbs-Thomson relation, which assigns a higher chemical potential to smaller particles thus causing the dissolution reaction to be faster than the precipitation for such particles at low monomer concentrations while the larger particles are more stable under the same conditions and gain extra stability by growing on expense of the smaller particles.(113)

The LaMer Diagram   The most basic but still surprisingly well-fitting description of the nucleation and growth processes of many systems is the LaMer diagram shown in figure 2.17.(110) It was originally devised to explain the size control in the hydrosol system in the 1940th.(114) It can be divided in three regions, the monomer accumulation, the nucleation, and the growth period. In case of a hot injection approach the first period, the monomer accumulation can be omitted, since the monomer concentration is increased abruptly via injection of the precursor.

2.5.2   Theoretical Description of the Nucleation Process

As was already discussed in the previous section the phenomenon of nucleation is understood as the formation of a new phase in another phase. The building blocks of the new phase are called monomers and can either precipitate onto other monomers (crystallization) or dissolve from a formed crystal or its preliminary form, the so-called *cluster*. In the classical theory of homogenous nucleation the formation of a solid phase within a liquid phase is usually described. However, other homogenous nucleation systems, such as the formation of a gas bubble in a liquid or the formation of a solid phase in another solid phase, can be treated in essentially the same way.(115)
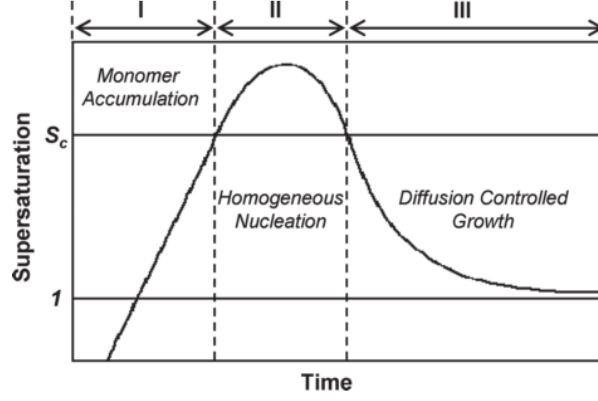
Figure 2.17: The LaMer diagram, showing the development of the monomer concentration with time. S_c is the critical supersaturation, i.e. the minimum supersaturation at which homogenous nucleation occurs.(110)

In the classical theory of homogenous nucleation the free energy ΔG of a nucleus with radius r is described by an equation consisting of two terms, one describing the surface and the other one describing the volume contribution to the total free energy.

$$\Delta G(r) = 4\pi r^2 \gamma + \frac{4}{3}\pi r^3 \Delta G_{\mathrm{V}} \tag{2.45}$$

Here, γ is the surface free energy per unit area and ΔG_{V} the free energy per unit volume of a formed crystal. The latter parameter, ΔG_{V}, can be expressed by

$$\Delta G_{\mathrm{V}} = -\frac{RT \ln S}{V_{\mathrm{m}}} \tag{2.46}$$

as the difference between the free energy of the monomer in solution and in the crystal. In equation 2.46 R is the ideal gas constant, T the temperature, S the saturation, and V_{m} the molar volume of the monomer within the crystal.(110)

Figure 2.18 shows the resulting dependency of the particle radius from the two different contributions of the free energy. As can be seen, a maximum is formed for $\Delta G(r)$ when $S > 1$ (supersaturation) at the critical radius r_{c}. The maximal free energy at the critical radius is the activation energy of the nucleation ΔG_{N}.(116) As long as the radius of a nucleus is smaller than r_{c} the contribution of the term expressing the surface free energy (first term in equation 2.45) is dominant. This leads to the dissolution of of such nuclei, since this is the only way for them to decrease their free energy. In contrast, nuclei with a radius larger than r_{c} are dominated by the volume contributions (second term in equation 2.45), resulting in their continued growth in order to decrease their
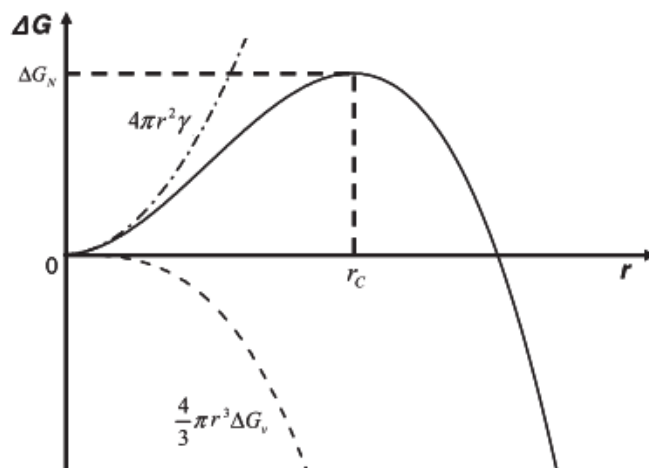
Figure 2.18: Plot of the different contributions of free energy and their influence on the radius of the forming crystal. Surface contributions (dash-dotted line) and volume contributions (dashed line) are shown individually, as is the resulting plot (solid line) in correlation to the particle radius.(111)

free energy further. The value of r_c can be found by the formation of the relation $\mathrm{d}\Delta G(r)/\mathrm{d}r = 0$ at $r = r_\mathrm{c}$.

$$r_\mathrm{c} = -\frac{2\gamma V_\mathrm{m}}{RT \ln S} \tag{2.47}$$

As can be seen from equations 2.45 and 2.46 the critical radius and thus the activation energy increase with increasing surface free energy and decrease with increasing temperature and supersaturation.(110)

3

Results and Discussion

3.1 Motivation and Chapter Survey

PtNi alloy nanoparticles are promising candidates for their use as electrocatalysts for the MOR.(12) First investigations into the effect of different Pt:Ni compositions on catalytic activity have already been published,(84) as has research on the effects of different treatments for ligand removal on particles employed as electrocatalysts.(11) However, investigations concerning the dependency of catalytic activity for the MOR not only on the composition but also on the size of PtNi nanoparticles are still missing to the best of our knowledge. So are studies giving detailed insight into the impact of different treatments (e.g., thermal, chemical, oxidative) on PtNi particles, especially in respect to their agglomeration under electrochemical conditions. The agglomeration of nanoparticles employed as electrocatalysts is a well-known but rarely investigated phenomenon, since it is hard to follow the respective changes of the catalytic particles in the 3D network of a catalyst ink (particles supported on carbon black). Gaining a better understanding of the evolution of size, shape, and composition under various treatments and (electro)chemical conditions has, however, been called "a focal point of future research" in the field of nanostructured catalysis and the value of flat surfaces in this context has been recognized.(14)

This work, therefore, is focused on gaining insight into the effects that composition and particle size have on the catalytic activity of PtNi alloy nanoparticles for the MOR. For that purpose the effect of various treatments on these particles was investigated, both their direct effect and the impact the respective treatment had on the evolution of the catalyst particles (size, shape, and composition), and thus ultimately on catalytic activity, under electrochemical conditions. To that end it was first necessary to adapt the existing colloidal PtNi nanoparticle synthesis in a way that allowed the production of

particles with comparable properties. Employing the hot injection approach for the synthesis of PtNi nanoparticles developed by Ahrenstorf *et al.*(117) yielded PtNi particles that showed a linear dependency between nickel content and particle size. To overcome that dependency the continuous injection method, which was already introduced by Ahrenstorf *et al.* as well,(118) was advanced. This, in addition to an adaptation of the hot injection synthesis approach, finally lead to suitable nanoparticles with comparable properties (see section 3.2).

The next step was to find a way to prepare particle electrodes which allowed the realization of accurate and reproducible electrochemical investigations of these comparable nanoparticles with respect to their catalytic activity. Usually, catalytic nanoparticles are investigated as part of a catalyst ink (see 2.4.2). However, the interaction between a nanoparticle and its support can have a significant impact on its catalytic activity.(104) In order to achieve a reduction of parameters we relinquished the use of carbon black and used only a glassy carbon disk, which is the usually employed substrate for the catalyst ink. PtNi nanoparticles were directly deposited onto this GC substrate via spin coating, thus implementing a very simple setup for the investigation of the respective particle properties (see section 3.3). Using a flat substrate as catalyst support had the additional advantage of being easy to investigate via SEM, thus rendering it possible to follow changes of the particle film, i.e. agglomeration phenomena, occurring under electrochemical conditions.

As was already mentioned in 2.4.2 nanoparticles from colloidal synthesis possess many favorable properties in regard to size distribution, homogeneity and adaptability of characteristics for electrocatalysis. However, such particles are also usually stabilized by organic molecules (ligands). These surfactants block active sites on the particle surface. Therefore, it is sensible to investigate methods for their removal and compare the effect of the respective treatment on the catalytic activity of the particles. Additionally, the agglomeration of the as-treated particles under electrochemical conditions was studied by means of SEM measurements. This was done for two sets of particles with different size and composition and for two methods of composite electrode preparation, namely the preparation with and without Nafion. The treatments investigated in this work were ligand exchange (LEx) with tetrabutylammonium hydroxide (TBAOH) in methanol, treatment in a muffle furnace, plasma treatment, ultra violet UV and ozone treatment (termed "UV/ozone" treatment, and treatment in a vacuum furnace (see section 3.4).

An important characteristic of each electrocatalyst is its stability in an electrochemical environment. For that reason long-term measurements were conducted with two sets of PtNi nanoparticles and for two very contrary treatments, the plasma treatment one

the one hand and no treatment on the other. From the obtained cyclic voltammograms the development of the ECSA and therefore the catalyst's stability can be determined. Additionally, SEM measurements were performed at different stages of the degradation curve to follow changes occurring at a particulate level (see section 3.5).

Finally an array of PtNi nanoparticles with different size or composition were compared in regard to their catalytic activity for the MOR. These experiments were done under consideration of the results of all previously executed investigations to ensure the observed effects were due to differences in size and composition and not some other factors (see section 3.6).

In the last section of this chapter the results of the electrochemical investigation of a bulk piece of platinum as a reference to the investigated particle electrodes are compiled in addition to an overview of effect the different settings of the employed potentiostat have on the determined ECSA. Furthermore, the influence of the concentration of the colloidal particle solution on the electrochemical performance of the GCEs prepared with it and the influence of employing different lines for the analysis of the recorded energy dispersive X-ray spectroscopy (EDX) spectra are discussed (see 3.7).

3.2 Synthesis of PtNi Nanoparticles

One goal of this work was to compare PtNi nanoparticles with different size and composition in respect to their catalytic activity for the MOR. The first step in order to accomplish this task is the synthesis of suitable nanoparticles with comparable properties. For this purpose a hot injection synthesis for PtNi nanoparticles developed by Ahrenstorf *et al.*(117) was chosen as starting point. Ahrenstorf had also already experimented with the continuous injection of a mixture of both metal precursor(118) to achieve a broader size and composition regime of the synthesized particles. However, the particles obtained from these approaches all exhibited a linear dependency of size and nickel content as shown in figure 3.1. In order to investigate the influence of size and composition of PtNi nanoparticles as electrocatalyst for the MOR it was necessary to synthesis particle sets with constant size but different composition or vice versa. Therefore, the original synthesis had to be advanced.

3.2.1 Comparison of Standard and Advanced Synthesis Approach

In figure 3.2 an overview of the results for the advanced synthesis approach (see 3.2.2 for a discussion of what this approach entails) in comparison to the standard synthesis approach is shown. As can be seen it was possible to synthesize nanoparticles that

Figure 3.1: Correlation between size and composition (Ni-content in at.% as determined via EDX) for the hot injection synthesis of PtNi nanoparticles as reported by Ahrenstorf(119).

deviated from the observed linear dependency of size and nickel content. A linear trend is still clearly recognizable for the particles obtained from the advanced synthesis approach, although pairs of comparable nanoparticles, i.e. particles that are constant in one of the variables size or composition but differ in the other, could be obtained. When taking a closer look at some of these pairs it becomes clear that the differences in the respective variable are quite significant. This is comprised in table 3.1 in regard to the size as determined via TEM and the composition as determined via EDX. Here, the parameter $\Delta_{\mathrm{Ni}} = 1 - (\mathrm{Ni}_1/\mathrm{Ni}_2)$ with $\mathrm{Ni}_1 < \mathrm{Ni}_2$ describes the difference in composition in respect to the nickel content of the particles from the standard and advanced synthesis approach, respectively.

However, in the course of this work a strong deviation for the compositional results as determined via EDX at the same transmission electron microscope (*Philips CM 300 UT*) that was used in Ahrenstorf's work was observed for the analysis of different elemental lines (see 3.7.3 for a discussion of this topic). Since a declaration of the lines used in Ahrenstorf's EDX investigation is missing there is therefore no guarantee that the same set of lines (Ni-L, Pt-M at the *Philips CM 300 UT* equipped with an *EDAX DX4* detector in this work) was employed so that the observed deviation between the standard and the advanced synthesis can not undoubtedly be attributed to a real difference in composition. On top of this a new detector was installed towards the end of Ahrenstorf's time at the *Institute of Physical Chemistry* of the *University of Hamburg* so that a comparison of the EDX results reported by her in comparison to the ones
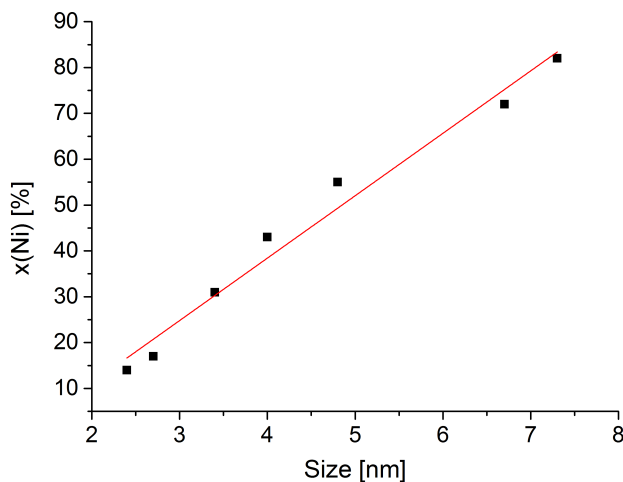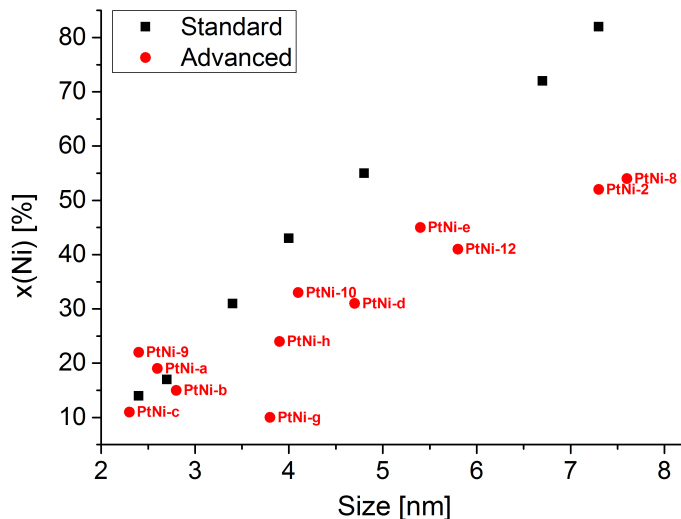
Figure 3.2: Correlation between size and composition (Ni-content in at.% as determined via EDX) for the hot injection synthesis of PtNi nanoparticles as reported by Ahrenstorf(119) (black squares) and for the advanced synthesis carried out in this work (red dots).

reported in this work should be undertaken with care.

For that reason the compositional results in this work were also determined via a X-ray diffraction (XRD) investigation by employing Vegard's law, which is an empirical law correlating the lattice parameters of two constituents of a material (here PtNi) and the composition of a mixture of the two in a linear fashion. However, it has to be kept in mind that in an XRD investigation only the crystalline portion of a particle is registered in contrast to a TEM or EDX investigation, where the whole particle is registered (see 3.6 for a more detailed discussion of this topic.) The results of this investigation in comparison to the ones shown in table 3.1 are shown in table 3.2.

As can be seen from the difference in composition (as determined via EDX, see table 3.1) for particles of comparable size ($\leq 10\,\%$ difference) from the standard synthesis strategy on the one hand and the advanced synthesis approach on the other, quite large values greater than $35\,\%$ are found for Δ_{Ni} in all three cases and the absolute amount of nickel in the particles is changed by a factor of two to three. Looking at the size and composition of the same particles as determined via XRD (see table 3.2) the major problem in the comparison of different nanoparticles batches becomes apparent, namely the difficult to make sure the particles really are comparable, not only in their total size and composition (TEM and EDX) but also in their interior organization, i.e. the mean

Table 3.1: Pairs of comparable PtNi nanoparticles with constant size. The syntheses of the nanoparticles obtained by the advanced synthesis strategy will be discussed in 3.2.2. The particle batches from this approach shown here correspond to PtNi-9 (1.), PtNi-d (2.), and PtNi-2 (3.). Values for the standard synthesis as reported by Ahrenstorf.(119)

No.	size (TEM) [nm]		Ni (EDX) [at.%]		Δ_{Ni} [%]	empirical formula Pt_xNi_y	
	standard	advanced	standard	advanced		standard	advanced
1.	2.4	2.3	14	22	36	Pt_6Ni	Pt_4Ni
2.	4.8	4.7	55	31	44	$PtNi$	Pt_2Ni
3.	7.3	7.3	82	52	37	$PtNi_4$	$PtNi$

size and composition of the crystalline domains which is determined via XRD. In table 3.2 a comparability of the mean crystallite size is only given for the second particle set (3.7 nm). For the first and third set a larger crystallite size is found for the advanced syntheses in comparison to the standard syntheses so that the obtained compositions should not be compared. Interestingly, for the advanced synthesis of the first set the size and composition determination via TEM and EDX on the one hand and XRD on the other hand yield exactly the same results, a size of 2.3 nm and a Ni content of 22 %. This indicates that the particles of this batch are almost perfect monocrystals thus resulting in the conformity in size determined via XRD and via TEM. Since in this case one would fully expect the composition of this monocrystals as determined via XRD to be the same as the one determined via EDX, the excellent agreement actually observed (22 % in both cases) indicates that the employed characterization methods produce meaningful data.

For the second set of particles the size as determined via XRD is the same for both the standard and the advanced synthesis approach so that the comparison of the respective compositional data obtained via XRD is reasonable. Since for this comparison a value comparable to those observed for the EDX investigation is obtained for Δ_{Ni} (35 %) it can be deduced, that the advanced synthesis approach developed in this work really does yield particles that broaden the hitherto achievable size and composition regime of PtNi nanoparticles.

3.2.2 The Advanced Synthesis Approach

In order to produce PtNi nanoparticles within a broad size and composition regime the hot injection and the continuous injection approach were employed. Experimental

Table 3.2: The same pairs of comparable PtNi nanoparticles with constant size (in regard to the TEM investigation) that were already introduced in table 3.1, here as characterized via XRD. The syntheses of the nanoparticles obtained by the advanced synthesis strategy will be discussed in 3.2.2. The particle batches from this approach shown here correspond to PtNi-9 (1.), PtNi-d (2.), and PtNi-2 (3.). Values for the standard synthesis as reported by Ahrenstorf.(119)

No.	size (XRD) [nm]		Ni (XRD) [at.%]		Δ_{Ni} [%]	empirical formula Pt_xNi_y	
	standard	advanced	standard	advanced		standard	advanced
1.	1.9	2.3	9	22	59	Pt_4Ni	$Pt_{13}Ni$
2.	3.7	3.7	37	24	35	PtNi	Pt_2Ni
3.	4.3	5.0	53	42	21	$PtNi_4$	PtNi

details concerning the syntheses of the discussed particle batches can be found in 4.1. In the following discussion different ratios will be given every now and again. This ratios are to be understood as factors of the respective components (e.g., Pt-precursor, ligands) in regard to their molar amounts as they are given in the typical syntheses described in 4.1.1 and 4.1.2. For the metal precursors that is a molar amount of 0.17 mmol, each, and for the ligands, which are oleylamine (OAm) and oleic acid (OA), a value of 0.6 mmol, each. The discussed particle batches are denominated "PtNi-" followed by either a letter or a number (e.g., "PtNi-a" or "PtNi-1"). The particle batches denominated by a letter will be discussed in this section of the chapter exclusively, whereas the ones denominated with a number will be mentioned again in the next chapters in the context of electrochemical measurements that were performed with this numbered group of particle batches.

Hot Injection In case of the hot injection method the parameters that were experimented with were the amount of ligands on the one hand and the concentration of the metal precursors employed in the synthesis on the other. The influence of the amount of used stabilizer, especially in regard to OA, was already investigated by Ahrenstorf, who found an exponential decrease of the particle size with an increasing OA to Pt-precursor ratio ($OA:Pt_p$).(119) The goal of the variation in concentration of the metal precursors was to achieve a different degree of supersaturation and thus produce more or less nuclei onto which the growth of the remaining precursor can then take place, thus leading to particles with a different size or composition as obtainable by the stan-

3. RESULTS AND DISCUSSION

Table 3.3: Characteristics of PtNi nanoparticles obtained under the same synthesis conditions except for the total volume of solvent employed.

name	size (TEM) [nm]	size (XRD) [nm]	Ni (EDX) [at%]	Ni (XRD) [at%]	V (solvent) [mL]
PtNi-a	2.6	2.1	19	14	10
PtNi-b	2.8	2.1	15	9	5

dard synthesis approach.

Surprisingly, employing a twofold concentration of the metal precursors in regard to the volume of solvent V (solvent) had no significant effect in regard to size or composition of the obtained particles, as can be seen in table 3.3. In comparison to the standard synthesis approach the concentration of metal precursors in regard to the volume of solvent in the synthesis of PtNi-a is already twice as high per precursor, resulting in a fourfold higher concentration in total. For the respective standard synthesis a size as determined via TEM around 2 nm is reported(119) in adequate agreement with the results discussed here. XRD and EDX data is not available. Since a variation of the precursor concentration by a factor higher than four is almost impossible to implement experimentally (limited by the solubility of the precursors on the one hand and size of the experimental set-up on the other) and the few experiments conducted in this regard did not yield successful results no further investigations in regard to a different supersaturation were undertaken.

Concerning the concentration of OA used in the hot injection synthesis of PtNi nanoparticles strong differences in size and composition could be observed for different OA to Pt-precursor ratios. In combination with the use of different precursor ratios (Pt_p:Ni_p) new size/composition combinations became thus feasible. In table 3.4 some of those results are compiled in comparison to particles of comparable size obtained from the standard synthesis approach, for which in this compilation a OA:Pt_p ratio of 1:1 was employed in all cases. As can be seen by comparing the compositions of the particle batches with comparable size from the standard and the advanced synthesis approach (see also figure 3.2) the described variations in the latter lead to particles with new size/composition combinations. For PtNi-c the difference in composition to a particle batch of the standard seems rather small (11 compared to 14 %) but still results in a value for Δ_{Ni} of 21 %. For the other sets of comparable particles shown here Δ_{Ni} values of 24 % (set incl. PtNi-9), 36 % (set incl. PtNi-10) and 44 % (set incl. PtNi-d) are obtained. No particles of a comparable size as that obtained for PtNi-e (5.4 nm as

Table 3.4: Characteristics of PtNi nanoparticles obtained under comparable synthesis conditions for the advanced synthesis approach under variation of the Pt_p:Ni_p and OA:Pt_p ratios. For comparison results of the standard synthesis approach are shown.(119) For PtNi-d and PtNi-e the temperature was also different with 180 °C instead of 200 °C as was the case for the other syntheses shown here.

name	size (TEM)		Ni (EDX)		OA:Pt_p	Pt_p:Ni_p
(advanced)	[nm]		[at.%]			
	standard	advanced	standard	advanced	advanced	advanced
PtNi-c	2.4	2.3	14	11	4:2	2:2
PtNi-9	2.4	2.3	14	22	2:2	2:2
PtNi-10	4.0	4.1	43	33	2:1	1:3
PtNi-d	4.8	4.7	55	31	0:2	2:1
PtNi-e	-	5.4	-	45	1:1	1:6

determined via TEM) are reported in correlation to the standard synthesis approach. Thus, the variation of the OA:Pt_p ratio under simultaneous variation of the Pt_p:Ni_p ratio is a successful approach to broadening the size and composition regime of PtNi nanoparticles.

Continuous Injection It was previously reported that the nucleation in case of the hot injection approach for the synthesis of PtNi nanoparticles consists of a single nucleation event followed by a growth phase that is exclusively based on the consumption of monomer. For that reason the continuous injection of a solution of both monomers was experimented with to extend the growth phase and thus obtain larger particles than with the standard hot injection synthesis approach. The obtained particles had a diameter of 6.4 nm with 15 % standard deviation and a composition of 54:46 (Pt:Ni) and are thus quite far from the linear dependency of size and composition found for the standard hot injection approach (compare figure 3.1). No further experiments were conducted in this regard so that there is still room for development. However, in comparing different injection rates and starting points of the continuous injection (in respect to the hot injection event) the optimal rate was determined to be 24 mL h^{-1} for a solution of 0.17 mol L^{-1} in respect to the metal precursors, which continuously injected starting 180 seconds after the hot injection event. This parameters are important to suppress a second nucleation event that would inevitably lead to a bimodal size distribution and
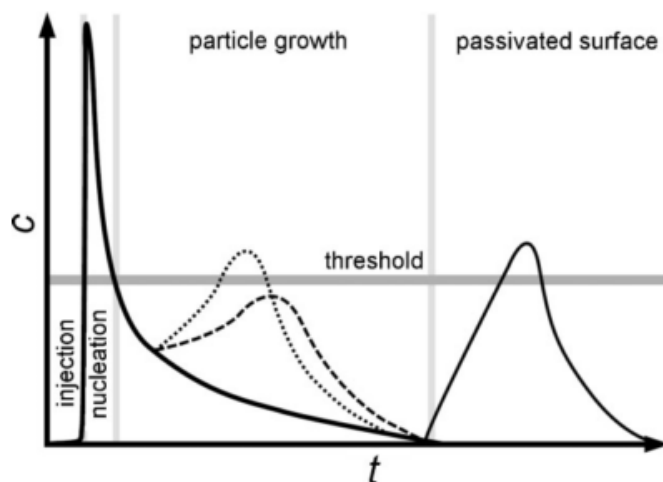
Figure 3.3: Monomer concentration profiles for different courses of a HI experiment (thick line), a CI experiment with an injection rate that is so high that the monomer concentration exceeds the nucleation threshold (dotted line), an optimal CI experiment (dashed line), and an CI experiment that is started too late (thin line).(119).

to make sure the surface of the forming particles is not already passivated when the injection is started as is depicted in figure 3.3.(118)

The continuous injection method as it was described above was advanced in this work by injecting only one of the metal precursors, not a mixture of both. The injection rate and starting point of the continuous injection, however, were adopted as reported (see above). The continuous injection of the nickel precursor yielded very different particles in respect to size and composition (see table 3.5). In order to vary the obtainable size/composition combinations of the synthesized particles further, the factors that already proved to be effective in achieving this with respect to the hot injection approach (Pt_p:Ni_p and OA:Pt_p ratio, respectively, see the paragraph "Hot Injection" above), were varied here as well. The obtained nanoparticles have quite different sizes and compositions that broaden the size and composition regime of the nanoparticle synthesis as can be seen in figure 3.2.

The successful synthesis of PtNi-f is especially remarkable, since previously no PtNi nanoparticles of this rather large size were obtained, neither by the standard nor the advanced synthesis approach. However, with their high Ni content this particles were less stable than less Ni rich ones (even the ones that sill exhibited a high Ni content of approx. 50 %, such as PtNi-2 or PtNi-8) and decomposed during storage (see figure 3.4). Comparing PtNi-8 and PtNi-12 in table 3.5, which are the product of the same

Table 3.5: Characteristics of PtNi nanoparticles obtained under continuous injection (CI) of the nickel precursor. Varied synthesis parameters include the Pt_p:Ni_p ratio of the hot injection (HI) section of the synthesis and the OA:Pt_p ratio that is present in total (sum of the OA amount present in the initial mixture (HI approach) and the amount in the continuously injected solution).

name	size (TEM)	Ni (EDX)	Pt_p:Ni_p	Ni_p	OA:Pt_p
	[nm]	[at%]	HI	CI	total
PtNi-12	5.8	43	1/2:1	3	1:1/2
PtNi-8	7.6	54	1/2:1	3	0:1/2
PtNi-f	18.0	91	1/4:1	3	1/2:1/4
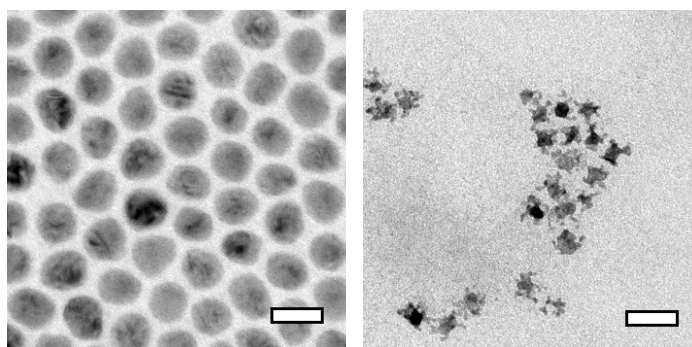
(a) PtNi-f directly after synthesis. (b) PtNi-f after two years in storage.

Figure 3.4: TEM images of PtNi-f (a) directly after the synthesis and (b) after two years in storage. Scale bar = 20 nm.

synthesis conditions except for the OA:Pt_p ratio employed (0:1/2 for PtNi-8 and 1:1/2 for PtNi-12) an increasing particle size and nickel content with decreasing OA amount is observed. Ahrenstorf reported the same trend and attributed it to a complexation of nickel monomer by oleic acid that suppresses the precipitation of the respective nickel monomers in a particle growth reaction.(119)

The results of the continuous injection of the platinum precursor are comprised in table 3.6. As can be seen in figure 3.2 this strategy is also successful in broadening the obtainable size and composition regime. Interestingly, both approaches, the continuous injection of the nickel precursor and that of the platinum precursor, yielded nanoparticles that were very similar in both size and composition, namely PtNi-2 (CI of platinum precursor) with a size of 7.3 nm and a Ni content of 52 % and PtNi-8 (CI of nickel precursor) with a size of 7.6 nm and a Ni content of 54 %. When taking a closer

Table 3.6: Characteristics of PtNi nanoparticles obtained under continuous injection of the platinum precursor. Varied synthesis parameters include the Pt_p:Ni_p ratio of the hot injection part of the synthesis and the OA:Pt_p ratio that is present in total (sum of the OA amount on the one hand and the Pt amount on the other that is present in the initial mixture (HI part) and in the continuously injected solution, respectively).

name	size (TEM)	Ni (EDX)	Pt_p:Ni_p	Pt_p	OA:Pt_p
	[nm]	[at%]	HI	CI	total
PtNi-g	3.8	10	1:1/2	4	1:5
PtNi-h	3.9	24	1:1	4	1:5
PtNi-2	7.3	52	1:3	2	1:1

look at PtNi-2 and PtNi-8 however, a difference in the shape of the obtained nanoparticles can be observed (see figure 3.5). The particles of PtNi-8 are not fully spherical, a fact that is not surprising considering that they were synthesized without the use of any OA. Ahrenstorf found comparable results when synthesizing nanoparticles without employing OA in a standard hot injection synthesis.(119)
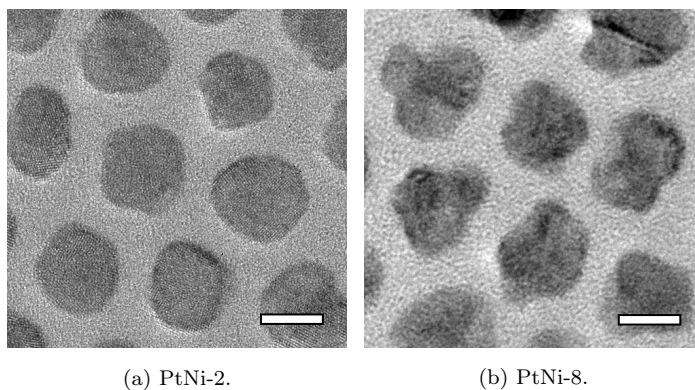

(a) PtNi-2.   (b) PtNi-8.

Figure 3.5: TEM images of (a) PtNi-2 and (b) PtNi-8. Both images were obtained directly after the synthesis, so the not fully spherical shape of PtNi-8 is not a consequence of decomposition setting in. TEM images of PtNi-f (a) directly after the synthesis and (b) after two years in storage. Scale bar = 5 nm.

Next to the broadening of the size and composition regime another upside of the advanced synthesis strategy in respect to the continuous injection of only one metal precursor at a time is the very good standard deviations the obtained particles exhibit in contrast to the standard approach under continuous injection of both precursors at once. For the particle batches just discussed, PtNi-2 and PtNi-8, a standard deviation

of only 7 % is observed, respectively, where for the particles obtained from the standard strategy a value of 15 % was reported.(118) The respective diagrams depicting the size distribution for PtNi-2 and PtNi-8 can be found in figure 3.51 in 3.6.1. The consequences of the non-spherical shape of the particles of PtNi-8 on their electrochemical properties will be discussed in 3.6.2.

3.3 Preparation of Composite Electrodes

In order to investigate different PtNi nanoparticles in respect to their electrochemical performance the preparation of composite electrodes suited to such investigations was the first step. The general idea concerning the preparation of electrodes for that task was to construct them as simple as possible, so that effects observed in the electrochemical measurements could be directly traced back to their origin, i.e. size and composition of the employed PtNi particles, without having to consider too many other possible sources for the observed behavior. Therefore, the use of carbon black, which is typically employed as a support for the electrocatalyst and is denoted "catalyst ink" after the deposition of nanoparticles and (in some cases) Nafion, was abstained from. Instead, the nanoparticles were spin coated directly onto a glassy carbon disk, the electrode substrate that is typically used as support for the catalyst ink.

Thus, the most basic composite electrode used in this work consisted only of two components, namely the GC disk and the particles on it. However, in the course of the experiments conducted with these composite electrodes strong agglomeration of the particles under electrochemical conditions was observed (see 3.4.2). In order to conduct a comparative electrocatalytic investigation focusing on size and composition of the catalytic PtNi particles, a way to prevent or at least attenuate this agglomeration was therefore required. For this reason Nafion was spin coated on top of the as-prepared composite electrodes in the cases where this comparability was desired, resulting in composite electrodes consisting of three components: GC disk, particles, and Nafion. The stabilizing effect of Nafion will be further discussed in 3.4.2. The two kinds of composite electrodes thus prepared are denoted "glassy carbon electrodes" in contrast to the "glassy carbon disk" or "glassy carbon substrate", which refer solely to the substrate without any deposited electrocatalyst. Schematics of the two types of glassy carbon electrodes are shown in figure3.6.

The direct deposition of the electrocatalytic particles onto a flat substrate rendered it possible to follow changes in the resulting particle film under electrochemical conditions at different stages via scanning electron microscopy. Being deposited onto a carbon support (GC disk), which is also the case for electrocatalysts prepared in form

Figure 3.6: Two types of composite electrodes. *Left*: Electrode consisting of GC disk and nanoparticles. *Right*: Electrode consisting of GC disk, nanoparticles and Nafion film.

of a catalyst ink (carbon black support), the as-prepared GCEs thus could be used as a model system for agglomeration processes on carbon surfaces. Agglomeration of the particles amounting to the electrocatalyst is an important topic in fuel cell research (see 2.4.2), as catalytic activity can be strongly influenced by particle agglomeration.(104) The intuitive assumption is that due to agglomeration, which leads to a decrease in electrocatalytic surface area, catalytic activity also decreases. This, however, is not generally the case as has been shown in the literature(13) and will be further discussed in 3.4.2.

3.3.1 Preparation of the Glassy Carbon Substrate

The first step in the preparation of any kind of composite electrode is the cleaning and polishing of the employed GC substrate. Ensuring that all electrocatalyst is completely removed from a GC disk prior to a new investigation is indispensable for acquiring meaningful and reproducible data that corresponds solely to the presently investigated electrocatalyst. Electrochemical measurements constitute a very sensitive method of investigation and electrode preparation plays an important role.(120) For that reason a reliable cleaning process is of the utmost importance. So is the preparation of the thus cleaned GC surface because the spin coating process and therefore the properties of the resulting particle film and its agglomeration behavior depend greatly on the substrate's cleanliness and surface quality.

Different approaches in respect to the cleaning of a particle coated GC surface were investigated and their success determined via SEM. Cleaning a GCE by means of wiping it down with KimWipes and chloroform (solvent for OAm/OA stabilized PtNi particles) did not result in a successful removal of the particles from the surface as could clearly be shown by SEM. Treating the GCE via sonication in chloroform or comparable solvents neither lead to a satisfactory cleaning of the surface. Treating the GCE in aqua regia for some hours, however, proved to yield satisfactory results and was thus implemented as first step in a succession of cleaning steps finally devised to produce clean surfaces even for other contaminants than just PtNi-particles. This first step is followed by a succession of sonication steps in solvents of different polarity to eliminate as many

different contaminants as possible.

The polishing of the thus cleaned GC disk followed the procedure commonly described in the literature, i.e. polishing with a series of abrasives of decreasing size employed in the form of slurries.(121) In this work alumina slurries were chosen for this task. The full cleaning and polishing process is described in detail in 4.2.1.

3.3.2   Deposition of Particle Films

For the preparation of a GCE suitable to be employed for the electrochemical investigation of a chosen particle batch, the reproducible deposition of a homogenous particle film in a monolayer is desired. This is because only in a monolayer all particles are exposed to the electrochemical environment to the same extend while simultaneously having contact to the electron conducting GC substrate and because only for a homogenous particle film the effects of agglomeration, governing catalytic activity as will be discussed in 3.4.3, are the same over the entire exposed surface of the GCE.

To prepare films in a reproducible fashion, i.e. with a comparable catalyst loading, is important because it has been shown that catalytic activity and product distribution depend on catalyst loading.(91)(93) For producing GCEs with a constant catalyst loading the drop-casting method is suitable, however, it does not produce mono-layered films and often leads to an inhomogeneous deposition of the nanoparticles, particularly around the edges of the drops where the particles tend to accumulate in a form similar to the "coffee-ring effect".(122)(123)

To obtain a homogenous and mono-layered particle film the spin coating procedure was thus chosen, which had shown to be very promising in producing well-ordered particle films over large surface areas for Pt_3Co nanoparticles.(124) A disadvantage of this method of GCE preparation is the need to determine the actual mass of electrocatalyst deposited onto each GC disk, individually, since under spin coating conditions most of the initially applied particle solution is lost. This determination of catalyst loading was performed after the electrochemical measurement and potential SEM measurements were conducted, since the chosen atomic absorption spectroscopy (AAS) demands for the metals of the electrocatalyst to be dissolved. However, the first step in the production of particle films via spin coating is the preparation of a well-stabilized, homogenous colloidal particle solution.

Preparation of colloidal Particle Solutions   In order to produce homogenous, mono-layered films from colloidal particle solutions the solutions need to contain an optimal amount of stabilizing ligands, since the degree of stabilization of the nanoparticles has a direct impact on the structure of the resulting film. In this work OAm and

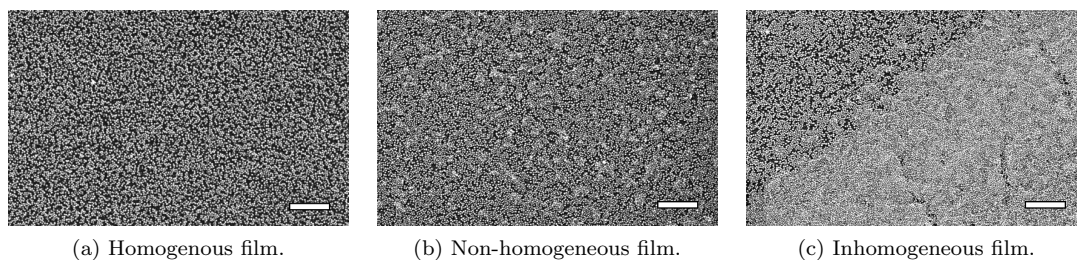(a) Homogenous film.　　　(b) Non-homogeneous film.　　　(c) Inhomogeneous film.

Figure 3.7: SEM images of different particle films produced from increasingly destabilized particles. The destabilization was achieved by washing the nanoparticles repeatedly with ethanol. Scale bar = 200 nm.

OA were used as ligands (see 4.1 for experimental details). However, after completion of the particle synthesis only the application of OAm leads to a restabilization of the PtNi particles in solution. Ahrenstorf suggested that a reversible binding of OAm on the surface of PtNi nanoparticles was responsible for this fact and took into account the ^{13}C-NMR spectroscopic investigation of Ramirez, who observed a reversible binding of amines on platinum nanoparticles.(119)(125) For this reason the degree of stabilization of a particle batch in solution was adjusted by the application of OAm or the removal of ligands by washing the particles with ethanol.

The importance of working with well-stabilized nanoparticles in a homogenous, colloidal solution becomes apparent when looking at the SEM images shown in figure 3.7. As can easily be seen too much washing (see 3.7c), i.e. removal of ligands and thus a destabilization of the particles, eventually leads to a beginning agglomeration of single particles, which in turn gives rise to an inhomogeneous particle film. The consequence of such an inhomogeneous film in respect to the agglomeration behavior during electrochemical measurements (see 3.4.2) is shown in figure 3.8. The zonular pattern on the GCE is a consequence of using a slightly destabilized particle solution for the spin coating procedure, resulting in different forms of agglomeration in regard to agglomerate size and density during the electrochemical investigation. As will be discussed in 3.4.3, which kinds of agglomerates are formed under electrochemical conditions is a crucial factor for the arising catalytic activity of an electrocatalyst. To obtain reproducible agglomeration and thus reproducible catalytic activity for GCEs prepared from the same particles it is thus necessary to prepare composite electrodes featuring homogenous particle films with a comparable loading, as was already stated above.

Preparing a GCE from a completely destabilized particle solution, which is readily identifiable by a black precipitate from an either still black or colorless solution, does not lead to the formation of a particle film anymore. Instead, large agglomerates of particles

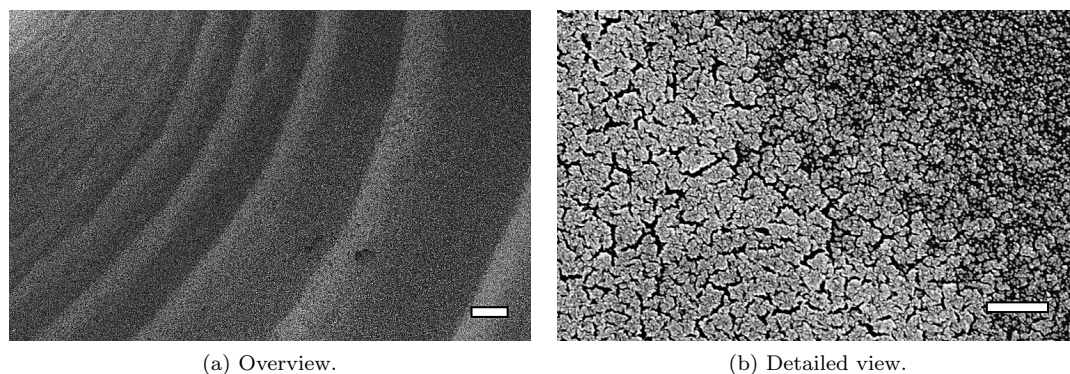(a) Overview.   (b) Detailed view.

Figure 3.8: SEM images of a GCE that was prepared with destabilized particles resulting in an inhomogeneous particle film exhibiting zonular patterns after a CV experiment (135 cycles). (a) Overview. (b) Detailed view of the differences in electrochemical-induced agglomeration of the previously agglomerated particles in the ring and the non-agglomerated particles next to the ring. Scale bar = (a) 20 µm, (b) 200 nm.

and some other contaminant, supposedly a form of reaction product (polymerization, oxidation, etc.) of OAm, are scattered over the GC substrate's surface (see figure3.9). Since obviously no reproducible preparation of a GCE is possible in this fashion either, the addition of a excess of OAm to a colloidal particle solution was examined next.

However, a destabilization of the nanoparticles in the solution that is to be used for the film preparation is not the only factor leading to inadequate particle films. If too much stabilizer (OAm) is present the production of homogenous, closed films is not possible, as well. This is shown in figure 3.10. The rather bad quality of the SEM images is a consequence of the large amount of organic contaminants (OAm) on the GCEs surface. This excess of stabilizer also lead to the absence of any MOR peaks in the cyclic voltammetry experiments conducted with GCEs prepared that way. Therefore, in the preparation of composite electrodes the addition of too much OAm as stabilizer has to be avoided just as much as using destabilized particle solutions.

The optimal amount of OAm was best reached by the preparation of a rather OAm-rich particle solution, which was then washed with ethanol twice prior to the film preparation. This resulted in homogenous, mono-layered particle films such as the one shown in figure 3.7a. However, OAm is bound to the particle surface reversibly and, as Ahrenstorf already described, the colloidal stability of PtNi solutions decreases with time, leading to the formation of a black precipitate from the solution, which was shown to consist of particle agglomerates by dynamic light scattering(117) and in this work additionally by SEM (see figure 3.9). The consequences of this reversibility of ligand bonding will be discussed in the next paragraph.
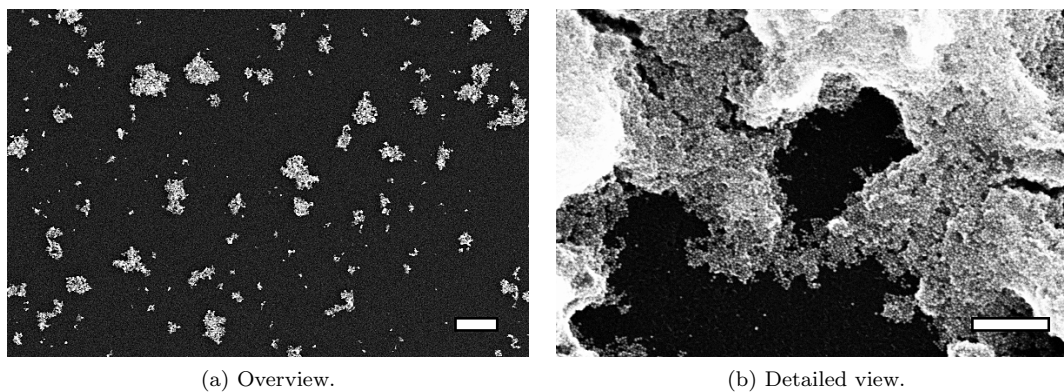
(a) Overview.

(b) Detailed view.

Figure 3.9: SEM images of a GCE prepared with completely destabilized particles, showing particle/OAm agglomerates on else wise bare GC surface. In the detailed view single particles within the agglomerate are clearly visible, as is the absence of a particle film on the surface of the GC. Scale bar = (a) 20 µm, (b) 200 nm.

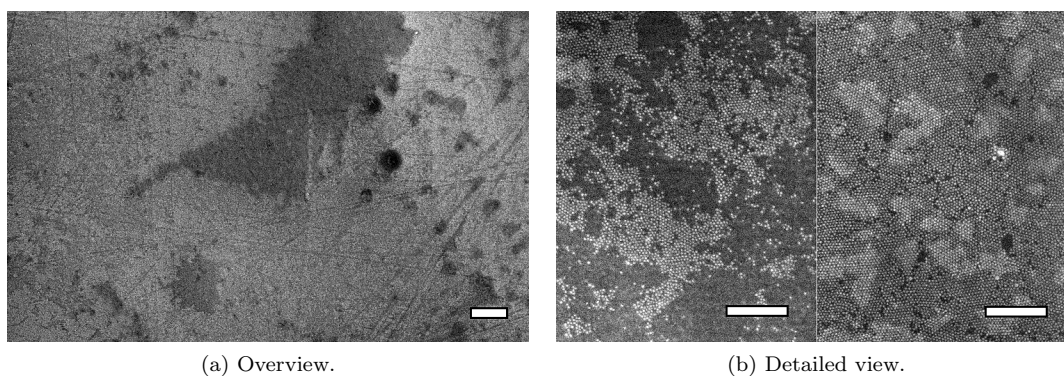(a) Overview.

(b) Detailed view.

Figure 3.10: SEM images of a GCE prepared with particles stabilized by an excess of OAm. Very different domains are found for this preparation method as shown in the detailed view. Domains with only incomplete surface coverage are present (b, *left*) as well as domains exhibiting more than a monolayer of particles (b, *right*). Scale bar = (a) 20 µm, (b) 200 nm.
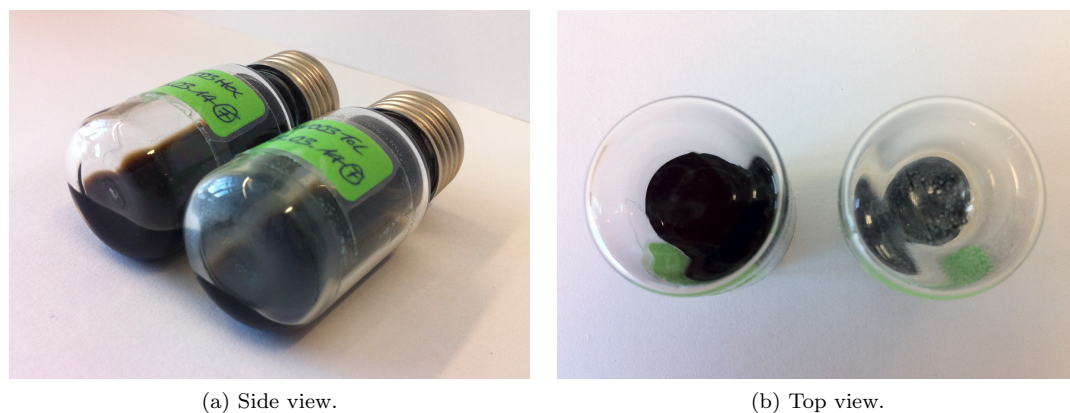
(a) Side view.   (b) Top view.

Figure 3.11: Photographs of colloidal PtNi nanoparticle solutions stabilized by OAm and OA after 5 month of storage under ambient conditions. The vial on the left contains n-hexanee as solvent, whereas the vial on the right contains the particles solved in toluene. A colorless precipitate can be observed only in the vial containing the particle solution in toluene (vial on the right).

Stability Enhancement of colloidal Particle Solutions The bonding of OAm to the surface of PtNi nanoparticles is a reversible process. With time the concentration of the bonded form of OAm from the particle surface decreases, leading to the formation of a black precipitate of agglomerated particles and organic residue. The organic residue is believed to be a reaction product of the free OAm in solution, decreasing its concentration by precipitating and leading to a constant adjustment of the chemical equilibrium between the bonded and free form of OAm and thus finally to the complete destabilization of the particles, identifiable as black precipitate from a colorless solution. This hypothesis is supported by the observation that after months of storage of PtNi particles in solution the formation of a colorless precipitate, which supposedly consists of the OAm reaction product, can be observed (see figure 3.11). It is further supported by the fact that this precipitate is only found in a particle solution of toluene, but not in one of n-hexanee. OAm is supposed to be by a factor of ten times more soluble in toluene than in n-hexanee(126), meaning that in toluene the adjustment of above mentioned equilibrium between bonded and free OAm would commence with a higher rate, thus producing more free OAm which in turn reacts to give the observed colorless precipitate.

To enhance the stability of the OAm-rich solutions, from which after two washing steps the solution finally used for the film preparation was won, n-hexane was thus employed as solvent and the resulting solution was stored cold and dark to further suppress any reaction of the free OAm. However, in order to sufficiently remove OAm during the

washing steps, the black precipitate obtained after centrifugation of the n-hexane solution with ethanol was redispersed in toluene and left to sit for at least 15 min in order to give the equilibrium between free and bonded OAm time to adjust and thus remove some of the bonded OAm from the particle surface. This solution was then washed again and again redispersed in toluene, thus finally giving the solution from which the GCE was prepared via spin coating.

Although the stability of colloidal PtNi solutions could greatly be enhanced by the use of n-hexane instead of toluene as solvent, the appearance of colorless precipitant was still sometimes observed in some of the stored solutions. This made it necessary to find a way to clean the respective solutions of this contamination. This process will be discussed in the next paragraph.

Processing of contaminated Particle Solutions In case of the appearance of colorless precipitate from the as-prepared particle solutions a processing of the respective solution became necessary, because otherwise films as the one shown in figure 3.12a were obtained. These films, although homogenous and mono-layered in respect to the particles, exhibit areas with very different degrees of contamination (see figure 3.12c), which in case of an electrochemical investigation of such a contaminated GCE must lead to a decrease of reproducibility in repeated measurements with the respective particle batch. A washing of the contaminated solutions with ethanol is not successful under these circumstances, since the precipitant is not soluble in ethanol (or other solvents used for washing, such as acetone and methanol) and precipitates during the following centrifugation step thus preventing its separation from the nanoparticles, which also precipitate. However, an easy way to clean a contaminated particle solution is the filtration of the respective solution in toluene via a syringe filter (see 4.2.2 for experimental details). The success of this cleaning step can be confirmed in the SEM images of the particle films prepared with the respective particle solution after this filtration step (figures 3.12b and 3.12d).

In case of a heavy contamination performing the above mentioned filtration method did not always suffice to completely remove all of the contaminants from the solution. In these cases a different cleaning method is more appropriate. This method consists of preparing a diluted solution of the particles in n-hexane and then performing a centrifugation without the addition of any precipitating agent (usually ethanol). This leads to the precipitation of the solid colorless OAm reaction product without the simultaneous precipitation of any particles (given the solution is well-stabilized). Thus the contaminants can easily be separated from the particle solution by carefully removing the particle solution from the top downwards using a pipette and discarding

(a) Overview - contaminated film.

(b) Overview - clean film.

(c) Contaminated film.

(d) Clean film.

Figure 3.12: SEM images of particle films (a) and (c) prepared from a solution containing colorless precipitate, (b) and (d) films prepared from the same solution after filtration with a syringe filter. Scale bar = (a) and (b) 100 μm, (c) and (d) 2 μm.

(a) Overview - contaminated film.　　(b) Overview - clean film.　　(c) Overview - film from residue.

(d) Contaminated film.　　　　(e) Clean film.　　　　(f) Film from residue.
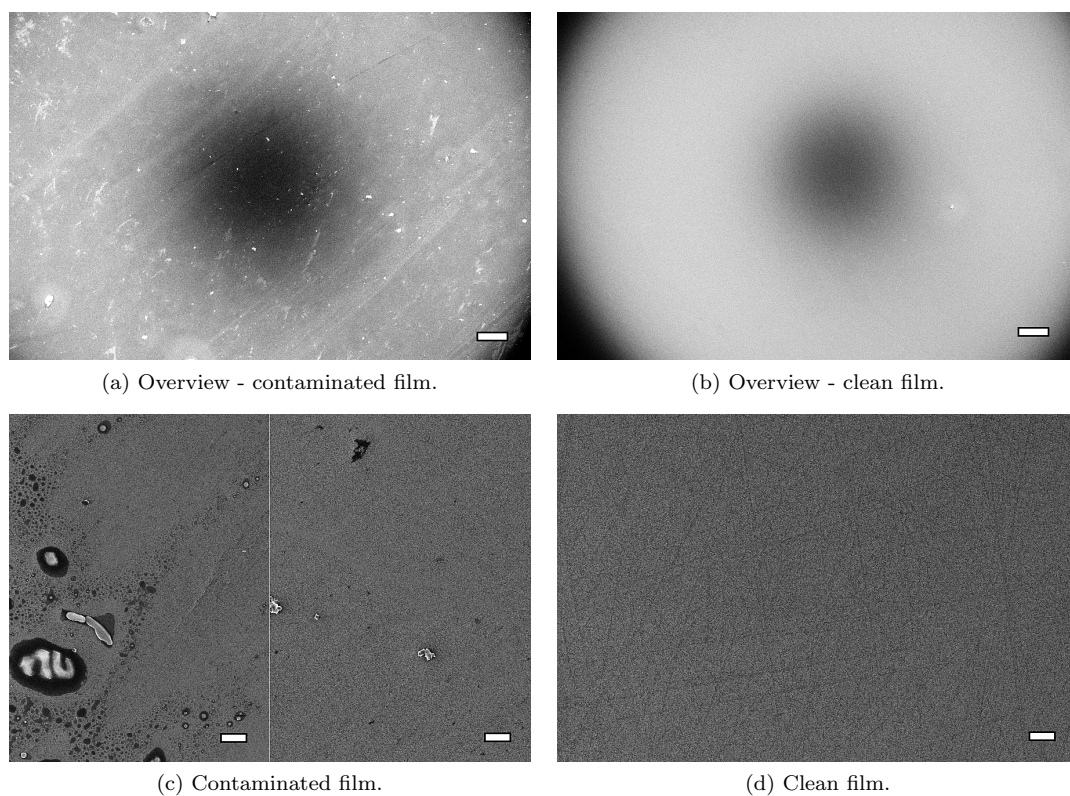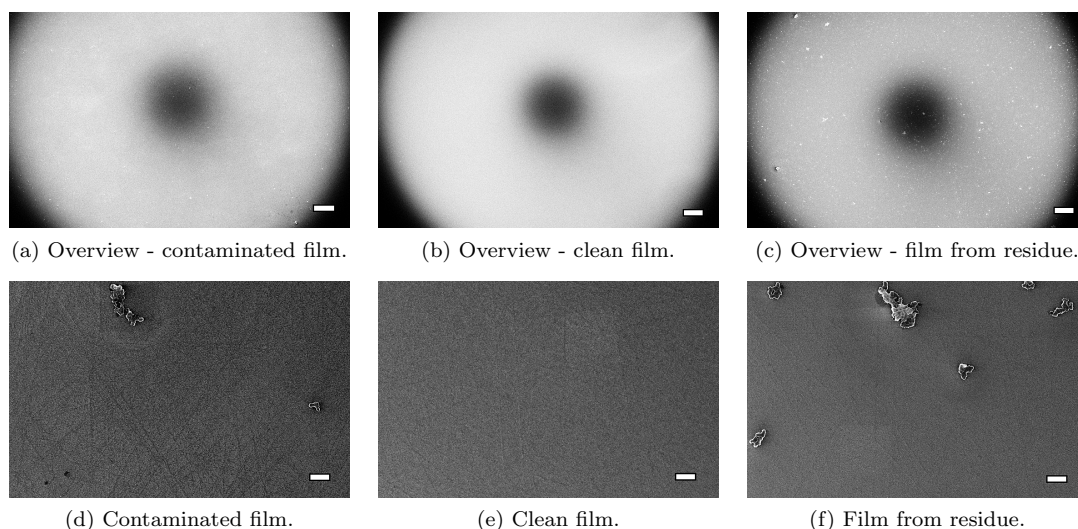
Figure 3.13: SEM images of particle films (a) and (d) prepared from a solution containing colorless precipitate, (b) and (e) films prepared from the same solution after centrifugation and separation of the contaminants and (c) and (f) film prepared from the solution to be discarded in the tip of the centrifuge tube, containing the contaminants. Scale bar = (a), (b) and (c) $100\,\mu m$, (d), (e) and (f) $2\,\mu m$.

the contaminant-rich part of the solution in the tip of the centrifuge tube. Experimental details can be found in 4.2.2. Respective SEM images confirming the success of this cleaning method can be found in figure 3.13. In addition to SEM images of the contaminated and clean films produced from the same solution prior to and after the processing via centrifugation (see figures 3.13a, 3.13b, 3.13d, and 3.13e) figure 3.13 contains SEM images of films prepared from the solution in the tip of the centrifuge tube, which is to be discarded (see figures 3.13c and 3.13f). The strong contamination of this GCE in comparison to the one prepared from the clean solution confirms the effectiveness of this centrifugation method to get rid of unwanted contaminants.

3.3.3　Application of Nafion Coating

As was already mentioned in the beginning of this section, there are two types of electrodes that were employed for the electrochemical investigations conducted in this work. One consists of just the GC substrate and the particle film deposited onto it, the other one possesses an additional Nafion coating on top of the particle film. For this film a thickness of $< 50\,nm$ is desirable. However, films obtained under employment of the as-purchased Nafion solution (5 wt.% in methanol) produced films with a thickness
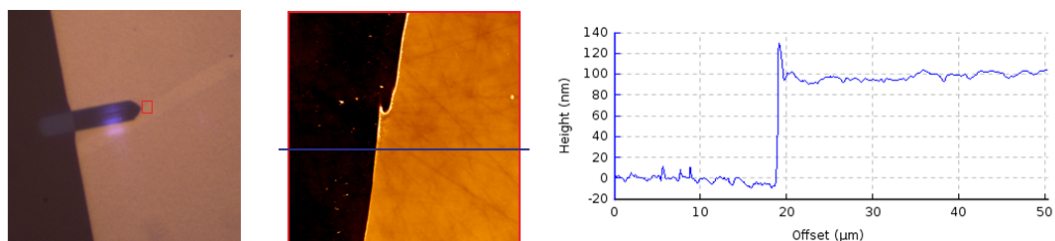
Figure 3.14: Schematic representation of the AFM investigation conducted to determine the thickness of a Nafion coating.

of approx. 100 nm as could be shown by carefully scratching the finished Nafion coating with the tip of a fine needle and then conducting AFM measurements in the region of the resulting edge. Therefore, differently concentrated solutions of Nafion (further diluted with methanol) were used for the film preparation. Additionally, different rotational speeds for the spin coating step were investigated in order to ascertain which one yielded the most homogenous film. After the spin coating of Nafion an increase of film thickness nearing the edge of the GC substrate had sometimes been observed, resulting in a changing Nafion film thickness over the surface area of the GCE and thus to a different exposure of the catalytic particles to the electrochemical environment. In order to examine the Nafion films obtained in this investigation in respect to this unwanted uneven distribution the film was scratched over the complete diagonal of the GC substrate and its thickness then determined in three places: in the middle of the GC disk, in the middle of its radius, and near the edge. This is depicted in figure 3.14. The results of the respective investigation are shown in table 3.7.

Additionally, a simple inspection of the Nafion-coated GCEs provided useful insight, as can be seen in figure 3.15. For all GCEs prepared at a rotational speed of 2000 rpm a visible ring of thrown up Nafion can be observed near the edge of the GC disk, indicating that the rotational speed is not high enough to produce an even coating.

For the GC disks spin coated at a higher rotational speed of 4000 rpm this phenomenon is less pronounced for each pair of GCEs prepared with a particular concentration of the Nafion solution and no bulging of Nafion near the GCEs edge is observable for the one prepared with a Nafion dilution of 1:9. Since the Nafion coatings applied from the solution with a dilution of 1:99 furthermore appeared to only incompletely cover the GC surface, a dilution of 1:9 and a rotational speed of 4000 rpm looked most promising after a first inspection.

This impression is supported by the results of the AFM investigation shown in table 3.7. For the Nafion dilutions greater than 1:9 a defined coating with Nafion could not be
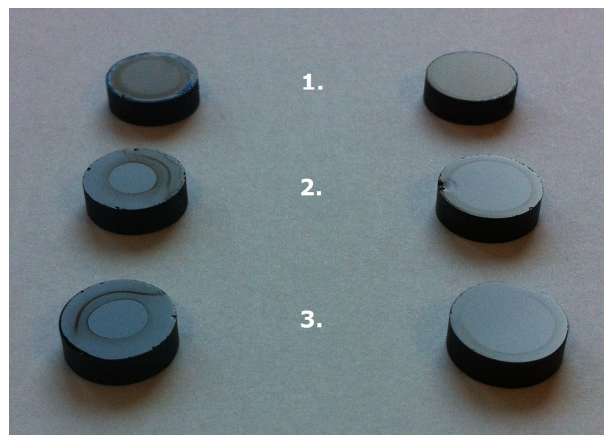
Figure 3.15: Photograph of the GCEs prepared with differently diluted Nafion solutions and at different rotational speeds. First row: Nafion diluted 1:9 with MeOH, second row: Nafion diluted 1:49 with MeOH, third row: Nafion diluted 1:99 with MeOH. Left column: Rotational speed of 2000 rpm, right column: Rotational speed of 4000 rpm.

Table 3.7: Results of the AFM investigation regarding the Nafion film thickness after spin coating GC disks with different rotational speeds and differently concentrated Nafion solutions. The second value given for a rotational speed of 2000 rpm for the GCE prepared from a Nafion solution diluted 1:9 was obtained in the region of the ring observable in figure 3.15.

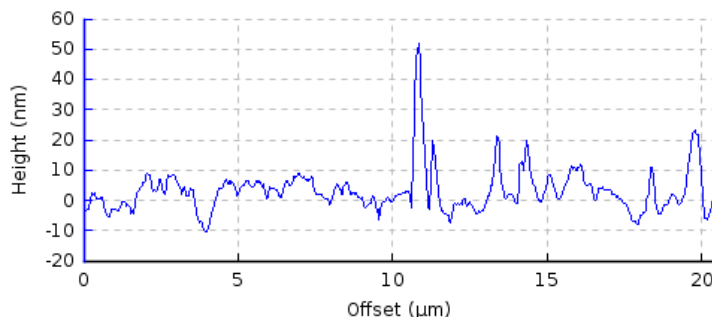| dilution (Nafion (as is):MeOH)	position	film thickness @ 2000 rpm [nm]	film thickness @ 4000 rpm [nm]
	middle	42	39
1:9	midway	36	40
	edge	59 (152)	-
	middle	≤ 10	≤ 10
1:49	midway	≤ 10	≤ 10
	edge	≤ 10	≤ 10
	middle	≤ 10	≤ 10
1:99	midway	≤ 10	≤ 10
	edge	≤ 10	≤ 10

Figure 3.16: Height trace of a scratched Nafion coating prepared from Nafion solution diluted 1:99 with MeOH at 4000 rpm. The spike at an offset of approx. 11 µm is probably a consequence of of the bulging of the Nafion near the edge of the scratch.

determined using the chosen technique, since the coating was $\leq 10\,\text{nm}$. An exemplary height trace of such a case is shown in figure 3.16. For the Nafion solution diluted 1:9 a strongly varying thickness of the Nafion coating is found for the GCE prepared at 2000 rpm, whereas the respective GCE prepared at 4000 rpm shows a homogenous film thickness and no Nafion bulging near the edge of the GC disk. In fact, due to the absence of a clearly visible bulging an AFM measurement at the edge could not be performed because the scratch applied to the coating could not be located with the naked eye in this region. However, the good agreement of the values for the film thickness found in the middle of the GC disk and halfway to the edge as well as the absence of a visible Nafion bulging near the edge of the GC disk show that this manner of Nafion film preparation meets the above mentioned requirements of a homogenous film with a thickness of $< 50\,\text{nm}$.

3.4 Treatments for Ligand Removal

In this work five different treatments for ligand removal were investigated. The treatments employed were ligand exchange with TBAOH/MeOH, treatment in a muffle furnace, plasma, and UV/ozone treatment, as well as treatment in a vacuum furnace (see section 4.3 for experimental details). Additionally, untreated GCEs were investigated as a reference.

All treatments were applied to the ready-made GCE, not to the particles in colloidal solution. The reason for this is the requirement of a thin particle film to ensure an equal exposure of all nanoparticles to oxidative treatments like muffle furnace, plasma, and UV/ozone, as well as to the heating treatment under vacuum. In case of the lig-

and exchange with TBAOH/MeOH a treatment in solution fulfilling the requirement of equal exposure is imaginable, but colloidal stability of those ligand exchanged particles would not be given. The deposition of a homogenous particle film comparable to the films prepared with OAm/OA stabilized particles would thus not be feasible anymore. The result of a spin coating experiment with a destabilized particle batch (readily identifiable by a black precipitate from the particle solution) can be seen in the SEM image in figure 3.9. Thus, the ligand exchange treatment with TBAOH/MeOH was performed by applying the respective solution for the exchange via spin coating after the deposition of the particle film onto the GC disk.

The objective of all treatments was the removal of ligand molecules (OAm and OA) bonded to the particles surface or, in case of the ligand exchange with TBAOH/MeOH, the exchange of the oleic acid against methoxide anions. Such an exchange has been realized for a thin film of OA stabilized PbSe quantum dots by Scheele *et al.* as could be shown via IR spectroscopy.(127) This ligand exchange is based on the equilibrium that exists in the employed solution of TBAOH in MeOH

$$CH_3OH + OH^- \rightleftharpoons CH_3O^- + H_2O \qquad \{3.21\}$$
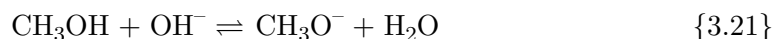
According to the law of mass action the ratio of MeO^- to OH^- in a 5 mM solution of TBAOH in MeOH will be 95:1, thus it forms a solution of methoxide with a very small (approx. 1 %) hydroxide contamination.

Oxidative treatments have been broadly and successfully used to remove organic ligands from the surface of nanoparticles. Li *et al.* examined the influence of heating platinum nanoparticles supported on carbon black (catalyst ink) to 185 °C in air, of washing them with acetic acid, and of exposing them to UV/ozone for 30 min on the catalytic activity for the ORR.(11) Their electrodes were prepared by placing an aliquot of the catalyst ink on a GC substrate and adding a droplet of Nafion. In the following electrochemical characterizations they observed both the highest specific activity ($mA\,cm^{-2}$) and specific surface area ($cm^2\,mg^{-1}$) for the heating treatment (in this work denoted "furnace" treatment).

The treatment of GCEs at 120 °C in a vacuum furnace was initially experimented with but abstained from rather early since the cyclic voltammograms obtained in the beginning of an electrochemical investigation (cycle 2) exhibited even less structuring in the hydrogen region than was found for untreated GCEs, indicating that the contamination of the catalyst surface is even greater than for the latter. For all other treatments an enhanced structuring in this region of the voltammogram was found, thus justifying a more extensive investigation. The topic of the appearance of the voltammogram in the hydrogen region will be further discussed in "Cyclic Voltammograms" in 3.4.1.

Table 3.8: Characteristics of PtNi nanoparticles used in ligand removal experiments and comparable PtNi nanoparticle batches, respectively.

name	size (TEM) [nm]	size (XRD) [nm]	Ni (EDX) [at%]	Ni (XRD) [at%]	comparable NP batches
PtNi-1	2.4	2.1	7	1	PtNi-3, PtNi-5
PtNi-2	7.3	5.0	52	42	PtNi-4, PtNi-6

Ligands block active sites on the particle surface and therefore potential binding sites for reactant molecules, thus decreasing the overall turnover number of the respective particle batch. However, a maximum of freely accessible active sites is not necessarily the optimum initial situation for PtNi nanoparticles when employed as catalysts for the MOR, as will be seen in the course of this discussion.

Details of the Investigation For the following investigation on the effect of different treatments for ligand removal on catalytic activity two sets of particles were employed. For an overview of their characteristics see table 3.8. They were chosen because of their complementary properties regarding size (PtNi-1: small, PtNi-2: large) and composition (PtNi-1: Pt-rich, PtNi-2: 1:1 alloy). Also given in table 3.8 are the denominations of nanoparticle (NP) batches with comparable properties regarding particle size and composition in respect to PtNi-1 and PtNi-2, respectively. Investigations concerning these particle batches will be discussed in 3.4.4.

Furthermore, two kinds of differently prepared composite electrodes were investigated in respect to the different treatments for both particle sets, PtNi-1 and PtNi-2. This refers to the the two kinds of GCEs introduced in 3.3. The first type, denoted "Nafion-free GCE" in the following, consists only of the GC substrate and the particle film deposited onto it. The second type, denoted "Nafion-covered GCE", encompasses an additional thin layer of Nafion spin coated onto the particle film.

3.4.1 Influence of Treatments on the ECSA

Mass related ECSA In order to determine the effect each treatment had on the catalytic activity of PtNi nanoparticles, cyclic voltammetry measurements were conducted and the electrochemically active surface area for each of the investigated GCEs was calculated by integration of the curve in the region of hydrogen underpotential deposition (H_{upd}: 0.05 - 0.40 V) for both the anodic and cathodic potential sweep as described in 2.2.3. To obtain meaningful results, not only with respect to comparability

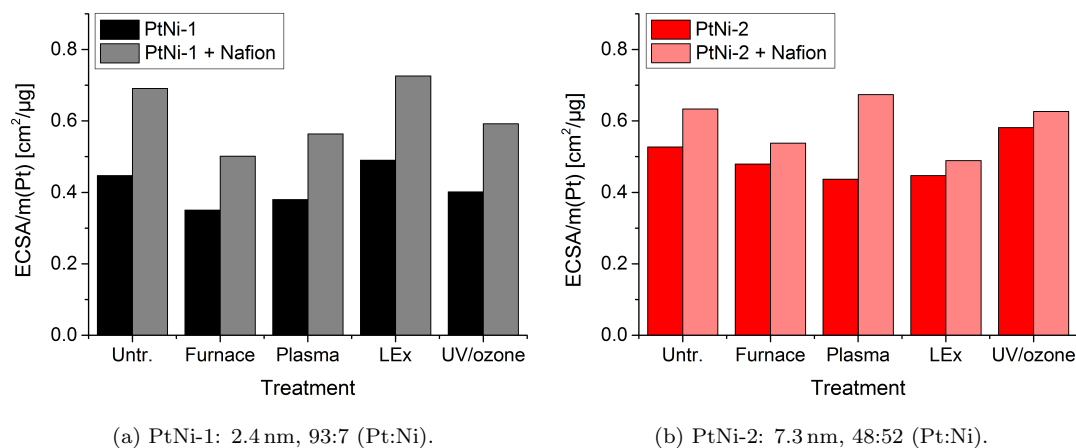(a) PtNi-1: 2.4 nm, 93:7 (Pt:Ni).　　　　(b) PtNi-2: 7.3 nm, 48:52 (Pt:Ni).

Figure 3.17: Results for the ECSA as determined by CV in $0.5\,\mathrm{M}$ H_2SO_4 and related to the mass of platinum as determined by AAS for each GCE. Each CV experiment was preceded by 150 cleaning cycles with fast sweep rates.

between different treatments applied to GCEs from the same particle batch but also between those from the two different particle batches, the obtained ECSA values were then related to the respective mass of platinum which was determined for each of the investigated GCEs after the respective CV experiment via atom absorption spectroscopy. Experimental details can be found in "Investigation into Treatments" in 4.5.3 and the results of this investigation are depicted in figure 3.17.

It can easily be seen that the values for the mass related ECSA of the GCEs prepared under addition of Nafion are higher for each of the treatments than for the ones prepared without Nafion. The reason for this can be found in the SEM images of the GCEs taken after they were subjected to the respective treatments and subsequent CV experiments and will be further discussed in 3.4.2. Besides this obvious ECSA-enhancing effect of Nafion only relatively small differences between the differently treated GCEs are found. For PtNi-1 all results for GCEs prepared without Nafion lie between 0.3 and $0.5\,\mathrm{cm}^2\,\mathrm{\mu g}^{-1}$, whereas the results for PtNi-2 with values between 0.4 and $0.6\,\mathrm{cm}^2\,\mathrm{\mu g}^{-1}$ are slightly higher. For the respective values for GCEs prepared with Nafion values between 0.5 and $0.8\,\mathrm{cm}^2\,\mathrm{\mu g}^{-1}$ are found for PtNi-1 and slightly smaller values between 0.4 and $0.7\,\mathrm{cm}^2\,\mathrm{\mu g}^{-1}$ for PtNi-2.

The greatest mass related ECSA for PtNi-1 is found for the ligand exchange treatment, both for the Nafion-free and Nafion-coated GCE. However, these values are closely followed by the values found for the untreated GCEs of PtNi-1. For this small and Pt-rich particles all oxidizing treatments (furnace, plasma and UV/ozone) lead to lower values of the mass related ECSA. For PtNi-2, however, the situation is different. Here,

the best results are found for the UV/ozone treatment for the GCE prepared without Nafion and for the plasma treatment for the Nafion-coated GCE. For Nafion-free GCEs the high value observed for the UV/ozone treatment is closely followed by the value found for no treatment and then successively by the ones for furnace, ligand exchange and plasma treatment. For the Nafion-coated GCEs the maximal value observed for the plasma treatment is followed by the one observed for the untreated GCE, which in turn has only a slightly higher value than the UV/ozone treated GCE. The values found for the Nafion-coated GCEs subjected to furnace and ligand exchange treatment exhibit the smallest value for the mass related ECSA.

Summing up these results leads to the conclusion that for particles similar to PtNi-1, i.e. rather small and Pt-rich nanoparticles, non-oxidizing treatments such as no treatment and ligand exchange yield the highest values for the mass related ECSA, both for GCEs prepared with and without Nafion. In case of the treatment denoted "untreated" in this work it has to be mentioned, however, that an electrochemical cleaning/activation process evidently takes place during the electrochemical measurement as will be further discussed in the next paragraphs. For bigger alloy nanoparticles (around 7 nm with a nickel content around 50 %), such as the PtNi-2 particles investigated here, strongly oxidizing treatments like plasma and UV/ozone lead to high values of mass related ECSA in case the GCE was prepared with Nafion. The untreated Nafion-coated GCE showed a high value for the mass related ECSA as well. However, for GCEs prepared without Nafion the situation was quite different with the lowest value found for the plasma treated GCE and the highest for the UV/ozone treated GCE followed in third place by the untreated GCE. The plasma treatment thus yields the highest mass related ECSA value when Nafion is used in GCE preparation and the lowest value when the GCE is prepared without Nafion for PtNi-2. A possible explanation for this observation will be given in 3.4.2.

Cyclic Voltammograms   To further investigate the influence of the different treatments on the electrochemical behavior, a selection of cyclic voltammograms of the GCEs discussed in the paragraph above are compiled in figures 3.18 and 3.19. Experimental details concerning measurement conditions can be found in "Investigation into Treatments" in 4.5.3. The voltammograms all exhibit the features that are expected for a platinum-based catalyst in an acidic medium (see 2.2.3). The hydrogen region is clearly discernible, as is the oxygen region including, to different extends, the platinum oxide reduction peak at approx. 0.8 V vs. RHE. Before beginning the discussion of the different features of the cyclic voltammograms one characteristic found in the double layer region for several of the treatments requires an explanation.
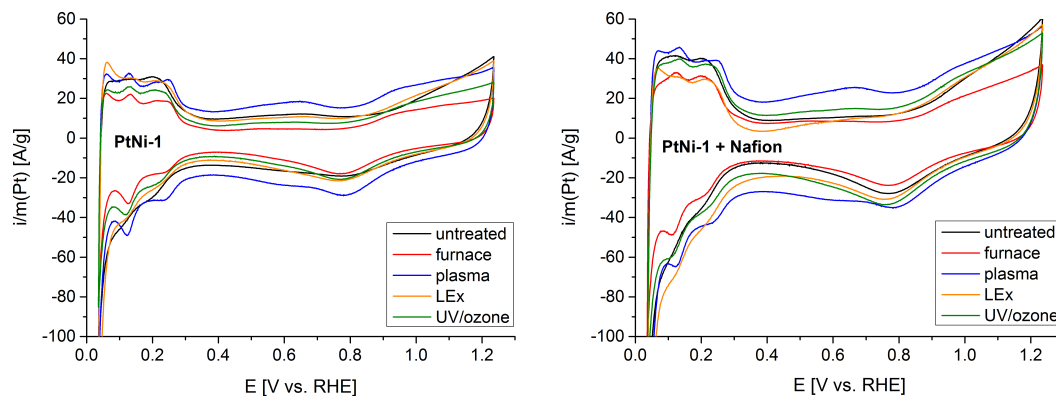
(a) Cyclic voltammograms of GCEs without Nafion.

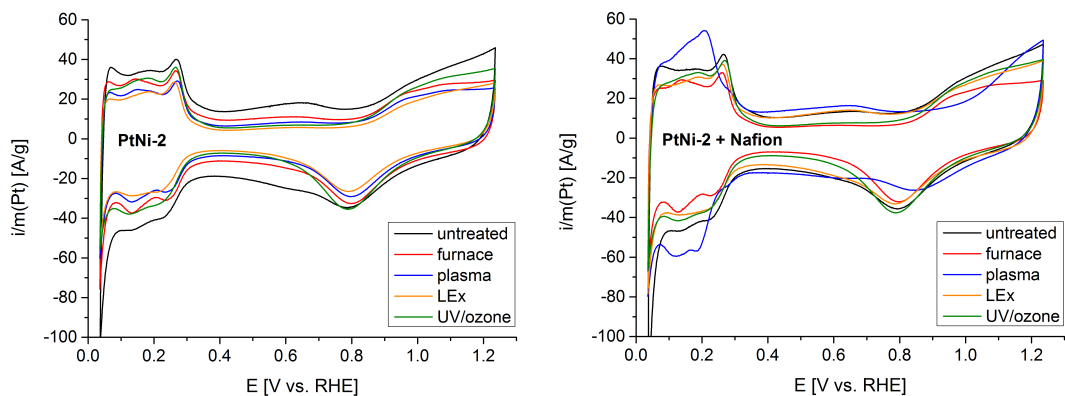(b) Cyclic voltammograms of GCEs with Nafion.

Figure 3.18: Cyclic voltammograms of differently treated GCEs of PtNi-1 prepared (a) without and (b) with Nafion. The voltammograms were obtained after 150 fast electrochemical cleaning cycles using the setting "current averaging" and a sweep rate of $50\,\mathrm{mV\,s^{-1}}$.

This refers to the enlarged current in the double layer region and the very small pair of peaks at approx. $0.65 - 0.70\,\mathrm{V}$ in the anodic and approx. $0.55 - 0.60\,\mathrm{V}$ in the cathodic sweep, which is clearly notable for the plasma treated GCEs, both Nafion-free and Nafion-coated, for PtNi-1 (figure 3.18) and can be observed for PtNi-2 (see figure 3.19) for the untreated Nafion-free GCE as well as the untreated, plasma and LEx treated Nafion-coated GCEs. Although it may seem so at a first glance this peak pair, as well as the enlarged current in the double layer region that is observed correspondently, are not a consequence of any treatment of the GCEs or of the investigated particles or a combination of the two. Instead, they are a result of the redox reaction of the GC substrates quinone-like (Q) groups corresponding to the following equation.(128)

$$Q + 2\,e^- + 2\,H^+ \rightleftharpoons QH_2 \qquad \{3.22\}$$

This peaks as well as the overall enlarged currents in the double layer region appear when glassy carbon is oxidized.(129) They were observed in this work in each CV experiment for which due to a gas bubble in the Haber-Luggin capillary or a similar error a strong oxidation of the electrode occurred and were usually accompanied by the formation of gas bubbles at the electrode. In these cases the formed peaks were far more pronounced (see figure 3.45c in 3.5.2) than the ones observed in figures 3.18 and 3.19. This leads to the conclusion, that the respective features in the cyclic voltammograms are an indication for the state of the GC substrate and not related to the applied treatments.

(a) Cyclic voltammograms of GCEs without Nafion.

(b) Cyclic voltammograms of GCEs with Nafion.

Figure 3.19: Cyclic voltammograms of differently treated GCEs of PtNi-2 prepared (a) without and (b) with Nafion. The voltammograms were obtained after 150 fast electrochemical cleaning cycles using the setting "current averaging" and a sweep rate of $50\,\mathrm{mV\,s^{-1}}$.

The progressing oxidation of the GC substrates even without the occurrence of an error in the CV experiment (such as the commonly occurring gas bubble in the Haber-Luggin capillary that inhibits the electrolytic contact between the reference and the working electrode and thus leads to an overmodulation of the potentiostat and to an oxidation of the GCE) is not surprising, considering that the they are heated in aqua regia repeatedly, submitted to oxidative (furnace, plasma, and UV/ozone) treatments and exposed to potentials of up to 1.2 V with each CV cycle they are subjected to. However, the application of a 5-step polishing procedure (see 4.2.1 for experimental details) is able to reproduce a surface finish as desired for a GC substrate. Since the features described above are not a direct consequence of the treatment applied in the respective case, they are ignored in the following discussion of the cyclic voltammograms.

A very interesting information in the cyclic voltammograms of figures 3.18 and 3.19 can be found in the characteristics of the H_{upd} region. The peaks observed in this region resemble the ones found for a polycrystalline platinum surface as can be seen in comparison to the cyclic voltammogram in figure 2.9 in 2.2.3 or in figure 3.55 in 3.7.1. For PtNi-1 well-structured curves in the H_{upd} region are observed for all oxidizing treatments, except for the untreated and LEx treated GCEs for both types of composite electrode (with and without Nafion).

The Nafion-free GCEs of PtNi-2 show well-defined peaks in the H_{upd} region only for furnace and plasma treatment, especially if the cathodic sweep is taken into consideration, for which the curves of the other three treatments exhibit rather flat features.

71

3. RESULTS AND DISCUSSION

For the Nafion-coated GCEs of PtNi-2 the most well-structured H_{upd} region is found in case of the furnace treatment. The untreated, ligand exchanged and, surprisingly, the UV/ozone treated GCE as well show comparably undefined features. In prior experiments regarding the influence of the respective treatments on Nafion-coated GCEs of PtNi-2 the cyclic voltammograms for the UV/ozone treatment repeatedly showed a strong structuring in the H_{upd} region. This will be further discussed throughout the following paragraphs and in 3.4.2.

Additionally to this differences in the H_{upd} region differences regarding the platinum oxide reduction peak between the particle batches and the GCEs prepared with and without Nafion can be observed. For the small and Pt-rich particles (PtNi-1) the platinum oxide reduction peak is more pronounced for the Nafion-coated GCEs, whereas for the larger, 1:1 alloy platinum nickel nanoparticles (PtNi-2) it is better developed in general, independently of the preparation method (with or without Nafion).

In summary only slightly different cyclic voltammograms for the different treatments applied to the two sets of particles were found. These treatment-induced differences were primarily observable in the H_{upd} region of the voltammograms. The platinum oxide reduction peak appears to be defined mostly by the sort of electrocatalyst employed as well as by the preparation method of the GCE.

Development of the ECSA In order to better understand how the very different voltammograms described in the last paragraph develop, the cyclic voltammograms of the electrochemical cleaning (ECC) cycles were thoroughly evaluated. For experimental details see "Investigation into Treatments" in 4.5.3. In order to facilitate the comparison between the investigated treatments the results are represented normalized to the treatment exhibiting the highest value of mass related ECSA in the 135th cycle for each set of particles and for Nafion-coated and Nafion-free GCEs, respectively. The resulting four sets of cyclic voltammograms are shown in figures 3.20 and 3.24. For each treatment the cycles 2, 45 and 135 are shown, representing the electrochemical conditions at the beginning of the measurement, after an intermediate number of cycles and right before the actual measurement starts, which then provides the data that was discussed in the paragraph above. The second instead of the first cycle is used for this purpose because during the first cycle of the CV experiment, which directly follows an amperometric pretreatment (see 4.5.3 for experimental details) in which the electrical double layer is charged, equilibrium conditions are not at once reached so that no meaningful information in respect to the ECSA of the GCE can be gained.

For the Pt-rich 2.4 nm particles (PtNi-1) the second cycles of the untreated and the ligand exchanged GCEs show considerably lower currents in the H_{upd} region for both
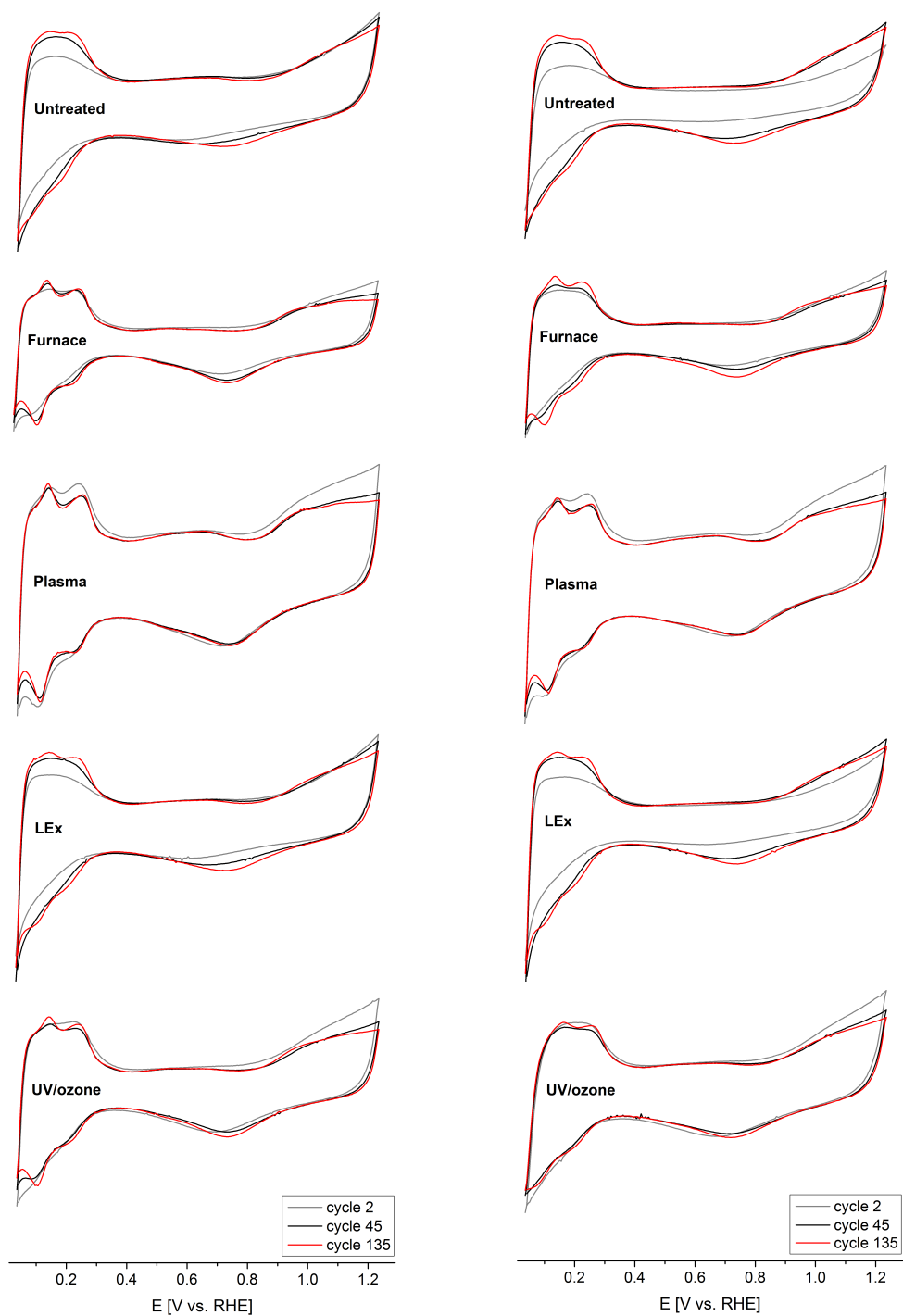
(a) PtNi-1 without Nafion.

(b) PtNi-1 with Nafion.

Figure 3.20: Mass related cyclic voltammograms of cycle 2 (gray), 45 (black) and 135 (red) of differently treated GCEs of PtNi-1 (a) without and (b) with Nafion. The voltammograms were obtained under "current averaging" and a sweep rate of $500\,\mathrm{mV\,s^{-1}}$.

73

preparation methods (with and without Nafion). This is contrary to the second cycles measured after oxidative treatments for which the second, the 45th and the 135th cycle show very similar currents. Additionally, the cyclic voltammograms of the oxidatively treated GCEs exhibit very well-defined peaks in the H_{upd} region, especially with furnace and plasma treatment. This structuring of the H_{upd} region is less pronounced for the untreated and ligand exchanged GCEs where it is only observable in the latest cycle, alas still rather weakly. These results lead to the conclusion that the oxidative treatments produce electrocatalysts (for further information on their shape and structure see 3.4.2) with a relatively well defined platinum surface, whereas in the case of untreated and ligand exchanged GCEs an electrochemical cleaning process during the initial potential cycling takes place. This coincides with the results discussed in the paragraph before, where the cyclic voltammograms for PtNi-1 showed more pronounced structuring of the H_{upd} region for the oxidative treatments as well.

Differences between the GCEs of PtNi-1 without Nafion on the one hand and with Nafion on the other hand are small. Since each set of measurements is normalized internally to the highest value of mass related ECSA of the 135th cycle, current intensities can not be compared between the two preparation methods (with and without Nafion). However, the shapes of the voltammograms are comparable and show a very good correspondence in respect to the applied treatments, a fact that underlines the reproducibility and thus validity of the setup and the applied measurements.

A more quantitative overview of the results discussed before is shown in figure 3.21, where the relative change in mass related ECSA from cycle 2 to cycle 135 is depicted. A relative change of $\geq 76\,\%$ is observed for the LEx treatment and with $\geq 95\,\%$ an even greater one for the untreated case, as one would expect when employing as-prepared, still ligand stabilized nanoparticles, which are successively cleaned by potential cycling. Compared to that the oxidative treatments show much lower percentages for the change from cycle 2 to cycle 135, indicating that their surface is already freed of a considerable quantity of ligand. The still significant relative changes from cycle 45 to cycle 135 for the untreated and LEx treated GCEs additionally show that the increase of the ECSA is a successive process that continues beyond the first few cycles. Apart from that, it is noteworthy that the plasma treatment is the only treatment for which the second cycle exhibits a higher mass related current than the 135th cycle for both cases with and without Nafion.

This can also be seen in figure 3.22 where the development of the normalized mass related ECSA is shown as a function of the number of cycles for PtNi-1 and PtNi-2, both with and without Nafion. All measurements have a very fast (within the first few cycles) decrease of current in the hydrogen region in common. Consequently, a decrease
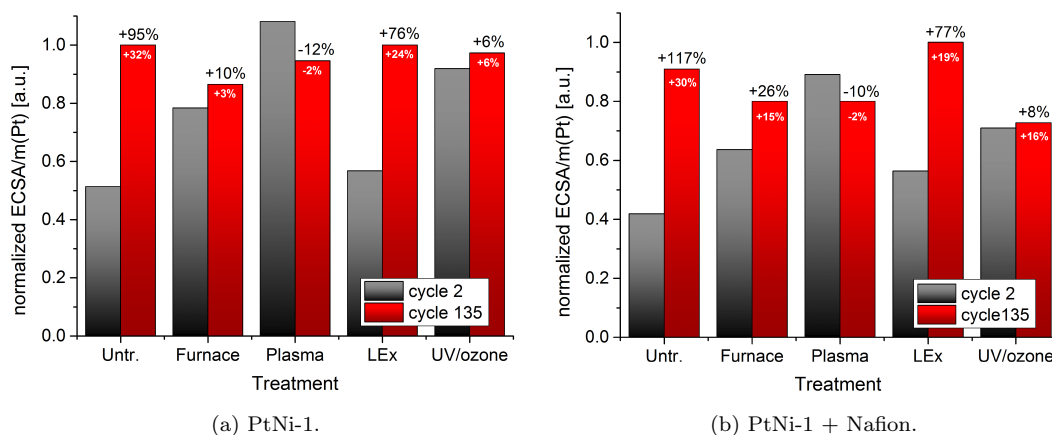
(a) PtNi-1.

(b) PtNi-1 + Nafion.

Figure 3.21: Normalized mass related ECSA of differently treated GCEs of PtNi-1 prepared (a) without and (b) with Nafion. Shown are the values for the second (gray) and the 135th (red) cycle with the respective relative change (black % value). Also given is the relative change from the 45th to the 135th cycle (small white % value).

in mass related ECSA is observed in the curves of figure 3.22. This phenomenon was only observed when an amperometric pretreatment was applied prior to the potential cycling. It is observed again for the 91th and the following few cycles, since after the initial 90 cycles a new measurement, comprised of 45 more cycles, was started. This second part of the measurements immediately followed the first, separated only by a short electrochemical treatment of $1\,s$ at $-0.244\,V$ vs. the saturated calomel electrode (SCE). This seems to be sufficiently long to disturb the equilibrium at the electrode in such a way that 2 - 7 cycles are required to reach values following the initial course of the curve again as can be seen in figure 3.22. However, the difference in value for the ECSA between this first 2 - 7 cycles become less pronounced with each additional cycle, which is why the second cycle can be used in good approximation of the initial ECSA value at equilibrium.

For PtNi-1 the initial increase in mass related ECSA is greatest for the untreated and ligand exchanged GCEs. In both cases the initially steep increase is followed by an increase with a lower rise. The turning point appears at a smaller number of cycles for the LEx treatment (approx. 40 cycles) than for the untreated GCEs (approx. 55 cycles) as expected, since for the latter some ligand removal supposedly already occurred during the treatment whereas for the former ligand removal only starts with the beginning of the electrochemical measurement. For furnace and UV/ozone treatment there is only a considerably smaller overall increase in mass related ECSA and for plasma treated GCEs an almost horizontal course is found.

3. RESULTS AND DISCUSSION

After the initial CV measurement for the evaluation on the ECSA in sulfuric acid, the MOR investigation is conducted. Following this is a second measurement in sulfuric acid for which a similar development of the mass related ECSA is found for all GCEs of PtNi-1 regardless of the treatment. This indicates that the processes leading to this behavior are the same for all five investigated treatments, which in turn leads to the conclusion that after the MOR measurement the particles are in a state that is dominated by the consequences of the MOR measurement, not the treatment. However, an interesting observation in this regard is that the highest values for the mass related ECSA in this second examination are found for the untreated and ligand exchanged GCEs of PtNi-1. After 135 cycles they almost reach the values they exhibited after the first 135 cycles and are thus markedly different from the course observed for the oxidative treatments, which at the end of this second evaluation all show lower values than before. A more thorough discussion of the development of the mass related ECSA will follow in 3.4.2 where the behavior of the particles under electrochemical conditions is investigated by means of SEM measurements.

For the second set of particles, PtNi-2, with a diameter of 7.3 nm and a nickel content of 52 % the changes in mass related ECSA from cycle 2 to cycle 45 and cycle 135 (see figure 3.23) are different compared to those of PtNi-1. The greatest similarity is found in the fact that for the untreated and ligand exchanged GCEs (with and without Nafion) a rather great relative change is found from cycle 2 to cycle 135 with an intermediate value for the change between cycle 45 and cycle 135. However, for PtNi-2 the relative change from cycle 2 to cycle 135 is greater for the ligand exchanged GCEs (78 and 95 % for the GCE prepared with and without Nafion, respectively) than for the untreated case, where it is only 31 and 37 % (for the GCE prepared with and without Nafion, respectively). Thus the relative change is smaller than it was for the non-oxidative treatments for PtNi-1 ($\geq$ 76 % for the ligand exchanged and $\geq$ 95 % for the untreated GCE) and the order is inverted as well.

The greatest difference to PtNi-1, as well as to other CV experiments preceding this one, is found for the UV/ozone treatment. In the investigation discussed here the relative change for the transition from cycle 2 to cycle 135 of the UV/ozone treatment of PtNi-2 exhibits a value in between the one found for the untreated and the ligand exchange treatment . Values of 58 and 63 % are found for the GCE with and without Nafion, respectively, with intermediate values of 23 and 33 % for the relative change from cycle 45 to cycle 135. The development of the mass related ECSA for the UV/ozone treated GCEs is thus unexpectedly similar to that of the untreated and ligand exchanged GCEs, instead of being similar to that of the other oxidative treatments as was the case for PtNi-1. Additionally, this relatively large change from the second to
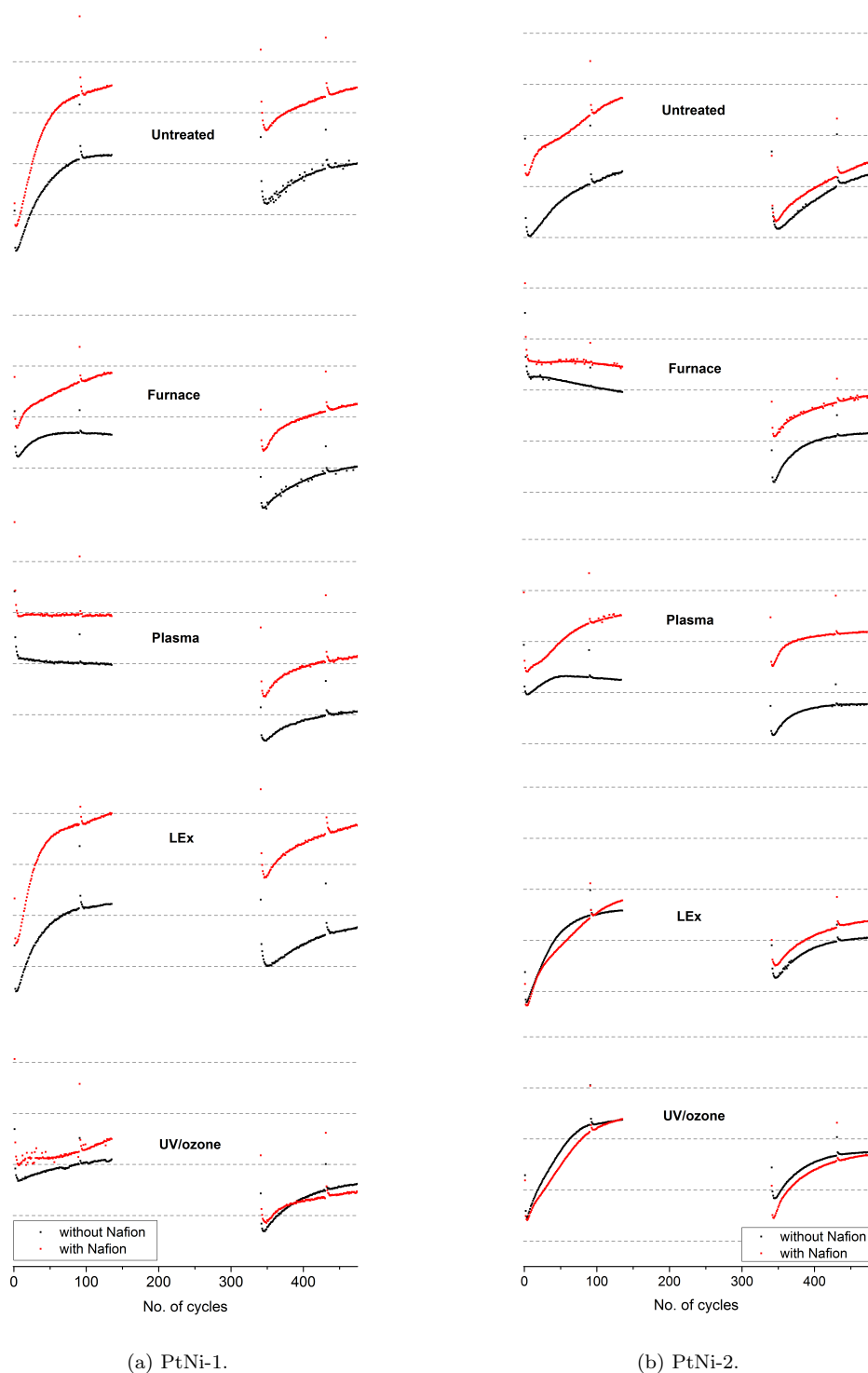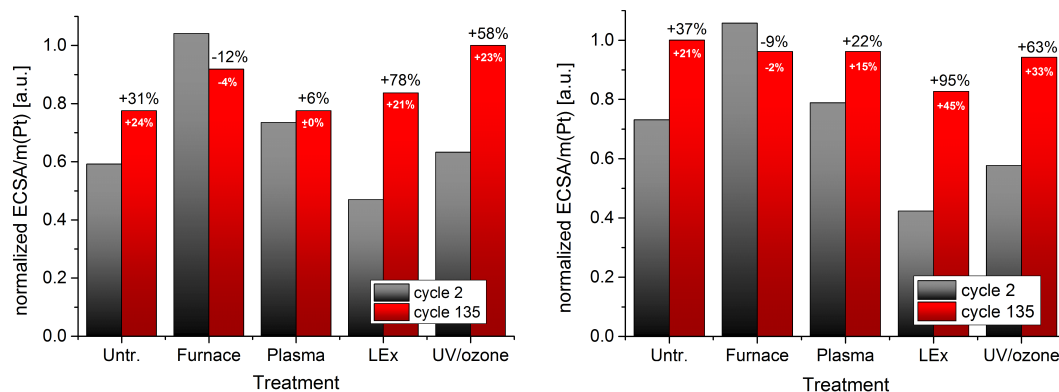
(a) PtNi-1.

(b) PtNi-2.

Figure 3.22: Development of the mass related ECSA during potential cycling for (a) PtNi-1 and (b) PtNi-2. The y-axis (ECSA) is omitted for illustrative purposes. Cyclic voltammograms were recorded prior to (cycles 1 - 135) and after (cycles 341 - 475) the MOR measurement with $\nu = 500\,\mathrm{mV\,s^{-1}}$ under "current averaging" in 0.5 M H_2SO_4.

(a) Cyclic voltammograms of GCEs without Nafion.

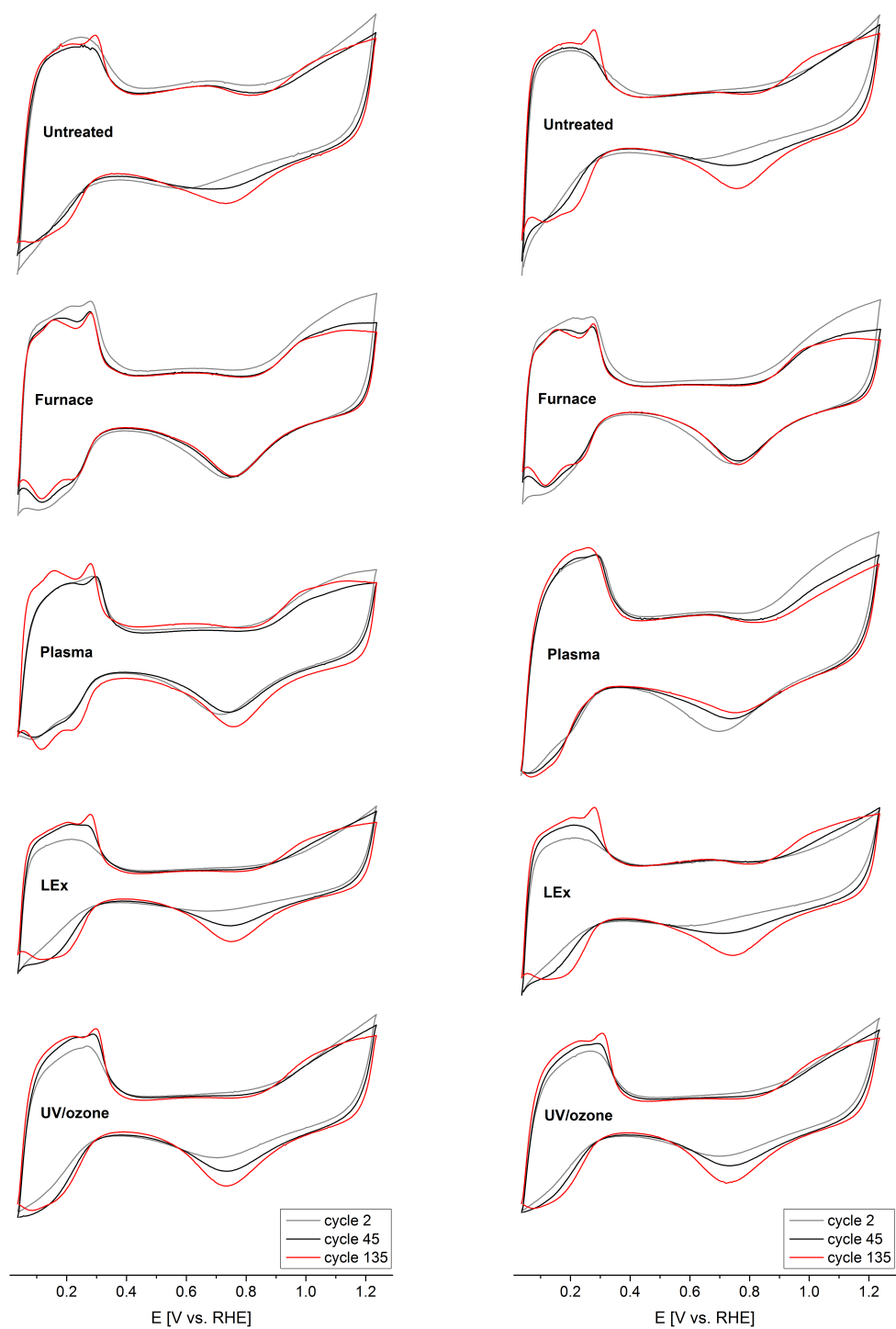(b) Cyclic voltammograms of GCEs with Nafion.

Figure 3.23: Normalized mass related ECSA of differently treated GCEs of PtNi-2 prepared (a) without and (b) with Nafion. Shown are the values for the second (gray) and the 135th (red) cycle with the respective relative change (black % value). Also given is the relative change from the 45th to the 135th cycle (small white % value).

the 135th cycle for the UV/ozone treatment has not been observed in prior investigations, where the respective percentage was 5 % (arithmetic mean of three measurements of GCEs prepared with Nafion featuring a small standard deviation of 1 % or 0.05 percentage points).

For the furnace and plasma treated GCEs of PtNi-2 small relative changes between the second and 135th cycle are found as was the case for PtNi-1. Interestingly, for PtNi-2 the furnace treatment is the only treatment for which the value of the mass related ECSA decreases from cycle 2 to cycle 135. For PtNi-1 this was true for the plasma treatment. For the plasma treatment a rather great relative change is found for the Nafion-coated GCE of PtNi-2, whereas a much smaller change is found for the Nafion-free GCE when looking at the transition from cycle 2 to cycle 135. More insight into this phenomenon is gained by investigating the mass related ECSA as a function of the number of cycles, as was already done for PtNi-1.

In figure 3.22 a strong initial increase of the mass related ECSA is found for PtNi-2 for the untreated GCEs as well as for the LEx and UV/ozone treatments as expected after the earlier observations. However, at this place it has to be remarked again that in prior investigations a different behavior has been observed for the UV/ozone treated GCEs of PtNi-2, namely a development of the mass related ECSA that is similar to that found for the UV/ozone treatment of PtNi-1, i.e. only a very slight increase of the curve with the number of cycles similar to the development observed for the plasma or furnace treatment .

(a) PtNi-2 without Nafion.

(b) PtNi-2 with Nafion.

Figure 3.24: Mass related cyclic voltammograms of cycle 2 (gray), 45 (black) and 135 (red) of differently treated GCEs of PtNi-2 (a) without and (b) with Nafion. The voltammograms were obtained under "current averaging" and a sweep rate of $500\,\mathrm{mV\,s^{-1}}$.

3. RESULTS AND DISCUSSION

For the furnace treatment of PtNi-2 an almost horizontal course of the first 135 cycles similar to that of the plasma treatment for PtNi-1 is observed, however, after approx. 30 - 40 cycles a slight decrease sets in which is more pronounced in case of the GCE prepared without Nafion. For the plasma treatment an initial increase in the normalized mass related ECSA is found, although by far not as strong as for the untreated, ligand exchanged and UV/ozone treated GCEs of PtNi-2. In case of the GCE prepared without Nafion the increase stops after approx. 50 cycles and passes over into an almost horizontal course, whereas for the GCE prepared with Nafion the increase continuous. A possible explanation of this behavior will be given in 3.4.2 where SEM images of GCEs treated according to the five treatments introduced here are discussed. For the 135 cycles directly after the MOR measurement a similar course of the mass related ECSA is found for all treatments of PtNi-2, agreeing well with the behavior found for PtNi-1. As was the case for the latter, this similarity indicates that influences of the MOR measurement dominate the development of the normalized mass related ECSA rather than influences of the respective treatments. Only in the case of the untreated GCE of PtNi-2 prepared without Nafion values for the mass related ECSA of comparable magnitude are reached for the measurements done prior to and after the MOR measurement. In all other cases the second 135 cycles do not reach the same values as the first ones did.

The cyclic voltammograms of PtNi-2 in figure 3.24 illustrate the general trend that from cycle 2 over cycle 45 to cycle 135 the structuring in the H_{upd} region, which is indicative of a polycrystalline platinum surface, becomes more pronounced. The most pronounced peaks in this region are found for the furnace treatment and for the plasma treatment, although in case of the latter only for the GCE prepared without Nafion. As expected after the earlier discussion the increase in current in the H_{upd} region (and thus the increase in mass related ECSA) from cycle 2 to cycle 135 for the LEx and UV/ozone treatment is clearly discernible and can be recognized for the untreated GCE, where it is slightly less obvious, as well. Another distinctive feature in all cyclic voltammograms of PtNi-2 is the pronounced platinum oxide reduction peak at approx. 0.8 V in the 135th cycle. Its development indicates the formation of a relatively clean platinum surface in all cases.

To sum up the results observed in investigating the development of the ECSA during electrochemical potential cycling it is sensible to differentiate two factors: the *value* of the mass related ECSA and its development as well as the *shape* of the respective cyclic voltammograms and their development. After an initial decrease in the value of the mass related ECSA, which is attributed to non-equilibrium conditions following the amperometric pretreatment, an increase with increasing number of cycles was found

for almost all treatments in this investigation in regard to the first 135 cycles in H_2SO_4 prior to and after the MOR measurement. This increase was attributed to an electrochemical cleaning process taking place during potential cycling, an assumption that is further confirmed by the development of the shape of the respective voltammograms. The more cycles are measured, the more the respective cyclic voltammogram gains features of the voltammogram of pure polycrystalline platinum (see figure 2.9 for comparison), especially in the H_{upd} region and in respect to the platinum oxide reduction peak. This leads to the conclusion that in the course of an electrochemical measurement the particle surface is cleaned of organic contamination as evidenced primarily by the increase in mass related ECSA. Secondly, the formation of a Pt-rich surface is strongly assumed since the shape of the cyclic voltammograms becomes increasingly similar to that of pure polycrystalline platinum under potential cycling. This formation of a platinum surface denoted "platinum skeleton surface" has been reported in the literature(67) and is believed to form due to leaching of the respective 3d metal from the alloy particle (see 2.2.5).

Exceptions from the increase in mass related ECSA under potential cycling are the plasma treatment for PtNi-1 and the furnace treatment for PtNi-2. In these cases an almost horizontal course for the development of the current in the H_{upd} region was found. Coupled with very pronounced Pt-like features of the respective cyclic voltammograms right from the beginning this leads to the conclusion that these treatments already produced a rather clean platinum surface so that no conceivable electrochemical cleaning process took place in these cases. Additionally, this were the only two treatments for which a decrease from cycle 2 to cycle 135 was observed.

The non-oxidative treatments (untreated and LEx) are distinguished by the strong increase in mass related ECSA with potential cycling for both PtNi-1 as well as PtNi-2. This is easily seen by the great relative change in the respective value from cycle 2 to cycle 135 (see figures 3.21 and 3.23) as well as in the diagram depicting the development of mass related ECSA under potential cycling (see figure 3.22). However, for PtNi-2 a likewise behavior was observed for the UV/ozone treatment. This is inconsistent with a prior investigation in which the voltammograms obtained were similar to the ones found for PtNi-1 after UV/ozone treatment, both regarding the structuring in the H_{upd} region as well as the development of the mass related ECSA with continued potential cycling.

The development of the mass related ECSA after the MOR measurements followed a similar course for all treatments and both sets of particles. This leads to the conclusion that the influences of the MOR measurement dominates this course rather than influences of the respective treatments.

Furthermore, the observed developments of the value of the mass related ECSA as well as the shape of the respective cyclic voltammogram are in good agreement when comparing measurements of the same treatment for GCEs prepared with and without Nafion within each set of particles. This gives reason to the conviction that the executed measurements as well as the setup of the experiment, including the GCE and particle preparation, are a valid way to investigate phenomena concerned with the effects of different treatments.

3.4.2 Agglomeration of Nanoparticles

Treatment-dependent Agglomeration The investigation of the electrochemical data obtained for different treatments discussed in the paragraph above leads to some very interesting conclusions regarding the development of the respective electrocatalyst under potential cycling. However, to complete our understanding of the involved processes the application of other, non-electrochemical methods of investigation is necessary. In order to follow processes at a particulate level SEM investigations were therefore conducted prior to and after CV experiments as well as directly after the treatment (see "Investigation into Treatments" in 4.5.3 for experimental details). Mainly PtNi-2 was used for these measurements since small particle sizes, e.g., PtNi-1 with a diameter of 2.4 nm strongly challenge the resolution of the employed SEM. In contrast, the investigated PtNi-2 particles with d $= 7.3$ nm and a nickel content of 52% can be very well resolved. All measurements shown in this paragraph are of GCEs prepared without Nafion. The CV experiment conducted in connection with this investigation consisted of 135 cycles at a sweep rate of $50\,\mathrm{mV\,s^{-1}}$ under the option "standard". The results of the respective SEM investigation in regard to the different treatments are compiled in figure 3.28.

As can be seen by comparing the SEM images taken after each of the treatments (c), (e), (g) and (i) to image (a) of an untreated particle film, the treatments alone do not change the appearance of the film. However, images (b), (d), (f), (h) and (j), which were taken after the respective CV experiment, show that the particles have agglomerated on the GC surface to different degrees. The strongest agglomeration is clearly found in the case of plasma treatment. Defining an order for the degree of agglomeration for the other treatments is not as easily done. However, a closer look at the images reveals that for the furnace and the UV/ozone treatment a smaller number of individually recognizable particles is still apparent after the CV experiment than for the untreated and ligand exchanged GCEs. Consequently, in case of the furnace and UV/ozone treatment more agglomerates without apparent grain-like structure are

(a) Untreated particle film.

(b) Untreated film after CV.

(c) Film after furnace treatment.

(d) Film after furnace and CV.

(e) Film after plasma treatment.

(f) Film after plasma and CV.

(g) Film after LEx treatment.

(h) Film after LEx and CV.

(i) Film after UV/ozone treatment.

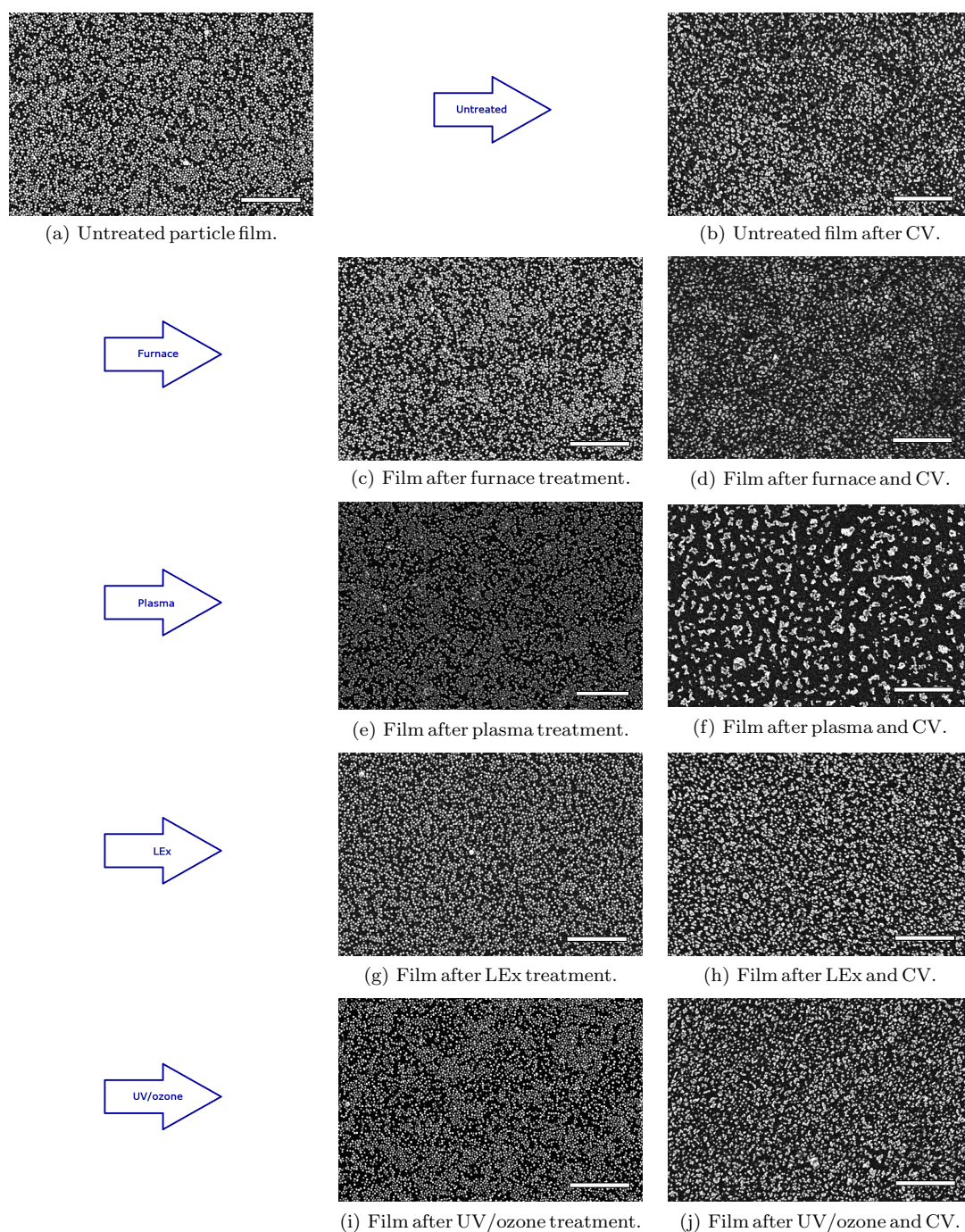(j) Film after UV/ozone and CV.

Figure 3.25: SEM images (scale bar = 200 nm) of GCEs of PtNi-2. In (a) a freshly deposited untreated particle film is shown. The second column contains SEM images of GCEs after they have been subjected to the respective treatments shown in the left column. The third column shows SEM images of the GCEs after the respective treatment and after exposure to an electrochemical environment (135 CV cycles between 0 and 1.2 V).

83

(a) H_{upd} region for the adsorption process.

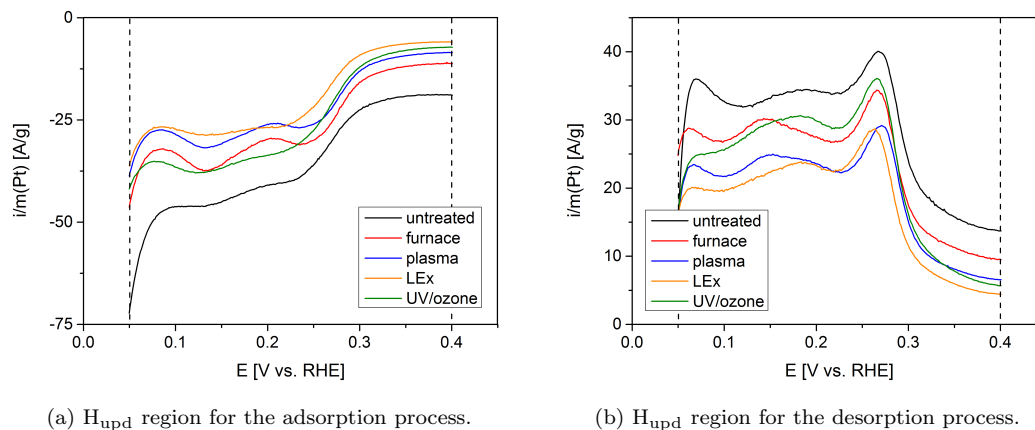(b) H_{upd} region for the desorption process.

Figure 3.26: H_{upd} region for the (a) adsorption and (b) desorption process of PtNi-2 after different treatments and 150 fast electrochemical cleaning cycles. Shown here is the 165th cycle (in total), recorded at a sweep rate of $50\,\mathrm{mV\,s^{-1}}$ under "current averaging".

found after the CV experiment. The order that is thus produced in respect to the magnitude of agglomeration for PtNi-2 is: 1. plasma, 2. furnace and UV/ozone closely followed by 3. untreated and ligand exchange.

By comparing these results to the voltammograms shown before and focusing on the H_{upd} region of the cathodic and anodic sweep (see figure 3.26) a correlation between the degree of agglomeration and the features of the i-E curves in this region can be recognized. The most structuring (clearly discernible peaks) are found for the furnace and plasma treatment as is easily seen for both sweep directions. Less structured curves are found for the untreated, ligand exchange and, as was discussed earlier, for the UV/ozone treated GCE as well, alas this is unexpected. In prior cyclic voltammograms a strong structuring similar to that of the furnace and plasma treatment was observed for the UV/ozone treatment.

Considering that, the conclusion from this SEM investigation is the existence of a correlation between the degree of agglomeration of the nanoparticles on the GC surface and the features of the H_{upd} region of the respective voltammogram. As was explained in 3.4.1 a well defined i-E curve in this region is indicative of a relatively clean platinum surface. Thus the oxidative treatments lead not only to stronger agglomeration but also to more expressed platinum surfaces as compared to the non-oxidative treatments. This leads to the combined conclusion that in fact the oxidative treatments do produce cleaner, i.e. less ligand covered, surfaces as supported by the slight or completely absent increase in the development of the respective values for the mass related ECSA with potential cycling and the well defined H_{upd} region. Alas, the highest values for the mass

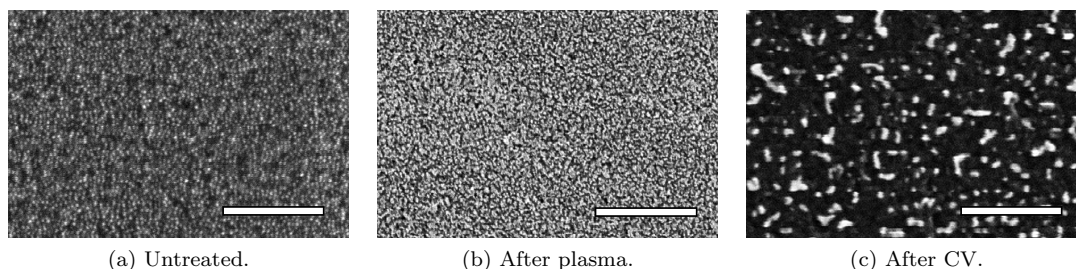(a) Untreated.   (b) After plasma.   (c) After CV.

Figure 3.27: SEM images of GCEs of PtNi-1 (a) untreated, (b) after plasma treatment, and (c) after CV experiment (360 cycles). Scale bar = 100 nm.

related ECSA are not necessarily found for these effective oxidative treatments since agglomeration of particles is stronger for cleaner, i.e. less stabilized particles. However, applying a means of stabilization during potential cycling of these oxidatively cleaned particles by means of a Nafion coating renders different results, as will be discussed in the following paragraph.

Before this is discussed further, however, the results of the SEM investigation of the plasma treated Nafion-free GCE of PtNi-1 are shortly introduced. As mentioned at the beginning of this paragraph the resolution of the SEM is approaching its limits of resolution with particles of a size in the 2 to 3 nm region, which is why SEM images of this discussion will be restricted to the case of the plasma treatment for which analogous to the results for PtNi-2 the strongest agglomeration of all treatments is observed. The respective development of agglomeration can be seen in figure 3.27. It is clearly discernible that for PtNi-1 an agglomeration already occurs during the plasma treatment itself, and does not only set in during the electrochemical measurement, as was the case for PtNi-2. The reason for this is most likely to be found in the different sizes of the particles rather than in their different compositions. Smaller particles have a greater mobility on a flat surface than bigger ones, since they naturally have fewer binding sites to the surface. However, the intensity of the agglomeration after the plasma treatment is weak when compared to that after the CV experiment.

For the muffle furnace and the UV/ozone treatment an agglomeration after the treatment was discernible as well. The respective SEM images are not shown here, because their resolution does not allow a more detailed description to be made than the general statement that a weak form of agglomeration already occurs. After the respective CV experiments the agglomeration is much stronger, as expected. Overall the same trend regarding the degree of agglomeration after CV is observed for PtNi-1 as for PtNi-2. Plasma treatment causes the strongest agglomeration, followed by UV/ozone and furnace treatment and finally by LEx and no treatment at all. In contrast to the

observations for PtNi-2, however, for PtNi-1 an agglomeration of particles is already discernible directly after the oxidative treatments, gaining strongly in intensity during the following electrochemical measurement.

Particle Film Stabilization via Nafion Coating It has been determined at the beginning of this section for both PtNi-1 and PtNi-2 and for each of the applied treatments that the Nafion-coated GCEs exhibit a higher mass related ECSA than the GCEs prepared without Nafion. The straightforward explanation for this is that Nafion stabilizes the treated, but still non-agglomerated (or only slightly agglomerated in the case of small particles such as PtNi-1) particle film to some degree by suppressing agglomeration. To prove this assumption SEM images of Nafion-coated GCEs of PtNi-2 were taken after the CV experiment for each of the treatments and compared to the images of the respective Nafion-free GCEs.

Since agglomeration has proven to be especially pronounced in connection with plasma treatment (see figure 3.28 and discussion in the preceding paragraph) a comparison of the SEM images obtained from three different GCEs for this treatment is shown in figure 3.28. One of the GCEs was prepared without Nafion whereas the other two were prepared with two differently concentrated Nafion solutions, thus producing coatings of different thicknesses (see 3.3.3). It becomes clear from looking at this comparison that Nafion is indeed able to stabilize the particle film, the appearance of which is unaltered after the treatment itself (see figure 3.28, second column), making it possible to apply the Nafion coating to the still intact (non-agglomerated) particle film at this point, thus enabling its stabilization (see 4.2.3 and 4.3.4 for experimental details regarding the procedure of the GCE preparation).

Nonetheless, a more quantitative investigation of the plasma treatment was undertaken. To this end suitable SEM images were transformed into binary images and the agglomerates then counted in addition to determining their mean size. This was done, as mentioned above, for two GCEs, each prepared with a differently concentrated Nafion solutions of which one was diluted 1:9 and the other one 1:99 with methanol. The results are shown in figure 3.28 as well as in table 3.9. As can clearly be seen the size of the formed agglomerates decreases with the use of Nafion and with increasing Nafion concentration of the applied solution. Consequently, an increase in the number of agglomerates found in a defined area is observed. This findings thus explain why the values for the mass related ECSA found for the different treatments of Nafion-coated GCEs are always higher than the corresponding values for GCEs prepared without Nafion. It is assumed that this explanation also holds true regarding the other treatments discussed in this work.
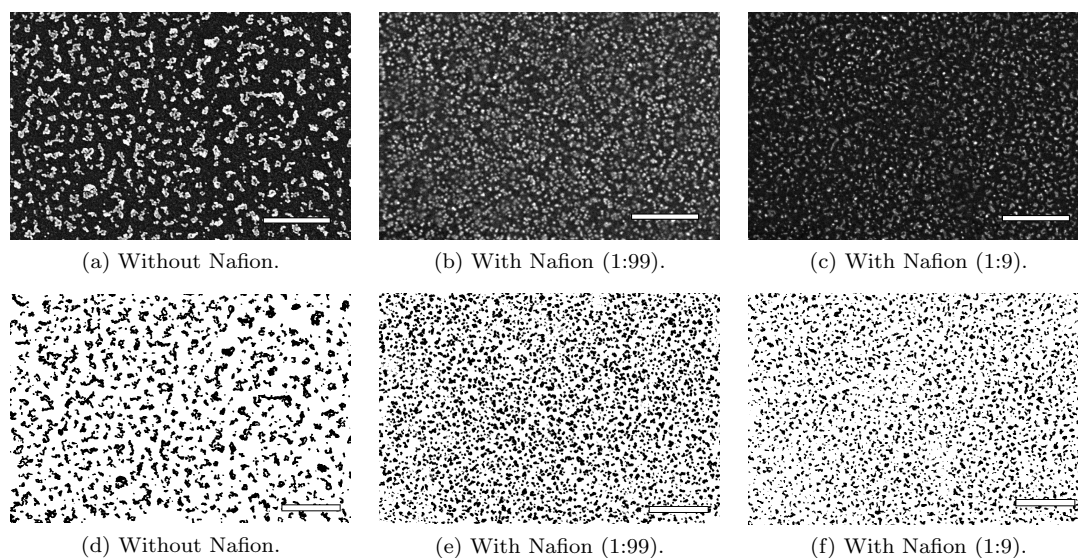
(a) Without Nafion.	(b) With Nafion (1:99).	(c) With Nafion (1:9).
(d) Without Nafion.	(e) With Nafion (1:99).	(f) With Nafion (1:9).

Figure 3.28: SEM images of GCEs of PtNi-2 (first line) and after transformation into binary form (second line). Readily identifiable are the different degrees of agglomeration after a CV experiment of the PtNi-2 particle film (a) and (d) without Nafion, (b) and (e) with a coating of Nafion:MeOH of 1:99 and (c) and (f) with a coating of Nafion:MeOH of 1:9. Scale bar = 200 nm.

Showing the respective SEM images of the other four treatments is abstained from at this point since the differences between the Nafion-free and Nafion-coated agglomerates are not as easy to distinguish with the naked eye as is the case for the plasma treatment. However, the stabilizing effect of a coating of Nafion is apparent for all treatments from the fact that the mass related ECSA is always higher in the cases of a GCE preparation with Nafion. It also explains the large difference found for the Nafion-free and the Nafion-stabilized plasma treated GCEs of PtNi-2 in regard to mass related ECSA (see figure 3.17b). The plasma treatment seemingly removes the blocking ligands on the particles surface quite effectively, leading to a high ECSA provided that the thus activated particle film is stabilized by a Nafion coating. Otherwise, strong agglomeration occurs leading to a much smaller value for the ECSA. In table 3.10 the relative differences between the values of the mass related ECSA of GCEs prepared with and without Nafion are compiled for each of the treatments and for both sets of the investigated nanoparticles.

As can be seen the respective difference between Nafion-free and Nafion-stabilized GCEs is much higher for PtNi-1 for each of the treatments (30-35 %) than for PtNi-2 (7-35 %). This means that the stabilization Nafion is capable of conveying has a greater impact

Table 3.9: Size and number of agglomerates found after CV experiments on plasma treated GCEs of PtNi-2 prepared without Nafion and stabilized by differently concentrated Nafion solutions.

GCE preparation	mean agglomerate size [nm]	agglomerates per unit area [/0.89 µm²]
without Nafion	17	595
with Nafion (1:99)	11	1906
with Nafion (1:9)	7	2345

Table 3.10: Differences between the values for the mass related ECSA of GCEs prepared with and without Nafion for each of the investigated treatments.

particle batch	Untreated [%]	Furnace [%]	Plasma [%]	LEx [%]	UV/ozone [%]
PtNi-1	35	30	33	33	32
PtNi-2	17	11	35	9	7

on the smaller Pt-rich particles (PtNi-1), which in turn indicates that agglomeration and eventual coalescing occurring for these particles under potential cycling is much stronger than for the bigger alloy particles (PtNi-2), a fact that has already been established in the previous paragraph and been attributed to a higher surface mobility of the smaller particles. The driving force of coalescence is the maximizing of the surface-to-volume ratio, which means that this process, too, is expected to have a stronger impact on smaller particles, thus agreeing well with the observations made in this regard.

Progression of Agglomeration In order to find out at which stage of the CV experiment agglomeration occurs another set of experiments was conducted, again using plasma treated GCEs of PtNi-2 without Nafion to obtain an optimal visualization of the agglomeration effects. The results of this investigation are shown in figure 3.29. Before the actual CV experiment was started the influence of the acidic media on the particle film was investigated by placing the GCE in $0.5\,\text{M}$ H_2SO_4 for some minutes and then employing SEM to follow any changes in the appearance of the particle film. Additionally, the effect of the electrochemical pretreatment (see 4.5.3 for experimental details) applied in connection with the CV experiments was investigated as well as the influence that electrochemical cycling with a smaller potential range (0 - $0.7\,\text{V}$

(a) Only H$_2$SO$_4$.   (b) Only pretreatment.   (c) After 2 cycles, 0 - 0.7 V.   (d) After 985 cycles.

(e) Prior to CV.   (f) After 1 cycle.   (g) After 10 cycles.   (h) After 45 cycles.
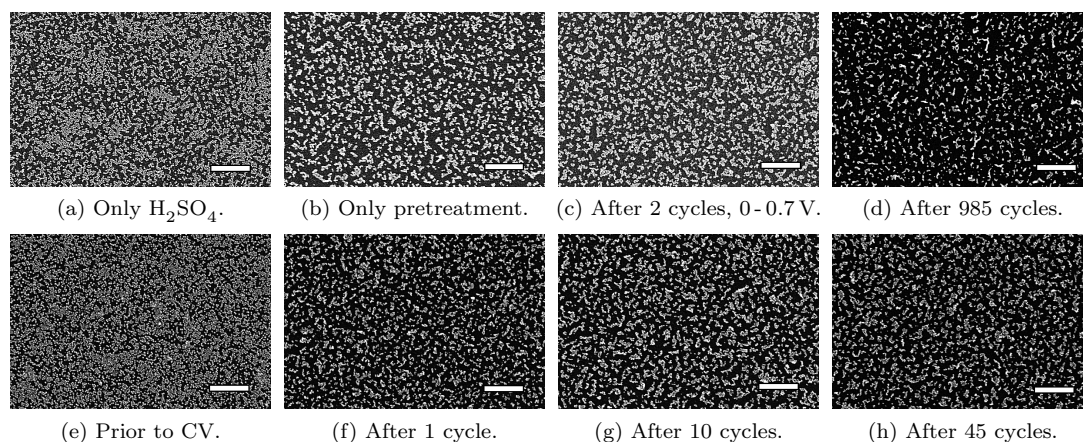
Figure 3.29: SEM images (scale bar = 200 nm) of plasma treated GCEs of PtNi-2 after different exposures to electrochemical environments, except the images on the left which were (a) exposed to H$_2$SO$_4$ only and (e) freshly plasma treated. The four images in the first line were obtained from different GCEs, whereas the images in the second line all arise from the same GCE.

vs. RHE) had. For comparison the state of agglomeration after (985) cycles was examined (see 4.5.3 for experimental details). After these initial investigations another CV experiment with a freshly plasma treated GCE was started and SEM measurements conducted after 1, 10 and 45 cycles on the same GCE. Experimental details can be found in 4.5.3, the results of this investigation are shown in figure 3.29.

The occurence of agglomeration is only observed in some of the above mentioned cases. For the plasma treated GCE that was only exposed to 0.5 M H$_2$SO$_4$ no definitive agglomeration can be observed (see figure 3.30a). Though the particle film looks a bit inhomogeneous, this is not necessarily a consequence of its exposure to the acidic media. It might as well be that the particle film was inhomogeneous to begin with. However, no real agglomerates, let alone coalesced particles forming larger structures, are observed. Single particles are the only species present, thus showing that no agglomeration takes place through exposition to the electrolyte alone.

In contrast, the GCE that was subjected to an electrochemical pretreatment (60 s at 0.1 V vs. RHE) shows distinct particle agglomeration, even though grain boundaries between the formerly separately spread out particles are still apparent (see figure 3.30b). The same result is found for the GCE that was cycled twice in the reduced potential range of 0 to 0.7 V vs. RHE (see figure 3.30c). For the GCE that was cycled between 0 to 1.2 V vs. RHE (the usually employed potential limits in this work) 985 times a different result is observed (see figure 3.29d). Here, the particles are not only agglomerated

(a) After 45 cycles. (b) After 135 cycles. (c) After 985 cycles.
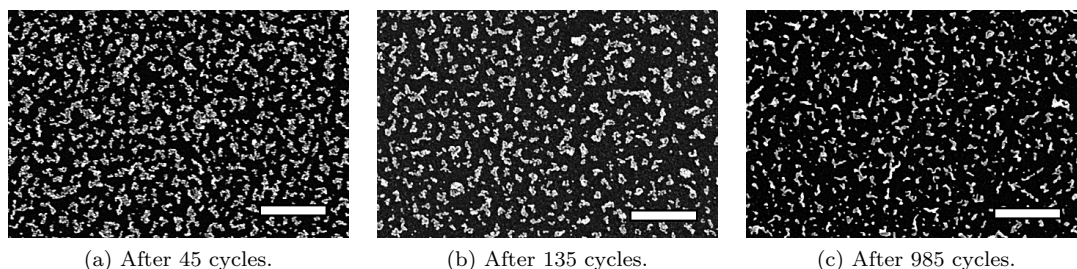
Figure 3.30: SEM images of three plasma treated GCEs of PtNi-2 at different stages of agglomeration or coalescing. (a) After 45 cycles, (b) after 135 and (c) after 985 cycles. Scale bar = 200 nm.

but have coalesced and form worm-like structures. Only a small number of apparently still single particles is observed and the overall electrode surface area covered by electrocatalyst has decreased noticeably.

In the second line of figure 3.29 the development of agglomeration over the first 45 cycles is shown in three stages. The image of the plasma treated film prior to the CV experiment shows no signs of agglomeration, as was observed before (see figure 3.28). After one cycle the state of the particle film is comparable to that of the solely electrochemically pretreated GCE or the one exposed to two cycles with a reduced potential range. The same is true for this GCE after 10 cycles. The state after 45 cycles is still very similar. This leads to the conclusion that an agglomeration of particles occurs very fast once a potential is applied to the GCE, though exposing it to H_2SO_4 alone does not lead to agglomeration for larger particles such as PtNi-2. After the initial assemblage of particles a coalescing of these closely arranged particles commences rather slowly over hundreds of cycles. This result is supported by the course that was found in regard to the development of the ECSA (see figure 3.22). In regard to the plasma treatment the immediate occurrence of agglomeration during the amperometric pretreatment explains why the process can not be recognized in the development of the ECSA - the time scale of the initial agglomeration is much shorter than that of the first CV cycles.

However, after the initial fast assemblage of particles a coalescing of this primary agglomerates can be observed over a much larger time span as is shown in figure 3.30 by means of a comparison of three of the SEM images shown before. This slower part of the agglomeration can be observed in form of a gradual decrease of the value for the mass related ECSA once the electrochemical cleaning of the catalyst surface is completed. The process of catalyst degradation will be further discussed in 3.5. In comparing the three SEM images of plasma treated GCEs of PtNi-2 after 45, 135 and 985 cycles the coalescing of already agglomerated particles is observable by the increasing area of
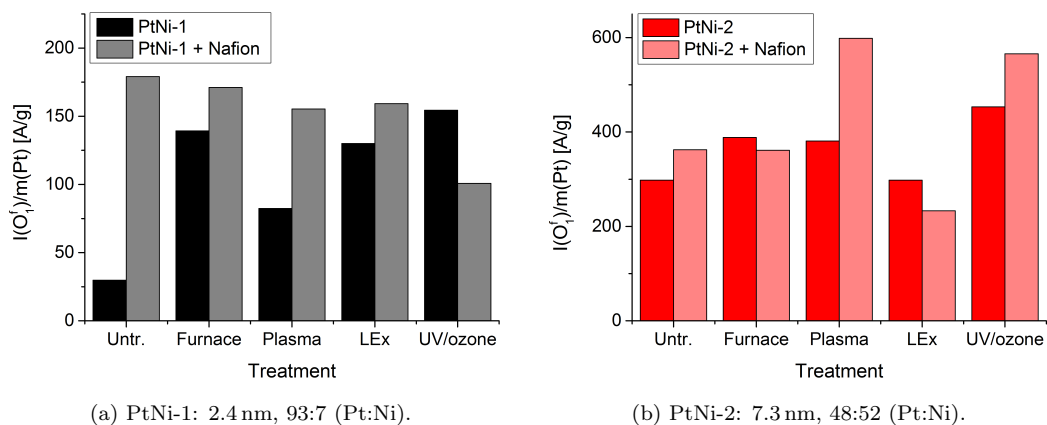
(a) PtNi-1: 2.4 nm, 93:7 (Pt:Ni).

(b) PtNi-2: 7.3 nm, 48:52 (Pt:Ni).

Figure 3.31: Mass activity as determined by CV in 0.5 M MeOH in 0.5 M H_2SO_4 for each treatment of GCEs prepared with and without Nafion. Each CV measurement was preceded by the CV experiment to determine the ECSA and an additional 150 cleaning cycles with fast sweep rates.

uncovered GC surface and the decreasing mean size of the agglomerates. Also, grain boundaries within the agglomerates, which are still discernible after 45 cycles, are not observed after 985 cycles anymore.

3.4.3 Influence of Treatments on the MOR

Mass Activity   After the effects of the different treatments for ligand removal have now been discussed in respect to the ECSA and related factors such as its development under potential cycling and the shape of the respective cyclic voltammograms, especially their H_{upd} region, (see 3.4.1) as well as the agglomeration occurring under electrochemical conditions (see 3.4.2), it is now time to take a closer look at the electrocatalytic activity of as-treated GCEs. For that purpose the mass activities (peak current of the O_1^f peak related to the respective mass of Pt of the GCE as determined via AAS) of the same GCEs that were discussed in 3.4.1 are compiled in figure 3.31. The first thing that stands out in comparison with the respective results for the mass related ECSA (see figure 3.4.1) is that the Nafion-coated GCEs here do not consistently show higher values than the ones prepared without Nafion as was the case for the former investigation. For UV/ozone treated PtNi-1 the Nafion-free GCE even shows a markedly higher mass activity than the Nafion-coated GCE. For PtNi-2 a slightly higher mass activity is found for the furnace and a moderately higher mass activity for the LEx treatment for the GCEs prepared without Nafion. Considering, as was discussed in 2.4.2, that agglomeration might lead to steps and defect sites on the agglomerates'

Table 3.11: Differences between the values for the mass activity of GCEs prepared with and without Nafion for each of the investigated treatments. Treatments for which the Nafion-coated GCE exhibits a lower mass activity than the Nafion-free are marked with the symbol (-).

particle batch	untreated [%]	furnace [%]	plasma [%]	LEx [%]	UV/ozone [%]
PtNi-1	83	19	47	18	35 (-)
PtNi-2	18	7 (-)	36	22 (-)	20

surface, which are known to be more active for the carbon monoxide oxidation than facet and terrace sites, explains this finding. In the three cases where the Nafion-free GCEs exhibit a higher mass activity the catalysis-enhancing changes during the formation of agglomerates thus seem to dominate the benefit of a larger ECSA on which the MOR can occur. The differences in percent between the Nafion-free and Nafion-coated GCE for each treatment are compiled in table 3.11. The most extreme difference in mass activity between Nafion-free and Nafion-coated GCEs is found for the untreated GCEs of PtNi-1. Indeed, these two GCEs are the ones with the lowest (Nafion-free) and highest (Nafion-coated) mass activities observed for PtNi-1.

For PtNi-1 and PtNi-2 a great difference between the two preparation methods is also found for the plasma treated GCEs. This result correlates well with the one found for the mass related ECSA (see table 3.10), where the plasma treated GCEs also exhibited rather large differences in comparison to the other treatments, a fact that was explained by the strong agglomeration caused by the plasma treatment (see 3.4.2). For the untreated GCEs of PtNi-1 a great difference was also observed for the mass related ECSA, again correlating well with the high value of 83 % found for the difference of Nafion-free and Nafion-coated GCEs for the untreated case in respect to mass activity. However, the difference in mass activity in this case is far more pronounced than that observed for the mass related ECSA.

Overall, the mass activities for PtNi-1 on GCEs prepared with Nafion are all very similar with values between approx. 160 and $180 \, \mathrm{A \, g^{-1}}$, except for the UV/ozone treatment which only reaches a value of $101 \, \mathrm{A \, g^{-1}}$. For the Nafion-free GCEs the variations are more distinctive with the highest value found for the UV/ozone treatment ($154 \, \mathrm{A \, g^{-1}}$) and the lowest for the untreated case ($30 \, \mathrm{A \, g^{-1}}$). Furnace and LEx treatment produce mass activities of 139 and $130 \, \mathrm{A \, g^{-1}}$, respectively, whereas for the plasma treatment a lower value of only $82 \, \mathrm{A \, g^{-1}}$ is observed.
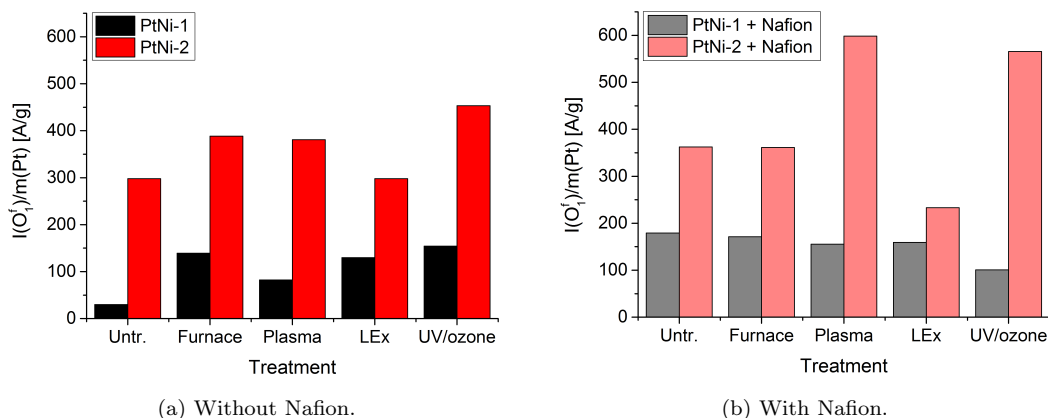
(a) Without Nafion.

(b) With Nafion.

Figure 3.32: Mass activities for PtNi-1 and PtNi-2 for each treatment in comparison (a) without and (b) with Nafion.

For PtNi-2 the by far highest mass activities are observed for the Nafion-coated plasma and UV/ozone treated GCEs with 599 and 566 $\mathrm{A\,g^{-1}}$, respectively. These values are by a factor of three higher than the greatest ones found for PtNi-1, which are the untreated and furnace treated Nafion-coated GCEs. Intermediate values of around 360 $\mathrm{A\,g^{-1}}$ are found for the untreated and furnace treated Nafion-stabilized GCEs and a comparably low value for the ligand exchanged case (233 $\mathrm{A\,g^{-1}}$). For the Nafion-free GCEs of PtNi-2 the highest mass activity is found for the UV/ozone treatment (453 $\mathrm{A\,g^{-1}}$), followed by the furnace and plasma treatment (389 and381 $\mathrm{A\,g^{-1}}$, respectively) and finally by the LEx treatment (298 $\mathrm{A\,g^{-1}}$).

In summary the mass activity of the Nafion-stabilized GCEs is generally higher than that of the Nafion-free GCEs. Only in case of the UV/ozone treated GCE for PtNi-1 and the furnace and LEx treatment for PtNi-2 was the GCE prepared without Nafion superior. This is believed to be due to the formation of particularly catalytically active surface sites via agglomeration. Overall, differences between the respective Nafion-free and Nafion-coated GCEs for each treatment correlated rather well with the analogous differences found for the mass related ECSA. In comparison PtNi-2 exhibited two- to fourfold higher mass activities than PtNi-1. This is illustrated again in figure 3.32.

Specific Activity   Next to the mass activity the specific activity of a catalyst is of interest when discussing its suitability for a given reaction. In figure 3.33 the specific activities for PtNi-1 and PtNi-2 are shown for each treatment and the Nafion-free and Nafion-coated case, respectively. The stabilizing effect of coating a GCE with Nafion and thus enhancing its ECSA (see 3.4.2) is excluded from this representation

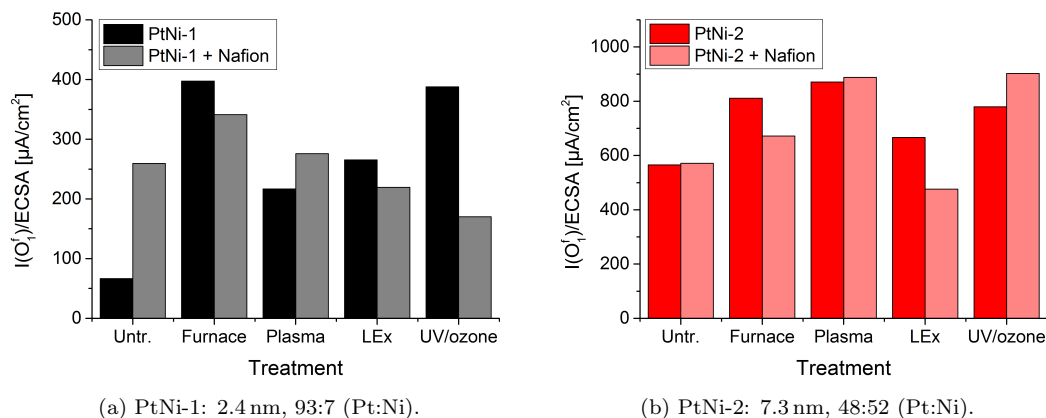(a) PtNi-1: 2.4 nm, 93:7 (Pt:Ni).   (b) PtNi-2: 7.3 nm, 48:52 (Pt:Ni).

Figure 3.33: Specific activity as determined by CV in 0.5 M MeOH in 0.5 M H_2SO_4 for each treatment of GCEs prepared with and without Nafion. Each CV measurement was preceded by a CV experiment for ECSA determination and an additional 150 cleaning cycles with fast sweep rates.

by correlating the O_1^f peak to the respective ECSA. Therefore the specific activities for Nafion-free and Nafion-coated GCEs for each treatment of either PtNi-1 or PtNi-2 are expected to be based mainly on the exhibition of different surface sites of the agglomerates forming to different degrees, provided the Nafion coating has no other effect than the stabilization of the particle film.

For most of the treatments rather small differences between the GCEs prepared with and without Nafion are observed, as can be seen in table 3.12. Differences lower than 30 % and in most cases even lower than 20 % are found for all sets of treatments except the untreated and UV/ozone treated GCEs of PtNi-1. For the untreated case it is the Nafion-free GCE that exhibits a much lower specific activity and for the UV/ozone treatment it is the Nafion-coated GCE. This can either be explained by the aforementioned differences in the surface structure of the electrocatalyst due to different degrees of agglomeration or by an inconsistency in the respective CV measurements. As was explained in 2.3.2 the MOR is very sensitive to many factors, among them differences in electrode preparation. Therefore it is possible that for the above mentioned two sets of treatments one of the respective measurements was conducted on an electrode that was not comparable to the others in respect to ,e.g., the structure of the particle film, the initial state of the particles regarding capping with ligands, oxidation state, etc., thus leading to inconsistent results.

Although it is feasible that Nafion has some activity-altering effect on the untreated and UV/ozone treated GCEs of PtNi-1, this is rather unlikely since no such effect is

Table 3.12: Differences between the values for the specific activity of GCEs prepared with and without Nafion for each of the investigated treatments. Treatments for which the Nafion-coated GCE exhibits a lower specific activity than the Nafion-free are marked with a (-).

particle batch	untreated [%]	furnace [%]	plasma [%]	LEx [%]	UV/ozone [%]
PtNi-1	74	14 (-)	21	17 (-)	56 (-)
PtNi-2	1	17 (-)	2	29 (-)	14

observed for any other treatment nor for the respective treatments of PtNi-2. The fact that differences between Nafion-free and Nafion-coated GCE are significantly larger than the ones observed for all other treatments in addition to the fact that the two concerned treatments are of a very different kind in comparison to each other further indicates that the reason for this large differences is a different one than the one found for the other treatments. Last but not least the inconsistency that for the untreated GCEs it is the one prepared without Nafion that exhibits the lower non-ECSA related activity whereas it is the other way around for the UV/ozone treatment leads to the conclusion that the results of these two experiments might be flawed. This circumstance will further be discussed in the following by means of a comparison with a previously conducted investigation.

In previous investigations of PtNi-1 a very similar mass activity was found for the untreated Nafion-free and Nafion-coated GCEs ($187\,\mathrm{A\,g^{-1}}$ and $185\,\mathrm{A\,g^{-1}}$, respectively) as compared to $179\,\mathrm{A\,g^{-1}}$ for the Nafion-coated GCE in this investigation. The results for the specific activity from this former investigation have to be interpreted very carefully since they were conducted under conditions not ideally suited for the determination of the ECSA (see 4.5.3 for experimental details). However, the difference between the two preparation methods with and without Nafion for the specific activity was only around $30\,\%$, significantly less than the $74\,\%$ found in this investigation. Therefore, it has to be assumed that the results of the electrochemical measurement for the untreated Nafion-free GCE observed for PtNi-1 are not representative and the experiment should be repeated. In the case of the UV/ozone treated GCEs of PtNi-1 previous experiments yielded a mass activity twice as high as the one observed here for the Nafion-coated GCE ($214\,\mathrm{A\,g^{-1}}$ as compared to $101\,\mathrm{A\,g^{-1}}$). This leads to the conclusion that this particular measurement should also be repeated to confirm the eligibility of any interpretations derived from it.

3. RESULTS AND DISCUSSION

Summing up the results of the investigation of the specific activity of differently treated GCEs of PtNi-1 and PtNi-2 for the MOR so far leads first and foremost to the realization that this investigation contains the means to carve out the effect of changes in the catalytic activity that appear due to agglomeration. This is possible because the influence of the respective ECSA of each investigated GCE is excluded from the specific activity.

In comparing the GCEs prepared with and without Nafion for each treatment and each particle set it was found that differences between the two preparation methods lead to deviations of the values found for the specific activity between 1 and 30 %. Higher values for this differences were found for the untreated and the UV/ozone treated GCEs of PtNi-1 and after comparison with previous experiments it is believed that they are based on flawed experiments. This is regarding the Nafion-free GCE in case of no treatment and the Nafion-coated GCE in case of the UV/ozone treatment. This two experiments will therefore not be discussed further. For the other experiments a favorable effect of agglomeration can be found for the cases for which a higher specific area is observed for the GCE prepared without Nafion than for the ones with a Nafion coating. This is the case for the furnace and the LEx treatment for both particle sets, PtNi-1 and PtNi-2.

Overall, two opposing effects on catalytic activity have been deduced in this investigation. One is the agglomeration of particles and the accompanying decrease in ECSA. The other one is a supposed formation of particularly active surface sites (probably step and defect sites, see 2.4.2) that enhance catalytic activity. An investigation of the specific activity focuses on the second effect since the catalytic activity is related to the respective ECSA thus excluding it from this consideration. In comparison to the mass activity a conclusion can then be made regarding the impact of the different effects on the respective GCEs as will be discussed in the following.

Taking another look at the results observed for the furnace and LEx treatment of PtNi-1 and PtNi-2 an inverse behavior to the one found for the mass activity (lower mass activity for the Nafion-free GCEs) for PtNi-1 is ascertained (higher specific activity for the Nafion-free GCEs), whereas for PtNi-2 the Nafion-free GCEs exhibit a higher mass activity and higher specific activity. This leads to the conclusion, that for PtNi-1 for the furnace and LEx treatment an enhancing effect occurs due to agglomeration (higher specific activity of Nafion-free GCEs) but that the stabilizing effect of Nafion has a greater impact on activity than the former (higher mass activity of Nafion-coated GCEs). For PtNi-2 the catalysis-enhancing effect of agglomeration is dominant, as can be seen by the higher mass and specific activity of the Nafion-free GCEs.

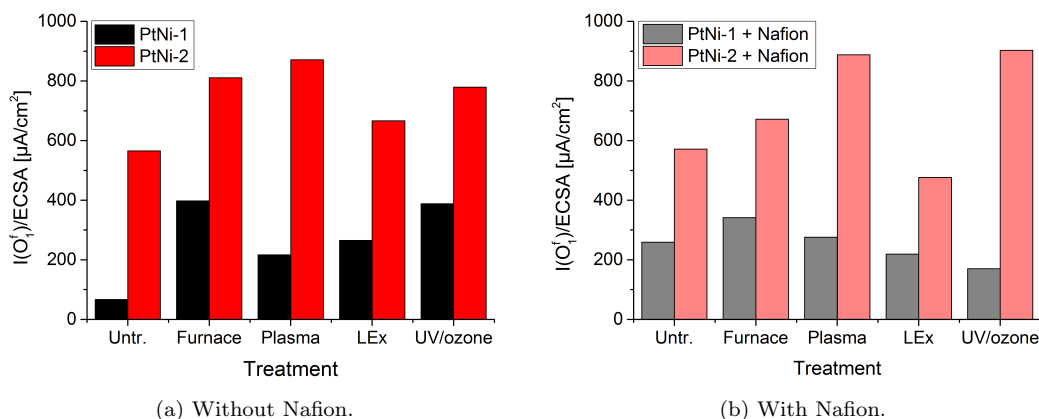(a) Without Nafion.

(b) With Nafion.

Figure 3.34: Specific activities for PtNi-1 and PtNi-2 for each treatment in comparison (a) without and (b) with Nafion.

This result is not unexpected, since for smaller particles (PtNi-1) a stronger agglomeration is supposed to occur. A stabilization via Nafion coating would thus have a greater impact on such small particles than on larger ones (PtNi-2). Evidence of that is also found in respect to the plasma treatment of which we know that it causes very strong agglomeration of PtNi-1 and PtNi-2 particles (see 3.4.2). Now, the assumption of a greater stabilizing effect of Nafion for smaller particles (PtNi-1) is further supported by the fact that the mass activity for the plasma treatment is much higher for the Nafion-stabilized GCEs for both PtNi-1 and PtNi-2, but only significantly higher for PtNi-1 in regard to the specific activity. For PtNi-2 the values found for the specific activity are almost the same (2 % difference), underlining that in this case the catalysis-enhancing effect of agglomeration is in the same order of magnitude as the stabilizing effect of Nafion coating, whereas for PtNi-1 the stabilizing effect of Nafion is dominant.

To complete the investigation of the specific activity of PtNi-1 and PtNi-2 in respect to the five investigated treatments a comparison of the values observed for the two sets of particles with and without Nafion is compiled in figure 3.34. As can be seen the specific activity is by a factor of approx. two to four higher for the larger Ni-alloy particles (PtNi-2) than for the smaller Pt-rich ones (PtNi-1).

Onset Potential The last part of the investigation of the catalytic activity of the investigated nanoparticles in regard to the different treatments concerns the onset potentials found for the MOR. In figure 3.35 the region of the onset of the O_1^f peak is shown for PtNi-1 and PtNi-2 with and without Nafion, respectively, and figure 3.36 shows the associated cyclic voltammograms. To determine exact onset potentials the

3. RESULTS AND DISCUSSION

Table 3.13: Onset Potentials (vs. RHE) of the O_1^f peak of the MOR for PtNi-1 and PtNi-2 for different treatments with and without Nafion, respectively.

particle batch	Untreated [V]	Furnace [V]	Plasma [V]	LEx [V]	UV/ozone [V]
PtNi-1	0.713	0.720	0.741	0.701	0.764
PtNi-1 + Nafion	0.753	0.746	0.750	0.751	0.726
PtNi-2	0.731	0.755	0.747	0.753	0.750
PtNi-2 + Nafion	0.746	0.762	0.748	0.761	0.735

maximum of the first derivation of the O_1^f peak was calculated using *Origin 9.0G*. Then the intersection of the tangent at this point with the baseline current of the anodic sweep (current at 0.4 V) was determined, leading the onset potential of the peak.

It can easily been seen that for PtNi-1 the onset potentials generally are lower than for PtNi-2. Furthermore, the Nafion-coated GCEs exhibit higher onset potentials in comparison to the Nafion-free GCEs for PtNi-1 and PtNi-2 for all treatments but the UV/ozone treatment. The results of the comparison of onset potentials for PtNi-1 and PtNi-2 underline that the treatment which produces the lowest value depends on composition and/or size of the employed nanoparticles. Park *et al.* determined much lower onset potentials of 0.320 V and 0.290 V vs. NHE for the carbon supported Pt_3Ni and PtNi nanoparticles (size: 3 - 4 nm) they investigated, respectively.(12) A description of how this onset potentials were determined, however, is unfortunately missing and the experimental conditions differ slightly so that a direct comparison with the results obtained here is not possible without restrictions. Agrawal and Rangarajan on the other hand report onset potentials for PtNi nanoparticles that are of the same order of magnitude as the ones observed in this work (0.685 V up to 0.722 V vs. RHE for particles with a composition of 1:0.05 up to 1:1 (Pt:Ni)).(130)

Conclusions Considering the results found for the mass and specific activity of the investigated particles in addition to the examination of the onset potential yields quite unambiguous results. For PtNi-1 the furnace treatment seems the most favorable in regard to catalytic activity whereas for PtNi-2 it is the UV/ozone treatment that produces the best results. Furthermore, the plasma treatment leads to a good catalytic activity for PtNi-2. In general an optimal treatment should produce a compromise between surface-preservation of the electrocatalyst and activity-enhancing agglomera-

(a) PtNi-1, without Nafion.

(b) PtNi-1, with Nafion.

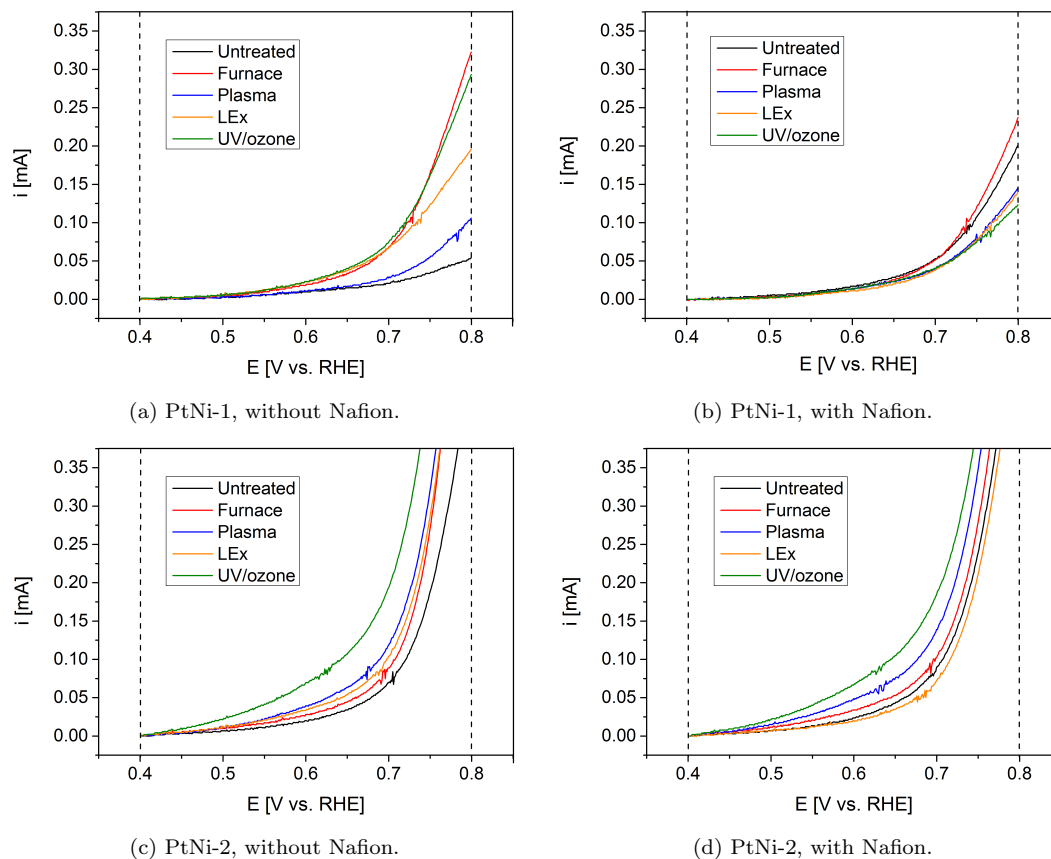(c) PtNi-2, without Nafion.

(d) PtNi-2, with Nafion.

Figure 3.35: Comparison of onset potentials of PtNi-1 (a) without and (b) with Nafion as well as for PtNi-2 (c) without and (d) with Nafion. Currents are normalized to 0 A at a potential of 0.4 V (only electrical double layer charging taking place).
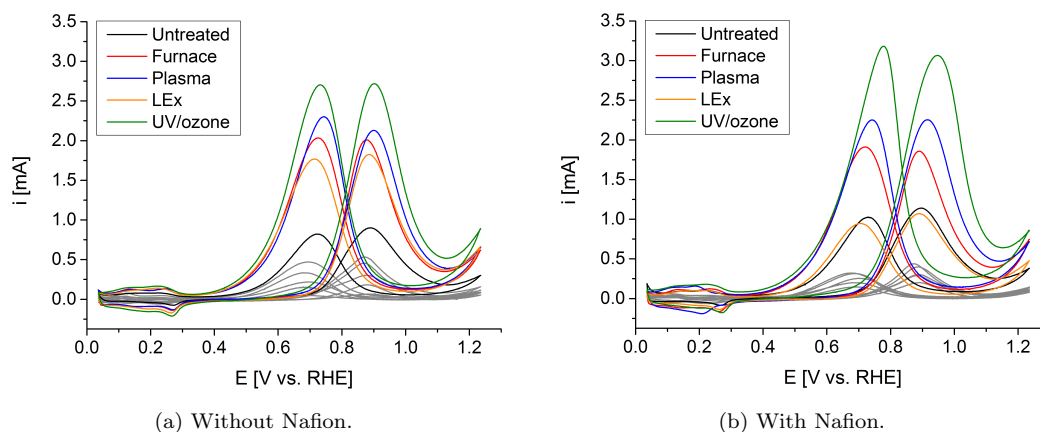

(a) Without Nafion.

(b) With Nafion.

Figure 3.36: Cyclic voltammograms of PtNi-1 (in gray) and PtNi-2 (colored) for each treatment in comparison (a) without and (b) with Nafion.

tion. For differently composed and sized particles this optimum is naturally found for different treatments. From this investigation it can be concluded that for smaller particles less aggressive oxidative (furnace and UV/ozone) treatments produce better results since with plasma as a stronger, more oxidative treatment agglomeration becomes too strong, maybe already during the treatment (see 3.4.2). For larger nanoparticles, which have a lower inherent tendency to agglomerate to begin with, the best catalytic activity is found for stronger treatments (UV/ozone and plasma). For both sets of particles investigated here, though, a form of oxidative treatment proved to produce superior catalytic activity as compared to no treatment at all or the rather mild ligand exchange treatment.

The results from this investigation show as well that an optimal (large) mass related ECSA is not necessarily the factor that dominates catalytic activity. Looking back at 3.4.1 for PtNi-1 the highest values for the mass related ECSA were found for the non-oxidative treatments, whereas the best catalytic activity for the MOR was found for the furnace treatment. For PtNi-2 UV/ozone and plasma treatment showed good results for both the mass related ECSA and catalytic activity. However, a high mass related ECSA was also found for the untreated GCEs for which catalytic activity was only mediocre.

3.4.4 Effect of Treatments on the Particles

TEM and EDX Investigation   In order to get a better understanding of how the different treatments employed in this work affected the particles of the electrocatalyst, PtNi-2 was investigated via TEM and EDX measurements after application of the most oxidative treatment (plasma) and in respect to the untreated case as a reference. Additionally, as a treatment of medium strength particles submitted to the UV/ozone treatment were investigated. For that purpose particles were deposited onto a TEM grid (a copper grid covered with a thin carbon film) and then exposed to the respective treatment (see "TEM and EDX" in 4.3 for experimental details). Since in the case described here, as well as in case of the application of a treatment to a ready-made GCE, the nanoparticles were deposited onto a carbon surface, it is assumed that the influence of particle–substrate interactions is similar for both cases and hence can be neglected in their comparison.

In figure 3.37 HR-TEM images obtained after the the different treatments are shown. As can be seen quite easily the appearance of the untreated and UV/ozone treated particles is very similar, whereas the appearance of the plasma treated particles is greatly changed. The plasma treated particles appear less smooth at the edges and
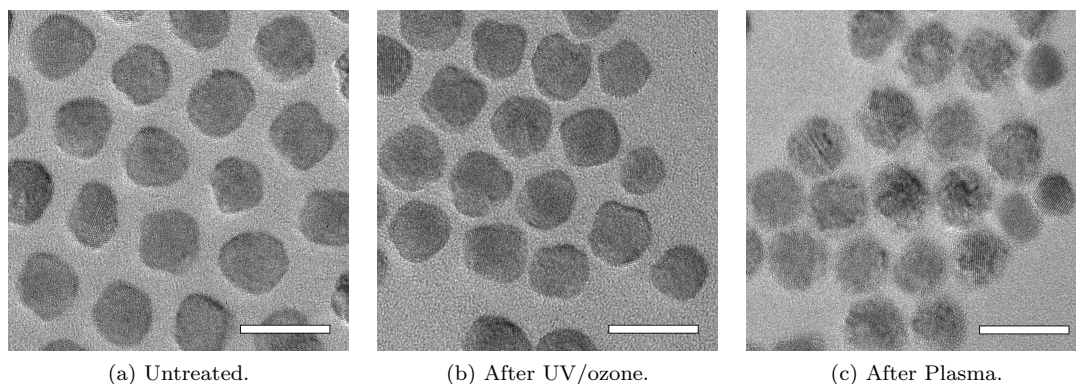
(a) Untreated.   (b) After UV/ozone.   (c) After Plasma.

Figure 3.37: HR-TEM images of PtNi-2 (a) untreated, (b) after UV/ozone treatment, and (c) after plasma treatment. Scale bar = 10 nm.

overall look very ragged and inhomogeneous. Another noteworthy change in the HR-TEM images concerns the inter-particle distance. It is greatest for the untreated sample and decreases successively for UV/ozone and plasma treatment. This was confirmed on the basis of a set of TEM images of the respectively treated nanoparticles to make sure it was not just a random effect found for the images shown here. This decreasing inter-particle distance confirms that a ligand removal actually takes place for the UV/ozone and plasma treatment and that it is stronger in case of the latter. This was already deduced in connection with the investigation of agglomeration phenomena via SEM measurements in 3.4.2. However, the realization that a slight agglomeration is already setting in during plasma and UV/ozone treatment for PtNi-2 is new. For PtNi-1 this could already be observed by means of SEM, but for PtNi-2 the agglomeration process becomes only observable by employing the TEM technique.

In addition to the TEM investigation into the PtNi-2 particles an EDX investigation was conducted to learn more about any possible changes in composition occurring due to the discussed treatments. The respective EDX investigation was conducted at a different transmission electron microscope than the the one used when determining the composition of the particles after synthesis, which explains why there is a slight deviation found in the respective results. For the untreated particles discussed here a nickel content of 54 % was found, in comparison to a value of 52 % determined using the other transmission electron microscope. More about this topic can be found in 3.7.3.

The results of the EDX investigation are summarized in table 3.14. As can be seen, the EDX investigation of the untreated particles yields a higher nickel content than the one found for any of the treated samples. Although the differences in percentage points are rather small at least a trend can be recognized that is correlating well with

Table 3.14: Compositions of PtNi-2 particles and oxygen content of the investigated samples after different treatments as determined via EDX.

analysis	untreated [at.%]	UV/ozone [at.%]	plasma [at.%]
Ni (of Pt + Ni)	54	51	48
O (of Pt + Ni + O)	11	12	30

the results regarding the strength of treatments and impact on particle structure found so far: plasma > UV/ozone > no treatment. This is supported further by the fact that the strength of oxidation of the respective treatments follows this trend as well, as evidenced by the oxygen content found for the different samples. According to this investigation the degree of oxidation of the untreated and UV/ozone treated samples is almost the same with a value of approx. 10 %. For the plasma treated sample an oxygen content of 30 % is found, although which component of the sample (platinum, nickle, or carbon) is oxidized can not be concluded from this investigation alone. This point will be further illuminated in the next paragraph.

The reason for the slight decrease in nickel content with increasing oxidative strength of the treatment is supposed to be found in the formation of volatile nickel compounds such as $Ni(CO)_4$ under oxidative conditions. A line scan (see Appendix B) performed for the untreated and plasma treated sample in comparison produced no evidence of any structural changes in respect to the composition, though. The distribution of nickel and platinum within the particle stays apparently unchanged by the plasma treatment.

XPS Investigation The X-ray photoelectron spectroscopy investigation discussed in the following was conducted in cooperation with B. Kaiser and J. Klett from the *Center of Smart Interfaces* at the *TU Darmstadt*. In table 3.15 an overview of the investigated samples is given. For experimental details see "XPS" in 4.3. Two kinds of GCEs were investigated, plasma treated and untreated ones, all covered with a particle film of PtNi-6 (d = 7.7 nm, 49:51 (Pt:Ni) and 60:40 (Pt:Ni)$_{XRD}$), a particle batch similar to PtNi-2 in size and composition. As a reference glassy carbon substrates (GC disks) subjected to the respective treatment were examined, as well.

The results of the investigation are shown in figure 3.38. As can be seen the overall platinum content is relatively constant at approx. 10 % for all GCEs (samples 3 - 6) independently of the treatment, indicating a comparable coverage with particles. What can also be seen is the increase in oxygen content for the GC disk and the GCEs that

Table 3.15: Denotation of XPS samples. Samples 1 and 2 are GC disks without any particles that were used as reference to the investigated GCEs. Samples 3 - 6 are coated with a particle film of PtNi-6.

Treatment	GC disk (without NPs)	GCE (after treatment)	GCE (after treatment and CV)
Untreated	1	3	5
Plasma	2	4	6

were subjected to the plasma treatment (samples 2, 4 and 6) in comparison to the respective untreated GC disk and GCEs. This observation is in good agreement with the results of the EDX measurement discussed in the preceding paragraph, where a significantly higher oxygen content for the plasma treated particles as compared to untreated ones was found.

When taking a closer look at the atomic Pt:Ni ratio of the GCEs a value of only 27 % for the nickel content of the untreated GCE (sample 3) and a considerably higher value of 43 % for the plasma treated GCE (sample 4) are found. Both these values are lower than expected in regard to the results of the EDX and XRD measurements, which yielded a nickel content of 52 % and 42 %, respectively. This deviation most likely has its reason in the different principles of measurement of EDX and XRD on the one hand and XPS on the other hand. EDX and XRD have a much larger depths of penetration and can, to some extend, be described as methods suitable for bulk characterizations, whereas XPS is a surface sensitive method of investigation. The differences in results obtained from EDX and XRD measurements have already been discussed in 3.2 and will not be repeated here.

The overall lower nickel content determined via XPS naturally leads to the assumption that the nanoparticles are enriched in platinum in their outer layers, thus explaining the greater platinum content determined via XPS, where the major part of the signal originates from a depth of a few monolayers of the sample surface and only a smaller part of the signal originates from a depth of up to approx. 10 nm.(131) Thus, the XPS measurement might contain a concentration gradient, given that above mentioned surface segregation within the examined particles exists.

In order to determine the effect of segregation in as-prepared PtNi alloy nanoparticles an EDX line-scan and mapping was conducted. The results are shown in Appendix B and in figure 3.39. The line scan referred to here was already shortly discussed in the preceding paragraph and it was concluded that in comparison to the line-scan of a

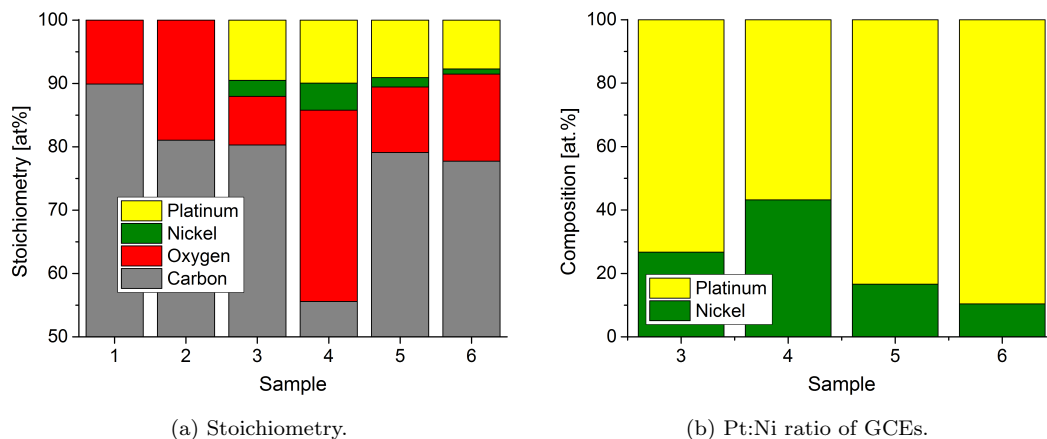(a) Stoichiometry.

(b) Pt:Ni ratio of GCEs.

Figure 3.38: Results of XPS measurements in regard to sample composition. (a) Stoichiometry of the investigated GCs and GCEs (samples 1 - 6) and (b) atomic Pt:Ni ratio of the GCEs (samples 1 - 6.

plasma treated PtNi-2 nanoparticle no structural changes were apparent. However, it is difficult to come to conclusions regarding the structure of a particle solely by means of a line scan. A clearer picture of the structure of an as-prepared PtNi-2 nanoparticle is gained via an element mapping as the one shown in figure 3.39. As can be seen by comparing the spacing between the element accumulations indicating the presence of a nanoparticle in that location, the particles have a homogenous core but are enriched in platinum in their outer layers.

This observation is in good agreement with Monte-Carlo simulations conducted by Wang *et al.* of disordered fcc cubo-octahedral PtNi nanoparticles,(132) which are the same structural details found for the particles synthesized by the hot injection approach followed in this work.(118) The Monte Carlo simulations were performed for a temperature of $600 \, \mathrm{K}$ ($356 \, °\mathrm{C}$) as a typical reduction temperature for bimetallic nanoparticles.(133) This temperature is about $150 \, °\mathrm{C}$ higher than the one employed for the synthesis of the respective particles discussed here. However, general trends found in the Monte Carlo simulations have been confirmed in experiments conducted by Cui *et al.* concerning octahedral particles, which were synthesized at only $120 \, °\mathrm{C}$, so there is a justified belief that the trends determined theoretically by Wang *et al.* may coincide with the results of this work, as well.

From the results of the Monte Carlo simulations Wang *et al.* predict a surface segregation that leads to a surface-sandwich structure (see 2.2.5) for $Pt_{50}Ni_{50}$ alloy nanoparticles of above mentioned structure that consist of less than 1289 atoms. For particles consisting of more than 2406 atoms a core-shell structure is predicted, i.e. a structure
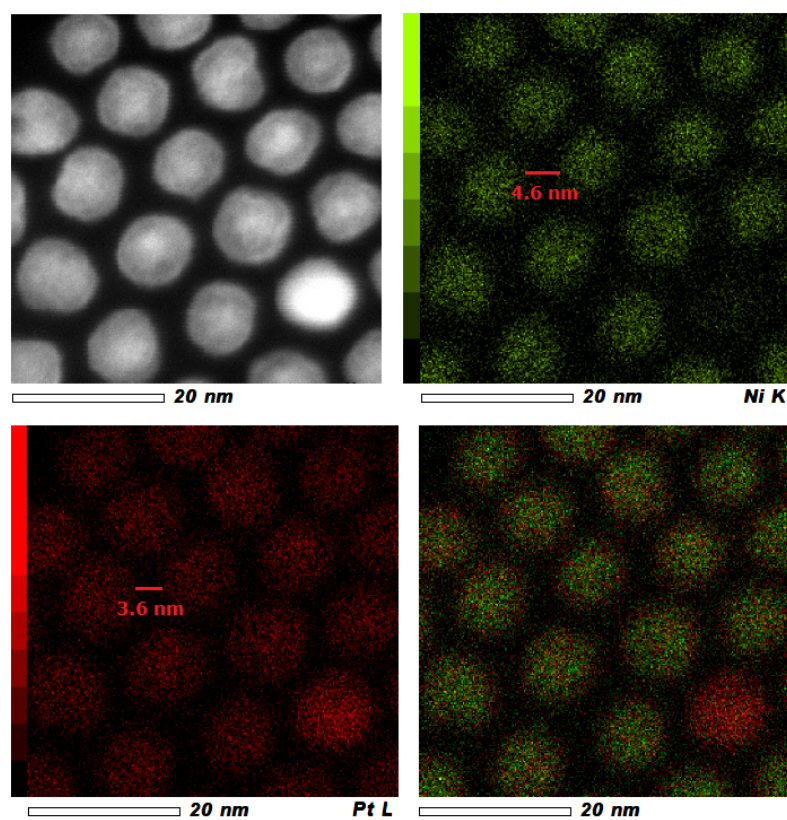
Figure 3.39: Element mapping of the area shown in the TEM image in the upper left corner. In the lower right corner, an overlap of the Ni and Pt mapping is shown. In the Ni and Pt mapping the red line indicates the inter-particle distance in regard to the respective element.

where platinum is only enriched in the outermost shell an its concentration is evenly distributed over the core of the particle. The nanoparticles that were investigated in this way consisted of 586 to 4033 atoms corresponding to particle sizes from 2.5 to 5.0 nm. PtNi-6 consists of particles with a diameter of 7.7 nm, which is larger than the particles the calculations were performed for. However, Cui *et al.* observed a good agreement between segregation effects predicted from the Monte Carlo simulations and experimentally obtained octahedral PtNi nanoparticles with a size of > 10 nm. Most importantly, the EDX mapping conducted in this work confirms a platinum enriched surface structure of the as-prepared particles and so it is sensible to suppose that either a surface-sandwich or a core-shell structure is responsible for that observation.

Having thus shown that the as-prepared alloy nanoparticles with a Pt:Ni ratio of approx. 1:1 and a diameter of 7 - 8 nm show a surface segregation effect with platinum enriched in the outermost layers the results obtained via XPS can easily be understood. The high platinum content found for the untreated GCE (sample 3) illustrates the structure of the particles with their alloy core and platinum enriched surface. The higher nickel content detected via XPS for the plasma treated GCE (sample 4) must therefore be the consequence of a vanishing of this platinum "shell", probably due to a sputtering effect of the plasma treatment, an assumption that is supported by the ragged look the particles exhibit after this treatment as could be shown via TEM (see figure 3.37c).

For the GCEs after potential cycling (samples 5 and 6) lower nickel contents as compared to the respective electrocatalyst prior to the CV experiment are observed. The values found are 17 % nickel content for the untreated GCE and 10 % for the plasma treated GCE. This observation strongly supports the general observation that nickel is leaching out of PtNi alloy electrocatalysts under electrochemical conditions (see 2.2.5). It also shows that for the plasma treated GCE the leaching is stronger (33 percentage points difference as compared to the untreated GCE that shows a difference of 10 percentage points) for the GCE prior to and after the CV experiment.

This further supports the theory of a preferential sputtering of platinum during the plasma treatment, which would lead to a particle surface exposing more nickel atoms as compared to an untreated one. After the CV experiment the plasma treated GCE exhibits a smaller nickel content than the respective untreated GCE, which can be explained by the existence of more nickel atoms at the particles surface at the beginning of the electrochemical measurement, which in turn would lead to a stronger dealloying. All the effects described here would additionally cause the detection a a greater platinum content in XPS investigations as compared to EDX or XRD measurements and thus explain the observed behavior accurately.

A closer look at the obtained spectra (see Appendix B) reveals that for all GCEs except the plasma treated one (sample 4) nickel is mainly found in its metallic form. For sample 4 oxidized nickel is observed in addition to metallic nickel. The structure indicates that it is $Ni(OH)_2$ that is formed rather than NiO, but it might also be an alloying effect that causes the change in the structure of the spectrum. After the CV experiment only metallic nickel is found for the plasma treated GCE (sample 6) again, indicating that the electrochemical conditions cause a reduction of the oxidized catalyst particles.

For platinum a similar result is found. For the plasma treated GCE (sample 4) Pt^{4+} is observed in form of PtO_2. All other GCEs exhibit only metallic platinum, which in case of the plasma treated GCE after the CV experiment (sample 6) again means that a reduction during potential cycling took place. For the carbon content of the sample an oxidation in respect with the plasma treatment was also observed, as expected. For the GCEs after the electrochemical investigation a reduced oxygen content is found, indicative of the reductive properties of the experimental conditions once more. In the correlating XPS spectra (see Appendix B) the tailing of the sp^2 carbon of the GC is distinctly exhibited.

The XPS investigation thus leads to the conclusion that the plasma treatment indeed is a very strong oxidative treatment that is even capable of oxidizing platinum. However, it was also observed that the exposure of a thus oxidized GCE to potential cycling between 0.0 and 1.2 V vs. RHE lead to a reduction of the oxidized metals. In case of the plasma treated GCE the dealloying of the electrocatalyst was much stronger as compared to the untreated catalyst, agreeing well with the assumption that nickel is exposed in the electrocatalyst outer layers during the plasma treatment due to preferential sputtering of platinum due to its enrichment in the outer layers of the particles.

TGA Investigation To get a better understanding of the processes leading to ligand removal in correlation with the furnace treatment a thermogravimetric analysis (TGA) was carried out. For this purpose the particles were washed with ethanol twice to produce comparable conditions in respect to ligand stabilization of the particles on a GCE (see "TGA" in 4.3 for experimental details). The particle batch used for this investigation was PtNi-3 (d = 2.3 nm, 92:8 $(Pt:Ni)_{XRD}$), a batch of rather small, Pt-rich particles comparable to PtNi-1. The result of this TGA is shown in figure 3.40. Additionally, another set of particles was investigated comparatively in regard to a linear heating ramp from room temperature to 800 °C. For this the particle batches PtNi-4 (d = 7.2 nm, 41:59 (Pt:Ni) and 55:45 $(Pt:Ni)_{XRD}$), which is similar to PtNi-2, and PtNi-5 (d = 2 nm, 98:2 (Pt:Ni)), which is similar to PtNi-1, were used. The results of this

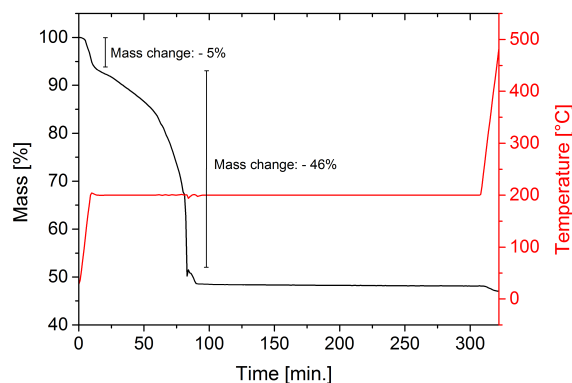**Figure 3.40:** TG investigation of PtNi-3. The sample was heated under air with a rate of $20\,\mathrm{K\,min^{-1}}$ and then kept at $200\,^{\circ}\mathrm{C}$ for $5\,\mathrm{h}$.

investigation are shown in figure 3.41.

The first investigation mentioned above (employing PtNi-3) was performed to simulate the ligand removal in respect to the furnace treatment, which consisted of heating the ready-made GCE for $5\,\mathrm{h}$ at $185\,^{\circ}\mathrm{C}$. A temperature of $200\,^{\circ}\mathrm{C}$ was chosen for the thermogravimetric (TG) measurement to compensate for possible overheating in the muffle furnace that was used for the treatment of the actual GCEs. As can be seen from the TG curve there is an initial mass change of $-5\,\%$ occurring during the heating ramp, which is probably due to the evaporation of residual solvent. Around a temperature of $200\,^{\circ}\mathrm{C}$ a second wave is found, leading to a mass change of $-46\,\%$ over approx. $80\,\mathrm{min}$. As was the case in previous TG investigations on OAm/OA stabilized PtNi nanoparticles(119) no steps in the curve relating to the decomposition of the different ligands can be observed. Thus, the occurring mass change is most likely the result of the decomposition of both ligands in overlapping temperature regions below $200\,^{\circ}\mathrm{C}$. The mass loss found in this TGA agrees well with the one observed in the previous investigation mentioned above, where a value of $-38\,\%$ was determined.(119) For the final heating ramp from 200 to $500\,^{\circ}\mathrm{C}$ an additional mass change of $-2\,\%$ is observed that is ascribed to the decomposition of residue from the ligand removal at lower temperatures. However, the gross amount of the ligands is removed at temperatures below $200\,^{\circ}\mathrm{C}$, showing that the furnace treatment is suited to this task.

In the second TG investigation shown in figure 3.41 two curves were recorded, one for the large, 1:1 alloy particles (PtNi-4) and one for the small, Pt-rich particles (PtNi-5). As can be seen the two TG curves are very different. The curve recorded for PtNi-5 shows an evolution as expected after the first TG experiment with comparably small, Pt-rich particles discussed above. A first wave with a correlating mass change of ap-
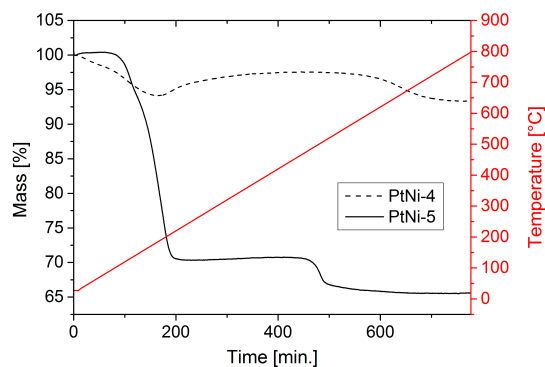
Figure 3.41: TG investigation of PtNi-4 (d = 7.2 nm, 41:59 (Pt:Ni)) in comparison with PtNi-5 (d = 2 nm, 98:2 (Pt:Ni)). The samples were heated under air with a rate of $1 \, \mathrm{K \, min^{-1}}$ from room temperature to 800 °C.

prox. $-28 \, \%$ is found below a temperature of approx. 215 °C which was reached after 195 min. The mass loss starts at a temperature of approx. 100 °C, which was reached after 85 min. After that no further mass change is observed until a temperature of approx. 480 °C is reached after 460 min. The mass change observed at that temperature has a value of approx. $-10 \, \%$ and continues over 30 °C until a temperature of approx. 490 °C is reached and the decrease slowly abates. After that no further mass change is observed.

The first TG wave observed here has a smaller value than the one found for PtNi-3 ($-28 \, \%$ as compared to $-46 \, \%$ found for the latter case). The reason for that can easily be explained by the fact that for PtNi-3 the particles were obtained from an OAm rich solution as it would be employed for the preparation of a GCE via spin coating, whereas for the TGA of PtNi-5 a slightly destabilized particle solution was used as the particle source. Therefore, for the latter case a smaller amount of stabilizer is to be expected leading to a smaller value for the observed mass change. Apart from that the agreement of the two TG experiments is excellent, showing that most of the ligand is lost up to a temperature of approx. 200 °C and another small part is lost at approx. 500 °C.

For the large, 1:1 alloy particles (PtNi-4) an overall smaller change in mass as compared to the smaller nanoparticles is to be expected due to the smaller surface-to-volume ratio of the larger particles and the resulting smaller ratio of mass of ligands to mass of metal. For PtNi-4 an initial mass change sets in at the same temperature and time (100 °C, 85 min) as was the case for the smaller, Pt-rich particles. However, the occurring negative mass change is superimposed by a positive mass change, which most likely is a consequence of the formation of nickel oxide with increasing temperature in air. This

increase is strong for temperatures up to approx. 225 °C and then slowly levels of. In the constant region of the resulting TG curve (> 420 °C, 400 min) an overall mass of only some percentage points below the initial mass is observed, showing that the mass lost through oxidation of ligand and the mass gained by oxidation of nickel are almost at equilibrium. At around 610 °C (600 min) a second wave is observed that initiates a mass change of approx. -4 %, a value that is in the order of magnitude with the one found for PtNi-5.

3.5 Investigation into Catalyst Stability

In the last section the importance of observing changes regarding the size, shape, and composition of an electrocatalyst during electrochemical measurements has been illustrated. In this section these changes will be observed for long-term measurements in 0.5 M H_2SO_4 comprised of 10 000 cycles, each. This investigation was conducted for two sets of particles, namely for the small, Pt-rich particles already used for the investigation on the effect of different treatments for ligand removal (PtNi-1, d = 2.4 nm, 93:7 (Pt:Ni)) and for the set of larger, alloy PtNi nanoparticles (PtNi-6, d = 7.7 nm, 49:51 (Pt:Ni)) that was also employed in the XPS experiments and is comparable to PtNi-2 in size and composition. Since in the last section the most contrary results regarding particle agglomeration were found for untreated GCEs on the one hand and plasma treated GCEs on the other hand, the long-term measurements were conducted for both of these treatments. In addition to the electrochemical investigation, for each of these two treatments a SEM investigation was performed with GCEs of PtNi-6 employing freshly prepared GCEs. For experimental details see "Investigation into Catalyst Stability" in 4.5.3.

The use of cyclic voltammetry to investigate catalyst degradation via loss of ECSA is an approach commonly used in experiments concerning the long-term stability of electrocatalysts.(134)(135) Next to activity and selectivity, catalyst stability is one of the key research challenges in the realizing a broad commercialization of fuel cells. Therefore, it is of great interest to gain a better understanding of the degradation mechanism that leads to the loss of ECSA.(136) Mayrhofer *et al.* summarize four main mechanisms that may contribute to this loss: (1) *Ostwald ripening*, which describes the growth of particles by means of the dissolution of smaller particles and the diffusion of the formed metal ions towards larger particles, where they are redeposited, thus inducing the particle to grow whilst minimizing the overall metal surface area and reducing surface energy; (2) *particle coalescence through agglomeration*, which describes the sintering of particles in close proximity under the formation of larger agglomerates with
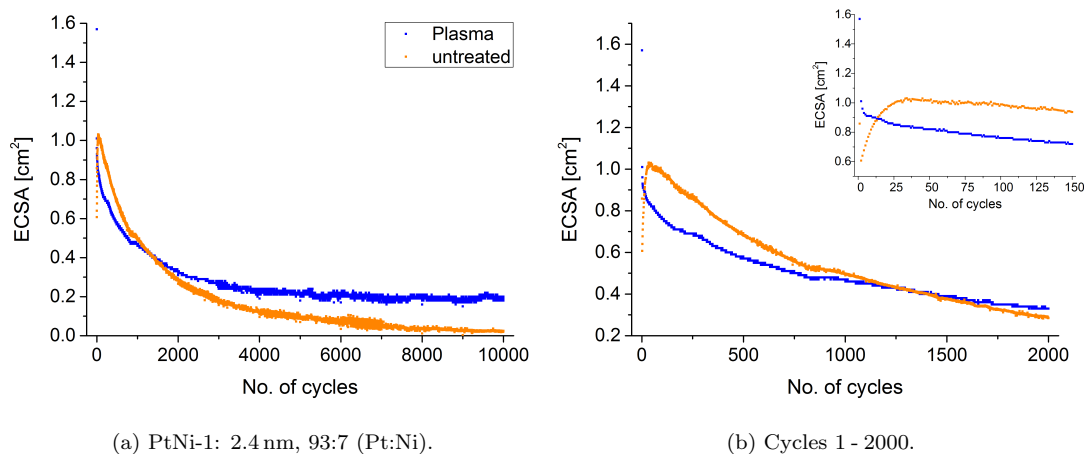
(a) PtNi-1: 2.4 nm, 93:7 (Pt:Ni).   (b) Cycles 1 - 2000.

Figure 3.42: Development of the ECSA for PtNi-1 over 10 000 cycles for an untreated GCE (yellow) and a plasma treated GCE (blue).

an overall reduced surface area and thus surface energy; (3) *corrosion of the carbon support* that anchors the electrocatalyst and provides electrical contact, thus leading to a loss of catalyst; (4) *reprecipitation*, which occurs in connection with a ionomer (e.g., Nafion) coating and entails the dissolution of the metal electrocatalyst and its subsequent precipitation as newly formed particles.(136)

3.5.1 Electrochemical Investigation of Catalyst Stability

The results of the electrochemical investigation in respect to the development of the ECSA are shown in figures 3.42 and 3.43. The little inlets in the the diagram depicting the development of the ECSA for cycles 1 - 2000 illustrates the development found over the first 150 cycles. Its course is comparable to the one shown in figure 3.22 for the respective treatment, as it should be. For the untreated GCEs of both PtNi-1 and PtNi-6 an initially strongly increasing ECSA is observed, whereas for the plasma treatment a slightly decreasing, but more or less horizontal course of the curve is found over the whole 150 cycles.

For both sets of particles, PtNi-1 and PtNi-6, the plasma treated GCE starts out with higher values for the ECSA over the first few cycles but quickly intersects with the curve found for the untreated GCE. For the development of the ECSA of the plasma treated GCEs an exponential decay is found, whereas for the untreated GCEs this decay is only found after an initial peak is traversed. Between approx. 1500 - 2000 cycles the curves intersect again, leading, after 10 000 cycles, to higher ECSA values in case of

111

Table 3.16: Summary of the results of the long-term investigation for the ECSA of the untreated and plasma treated GCEs of PtNi-1 and PtNi-6. For the plasma treatment the 5th cycle was chosen as the one exhibiting the highest ECSA to exclude values influenced by the amperometric treatment (see 3.4.1.

GCE & Treatment	ECSA$_{\mathbf{max}}$ (@ cycle) [cm^2]	ECSA$_{10000}$ [cm^2]	Δ(ECSA$_{10000/\mathbf{max}}$) [%]
PtNi-1, untr.	1.0 (@ cycle 34)	0.02	2
PtNi-1, plasma	0.9 (@ cycle 5)	0.19	21
PtNi-6, untr.	2.6 (@ cycle 72)	0.18	7
PtNi-6, plasma	2.5 (@ cycle 5)	0.47	19

the plasma treated GCEs for both PtNi-1 and PtNi-2. The general progression of the curve is thus independent of the employed set of particles, indicating that the effects leading to this trend are the same for the respective particles and are dominant over the initial particle size and composition.

Comparing the values of the ECSA after 10 000 cycles for PtNi-1 and PtNi-6, the overall larger values are found for the larger, Pt:Ni alloy nanoparticles (PtNi-6) with 0.18 cm^2 for the untreated and 0.47 cm^2 for the plasma treated GCE as compared to 0.02 cm^2 found for the untreated GCE of PtNi-1 and 0.19 cm^2 observed for the plasma treated GCE of this smaller, Pt-rich particles. The maximal ECSA values traversed in the first region of the degradation curve are more than twice as large for the larger, alloy particles (approx. 2.5 cm^2) as compared to the ones of the smaller, Pt-rich particles (approx. 1.0 cm^2) as one would expect after the results obtained in 3.4.1. These results are comprised in table 3.16 in addition to the percentage of ECSA retained after 10 000 cycles. For the untreated GCEs values of only 2 % (PtNi-1) and 7 % (PtNi-6) are found, whereas for the plasma treated GCEs values around 20 % are observed, independently of the particle set employed.

As has already been discussed in 3.4.2 one factor having an impact on the development on the ECSA in the long run is the agglomeration of the particles. Thus, a freshly prepared plasma treated and untreated GCE were investigated via SEM at different stages of the long-term measurement for PtNi-6, the larger alloy particles that are better suited for a SEM investigation than the smaller, Pt-rich particles (PtNi-1). The results of this investigation will be discussed in the following.
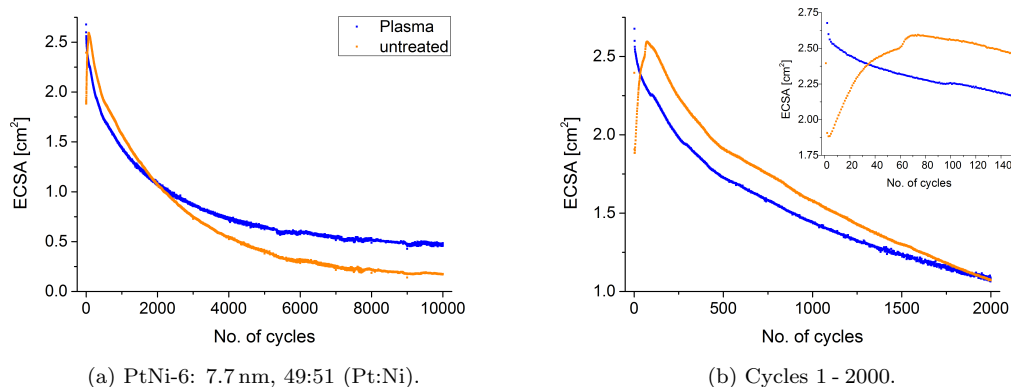
(a) PtNi-6: 7.7 nm, 49:51 (Pt:Ni).

(b) Cycles 1 - 2000.

Figure 3.43: Development of the ECSA for PtNi-6 over 10 000 cycles for an untreated GCE (yellow) and a plasma treated GCE (blue).

3.5.2 Agglomeration during long-term Potential Cycling

SEM Investigation of the First Part of the Degradation Curve The results of the SEM investigation up to cycle 450 are shown in figure 3.44. As can be seen in this comparison the particles on the plasma treated GCE agglomerate strongly already during the amperometric pretreatment, as was already observed in previous experiments and was discussed in 3.4.2. For the untreated GCE, however, agglomeration sets in much more slowly. No real change in the appearance of the particle film is observable after the pretreatment and 10 subsequent cycles. Even after 30 cycles (not shown here) there is still no change to be found. Agglomeration is first observed for the untreated GCE after 60 cycles, at which point it is, however, still much weaker than in the case of the plasma treatment. As was discussed above the curves of the two differently treated GCEs intersect for a first time after approx. 30 cycles. At this point the ECSA of the plasma treated GCE, decreasing due to increasing agglomeration, and the ECSA of the untreated GCE, increasing due to an electrochemical cleaning process taking place, are of the same value. Each GCE then continues this trend until around cycle 70 the agglomeration becomes dominant over the electrochemical cleaning for the untreated GCE, as well, and the ECSA starts decreasing exponentially.

After the SEM measurement that was performed on the untreated GCE after 450 cycles (see figure 3.44k) an error occurred. The banana plug of the wire connecting the potentiostat and the reference electrode was not properly contacted to the latter before the measurement was started. This lead to an oxidation of the untreated GCE as can be seen by the change in the cyclic voltammograms recorded right before and approx. 1500 cycles (to give the GCE enough time to reach equilibrium again) after
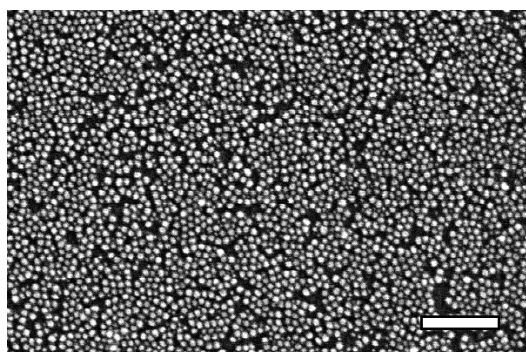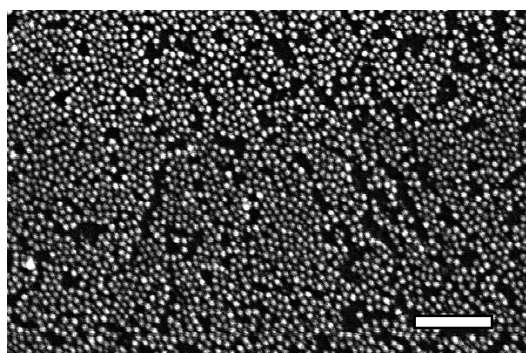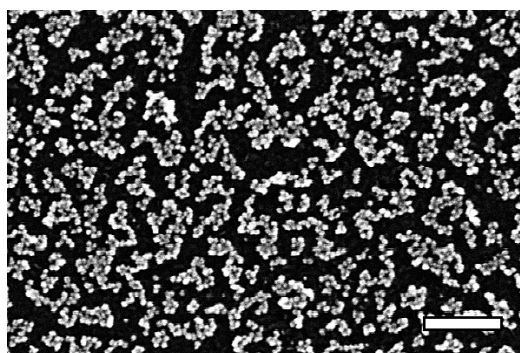
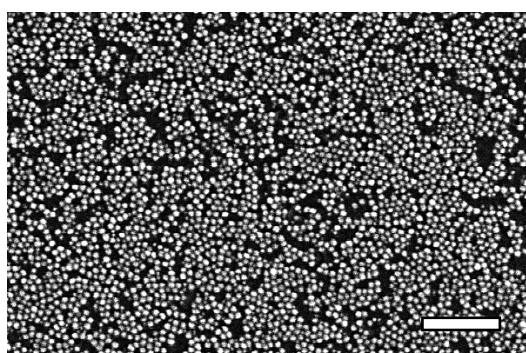(a) Untreated particle film.
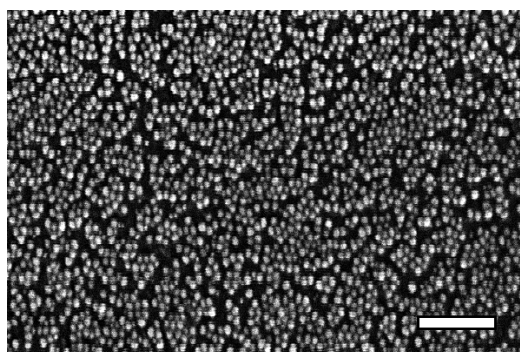
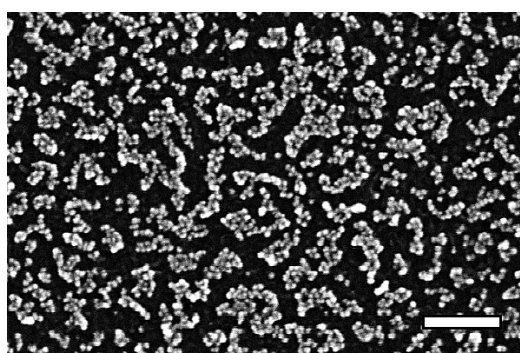(b) Film after plasma treatment.

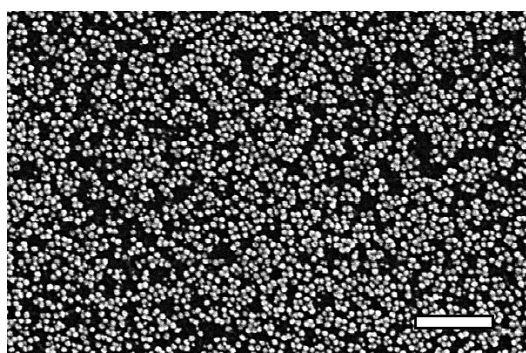
(c) Untreated film after pretreatment.

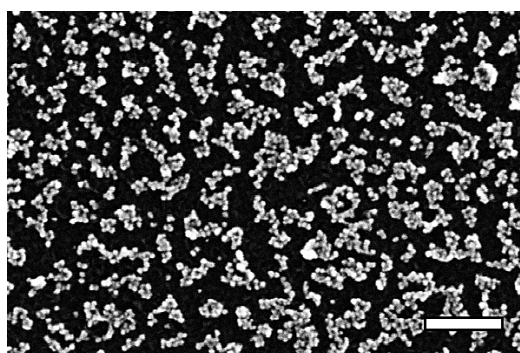(d) Plasma treated film after pretreatment.

(e) Untreated film after 10 cycles.

(f) Plasma treated film after 10 cycles.

(g) Untreated film after 60 cycles.

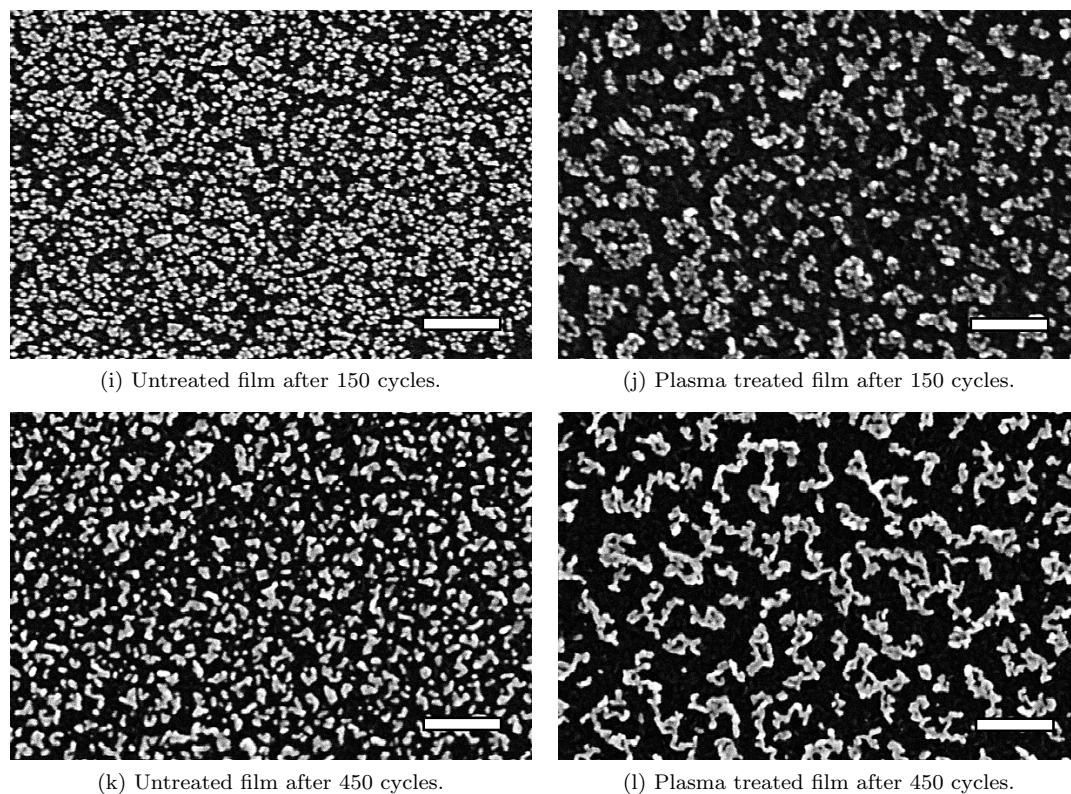(h) Plasma treated film after 60 cycles.

(i) Untreated film after 150 cycles.

(j) Plasma treated film after 150 cycles.

(k) Untreated film after 450 cycles.

(l) Plasma treated film after 450 cycles.

Figure 3.44: SEM images of particle films of PtNi-6 at different stages of agglomeration and coalescence. The left column contains SEM images of the untreated GCE and the right column images of the plasma treated GCE up to the 450th cycle. Scale bar = 100 µm.
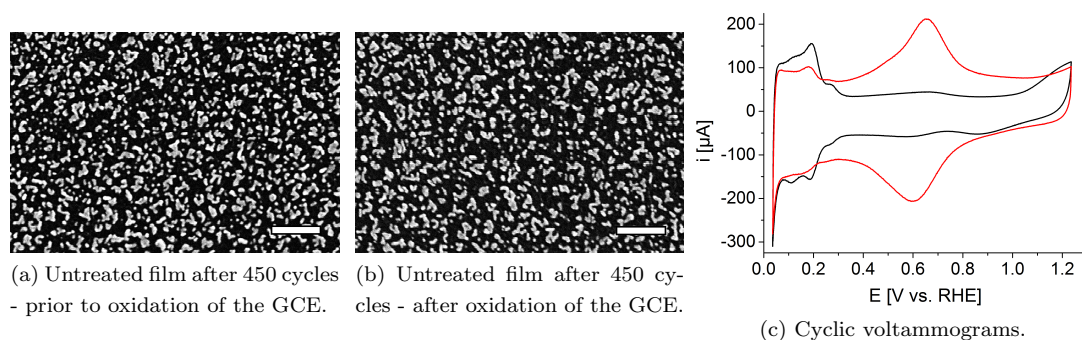

(a) Untreated film after 450 cycles - prior to oxidation of the GCE.

(b) Untreated film after 450 cycles - after oxidation of the GCE.

(c) Cyclic voltammograms.

Figure 3.45: SEM images of particle films (a) directly prior to and (b) after the oxidation of the GC substrate. Scale bar = 100 µm. In (c) the cyclic voltammograms of the GCE just prior to (black line) and approx. 1500 cycles after the oxidation (red line) are shown.

115

this event (see figure 3.45). The appearance of a set of peaks around $0.6\,\mathrm{V}$ was already discussed in "Cyclic Voltammograms" in 3.4.1 and attributed to an oxidation of the GC substrate. However, in the SEM images obtained right before and directly after the oxidation no change in the state of agglomeration was apparent (see figures 3.45a and 3.45b). The value of the ECSA on the other hand decreased strongly as can easily be seen by comparing the area under the curves in the H_{upd} region in figure 3.45c. This decrease is much stronger than for the untreated and non-oxidized GCE that was employed for the electrochemical investigation shown in figure 3.43, where from cycle 450 to cycle 2000 the ECSA decreases by $46\,\%$. For the oxidized GCE discussed here a decrease of $71\,\%$ is observed. In both cases, the GCEs were not removed from the cell in between these cycles.

Due to this error the remainder of the SEM investigation concerning the untreated GCE is not useful in regard to modeling the behavior of the ECSA of the untreated GCE as it is depicted in figure 3.43. However, it is interesting to note that for the oxidized GCE the loss of ECSA in the long run is smaller than without it. Actually, its ECSA develops contrary to the ones of the other examined GCEs, increasing from cycle 2000 onwards and thus leading to a value of $1.1\,\mathrm{cm}^2$ at the end of the electrochemical measurement after 8000 cycles. The topic of the final state of the different GCEs will be picked up again at the end of this section, after some considerations about the reason for these observations have been made.

Investigation of Stability Enhancement through Oxidation The effect that is believed to be responsible for the enhanced stability observed for the oxidized GCE is the surface roughening that accompanies its oxidation.(129) This effect can be seen with the naked eye and is evidenced by the strong increase in double layer charging current at $0.4\,\mathrm{V}$ vs. RHE (difference between anodic and cathodic scan direction) in figure 3.45c. The fact that compared to the untreated GCEs of PtNi-1 and PtNi-6 the plasma treated and thus oxidized (see "XPS investigation" in 3.4.4) GCEs of both particle sets are the ones exhibiting higher values for the ECSA at the end of the respective long-term investigation supports the assumption that it is indeed the oxidation of the GCE that is responsible for the enhanced stability. For a rougher GC surface the interactions between electrocatalyst and substrate are assumed to be stronger due to a potentially larger contact area. Also, it has been shown that graphitized carbons show better corrosion resistance than non-graphitized substrates(137) and it is feasible that the oxidation of the GCE and the subsequent potential cycling lead to such a graphitization, thus incorporating the electrocatalyst in its structure and stabilizing it. A graphitization of the GCE surface has also been observed in correlation with
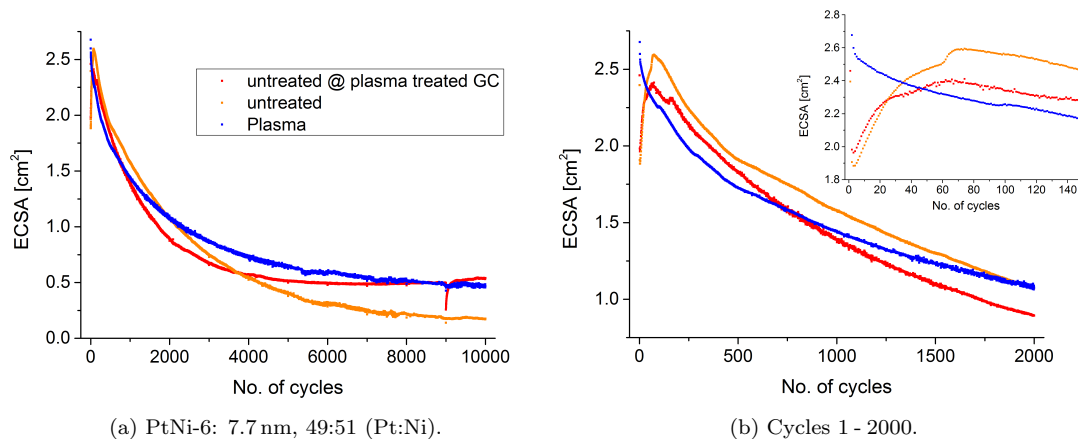
(a) PtNi-6: 7.7 nm, 49:51 (Pt:Ni).   (b) Cycles 1 - 2000.

Figure 3.46: Development of the ECSA for PtNi-6 over 10 000 cycles for a GCE that was prepared by exposing the GC substrate to the plasma treatment and then depositing particles on it (red). In comparison the development of the ECSA of an untreated GCE (yellow) and a plasma treated GCE (blue) of PtNi-6 are shown again.

SEM measurements, where the electron beam causes the graphitization of the scanned area on the GCEs surface. For these areas no agglomeration in the subsequent CV experiments could be observed (even for the plasma treatment, where agglomeration is strong), in contrast to the rest of the GCE, where agglomeration was observed as expected.

Whether this kind of graphitization occurred here in addition to the surface roughening of the GC substrate, however, can not be deduced for sure and further experiments would be needed to clarify this. Additionally, the increased hydrophilicity of an oxidized GC surface(129) may increase the wettability of the entire electrode, thereby increasing the contact area between electrolyte and electrocatalyst and thus the observed ECSA. Lastly, the increased quantity of oxygen-capped groups at the GC surface might provide additional stabilization through electron donation to the particle surface, comparable to the stabilizing effect of a ligand.

In order to investigate this further, a GC substrate was first plasma treated and only then coated with a particle film of PtNi-6. The results of this experiment regarding the development of the ECSA are shown in figure 3.46. As can be seen the initial course found for this substrate-only plasma treated GCE is similar to the one observed for the untreated GCE as it should be considering the effect of the electrochemical cleaning on untreated particles that was deduced earlier (see 3.4.1). However, between 3500 and 4000 cycles the curves intersect and the course of the curve for the substrate-only plasma treated GCE becomes similar to that of the plasma treated GCE. After the

Table 3.17: Summary of the results of the long-term investigation for the ECSA of the three differently prepared GCEs. The treatment "Untreated @ GC*" refers to the substrate-only plasma treated GCE (untreated particles). For the plasma treatment the 5th cycle was chosen as the one exhibiting the highest ECSA to exclude values influenced by the amperometric treatment (see 3.4.1).

Treatment	$\mathbf{ECSA_{max}}$ (@ cycle) [cm^2]	$\mathbf{ECSA_{10000}}$ [cm^2]	$\Delta(\mathbf{ECSA_{10000/max}})$ [%]
Untreated	2.6 (@ cycle 72)	0.18	7
Plasma	2.5 (@ cycle 5)	0.47	19
Untreated @ GC*	2.4 (@ cycle 66)	0.54	23

10 000 cycles of the long-term investigation the substrate-only plasma treated GCE exhibits the largest ECSA of the three GCEs (0.54 cm^2), which is in the same order of magnitude as was found for the plasma treated GCE (0.47 cm) and three times larger than the value found for the untreated GCE (0.18 cm). Table 3.17 summarizes this results and correlates them to the maximum value of the ECSA observed for each GCE, respectively. The sudden decrease and following increase in ECSA starting at cycle 9000 is a consequence of a crash of the software just after starting the last 1000 cycles of the long-term measurement. This lead to an interruption of the measurement for several hours after which the last 1000 were started again manually. The initial decrease in ECSA is compensated during the next few hundred cycles, eventually resulting in a value for the ECSA as it is expected from the general course of the curve, showing that an interruption of the CV measurement leads to a reversible change in ECSA.

In figure 3.47 the SEM images obtained at the end of the undisturbed CV experiments (see figure 3.43) for the untreated and plasma treated GCEs of PtNi-6 are shown in comparison to the ones obtained for the untreated and plasma treated GCE after 8000 cycles and the several intermediate SEM measurements, some of which are shown in figure 3.44. Only 8000 cycles were recorded here since for the plasma treated GCE almost no electrocatalyst was left on the GCE surface at that stage, rendering a continued measurement unreasonable. In addition figure 3.48 shows the SEM images obtained at the end of the CV experiments for the untreated and plasma treated GCEs of PtNi-1 (see figure 3.42).

It can be seen from the SEM images of PtNi-6 (see 3.47) that quite different results are obtained, which is to be expected for the untreated GCEs, since the one employed in the SEM investigation was oxidized in the course of the experiment as was discussed
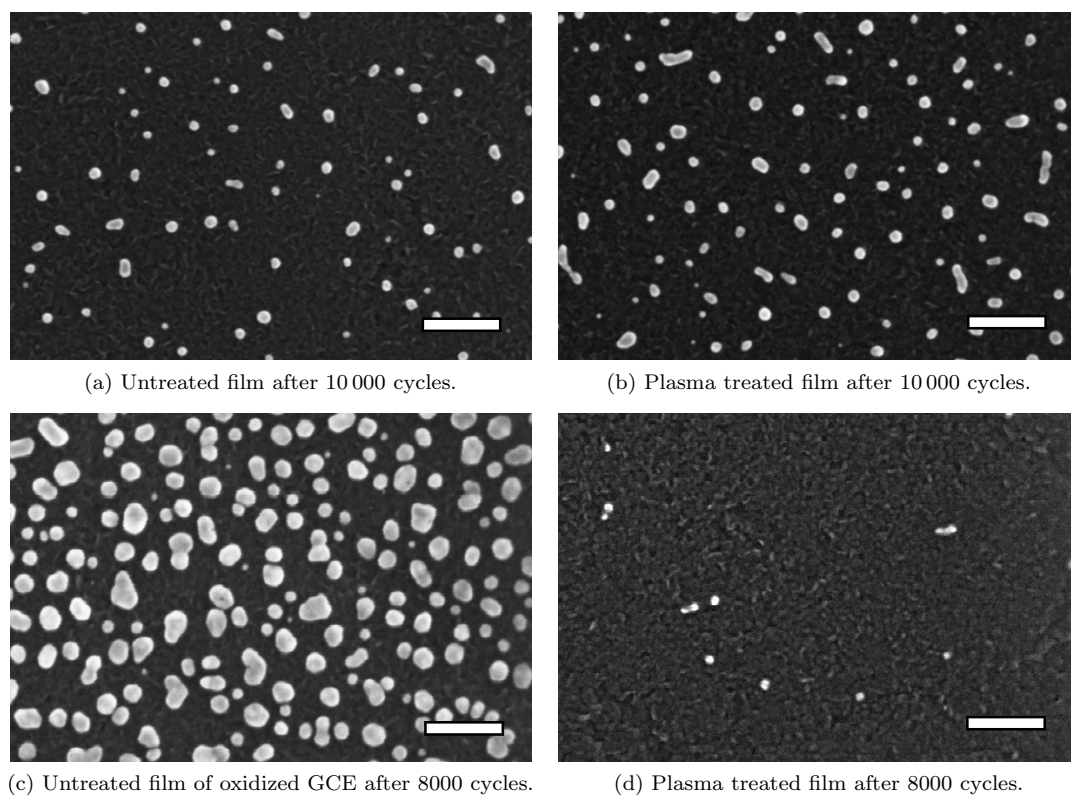
(a) Untreated film after 10 000 cycles.

(b) Plasma treated film after 10 000 cycles.

(c) Untreated film of oxidized GCE after 8000 cycles.

(d) Plasma treated film after 8000 cycles.

Figure 3.47: SEM images of PtNi-6 particle films (a) and (c) untreated and (b) and (d) plasma treated at the end of the long-term investigation. Scale bar = 100 µm.

at length above. The differences between the plasma treated GCEs (figures 3.47b and 3.47d) are probably a consequence of the repeated washing steps under use of the spin coating procedure the GCE employed for the SEM investigation was exposed to (figure 3.47d, see "Investigation into Catalyst Stability" in 4.5.3 for experimental details). During this washing steps electrocatalyst is assumed to get lost from the GCE surface, leading to the decreased surface coverage after 8000 cycles as compared to the plasma treated GCE that was only washed once, prior to the only SEM measurement conducted on it after 10 000 cycles (figure 3.47b). However, the possibility that catalyst was lost in the latter case, as well as in case of the untreated, non-oxidized GCE (figure 3.47a) or any of the GCEs of PtNi-1 (see figure 3.48) can not be precluded.

For PtNi-1 the SEM images obtained at the end of the long-term measurement for the untreated (figure 3.48a) and plasma treated (figure 3.48b) GCE are very similar to the ones of the undisturbed CV experiments of PtNi-6 (figures 3.47a and 3.47b). The formed agglomerates for PtNi-1 as well as for PtNi-6 in these cases have a size between

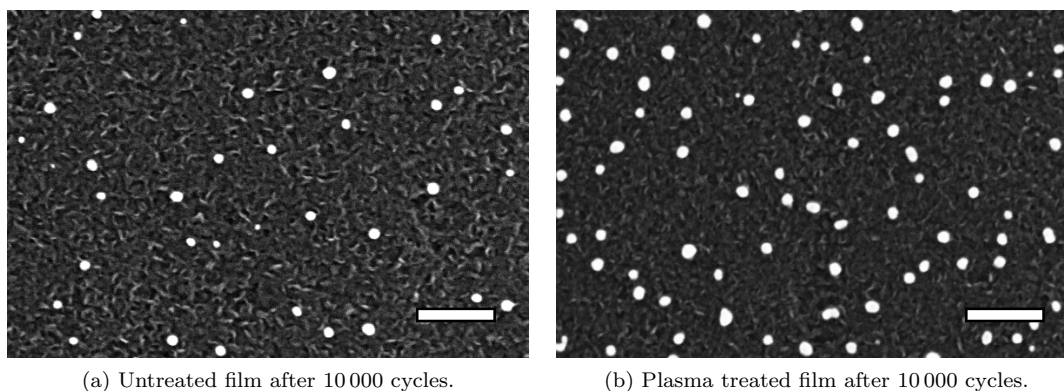(a) Untreated film after 10 000 cycles. (b) Plasma treated film after 10 000 cycles.

Figure 3.48: SEM images of PtNi-1 particle films (a) untreated and (b) plasma treated at the end of the long-term investigation. Scale bar = 100 µm.

approx. 10 and 20 nm and are mostly round or slightly elongated. Less electrocatalyst is observed for the untreated GCEs in comparison to the plasma treated ones in both cases, agreeing well with the results of the ECSA determination at the end of the electrochemical investigation (see table 3.16). This developing similarity in agglomerate structure and size independently of the employed particle size and composition once more indicates that other factors than the properties of the utilized particles determine catalyst stability.

For the untreated GCE that was accidentally oxidized after 450 cycles (figure 3.47c) the most electrocatalyst is apparent at the GCE surface at the end of the investigation. This coincides with the high value of $1.1\,\mathrm{cm}^2$ found for the ECSA after 8000 cycles. The ECSA maximum value exhibited by this GCE can only be determined by approximation because the GCE was so often removed from the cell during the first few hundred potential cycles that the respective graph depicting the development of the ECSA is dominated by the ECSA increase that occurs in connection with a measurement interruption (see development after cycle 9000 of the substrate-only plasma treated GCE in figure 3.46 for comparison). This is illustrated in figure 3.49b. In figure 3.49a the development of the ECSA after the accidental oxidation is shown starting at cycle 1000. As can be seen the maximum value for the ECSA ($2.3\,\mathrm{cm}^2$) determined from the initial part of the diagram around 60 cycles is comparable to the one found for both the untreated GCE and the substrate-only plasma treated GCE. Relating this value to the one determined at the end of the measurement (after 8000 cycles) results in a value of 48 % for the final value compared to the maximal one. Although this percentage can only be seen as an approximation as was explained above, this value is much higher than the ones found for the other three GCEs discussed here, which
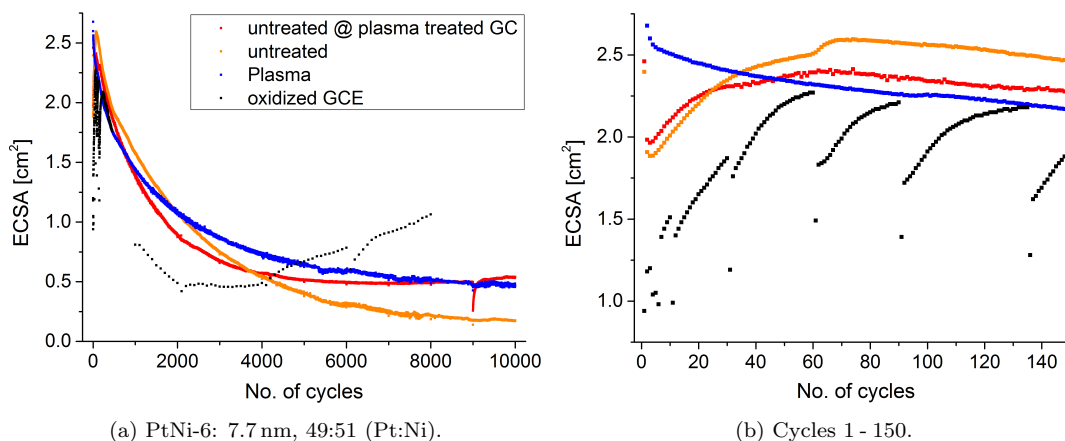
(a) PtNi-6: 7.7 nm, 49:51 (Pt:Ni).

(b) Cycles 1 - 150.

Figure 3.49: In (a) and (b) the development of the ECSA with potential cycling from figure 3.46 is shown again. In comparison the development of the ECSA of the GCE that was accidentally oxidized is shown in the parts where the recorded data was usable. Starting from cycle 1000 for this GCE only every 100th cycle is plotted.

were 7, 19, and 23 % (see table 3.17). In contrast to the GCEs for which these values were determined, the development of the ECSA for the oxidized GCE was moreover still increasing so that the actual value found at the end of this still developing curve might very well be even higher than the $1.1\,cm^2$ reported here. Performing additional experiments would be necessary to elucidate this point further.

For the oxidized GCE an initial loss of ECSA is found following the oxidation event. This is not surprising, but the consecutive increase in ECSA starting at approximately at cycle 4000 is. The reason for this unexpected increase, that finally leads to the highest value observed for the ECSA of a GCE after the different long-term measurements conducted for this investigation, is not found easily. It is interesting to note, though, that the development of the ECSA for the oxidized GCE changes with each removal from the electrochemical cell and thus washing step applied as well as the subsequent SEM investigation under vacuum conditions (after 2000, 4000, and 6000 cycles, see figure 3.49 and "Investigation into Catalyst Stability" in 4.5.3 for comparison). Which of these factors (exposure to air, washing, or exposure to vacuum) is responsible for the change in the development of the ECSA is not entirely clear and would need to be further investigated to come to a conclusion in this matter.

To complete this discussion the SEM images recorded after 2000, 4000, 6000, and 8000 cycles for the oxidized GCE as well as for the plasma treated GCE of the SEM investigation are shown in figure 3.50. For both the oxidized GCE and the plasma treated GCE agglomeration continues to progress. For the oxidized GCE smooth agglomer-

(a) After 2000 cycles.   (b) After 4000 cycles.   (c) After 6000 cycles.   (d) After 8000 cycles.

(e) After 2000 cycles.   (f) After 4000 cycles.   (g) After 6000 cycles.   (h) After 8000 cycles.
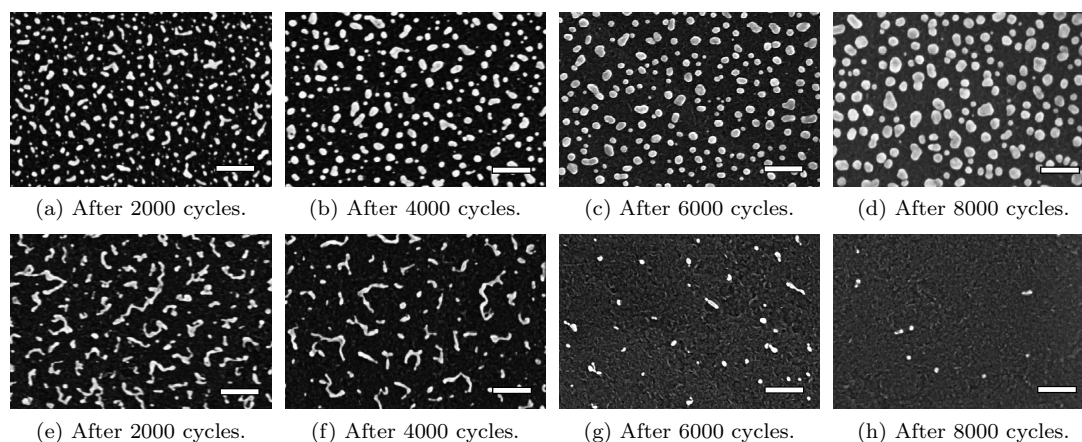
Figure 3.50: SEM images (scale bar = 100 nm) of the oxidized GCE of PtNi-6 (first line) and of the plasma treated GCE (second line) at different states of potential cycling.

ates with a diameter of approx. 10 - 50 nm are finally apparent, whereas for the plasma treated GCE round and elongated agglomerates with a diameter of about 15 nm are found aw was already discussed and can better be recognized in figure 3.47b, where more electrocatalyst is still present at the GCE surface after the investigation.

In summary it can be concluded that the behavior of a GCE over the first few hundred cycles is determined by the state of the particles and thus by any treatments they might have been subjected to. Differences in size and composition of the employed nanoparticles cause slight variations concerning factors like the maximal and minimal (end) values found for the ECSA but no change in the general course of the degradation curve is observed for the two sets of particles (PtNi-1 and PtNi-6) investigated here. This indicates that other factors determine long time catalyst stability. In the second region of the degradation curve an exponential decrease for the values of the ECSA is observed, independently of the initial treatment. The reason for this decrease is believed to be found in an increasing agglomeration of the particles of the electrocatalyst leading to particle sintering and thus a reduced surface area. Additionally, well-known factors such as catalyst loss due to loss of whole particles mainly due to corrosion of the carbon support that anchors the nanoparticles or diffusion of dissolved metal from the catalyst often play a role(136), as well, and their possible influence shell not be neglected in this discussion. However, from the SEM measurements conducted at certain points of the long-term potential cycling the increase in agglomeration and the consequential particle coalescence for both treatments can clearly been seen and thus it is sensible to assign the loss of ECSA in this region of the degradation curve to the influence of this agglomeration.

From the high values found for the ECSA at the end of the long-term measurement for the substrate-only plasma treated GCE as well as the oxidized GCE, the first of which is comparable to the plasma treated GCE and the second of which exhibits a value more than twice as high that is furthermore still increasing when the investigation was ended, it becomes clear that electrocatalyst–substrate interaction is the factor determining the stability of the GCEs in the last region of the degradation curve. This also means that the state of the GC substrate is a very important factor determining the long time stability of the GCE. It was further shown that an oxidation and the connected roughening of the surface of a GC improve stability. The oxidation of an already particle covered carbon surface seems to open a new way towards excellent long-term stability in this respect and further investigations into this approach are highly recommendable.

3.6 Comparison of PtNi Nanoparticles

In order to investigate the dependency of size or composition of nanoparticles in regard to their electrocatalytic activity the synthesized particles first need to be characterized thoroughly. This is usually done by means of a TEM and XRD investigation, from which the size of the particles is determined. Additionally, the XRD results are used to investigate the composition of the particles by utilizing Vegard's law. The composition of the particles is furthermore determined using EDX analysis. As was already described in 3.2.1 these measurement techniques are based on different principles and thus lead to different results, which in combination provide a comprehensive description of the particle batch and its properties.

From the XRD analysis the mean size of the crystalline domain of a particle ensemble is gained via the Scherrer equation (see "XRD" in 4.1.3), which in turn is based on a peak fitting of the obtained diffractogram. The composition of the ensemble is determined employing Vegard's law, which is an empirical law correlating the lattice parameters of two constituents and the composition of a mixture of the two in a linear fashion. Both these approaches provide information about a particle ensemble, i.e. a mean size and mean composition of the crystalline part of the investigated particle batch.

The TEM investigation of the synthesized nanoparticles shows a much smaller part of the entire particle ensemble than the XRD investigation. For the size determination of the particles at least 500 particles were analyzed for each batch, a number that from experience is completely adequate to represent the size distribution in the respective particle ensemble. Contrary to the result regarding particle size that is obtained from the XRD investigation, this size analysis on the basis of a TEM measurement yields a size distribution of the investigated particle batch and thus introduces an additional

dimension by which a particle batch can and should be characterized. The particle size determined from TEM analysis furthermore entails the whole metallic portion of the respective particle, independently of the mean size of its monocrystalline domains. For that reason an increasing difference between particle size determined via XRD and via TEM is observed for increasing particle sizes (> 4 - $5\,\mathrm{nm}$). In these cases the metallic particle that is registered by the TEM investigation consists of multiple crystalline domains and possible regions of amorphous metal oxide, whereas only the mean size of the crystalline domains is registered via XRD.

As was the case for the size determination via TEM, the portion of the particle batch that is analyzed in a compositional investigation by using the EDX option in context of a TEM analysis is smaller than that registered for a typical XRD analysis. Contrary to the determination of particle size via TEM, however, the EDX analysis does not inherently yield information about the distribution of the obtained compositional data. This information needs to be acquired individually by an element mapping or line scan in scanning transmission electron microscopy (STEM) mode in combination with an EDX measurement. However, regularly obtained EDX results contain the composition of the entire particle, not only that of the monocrystalline domains of the particle ensemble as is the case for the particle composition obtained from XRD analysis, and thus further expand the knowledge about the investigated particles.

Employing all the above techniques for the characterization of a particle batch thus yields a comprehensive description of its constituents, although there are still many important factors in regard to the use of a particle as electrocatalyst that are not covered by them. Among those are, for example, the knowledge about the crystal facets expressed by a particle, their ratio for a single particle, as well as the distribution of this ratio over the particle ensemble. Another important factor in regard to electrocatalysis is the amount of ligand and, if more than one kind of ligand is used, the ratio of theses ligands present at the particle surface. Also, the kind of bonds formed between ligand and particle surface and potentially preferential bonding to one of the elements the particle is comprised of are of interest. Of course the distribution of these characteristics over the particle ensemble is important as well. Additionally, the oxidation state of the particles employed as electrocatalyst might influence catalytic activity, as might any contaminants present in the particle solution, the ligand network around the particle or at the particle surface. A summary of the most common factors influencing electrocatalysis can be found here.(138)

In context with the electrodes used in this work, all questions regarding the distribution of the electrocatalytic particles on their support are of the utmost importance for catalytic activity since they determine their agglomeration behavior as was already

described in 3.3.2. This catalyst distribution in turn depends on the colloidal stabilization of the particles and thus on the amount of ligand present. Finally, the state of the GC support is influencing both, catalyst distribution (mainly through its surface properties during the spin coating procedure by which the particles are deposited on the GC substrate) and also catalyst stability (see 3.5.2), which is correlated with particle agglomeration and thus also with catalytic activity as was discussed in 3.4.2.

From this by no means comprehensive compilation of factors contributing to the catalytic activity of an investigated ensemble of electrocatalytic nanoparticles it becomes clear that such a determination is no trivial task. Furthermore, the results obtained from this kind of analysis can only be regarded in respect to the known properties of the investigated system and the controlled factors of the employed set-up and it has to be kept in mind that other properties and factors might play an important role, as well. The goal of each investigation into the electrocatalytic properties of a particle batch is therefore to generate conditions under which the unknown factors are kept constant, so that the differences in results obtained can be ascribed to the known properties of the system. However, given the multitude of factors that might influence electrocatalytic activity and the difficulty to pinpoint their origin by means of electrochemistry constitutes a major problem in these kinds of studies.

In this work, the rigorous production procedure of the GCEs, starting from a solution containing a certain ligand excess, followed by a certain number of washing steps and finally the deposition of the particles onto an always equally prepare support are the means by which a comparability between at least some of the factors influencing catalytic activity are achieved. In respect to this production procedure for the GCEs (see 3.3) it can be assumed that the coverage of the particles with ligand is comparable when inherent factors like particle size or composition are comparable. A factor that is not controlled is the kind of crystal facets expressed by the particles, although the employing of more or less the same synthesis conditions (regarding reactants, temperature range, ligands, etc.) for the preparation of the different nanoparticles supports the assumption that under these comparable conditions the same crystal facets might be expressed by the particles.

In the literature the influence of size and composition of PtNi nanoparticles on catalytic activity has mostly been examined in correlation with the ORR and less often for the MOR. Wang *et al.* examined nanoparticles synthesized following the solvothermal approach which was developed by Ahrenstorf(117) and used in this work as well. The obtained particles had an average size of $5\,\text{nm}$ as determined via TEM with compositions of Pt_3Ni, $PtNi$, $PtNi_2$, and $PtNi_3$ as determined via EDX and were investigated in regard to the ORR. The best specific and mass activity (approx. $1500\,\text{A}\,\text{g}^{-1}$) was

found for the PtNi nanoparticles, although differences in catalytic activity between the different particle batches were not as significant as expected for the rather large differences in composition. In this respect a factor of 2 to 3 was found between the lowest and the highest mass activity determined. For this investigation the particles were supported on carbon black and treated by heating in air for ligand removal. No changes in particle size and composition were found prior to and after the treatment according to XRD measurements. After the electrochemical investigation the particles showed Ni loss and a slightly reduced size, but no agglomeration was observed. A diffractogram of the as-synthesized particles is shown in this publication, but no data concerning the size and composition determined from this XRD analysis is given.(94)

Park *et al.* examined PtNi nanoparticles synthesized at room temperature using a reduction method with $NaBH_4$ and investigated them using XRD and TEM analysis. The size of the particles as determined using the XRD data is reported to have a value of 3 - 4 nm. A TEM image of the particles is also shown. Although in it no individual, well-defined particles are recognizable the particle size as determined from the obtained TEM images is reported to also have values of approximately 3 - 4 nm. The composition is determined to be Pt_3Ni and PtNi for the two sets of PtNi particles examined. Additionally, PtRu, PtRuNi and pure Pt nanoparticles are investigated. A comparison of these unsupported particles on the one hand and supported nanoparticles on the other hand is then made, stating that unlike the unsupported particles the latter "on carbon support showed a homogeneous dispersion with a similar particle size ... (and were) largely spherical in shape".(12) However, no data confirming this is shown. For the electrochemical investigation a better catalytic activity as determined via a lower onset potential is found for both PtNi compositions in comparison to pure Pt. Among the two alloys PtNi has an even lower onset potential than Pt_3Ni. Furthermore, no Ni dissolution during electrochemical measurements is observed in this study.(12)

Deivaraj *et al.* prepared carbon supported PtNi nanoparticles and investigated them with respect to the MOR using CV. The particles showing the best current density ($0.82\,\mathrm{mA\,cm^{-2}}$) had a composition of 1:4 (Pt:Ni) and a size of 3 - 6 nm.(139) Whether the given current density is referenced to the real surface area of the catalyst or the geometric area of the electrode is, however, unfortunately not reported.

Agrawal and Rangarajan report the synthesis of a series of carbon supported PtNi nanoparticles with different compositions and the results of the respective CV investigation. They find the best specific activities for the 1:0.5 and 1:1 (Pt:Ni) nanoparticles ($0.22\,\mathrm{mA\,cm^{-2}}$ and $0.19\,\mathrm{mA\,cm^{-2}}$, respectively) and obtain the best values for the mass activities also from those two particle batches (with a respective value of $0.35\,\mathrm{A\,g^{-1}}$ for both batches). The other particle batches investigated have a lower Ni content (as low

as 1:0.05 (Pt:Ni)) and exhibit values for the specific activity as low as $0.13\,\mathrm{mA\,cm^{-2}}$ and for the mass activity as low as $0.22\,\mathrm{A\,g^{-1}}$. The size of the investigated nanoparticles was found to be between 9 - 11 nm and increase with increasing Ni content in agreement with the findings of this work.(130)

As can be seen from the short literature survey given above, a complete characterization of the employed electrocatalyst is very hard to find when size and composition dependent investigations of catalytic activity are published, although the information gained from these investigations might in some cases play an important role in this regard. A sensible experimental set-up as, e.g., the one employed by Wang *et al.* and the one by Agrawal and Rangarajan, nevertheless allows the comparison of size and composition effects under the assumption that the influence of other parameters, such as for example an initially different ligand stabilization due to the different composition of the particle batches, can be neglected. However, on account of the nontrivial character of the investigation into the electrochemistry and electrocatalysis of nanoparticles, comparing data from different experiments may easily lead to ambiguities due to differences in the experimental set-up or slight differences in the employed particles.(107) An accurate description of all parameters is therefore absolutely necessary to classify and compare the obtained results.

Details of the Investigation   In this investigation PtNi nanoparticles in the size range from approx. 2 to 8 nm as determined via TEM and a Ni content from approx. 1 to 60 % as determined via EDX were employed. The particles were deposited on the GC substrate according to the procedure described in 3.3 and coated with a Nafion film to suppress agglomeration and contain a particulate structure of the electrocatalyst as much as possible under the given experimental conditions. A treatment was not applied for the same reason. The particles examined in this respect are compiled in table A.2. Experimental details can be found in "Comparison of Nanoparticles" in 4.5.3. In addition to the nanoparticles that differ in either size or composition, particle batches that are comparable in both aspects were investigated to examine the overall influence of these two factors amidst all the other possible parameters determining catalytic activity.

3.6.1   PtNi Nanoparticles with comparable Size and Composition

In order to determine which influence the size and composition of different nanoparticles have in regard to their catalytic activity it is important to know as much as possible about the general magnitude of these factors, especially in comparison to the effect of other parameters like particle shape, crystal facets exposed, ligand stabilization, etc.

Table 3.18: Characteristics of PtNi nanoparticles used in comparison experiments and nanoparticle batches that are comparable in size and composition, respectively.

name	size (TEM) [nm]	size (XRD) [nm]	Ni (EDX) [at%]	Ni (XRD) [at%]	comparable NP batches
PtNi-1	2.4	2.1	7	1	
PtNi-2	7.3	5.0	52	42	PtNi-6, PtNi-8
PtNi-6	7.7	5.6	51	40	PtNi-2, PtNi-8
PtNi-7	2.3	2.2	18	10	
PtNi-8	7.6	4.8	54	44	PtNi-2, PtNi-6
PtNi-9	2.3	2.3	22	22	
PtNi-10	4.1	3.6	33	24	
PtNi-11	4.3	3.6	46	30	
PtNi-12	5.8	4.3	43	37	

(see 3.6). For that reason three different particle batches with particles of the same size and composition were investigated electrochemically. The particle batches employed for this task are compiled in table 3.19 and the respective TEM images can be found in figure 3.51. As can be seen from the table the differences in size and composition are small ($\leq 5\,\%$), except for the size as determined via XRD, where PtNi-6 exhibits a mean size of the monocrystalline domains of 5.6 nm, which is 12 % larger than that of PtNi-2 and 16 % larger than that of PtNi-8. However, since the determination of the particle size via XRD is based on the Scherrer equation, which in turn is based on a peak fit, a margin of error that is slightly larger than that found for the determination of particle size from a TEM investigation is to be expected.

The TEM images and size distribution diagrams shown in figure 3.51 underline the comparability of the size of the different particles investigated here. However, a closer look at the TEM image of PtNi-8 reveals that the shape of the respective nanoparticles is not the same as for PtNi-2 and PtNi-6. Whilst the latter appear more or less round and smooth, the particles of PtNi-8 appear polygonal and are less smooth. For this reason, a catalytic activity that is different to that of PtNi-2 and PtNi-6 is expected, whereas the catalytic activity of the latter two is expected to be comparable to some degree if size and composition really are the main factors determining activity under the given experimental conditions.

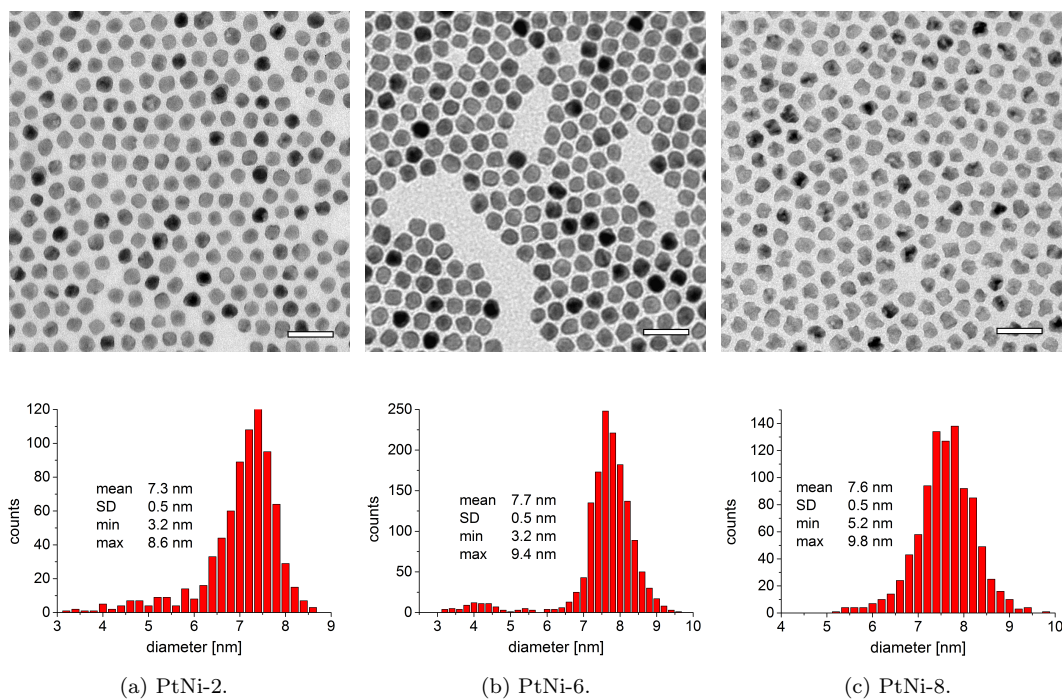(a) PtNi-2.   (b) PtNi-6.   (c) PtNi-8.

Figure 3.51: TEM images of different particle batches (first line) and the size distribution of the respective particle batch (second line). Scale bar = 20 nm.
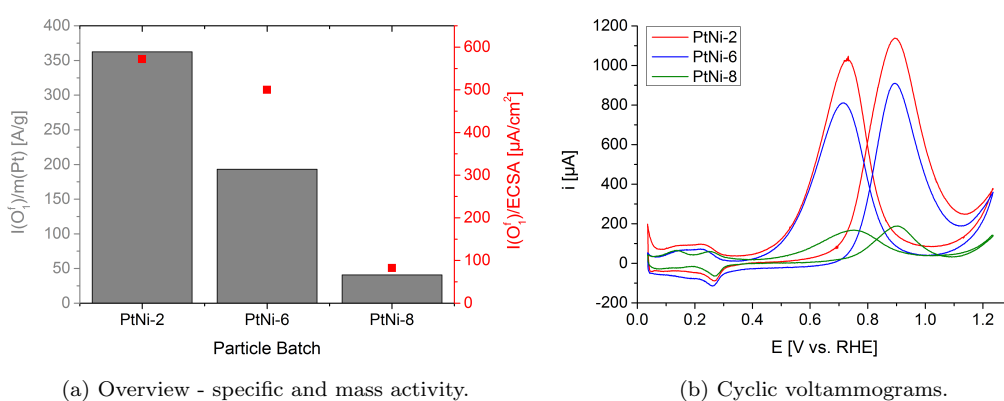

(a) Overview - specific and mass activity.   (b) Cyclic voltammograms.

Figure 3.52: Results of the electrochemical investigation of comparable PtNi nanoparticles, (a) comparison of specific and mass activity and (b) comparison of the cyclic voltammograms obtained after 160 cycles.

3. RESULTS AND DISCUSSION

Table 3.19: Characteristics of PtNi nanoparticles that are comparable in size and composition.

name	size (TEM) [nm]	size (XRD) [nm]	Ni (EDX) [at%]	Ni (XRD) [at%]
PtNi-2	7.3	5.0	52	42
PtNi-6	7.7	5.6	51	40
PtNi-8	7.6	4.8	54	44

The results of the electrochemical investigation are shown in figure 3.52. As can be seen from the bar graph the specific activity of PtNi-8 ($82\,\mu A\,cm^{-2}$) is much smaller than that of PtNi-2 and PtNi-6 (572 and $500\,\mu A\,cm^{-2}$, respectively). The deviation of the latter two values is smaller than $15\,\%$, whereas the value obtained for PtNi-8 shows a deviation of more than $80\,\%$. In regard to the specific activity the relationship of the values found are thus as expected. The results in regard to the mass activity of the three sets of particles show a similar picture. The highest value is obtained for PtNi-2 ($362\,A\,g^{-1}$), as was already the case for the specific activity. This value is followed by an intermediate value of $193\,A\,g^{-1}$ for PtNi-6 and finally by a very low value of $40\,A\,g^{-1}$ for PtNi-8.

Since the mass of the respective GCEs is only determined after the electrochemical measurement was conducted and since it is possible that this determination actually registers platinum that was not electrocatalytically involved in the preceding CV experiment, this deviation becomes comprehensible. In contrast, the ECSA of a GCE is a direct measure of the meaning of its abbreviation/acronym, the *electrochemically active surface area*, and thus might be better suited to relate the results of the different electrocatalysts to each other.

One look at the cyclic voltammograms obtained for the three comparable particle batches underlines the similarity between PtNi-2 and PtNi-6 as well as the deviation of the differently shaped nanoparticles of PtNi-8. Peak and onset potentials of the these voltammograms are comprised in table 3.20. As expected, the peak potentials of PtNi-2 and PtNi-6 are very similar, compared to a higher value found for PtNi-8. Accordingly, the onset potential for PtNi-2 is lowest, followed by the onset potentials for PtNi-8 and PtNi-6. The reversal in the expected order is a consequence of the much lower slope of the tangent to the O_1^f peak of PtNi-8 than that of the other two particle sets.

In summary, the comparison of the three sets of nanoparticles with comparable size and

Table 3.20: Onset and peak potentials of the O_1^f peak of the three sets of comparable PtNi nanoparticles.

name	onset potential [V vs. RHE]	peak potential [V vs. RHE]
PtNi-2	0.72	0.896
PtNi-6	0.76	0.894
PtNi-8	0.75	0.905

composition provided results that lay within the expectations in regard to the specific activity at least. From the three particle sets the two that, to the best of the experimenters knowledge, were similar to each other in all other accessible or observable parameters other than size and composition (PtNi-2 and PtNi-6), showed a comparable specific activity of approx. $540\,\mu A\,cm^{-2}$. The set that differed from these two in the shape of the constituting nanoparticles (PtNi-8) exhibited a much lower specific activity of approx. $80\,\mu A\,cm^{-2}$. Assuming this large difference in specific activity is a result of the different shape of the investigated particle sets and not the consequence of some other unknown parameter, the obtained value gives an idea about the magnitude of the influence that the particle shape of PtNi nanoparticles has on catalytic activity. The rather good correspondence ($\leq 15\,\%$) of the two values obtained for the particle sets with the same shape is almost surprising when keeping in mind the multitude of factors influencing catalytic activity and the lack of methods for their detection.

For the mass activity of the three particle sets the general trend found was the same as for the specific activity, although the value obtained for PtNi-6 was lower than expected in comparison to PtNi-2. As a reason the possibility of detecting platinum, which did not take part in the electrocatalytic conversion, via AAS was mentioned. This would for example be the case if some of the nanoparticles of the GCE had no electric contact to the GC substrate or if a disproportionately large amount of electrocatalyst was present in the area of the GCE where the O-ring is pressed onto (see 4.5.1 for details on the experimental set-up). Since these errors can not occur in respect with the specific activity, where catalytic activity is related to an itself electrochemically determined value (the ECSA) for the following investigation only the specific activity was regarded.

Table 3.21: Particle sets of same size or same composition, respectively. The comparability is oriented on the size obtained by TEM and the composition obtained by EDX. The comparable values are set in bold font.

No.	size (TEM) [nm]		Δ_{size} [%]	Ni (EDX) [at.%]		Δ_{Ni} [%]	particle batches	
	set 1	set 2		set 1	set 2		set 1	set 2
I.	**2.4**	**2.3**	4	7 $Pt_{13}Ni$	18 Pt_4Ni	61	PtNi-1	PtNi-7
II.	**2.4**	**2.3**	4	7 $Pt_{13}Ni$	22 Pt_4Ni	68	PtNi-1	PtNi-9
III.	**4.1**	**4.3**	5	33 Pt_2Ni	46 PtNi	28	PtNi-10	PtNi-11
IV.	5.8	4.3	26	**43** PtNi	**46** PtNi	7	PtNi-12	PtNi-11
V.	**7.3**	**7.7**	5	**52** PtNi	**51** PtNi	2	PtNi-2	PtNi-6

3.6.2 PtNi Nanoparticles with either comparable Size or Composition

In this section the results of some comparisons of PtNi nanoparticles which are comparable in one of their properties, size and composition, but differ in the other one, are presented. Comparability is per definition given when the second value lies within a deviation of $\leq 7.5\%$ of the smaller of the two values. Two values are considered to be sufficiently different, if the deviation between them is at least three times as large, i.e. $\geq 22.5\%$ of the higher value. Table 3.21 gives an overview of the comparable sets. In figure 3.53 the respective specific activities are compiled. In addition to the particle sets that differ in one property, size or composition, the set that is comparable in both these factors (PtNi-2 and PtNi-6, see 3.6.1) is included as a reference.

As can be seen all values obtained lie between 100 and 600 $\mu A\,cm^{-2}$ and most values even can be found between 350 and 600 $\mu A\,cm^{-2}$. Given the very different sizes and compositions comprised in this investigation, this range is surprisingly small. In this regard the result found here agrees well with the findings of Wang *et al.* (see discussion in 3.6), who investigated PtNi nanoparticles of different compositions in respect to their activity for the ORR and also observed rather insignificant differences between the different particles.(94)
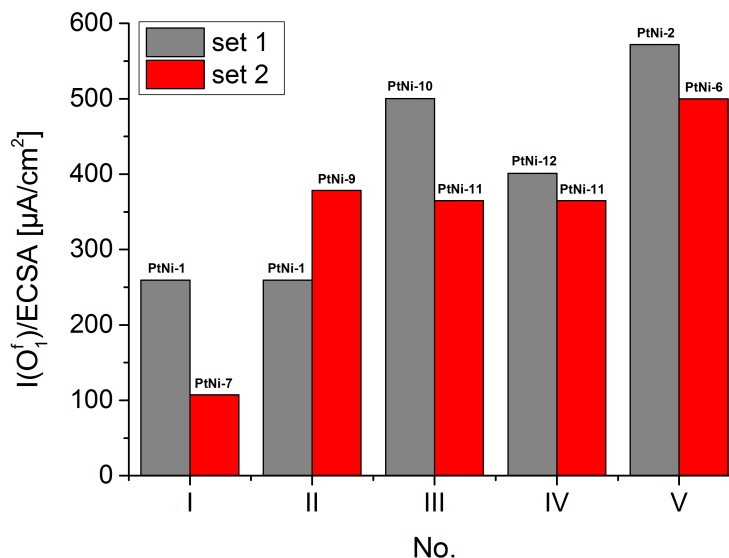
Figure 3.53: Compilation of the specific activities of the comparable sets of particles given in table 3.21. I - IV differ in one property (size or composition) but are similar in the other, whereas V is comparable in size and composition.

However, regarding the size of the investigated particles a clear trend can be deduced. This can better be seen in figure 3.54, where the relationship between size, composition and specific activity is shown and it becomes clear that the larger PtNi alloy nanoparticles are better electrocatalysts than the smaller Pt-rich particles. This result also agrees well with the results of the investigation of Wang *et al.*, who also found the best specific activity for the PtNi nanoparticles, as compared to Pt_3Ni, $PtNi_2$ and $PtNi_3$ and to the result of Agrawal and Rangarajan, who also found the best results for 1:1 (Pt:Ni) nanoparticles and found specific and mass activities ($0.19\,\mathrm{mA\,cm^{-2}}$ and $0.35\,\mathrm{A\,g^{-1}}$, respectively) in the same order of magnitude as reported in this work.(130) Nanoparticles with a higher Ni content than approx. 50 % were not examined in this investigation, so that no statement about their catalytic activity can be made.

In summary, the size and the composition of PtNi nanoparticles do not seem to influence the catalytic activity for the MOR significantly. Other factors, like the shape of the particles and therefore most likely their crystal facets, have a greater influence on the activity than composition and size, as could be seen in 3.6.1, where a pair of nanoparticles with comparable size and composition but different shape yielded both the maximal and minimal specific activity obtained in respect to all the measurements conducted for this investigation. However, from the investigated nanoparticles the ones
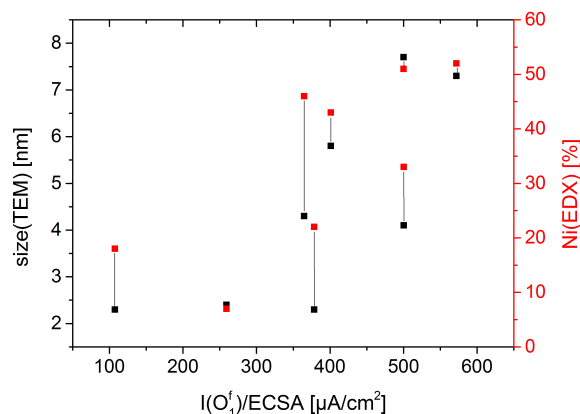
Figure 3.54: Correlation of the factors size, composition and specific activity. Sets of values belonging to one particle batch are connected by a black line.

with a size $\geq 5\,\text{nm}$ and a Ni content $\geq 40\,\%$ exhibited a better specific activity than the smaller, more Pt-rich particle batches. This observation is in line with the well-known observation that alloys of platinum are generally better electrocatalysts than pure platinum particles.

3.7 Additional Investigations

In this section the results of some important additional investigations are compiled. This includes a reference measurement with a bulk electrode of polycrystalline platinum (see 3.7.1), which was also used to test different settings of the software program used in connection with the employed potentiostat. Also, an investigation into the influence the use of differently concentrated colloidal particle solutions on electrode preparation had on catalytic activity (see 3.7.2) is introduced. Additionally, the influence of using different lines for the EDX analysis at the different transmission electron microscopes employed for the characterization of the synthesized nanoparticles is discussed (see 3.7.3).

3.7.1 Investigation of Polycrystalline Pt Bulk

As a reference to the investigated nanoparticles of different size and composition a bulk polycrystalline platinum electrode was examined electrochemically. The preparation of the platinum is described in 4.4. In figure 3.55 a cyclic voltammogram of this platinum electrode in $0.5\,\text{M}\ H_2SO_4$ is shown. The ECSA obtained from this curve is $3.4\,\text{cm}^2$.
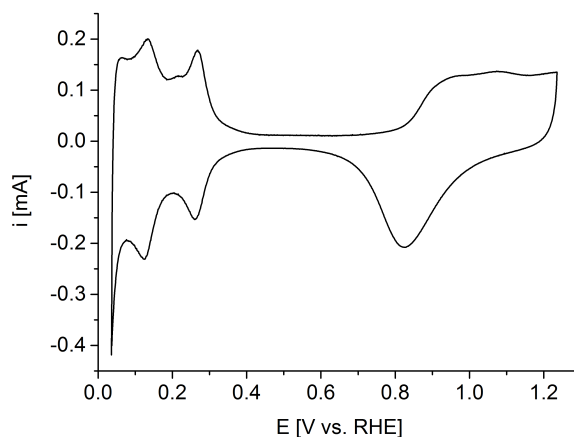
Figure 3.55: Cyclic voltammogram of a polycrystalline platinum bulk electrode in $0.5\,\text{M}$ H_2SO_4 recorded under "current averaging" and with a scan rate of $5\,\text{mV}\,\text{s}^{-1}$.

The specific activity obtained is approx. $990\,\mu\text{A}\,\text{cm}^{-2}$ and is thus higher than the values found during the comparative investigation in respect to size and composition of the nanoparticles employed as electrocatalyst (see 3.6.2). The highest value obtained there was approx. $770\,\mu\text{A}\,\text{cm}^{-2}$ by 48:52 PtNi alloy particles with a diameter of $7.3\,\text{nm}$ (PtNi-2). However, in correlation with the investigation of different treatments for ligand removal in 3.4 specific activities in the order of magnitude as the one found for pure platinum here were observed. This was the case for the same batch of particles that was just mentioned, PtNi-2, after application of an oxidative treatment (see 3.4.3). With the use of PtNi alloy nanoparticles as electrocatalyst one would expect a higher specific activity than for pure platinum - be it in bulk form or in form of nanoparticles. The investigations conducted in this work were so far in line with this expectation (see 3.6.2) but clearly deviate in respect to the comparison made here. An explanation for this unexpected result is not easily obtained and more experiments, especially with a batch of pure platinum particles, would be necessary to obtain clarity in this matter.

The results of the investigation of a polycrystalline platinum bulk electrode in respect to different settings of the measurement software *IviumSoft* are shown in figure 3.56. From this it can be seen that different settings lead to very different results regarding the value of the ECSA. Although the highest ECSA value is reached when using the α parameter ($\alpha = 0.400$), which determines at which point of the current response to an applied potential the measurement of the current takes place, from this set of experiments and after consultation with a technician from *Ivium Technologies* the use of this parameter was abstained from. The true value of the ECSA of the platinum electrode was determined to be $3.4\,\text{cm}^2$, as this was the value consistently found under use of
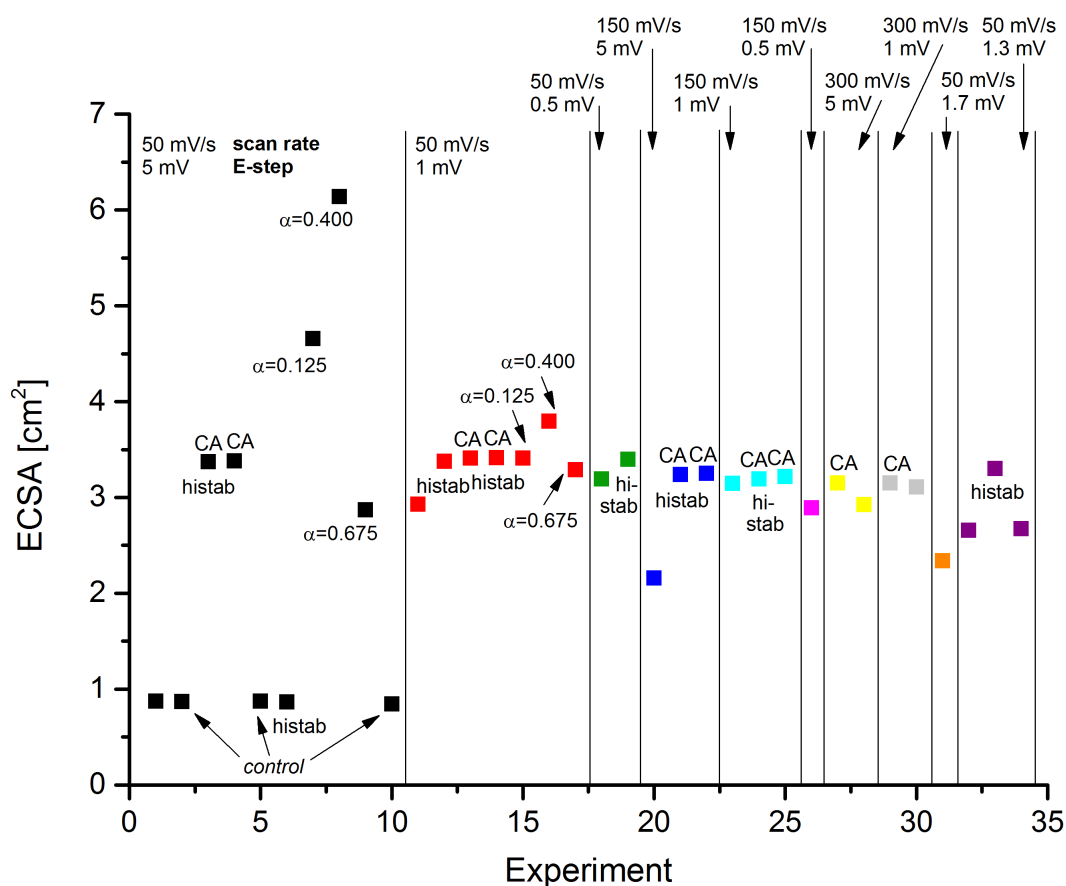
Figure 3.56: Results of CV experiments on a polycrystalline platinum bulk electrode in 0.5 M H_2SO_4 recorded with different settings of the *IviumSoft* software. CA in this case stands for "current averaging", histab for "high stability", the α parameter is always given with its value. If no comment is made the measurement was conducted with "automatic" stability and in "standard" mode. As filter option "automatic" was chosen for all measurements. The control measurements were evenly spread out over the whole investigation.

Table 3.22: Concentrations of colloidal particle solutions used to prepare GCEs for the investigation of the influence of this value on catalytic activity and the obtained ECSA. The volumes given are those taken from the initial OAm-rich colloidal particle solution to produce 110 mL solution of the desired concentration. The mass of platinum given is the one obtained from the AAS measurement performed at the end of each experiment.

dilution factor	0.10	0.50	0.67	1.0	1.5	2.0
volume [mL]	11	55	83	110	165	220
concentration $[\mathrm{g\,L^{-1}}]$	0.2	0.8	1.2	1.6	2.4	3.2
m(Pt) [µg]	0.65	1.57	1.99	2.20	2.96	4.22

the recommended "current averaging" mode for a sensible scan rate of $0.05\,\mathrm{V\,s^{-1}}$. The experimental procedure given in for 4.5.3 is based on the findings of this investigation. In short it entails CV experiments to be conducted in "current averaging" mode, with a scan rate of $0.05\,\mathrm{V\,s^{-1}}$, an E-step of $1\,\mathrm{mV}$ and "automatic" as stability and filter setting, respectively. Alternatively, a measurement in "standard" mode, with a scan rate of $0.05\,\mathrm{V\,s^{-1}}$, an E-step of $1\,\mathrm{mV}$, "automatic" as filter setting and "high stability" as stability setting is possible. This two options are represented by the data points 13 and 12 in figure 3.56, respectively.

3.7.2 Influence of Concentration of Colloidal Particle Solution

In order to make sure that slight variations in the concentration of the colloidal particle solution employed for the preparation of the GCE had no unexpected non-linear influence on catalytic activity or the ECSA electrochemical experiments with GCEs prepared from differently concentrated solutions were conducted. The concentrations employed are given in table 3.22. Experimental details can be found in "Influence of Particle Concentration" in 4.5.3.

In figure 3.57 the results of this investigation are depicted. As can be seen from the linear relationship between the concentration of the employed colloidal particle solution and the mass determined of platinum via AAS a change in the first factor induces a change in the second in a predictable way. This is as it should be for a sensible experimental set-up. The more important fact is that the ECSA and the peak current of the O_1^f peak also correlate with the concentration of the colloidal particle solution in a linear fashion as expected. This indicates that the mass concentration chosen for the preparation of the GCEs in this work $(2\,\mathrm{g\,L^{-1}})$ lies within a stable range, where slight variations in this factor do not lead to unexpected, non-linear results. Non-linearity

(a) Correlation: Concentration and m(Pt).

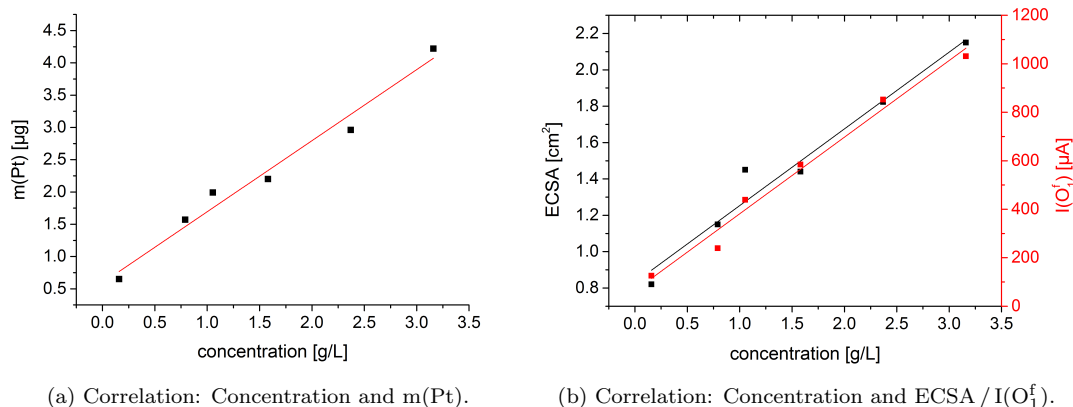(b) Correlation: Concentration and ECSA / I(O_1^f).

Figure 3.57: Relationship between the concentration of the colloidal particle solution used to prepare the GCEs and (a) the mass of platinum detected via AAS after the CV experiment and (b) the ECSA and peak current of the O_1^f peak.

would be expected to set in with increasing coverage of the GC with electrocatalyst due to the eventual formation of more than a monolayer of nanoparticles. In that case not all of the particle surface of a particle in a lower layer would be able to take part in the electrochemical processes but would still contribute to the mass of platinum present in total, thus lowering the obtained mass activity and leading to incomprehensible results for the catalytic activity.

3.7.3 Influence of Lines in EDX Analysis

Since one of the major characterizing tools for the particles employed in this work is EDX the influence of employing different sets of lines for the analysis was investigated. For this purpose a comparison of the results obtained from AAS analysis, from an EDX and wavelength dispersive X-ray spectroscopy (WDX) analysis performed at a scanning electron microscope (*Leo 1550 Gemini* from *Zeiss*), and the results from the EDX investigation of two different transmission electron microscopes, TEM A (*Philips CM 300 UT*) and TEM B (*Jeol JEM-2200FS*) was conducted. Details concerning the experimental procedure of these investigation methods can be found in 4.1.3. The results of the investigation obtained for three particle charges (PtNi-1, PtNi-4, and PtNi-10) are compiled in table 3.23.

As can easily been seen by comparing the results obtained at TEM A the influence of choosing different sets of lines for the analysis of the particle composition yields very different results. For the small, Pt-rich nanoparticles of PtNi-1 a Ni-content of either 2,

Table 3.23: Ni content of three nanoparticle batches determined via different characterization methods at different devices. The element lines chosen for the analysis in respect to EDX and WDX investigations are also given.

particle batch	Ni (EDX)					Ni (WDX)	Ni (AAS)
	TEM A [at%]			TEM B [at%]	SEM [at%]	SEM [at%]	[at%]
	Ni-L Pt-L	Ni-K Pt-M	Ni-L Pt-M	Ni-K Pt-M	Ni-K Pt-M	Ni-K Pt-L	
PtNi-1	21	2	7	12	6	5	6
PtNi-4	62	11	33	36	31	32	31
PtNi-10	83	26	59	62	56	54	57

7, or 21 % is thus determined. The factor of 10 between the minimal and maximal value that is found for these particles is especially striking but the factors of 2 and 3 found for PtNi-4 and PtNi-10, respectively, are still much too large to sensibly characterize a set of nanoparticles.

The great deviations observed when employing different lines for the EDX analysis are a consequence of measurement artifacts distorting the signal. However, the result of the EDX determination using the Ni-L, Pt-M set of lines on TEM A is consistent with the composition found for the three batches of nanoparticles as determined by other means. In this regard EDX at a different transmission electron microscope (TEM B), as well as at a scanning electron microscope, where a WDX measurement was also performed, were conducted. In all these cases the set of lines proposed by the analysis software of the respective device was used. Additionally, the composition of the particles was determined via AAS. As can be seen from table 3.23 the Ni content determined by all of this methods is in good agreement. The strongest deviation is found in case of the determination via EDX at TEM B, where a value of 12 % nickel is obtained, whereas 5 to 6 % nickel are determined via EDX and WDX at the scanning electron microscope and via AAS. For the two other particle batches the deviation is smaller, although the Ni content determined via EDX at TEM B in all cases is higher than that of the determinations at the scanning electron microscope and of the AAS analysis. With respect to the results of the EDX investigation using TEM A with the Ni-L, Pt-M set of lines, however, a good agreement with the results of these other investigation methods is found.

4

Experimental

4.1 Synthesis of PtNi Nanoparticles

Spherical Pt_xNi_{1-x} nanoparticles were synthesized via reduction of $Ni(ac)_2$ and $Pt(acac)_2$ in the presence of oleylamine and oleic acid as stabilizing agents. This method was first described by Ahrenstorf et $al.$, who also investigated important factors like injection rate and reaction time in the context of the continuous injection method.(117; 118) All chemicals used in this work were employed without any further pretreatment or purification. The syntheses were carried out under nitrogen atmosphere.

4.1.1 Hot Injection

In a typical synthesis of spherical particles 41.5 mg (0.167 mmol) $Ni(ac)_2$, 43.2 mg (0.167 mmol) 1,2-hexadecanediol (HDD), 0.2 ml (0.6 mmol) OAm and 0.2 ml (0.6 mmol) OA as well as 10 ml diphenyl ether (DPE) were mixed in a three-neck round-bottom flask equipped with a reflux condenser, a thermocouple and a septum. This mixture was heated to 80 °C for 60 min under vacuum conditions to remove traces of water. Afterwards, the temperature was raised to 200 °C under nitrogen atmosphere and 65.5 mg (0.167 mmol) $Pt(acac)_2$ dissolved under mild heating in 0.6 ml 1,2-dichlorobenzene (DCB) was injected under vigorous stirring. The resulting black dispersion was stirred for another 60 min and then cooled to room temperature by removing the heating mantle, adding 5 ml chloroform at a temperature of 120 °C. To precipitate the nanoparticles 45 ml ethanol was added to the dispersion followed by a centrifugation step (5 min, $g_n = 10\,000$). The yellow supernatant was discarded and the black precipitate was dispersed in 5 to 10 ml toluene. The nanoparticles were washed with a threefold excess of ethanol (15 to 30 ml) again and then redispersed in toluene. The addition of small

amounts of OAm (ca. 200 µl) ensured a good colloidal solubility of the particles in chloroform, n-hexane or toluene even after precipitation had occurred.

4.1.2   Continuous Injection

In a typical synthesis of spherical particles 41.5 mg (0.176 mmol) Ni(ac)$_2$, 43.2 mg (0.167 mmol) HDD, 0.2 ml (0.6 mmol) OAm, 0.2 ml (0.6 mmol) OA and 10 ml DPE were mixed in a three-neck round-bottom flask equipped with a reflux condenser, a thermocouple and a septum. The mixture was then heated to 80 °C for 60 min under vacuum conditions to remove traces of water. In a second three-neck round-bottom flask, also equipped with a reflux condenser, a thermocouple and a septum, 65.5 mg (0.167 mmol) Pt(acac)$_2$, 0.2 ml (0.6 mmol) OAm and 1 ml DPE were mixed. This mixture too was heated to 80 °C for 60 min under vacuum conditions to remove traces of water. After the conditioning of the two reaction mixtures, the temperature of the green solution containing the Ni-precursor was raised to 200 °C under nitrogen atmosphere. Then 65.5 mg (0.167 mmol) Pt(acac)$_2$ dissolved under mild heating in 0.6 ml DCB was injected under vigorous stirring, starting a countdown at the time of the injection. After a reaction time of 180 s the continuous injection of the second prepared solution, containing the Pt-precursor, via a syringe pump and with an injection rate of 24 ml h^{-1} was started. To suppress precipitation in the Pt solution the syringe containing it was heated mildly with a heat gun for the duration of the addition. The resulting black dispersion was stirred for another 60 min and then cooled to room temperature by removing the heating mantle, adding 5 ml chloroform at a temperature of 120 °C. To precipitate the nanoparticles 45 ml ethanol was added to the dispersion followed by a centrifugation step (5 min, $g_\mathrm{n} = 10\,000$). The yellow supernatant was discarded and the black precipitate was dispersed in 5 to 10 ml toluene. The nanoparticles were washed with a threefold excess of ethanol (15 to 30 ml) again and then redispersed in toluene. The addition of small amounts of OAm (ca. 200 µl) ensured a good colloidal solubility of the particles in chloroform, n-hexane or toluene at any time.

4.1.3   Characterization of PtNi nanoparticles

XRD   The synthesized nanoparticles were characterized via XRD using a *Philips X'Pert PRO MPD* diffractogram with Bragg-Brentano geometry employing a copper cathode with nickel filter ($\lambda = \mathrm{K}_\alpha$ 1.541 78 Å). The sample for the XRD investigation was prepared by successively applying drops of the colloidal particle solution onto a Si wafer and evaporating the solvent until a film of sufficient thickness had formed. The diameter d of the nanoparticles was determined according to the Scherrer equation(140),

which is often erroneously termed Debye-Scherrer equation(141)

$$d = \frac{57.3 \, \lambda \, K}{\beta_{1/2} \cos \theta} \tag{4.1}$$

with λ being the wavelength of the employed X-ray source (0.154 nm), K being a form factor, typically referred to as the *crystallite-shape factor*,(142) with a value between 0.8 and 1.2 (0.89 for spherical particles), $\beta_{1/2}$ the full width at half maximum (FWHM) of the respective reflex an θ its diffraction angle. The obtained reflexes were fitted using the program *fityk 0.9.8* with *PseudoVoigt* as fitting option.

TEM ad EDX For the TEM and EDX investigation a *Philips CM 300 UT* transmission electron microscope with a LaB_6 cathode and an *EDAX DX4* detector was used. The X-ray lines chosen for analysis of the EDX spectrum were the Ni-L and Pt-M lines. The TEM and EDX samples were prepared by diluting some of the colloidal particle solution with toluene until it appeared transparent and then depositing a droplet of the solution onto a carbon-coated copper grid. Excessive solution was sucked away with a filter paper and the grid was left to dry in air. The obtained TEM images were analyzed using the program *ImageJ 1.48v.*

AAS In order to obtain the concentration of the respective colloidal particle solution and determine the composition of the particles in an additional way, AAS measurements employing either a *ContrAA 700* spectrometer from *analytik jena* or a *Perkin Elmer 4100 THGA* spectrometer were conducted. The used wavelengths were 232.0 nm for nickel and 265.9 nm for platinum. Samples for this investigation were always prepared in triplicate and the arithmetical mean of the results was used for the compositional investigation. Depending on the estimated concentration of the colloidal particle solution 10 - 100 µL of the solution were used per sample followed by evaporation of the solvent and an aqua regia digestion under mild heating (approx. 60 °C) to solve all metallic nickel and platinum present in the respective sample.

4.2   Preparation of Composite Electrodes

In this work two types of composite electrodes were used. The first is an electrode consisting of a glassy carbon substrate which is covered with a monolayer of particles. The second type is composed of the GC substrate, a layer of particles and a thin Nafion film. Each electrode preparation consisted of at least three separate steps, namely the preparation of the glassy carbon substrate, the preparation of the colloidal particle

solution and the spin coating procedure to obtain a particle film. In the case of the composite electrode featuring a Nafion coating, the spin coating of the Nafion solution constitutes an additional step. All the above mentioned procedures are described in the following sections.

4.2.1 Preparation of the Glassy Carbon Substrate

Procedure GC Sigradur G disks purchased from *HTW Hochtemperatur-Werkstoffe GmbH* were used as electrode substrates. They had a diameter of 20 mm and a thickness of 3 mm. Upon receipt the GC disks were cleaned via mild heating (approx. 60 °C in aqua regia (nitric and hydrochloric acid in a volume ratio of 1:3) 30 min and after rinsing with millipore water via successive sonication (3 min each) in toluene, acetone, ethanol and millipore water again. In between the sonication steps the GC disks were wiped down with precision wipes from *Kimberly Clark*. This was the cleaning procedure also followed in between different experiments to remove all particles from the GC disk. In case the GCE was analyzed via AAS after a CV experiment an aqua regia digestion was employed to solve all platinum and nickel traces from the GC disk. A second aqua regia treatment was then abstained from. For GCEs that were additionally covered with a Nafion film prior to the aqua regia treatment a wiping down with methanol or, in case of the requirement of a AAS analysis, a dissolution of the Nafion coating was accomplished by sonication in a mixture of water and methanol (1:1). The solvent of the obtained solution was then evaporated and the residue was treated via aqua regia digestion to make sure no platinum or nickel was lost for analysis due to the dissolution of the Nafion film. Shortly prior to the preparation of a composite electrode (generally on the same day) the thus cleaned GC disk was freshly polished. Depending on the condition of the GC disk's surface one or three polishing steps were applied. In case gross scratches or defects were apparent two extra, more abrasive polishing steps (step 1 and 2, see table 4.1) needed to be performed. Small defects on the other hand could be treated by applying only the last three polishing steps (step 3, 4 and 5, see table 4.1). If the GC surface appeared smooth and exhibited a mirror finish only the last, least abrasive polishing step was applied to refresh the surface. All polishing materials were acquired from *Buehler*. An overview of the utilized polishing cloths and abrasives is given in table 4.1. The polishing procedure followed common routine(121), that is the GC disk was moved in a figure-8 motion over the respective emery paper or polishing cloth for some minutes. In each case a flat mounting and air bubble free fixation of the cloth was paramount. The emery paper or cloth was then wetted with millipore water and, in case of steps 3 - 5, MicroPolish Al_2O_3 suspension. The latter needed to

Table 4.1: 5-step method for polishing glassy carbon.

step	cloth	abrasive	grain size	time
1	CarbiMet	P1000 SiC	15.3 µm	until flat
2	CarbiMet	P4000 SiC	5.5 µm	until smooth
3	TexMet C	MicroPolish Al_2O_3 suspension	1.0 µm	until mirror finish
4	G-Cloth	MicroPolish Al_2O_3 suspension	0.3 µm	6 min
5	MicroCloth	MicroPolish Al_2O_3 suspension	0.05 µm	4 min

be shaken well prior to application and the first small amount out of the bottle was discarded to get rid of dried and agglomerated Al_2O_3 suspension that could scratch the substrates surface during polishing. When the desired surface finish was attained the GC disk was rinsed with millipore water, cleaned via sonication in millipore water (two times for 3 min each) and wiped down with precision wipes. Finally the GC disk was cleaned in a nitrogen flow with a pressure of 2 bar.

General Comments It is very important to avoid contamination of the polishing pads and/or the GC substrates with dust. For that reason the polishing pads, fixated on a glass plate, should be stored facing downwards in a place as dust-free as possible. The GC disks should be checked for dust or other contaminants prior to polishing as well, since those will scratch the surface during polishing. Dust can simply be removed by a stream of nitrogen passed over the surface, whereas for other, more sticky contaminants (e.g., fingerprints) a wiping down with KimWipes and water, ethanol, or acetone is necessary. Prior to the actual polishing the polishing cloth has to be thoroughly wetted, best some minutes before polishing is started to give the cloth enough time to soak through and potentially present dried polishing paste remaining from the last use time to break up. To support the latter a careful rubbing of the cloth with gloved hands can be helpful. Excess water gathering on the cloth in puddles should be should decanted prior to starting the polishing process. When applying the suitable polishing paste to the cloth, the first small amount from the flask should be discarded, since there is

usually some desiccated slurry stuck in the protruding opening of the flask from the last application. Then an amount sufficient to cover the whole pad when spread out should be applied to the cloth and gently rubbed in, checking for dried up agglomerates once more. After that the actual polishing process can finally begin. Afterwards, the cloth should be rinsed thoroughly and under gentle rubbing in a stream of deionized water until the water draining off it is clear.

4.2.2 Preparation of the Colloidal Particle Solution

After synthesis the obtained PtNi nanoparticles were stored in toluene solution in the dark. Prior to their use in the preparation of composite electrodes the colloidal particle solutions were regenerated. Depending on their condition at the beginning of the regeneration process, the addition of oleylamine and, if necessary, additional solvent to obtain a stable solution was generally the first step. In some cases it was indicated to let the mixture settle for some time (up to 72 h) after this addition to give the system time to stabilize. After long storage times (months) the colloidal particle solutions sometimes exhibited not or not only a black precipitate of nanoparticles, but a colorless, film-like precipitate of (supposedly) reacted OAm. In these cases it was necessary to include a couple of centrifugation steps after the generation of a stable solution. For this the toluene solution was first centrifuged with a threefold excess of ethanol (5 min, $g_n = 10\,000$) and the black precipitate then redispersed in the five- to tenfold volume of n-hexane. This diluted n-hexane solution was then centrifuged for (5 min at maximum acceleration (approx. $g_n = 15\,000$) and removed from the centrifuge carefully. The goal of this centrifugation step is to precipitate the colorless OAm reaction products, while keeping the nanoparticles in solution. If, however, nanoparticles had precipitated an addition of some OAm and giving the solution some time (up to 72 h) to settle usually resolved the issue. After successful centrifugation a mass of transparent precipitate could sometimes be observed in the tip of the centrifuge tube. In any case the supernatant liquid was carefully removed from the top downwards using a pipette. The bottom tenth of the solution was left in the centrifuge tube and discarded. The supernatant was again centrifuged with a threefold excess of ethanol (5 min, $g_n = 10\,000$) and the black precipitate dispersed in enough toluene to give a stable solution without any remaining precipitate. If no precipitate had formed during storage, this steps could be omitted and the next step, the addition of an excess of oleylamine (50 µl OAm per 1 ml colloidal particle solution) was performed at once. After this the oleylamine-rich solution was allowed to settle for 48 h, followed by a filtration step using a syringe filter (*Rotilabo*, PTFE, unsterile, pore size 0.20 µm, ⌀ 25 mm). After the filtration the

nanoparticles were precipitated via addition of a threefold excess of ethanol or acetone and centrifugation (5 min, $g_n = 10\,000$). The yellow supernatant was discarded and the black precipitate was redispersed in n-hexane to an extend that resulted in a rather concentrated solution. From this solution samples were then taken to investigate the metal concentration via AAS (see 4.1.3). The concentration desired for the spin coating step could subsequently be adjusted by dilution, adding OAm (freshly filtered using a syringe filter) to an extend that preserved an overall concentration of 50 µl OAm per 1 ml colloidal particle solution. The solution thus prepared was stored in the refrigerator and viable for about one to two months.

4.2.3 Spin Coating Procedure

For the spin coating procedure a small excess-volume of the desired particle solution (prepared according to the procedure in 4.2.2) was washed with a threefold excess of ethanol. For the spin coating of one GC substrate 80 µl of particle solution are required, plus some extra volume to compensate for losses due to wetting of the *Eppendorf* tube and the pipette tip. Therefore a volume of 90 µl was usually employed and, consequentially, washed with 270 µl of ethanol. This mixture was then centrifuged for 5 min at $g_n = 10\,000$, the light yellow supernatant discarded and the black precipitate redispersed in 90 µl toluene. The solution was left to settle for at least 15 min and then washed and centrifuged once more under the same conditions as before. The black precipitate again was redispersed in 90 µl toluene. A freshly polished glassy carbon disk (see 4.2.1) was then mounted on the stub of a *Spincoat G3P-8* from *Specialty Coating Systems*. Prior to the coating with particles the GC was cleaned once more by completely covering it with toluene and starting program 1 (see table 4.2), adding a jet of another 1 ml of toluene during the rotation. Using an *Eppendorf* pipette 80 µl of the prepared particle solution was then deposited onto the surface of the GC disk, forming a drop that covered the surface area wholly. Immediately afterwards program 1 was started again. After the deposition of the particle film the GCE was then exposed to any desired treatment (see 4.3 before it was either directly used in a CV experiment or first covered with a Nafion coating and afterwards electrochemically investigated. Depending on whether or not a Nafion coating was desired, 80 µl Nafion solution (5 wt% in MeOH), generally diluted 1:9 with MeOH, was carefully applied to the GC disk without touching the particle coated surface with the nozzle of the pipette, directly followed by starting program 1 once more. If desired, an investigation of the thus prepared GCEs could be performed at any point of the GCE preparation using SEM. The employed scanning electron microscope was a *Leo 1550 Gemini* from *Zeiss*

Table 4.2: Employed spin coating programs.

program	ramp	rotational speed	duration	use
	[s]	[rpm]	[s]	
1	1.0	4000	30	coating (NPs and Nafion)
2	1.0	2000	30	coating (Nafion)
3	2.0	2000	600	ligand exchange (see 4.3.4)

with a field emitter and was equipped with EDX (Si(Li) detector) and WDX *Inca* from *Oxford Instruments*.

Thickness of Nafion coating In order to investigate the thickness, smoothness and homogeneity of the Nafion film different degrees of Nafion dilution (1:2, 1:9 and 1:49), as well as different rotational speeds (2000 and 4000 rpm) were investigated. This was done without prior coating with particles, directly after the toluene cleaning step. The thus generated films were then investigated via atomic force microscopy by carefully scratching the film with the tip of 27-gauge needle and measuring in the region of the resulting edge. The employed atomic force microscope was a *Nanowizard II* from *JPK Instruments* with the standard accessories and the included *JPK Software - release 4.2*.

4.3 Treatments for Ligand Removal

The nanoparticles synthesized according to the procedures described in 4.1.1 and 4.1.2 are stabilized by the ligands oleylamine and oleic acid. For catalytic applications the removal of those ligands might be favorable, which is why different treatments for ligand removal were investigated. The treatments were all applied after preparation of the respective composite electrode but before the application of Nafion. Every thus prepared composite electrode was investigated via SEM (see 4.2.3) prior to and after the treatment, as well as after the respective CV experiment. For some of the treatments some additional characterization measurements were conducted. Those are described in the following.

TEM and EDX These investigations were conducted for the plasma and the UV/ozone treatment as well as for the untreated particles. A solution of PtNi-2 (7.3 nm, 48:52 (Pt:Ni)) prepared according to the procedure introduced in 4.2.2 was diluted

with toluene until it appeared transparent and then a droplet of the solution was deposited onto a carbon-coated copper grid. Excessive solution was sucked away with a filter paper and the grid was left to dry in air. The sample denoted as "untreated" was then investigated as it was, whereas the other two grids were subjected to the plasma and UV/ozone treatment described in 4.3.3 and 4.3.5, respectively. For this investigation a *Jeol JEM-2200FS* transmission electron microscope with *CETCOR* and *CESCOR* correctors and equipped with a *Jeol JED-2300* detector was used. The X-ray lines chosen for analysis of the EDX spectrum were the O-K, Ni-K and Pt-M line.

XPS   X-ray photoelectron spectroscopy analysis was performed at the *Center of Smart Interfaces* at the *TU Darmstadt* by J. Klett. It was done using a hemispherical analyzer (*Phoibos* 150), which was operated in combination with a high-resolution monochromatic Al-Kα X-ray source at 1486.74 eV (*SPECS GmbH*). All photoelectron peaks were fitted by Gauss-Lorentz functions after subtraction of a Shirley-type background. For the evaluation of the spectra a dedicated software package (*CasaXPS* from *Casa Software Ltd.*) was used, which had already built-in sensitivity factors for the quantitative analysis of the surface composition. The spectrometer itself was calibrated to the Fermi edge of a clean Ag foil assigned to a binding energy of 0 eV.

TGA   To investigate to which extend OAm and OA decompose during heating under atmospheric conditions and thus gain insight into the effect of the furnace treatment (see 4.3.2) a thermogravimetric analysis was carried out. For this an appropriate volume of colloidal particle solution (approx. 2 to 5 ml) was prepared in the same way as it would be prepared for its use in the spin coating of a GCE (see 4.2.2 and 4.2.3). After the second EtOH washing step of the previously prepared OAm rich particle solution, the black precipitate is dried in a nitrogen flow and then moved to a drying oven (70 °C for at least 2 h) to get rid of rest solvent. The dried particles are then transferred into an alumina crucible, weighed and analyzed using a *TG 209 F1* instrument from *Netzsch*. The mass of particles used for a typical TGA experiment was approx. 5 mg.

4.3.1   Untreated

Untreated composite electrodes were deployed without any further treatment, thus permitting an assessment of the effectiveness of the other treatments.

4.3.2 Furnace

Treatment in the muffle furnace consisted of treating the composite electrode at 185 °C for 5 h under atmospheric conditions. This approach was first described by Li *et al.* to remove OAm from pure Pt nanoparticles.(11)

4.3.3 Plasma

Plasma treatment was carried out using a *Plasma ACE 1* bench top instrument from *Gala Instrumente* to generate an oxygen plasma. The prepared composite electrodes were treated for 2 min at 50 W with a pressure of 31 to 33 Pa.

4.3.4 Ligand Exchange with TBAOH/MeOH

The ligand exchange with tetrabutylammonium hydroxide and MeOH is based on a method first described by Scheele *et al.*(127) For it a 1.0 M solution of TBAOH in MeOH is diluted 1:99 with MeOH, thus giving a 10 mM solution. 80 µl of this solution are applied dropwise to a ready-made composite electrode rotating with a speed of 2000 rpm (program 3, see table 4.2). Successively 80 µl of each MeOH and then toluene were applied in a dropwise fashion also, still rotating the composite electrode with a speed of 2000 rpm. After the addition of the last of the solutions the spin coating program 3 was left running for another 30 s to evaporate the last of the toluene, leaving the respective composite electrode ready for use.

4.3.5 UV/Ozone

UV/ozone treatment consisted of exposing the respective composite electrode to the conditions of a custom-made UV/ozone chamber for 10 min. The chamber consisted of a low pressure mercury lamp (*Pen-Ray* from *UVP*) emitting at 254 nm in an aluminum box. The sample sat approx. 4 cm below the lamp.

4.3.6 Vacuum Furnace

This treatment was applied using a *Heraeus* vacuum tube furnace with a panel from *Grabosch König* and a temperature control module from *Enda*. The prepared GCEs were treated at 120 °C for 1 h and then cool to room temperature under vacuum conditions.

Table 4.3: 5-step method for polishing platinum.

step	cloth	abrasive	grain size	time
1	CarbiMet	P1000 SiC	15.3 µm	until flat
2	CarbiMet	P4000 SiC	5.5 µm	until smooth
3	TexMet C	MetaDi Supreme diamond suspension	3 µm	5 min
4	TexMet C	MetaDi Supreme diamond suspension	1 µm	5 min
5	ChemoMet	MasterPrep Al_2O_3 suspension	0.05 µm	3 min

4.4 Polishing and Cleaning of Platinum bulk

A bulk piece of polycrystalline platinum (thickness: approx. 2 mm, diameter: approx. 3 cm) was used for comparative electrochemical measurements. Like the glassy carbon substrates, this bulk piece of platinum needed to be polished prior to it's investigation via cyclic voltammetry. The polishing procedure followed here is based on the "5-step method for polishing noble metals" from *Buehler* (143). Depending on the quality of the surface finish five, three or no polishing steps were applied. In case of gross scratches or defects the polishing started with step 1 (see table 4.3) and all 5 steps were applied successively. Small defects on the other hand were treated by applying only the last three polishing steps (step 3, 4 and 5, see table 4.3). If the surface exhibited a mirror finish no polishing was necessary and only the cleaning step describes below was performed. All polishing materials were acquired from *Buehler*. An overview of the utilized polishing cloths and abrasives is given in table 4.3. In contrast to the polishing of glassy carbon the pressure applied during the polishing of platinum needs to be quite low, since otherwise the surface is easily scratched due to it's softness. Apart from that the polishing procedure followed the routine that was described in 4.2.1. Directly prior to it's use in electrochemical measurements the polished bulk piece of platinum was cleaned in a mixture of 50 mL deionized water, 10 mL ammonia (30 %) and 10 mL hydrogen peroxide (25 %) ("RCA clean") at a temperature of approx. 60 °C for 10 min whilst stirring. The platinum substrate was then transferred into a beaker with deion-

ized water and stored there until it was ready to be placed in the electrochemical cell, whereupon it was dried carefully using precision wipes and covered with electrolyte as quickly as possible.

4.5 Electrochemical Investigations

All potentials in this work are referenced to the RHE unless stated otherwise. In order to determine the electrocatalytic properties of each composite electrode they were investigated via cyclic voltammetry. The information gained from those experiments allows the calculation of the electrochemically active surface area (see 2.2.3 for theoretical background information) and the catalytic activity. The ECSA is determined via integration of the obtained cyclic voltammogram in the H_{upd} region between 0.05 and 0.40 V vs. RHE after subtraction of the capacitive contributions to the current. The ECSA in this work is always reported as the average value obtained from the anodic and cathodic part of the voltammogram, respectively. After the completion of the CV experiment the composite electrodes were carefully removed from the cell, rinsed with deionized water and then submitted to a aqua regia digestion to subsequently analyze the respective metal concentration via AAS. In case a Nafion coating was present this was dissolved prior to the aqua regia digestion by sonication in a 1:1 mixture of water and methanol. The residue of this solvent was then exposed to an aqua regia digestion as well and also analyzed via AAS to make sure no electrocatalyst was lost this way. Of the total amount of platinum and nickel determined via AAS, 68 % were finally assigned to have taken part in the electrochemical conversion, because only 68 % of the GCEs surface were exposed to the electrolyte. The outer 32 % are covered by an O-ring (see 4.5.1, especially figure 4.1).

4.5.1 Experimental Set-Up

The electrochemical cell used for CV experiments was acquired from *Amel Electrochemistry* and is shown in figure 4.1.It is made of acrylic resin and therefore was only cleaned by wiping it down with water or isopropyl alcohol. As counter electrode a platinized Nb-mesh was used, the reference electrode was a saturated calomel electrode fitted into a Haber-Luggin capillary. A two-way gas bubbler was attached to provide nitrogen. The potentiostat used in this work was an *IviumStat* from *Ivium Technologies*. Analyses were done using *IviumSoft - Release* 1.807 and *Origin 9.0G*.
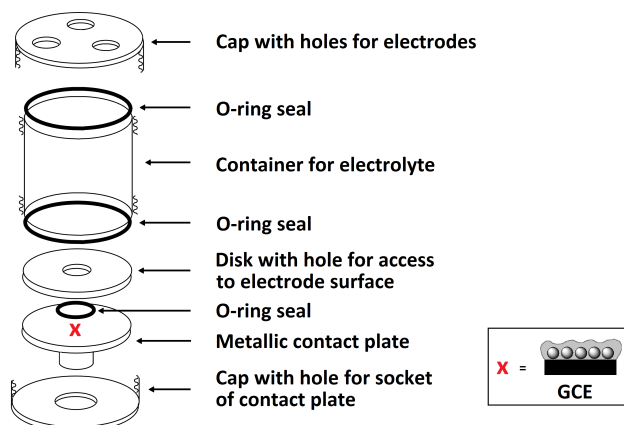
Figure 4.1: Schematic of the electrochemical cell used in this work. The red x indicates at which place the glassy carbon electrode is fitted into the set-up.

4.5.2 Experimental Procedure

The electrochemical cell was assembled directly prior to each experiment, making sure that the respective glassy carbon electrode was centered in respect to the O-ring pressing down on it, thus tightly holding it in place. The cell was then filled with approx. 150 mL 0.5 M sulfuric acid and flushed with nitrogen for a minimum of 12 min. Afterwards, the Haber-Luggin capillary was filled with the deoxygenate solution with the help of a Peleus ball and the chosen CV program was started, keeping the cell under a nitrogen atmosphere for the duration of the measurement. After the recording of the voltammogram of the GCE in sulfuric acid (ECSA measurement) the electrolyte was removed from the cell. It was dried with paper towels and approx. 150 mL of a 0.5 M MeOH and sulfuric acid solution was filled in to conduct the MOR measurement, again flushing the cell with nitrogen for a minimum of 12 min and keeping it under nitrogen during the time of the measurement. After the ECSA and MOR measurements were completed a third measurement (ECSA2 measurement), again using approx. 150 mL 0.5 M sulfuric acid as electrolyte, was performed. For this measurement the sulfuric acid from the first round was used again, freshly flushing the cell with nitrogen for a minimum of 12 min and keeping it under nitrogen during the measurement.

4.5.3 Cyclic Voltammetry Program

Cyclic voltammetry experiments were done using the *IviumSoft - release* 1.807 or 2.471 software from *Ivium Technologies*. As method "cyclic voltammetry" with either "standard" or "current averaging" (CAv) was chosen. The exact experimental conditions are

Table 4.4: Electrochemical cleaning sequence at the beginning of each measurement. Potentials are given vs. SCE. The parameters "filter" and "stability" are set to automatic.

type	scan rate [V/s]	N_{scans}	E_{step} [mV]	current range [mA]	time [s]	potential [V]
APT-1	-	-	-	-	60	-0.2440
CV-ECC	0.5	90	5	10	-	-
APT	-	-	-	-	1	-0.2440
CV-ECC(b)	0.5	45	5	10	-	-
APT	-	-	-	-	1	-0.2440
CV-ECC(c)	0.1	15	2	1	-	-

specified in the paragraphs below for each of the electrochemical investigations discussed in chapter 3. Generally, each measurement (ECSA, MOR and ECSA2 measurement) started with some fast potential cycling between $-0.2440\,V$ and $0.9560\,V$ vs. SCE to clean the electrode surface and achieve a stable voltammogram. An overview of the electrochemical cleaning sequence is given in table 4.4. E(start), the initial potential, is $-0.2440\,V$ vs. SCE in each case, following directly from an amperometric pretreatment (APT) at that potential. This pretreatment can be chosen in the "method" menu, which provides options for setting time and potential, and was applied prior to each new cyclic voltammetry measurement. All desired experiments are done directly following the electrochemical cleaning sequence introduced in table 4.4. The settings of a typical measurement to determine the ECSA of the investigated electrode are given in table 4.5. When conducting an MOR experiment the settings chosen are the same, except for the parameter "current range" which is kept at $10\,mV$ for all measurements. Each measurement (ECSA, MOR and ECSA2) was run using "batch mode", which allowed the programming of different measurements as a sequence.

Investigation into Treatments For this investigation two sets of particles were employed: PtNi-1 ($2.4\,nm$, 93:7 (Pt:Ni)) and PtNi-2 ($7.3\,nm$, 48:52 (Pt:Ni)). The colloidal particle solutions used for GCE preparation were adjusted to each have a concentration of approx. $2\,g\,L^{-1}$ in regard to the sum of the mass of platinum and nickel, both. The electrochemical investigations into the influence of the different treatments (see 4.3) on the ECSA and catalytic activity of the employed PtNi electrocatalyst followed the above stated process and settings. After the first 150 fast cleaning cycles

Table 4.5: Settings of a typical experiment to determine the ECSA. Potentials are given vs. SCE. It is important that "current averaging" is selected or an appropriate E(step) value in combination with "high stability" is chosen for this kind of investigation.

E(start):	$-0.2440\,\text{V}$	Scan rate:	$0.05\,\text{V s}^{-1}$
Vertex 1:	$+0.9560\,\text{V}$	Equilibration time:	$0\,\text{s}$
Vertex 2:	$-0.2440\,\text{V}$	Current Range:	$1\,\text{mA}$
E(step):	$1\,\text{mV}$	Filter:	automatic
N(scans):	5	Stability:	automatic

Table 4.6: Electrochemical settings for each of the four conducted measurements following the 150 fast cleaning cycles described in table 4.4.

No.	type	scan rate [V/s]	N_{scans}	E_{step} [mV]	filter	stability
1	CV-Standard	0.15	5	5	automatic	automatic
2	CV-CAv	0.15	5	3	automatic	automatic
3	CV-CAv	0.05	5	1	automatic	automatic
4	CV-Standard	0.05	5	1	automatic	high stability

4×5 (20) cycles were recorded with the settings comprised in table 4.6. Prior to each of this measurements an APT ($-0.2440\,\text{V}$ for $1\,\text{s}$) was applied. This sequence of 150 fast cleaning cycles followed by another 20 cycles with the settings from table table 4.6 was applied three times to each GCE (with the minor modification of "current range" for the MOR that was mentioned above), once in $0.5\,\text{M}$ sulfuric acid as electrolyte (ECSA), then in $0.5\,\text{M}$ MeOH and sulfuric acid solution (MOR), and again in $0.5\,\text{M}$ sulfuric acid (ECSA2). Each of these measurements consisted of 170 cycles leading to a total number of 510 cycles each of the investigated GCEs was subjected to. The cyclic voltammograms and values obtained from these that are discussed in 3.4 are either from the ECC phase (first 150 cycles, denoted "fast cleaning cycles") or obtained from the fifth cycle recorded for the CV-CAv measurement at $0.05\,\text{V s}^{-1}$ (No. 3) from table 4.6 unless stated otherwise. For the latter case that means that for the ECSA the 165th cycle is discussed and for the MOR the 335 cycle (170 of which were recorded in $0.5\,\text{M}$ sulfuric acid prior to the MOR measurement). SEM images of the GCEs were recorded directly after the each treatment and then again after the CV experiment, i.e. after 510 cycles. In order to clean the GCEs of electrolyte and to avoid a change in the

surface arrangement due to drying effects the GCEs were spin-coated with millipore water immediately (while still wet) after they were removed from the cell.

Investigation into Catalyst Stability   For the investigation into the catalyst degradation two sets of particles were employed: PtNi-1 (2.4 nm, 93:7 (Pt:Ni)) and PtNi-6 (7.7 nm, 49:51 (Pt:Ni)). For each particle batch an untreated an a plasma treated GCE prepared from a colloidal particle solution with approx. $2\,\mathrm{g\,L^{-1}}$ in regard to the sum of the mass of platinum and nickel, both, were examined. The electrochemical investigation started with an amperometric pretreatment (APT-1, see above). Then 10 000 potential cycles were measured according to the settings No. 3 in table 4.6 in 10 sets of 1000 cycles programmed in batch mode. After the first 1000 cycles each consecutive set was started with a short amperometric pretreatment (APT, see above). The results of this investigation are shown in figures 3.42 and 3.43. For the SEM measurements a set of fresh electrodes with PtNi-6 was prepared. One GCE was treated in a plasma, while the other one was left untreated. Both GCEs were then again subjected to APT-1 and an electrochemical potential cycling over 10 000 cycles with an intermediate short APT prior to each consecutive measurement of 1000 cycles. In this case, however, the GCE was investigated via SEM at certain points of the electrochemical measurement. SEM measurements were conducted after the pretreatment, after cycles 1, 2, 3, 4, 5, 10, 30, 60, 90, 135, 150, 450, 1000 (only for the plasma treated GCE), 2000, 4000, 6000, and 8000. No amperometric pretreatment was applied additionally to the ones at the beginning of each 1000 cycles. In order to clean the GCEs of electrolyte and to avoid a change in the surface arrangement due to drying effects the GCEs were spin-coated with millipore water immediately (while still wet) after they were removed from the cell. For the substrate-only plasma treated GCE a freshly polished GC substrate (see 4.2.1) was subjected to the plasma treatment (see 4.3.3) and then spin coated with particles (PtNi-6). Afterwards, the GCE was electrochemically investigated according to the procedure described above (without simultaneous SEM investigation).

Comparison of Nanoparticles   For the comparison of nanoparticles with different size or composition OAm-rich solutions were freshly prepared prior to the experiment according to the procedure described in 4.2.2. The colloidal particle solutions were adjusted to each have a concentration of approx. $2\,\mathrm{g\,L^{-1}}$ in regard to the sum of the mass of platinum and nickel, both. An overview over the employed particle batches and their characteristics is given in table A.2 in 3.6. The spin coating procedure followed the description given in 4.2.3 including the addition of Nafion diluted 1:9 with MeOH.

No treatment was applied in any case. The electrochemical investigation followed the general procedure given in "Investigation into Treatments" described above.

Influence of Particle Concentration   For the investigation into the influence of the concentration of the colloidal particle solution used to prepare the GCEs particles of the batch PtNi-1 with a diameter of 2.4 nm and a composition of 93:7 (Pt:Ni) were used. The concentration of the initial OAm-rich solution (prepared according to the procedure given in 4.2.2) was $1.6\,\mathrm{g\,L^{-1}}$ in regard to the sum of the mass of platinum and nickel, both. A sufficient volume of this solution was washed with a threefold excess of ethanol and the volumes for the preparation of the desired concentrations then transferred into individual centrifugation tubes. Each of these aliquots was washed again with a threefold excess of ethanol and the black precipitate then each time redispersed in 110 mL toluene. An overview of the prepared concentrations and the volumes of solution used to obtain them is given in table 3.22 in 3.7.2. The spin coating procedure followed the description given in 4.2.3 including the addition of Nafion diluted 1:9 with MeOH. No treatment was applied in any case. The electrochemical investigation followed the general procedure given in "Investigation into Treatments" described above.

5

Summary

In this work PtNi nanoparticles stabilized by oleylamine (OAm) and oleic acid (OA) ligands were investigated with respect to their electrocatalytic properties regarding the methanol oxidation reaction (MOR), the anode reaction of the direct methanol fuel cell (DMFC). The goal was to investigate the dependency of the catalytic activity on size and composition of the employed particles. For that purpose PtNi nanoparticles that are comparable in one of those properties but different in the other were synthesized. This was achieved by advancing the existing hot injection (HI) approach(117), which exhibited a strictly linear size-to-composition dependency, through a variation of the reaction parameters, mainly the ligand-to-precursor ratio and the nickel-to-platinum precursor ratio. Furthermore, the existing continuous injection (CI) strategy(118) was improved by continuously injecting only one of the two metallic precursors instead of a mixture of both. In additionally varying the above mentioned reaction parameters this approach yielded PtNi nanoparticles that broadened the previously obtainable size and composition regime and lead to pairs of comparable particles.

To examine nanoparticles in regard to their catalytic activity they need to be applied to a conductive substrate, which can be set up as the working electrode in a cyclic voltammetry (CV) experiment. Therefore, an electrode preparation that allowed an accurate and reproducible investigation of the electrocatalytic activity of the synthesized particles had to be conceived next. The MOR is very sensitive to many factors,(90) so in order to minimize possible influences of constituents other than the PtNi particles employed as electrocatalyst, a set-up consisting of as few components as possible was developed. To that end, instead of employing the respective nanoparticles supported on carbon black, mixed or covered with Nafion, on a glassy carbon (GC) substrate as the usual means of electrode preparation,(144) in this work the nanoparticles were spin coated directly onto the GC substrate forming a mono-layered particle film. The

resulting glassy carbon electrode (GCE) is composed of only two components, the electrocatalyst and its support, thus strongly reducing the complexity of the set-up. In addition, the chosen electrode preparation lead to flat electrodes, permitting an investigation of the GCEs via scanning electron microscopy (SEM), which provided information about the behavior of the electrocatalytic particle film at different stages of the electrochemical investigation. In this context a strong agglomeration of the individual nanoparticles was observed under potential cycling in an electrochemical environment. For that reason, the application of Nafion via spin coating to the simple two-component GCEs was examined and it was shown by SEM that this modification stabilized the particle film substantially.

The agglomeration of the electrocatalytic PtNi nanoparticles was further investigated in regard to different treatments for ligand removal. Particles from solution synthesis posses many favorable properties with respect to their use in catalytic applications, such as a narrow size distribution, a homogeneous composition and morphology, as well as a broadly tunable size and composition range.(10) However, their ligands block active sites on the particle surface, thus decreasing the possible catalytic turnover number of each particle. Therefore, approaches to remove the ligands from nanoparticles obtained from solution synthesis are of interest.(11) The methods for ligand removal examined in this work were ligand exchange with tetrabutylammonium hydroxide (TBAOH) in methanol, treatment in a muffle furnace, plasma treatment, UV/ozone treatment, and treatment in a vacuum furnace. Additionally, untreated particles were examined as a reference.

The investigation was carried out for two sets of PtNi particles with very different characteristics - one batch of small (d = 2.4 nm) Pt-rich (93:7, Pt:Ni) nanoparticles and another one of rather large (d = 7.3 nm) alloy (48:52, Pt:Ni) nanoparticles. The electrochemical examination of these particles consisted of conducting CV experiments in sulfuric acid and sulfuric acid under the addition of methanol to determine the electrochemical surface area (ECSA) and the catalytic activity of the particles for the MOR, respectively. Moreover, each investigations was executed once with a Nafion-free, two-component GCE and once with a Nafion-covered GCE. The above mentioned stabilizing effect of the Nafion coating with respect to the particle film was apparent for all treatments. Additionally, a highly treatment-dependent degree of agglomeration of the catalytic nanoparticles was observed, which was strongest for the plasma treatment and weakest for the untreated GCEs. As expected, agglomeration decreased the observed ECSA of a GCE but the formation of agglomerates had a positive effect in regard to catalytic activity in some cases. This phenomenon has also been reported in

the literature,(13) where awareness for the importance of following changes of the electrocatalyst under electrochemical conditions is recently growing.(104) The best results with respect to catalytic activity were found to be different for the two investigated particle sets. For the small and Pt-rich particles the furnace treatment yield the best results, whereas for the larger alloy nanoparticles the GCEs subjected to the UV/ozone and the stronger oxidizing plasma treatment exhibit the best catalytic activities. In comparing the two sets of nanoparticles an approximately threefold higher catalytic activity was found for the larger alloy nanoparticles than for the smaller Pt-rich ones, independently of the treatment.

In order to investigate the influence of the different treatments on the particles itself, transmission electron microscopy (TEM) and energy dispersive X-ray (EDX) measurements were performed. These clearly showed the success of the ligand removal for the UV/ozone and plasma treatment investigated here, and an increasing oxidation in the order untreated < UV/ozone < plasma.

An X-ray photoelectron spectroscopy (XPS) investigation performed by a cooperation partner at the *Center of Smart Interfaces* at the *TU Darmstadt* additionally showed that both platinum and nickel were oxidized under the plasma treatment but a successive reduction took place under electrochemical conditions. Furthermore, a decrease in the Pt-content was observed in connection with the plasma treatment, which was attributed to a preferential sputtering of platinum during this treatment due to a segregation in the respective nanoparticles that lead to a higher Pt-content in the outer atomic layers of the particles. This assumption was supported by Monte-Carlo simulations of disordered fcc cubo-octahedral PtNi nanoparticles(132) on the one hand and by an EDX element mapping performed with the respective particles on the other. In connection with the electrochemical measurements performed a Ni-leaching was moreover observed, which is stronger for the plasma treated particles than for the untreated ones, supporting the theory of a preferential sputtering of platinum due to its enrichment in the outer layers of the investigated particles. The resulting nickel enriched surface consequentially exhibits stronger Ni-leaching than the platinum enriched surface of the untreated particles. The dissolution of nickel from PtNi nanoparticles during electrochemical measurements has been reported previously and the resulting Pt-rich surface of the nanoparticles has been termed "skeleton structure".(94)

With respect to the furnace treatment a thermogravimetric analysis (TGA) revealed that the chosen temperature of $185\,°C$ applied over $5\,h$ in air was sufficient to remove almost the whole amount of thermally decomposable constituents (ligands and possible residual solvent) that contributed to a mass change in the temperature interval from room temperature to $800\,°C$.

An important characteristic of each electrocatalyst is its stability in an electrochemical environment. For that reason, long term measurements were conducted with two sets of PtNi nanoparticles (small Pt-rich in contrast to larger alloy PtNi nanoparticles, as was the case for the investigation into treatments for ligand removal) and for the two most contrary treatments, the plasma treatment on the one hand and no treatment on the other. As a parameter of stability the ECSA of the respective GCEs was recorded over 10 000 potential cycles, each. The results obtained from this investigation showed a development that was characteristic with respect to the applied treatment only over the first few hundred cycles. After that an exponential decrease of the ECSA was observed, independently of the treatment or the particle batch. The values found for the ECSA after 10 000 cycles were overall higher in case of the larger alloy nanoparticles. For both particle sets, however, a higher value was obtained for the plasma treated GCE in comparison with the untreated GCE. To gain further insight in this phenomenon an investigation with a plasma treated GC substrate covered with a particle film of untreated nanoparticles was electrochemically examined. For this substrate-only plasma treated GCE the initial part of the curve was similar to that of the respective untreated GCE. However, between 3500 and 4000 cycles the development of the ECSA of the substrate-only plasma treated GCE became similar to that of the plasma treated GCE. This indicates that in regard to long term stability the substrate dominates the electrode stability, whereas in the short run the particles properties are dominant. SEM images recorded at the end of the measurements showed almost perfectly round, smooth agglomerates of approx. 10 to 20 nm next to some elongated forms.

The development of the agglomeration in this long term investigations was comparable at first to that observed in connection with the investigation into treatments for ligand removal. It set in slowly in case of the untreated GCE, whereas it was immediately apparent for the plasma treated GCE. Interestingly, a GCE that accidentally was oxidized due to an air bubble in the connecting part (Haber-Luggin capillary) of the electrochemical cell set-up between working and reference electrode, leading to an overmodulation of the potentiostat, showed by far the highest value for the ECSA at the end of the long term investigation. This result was echoed in the SEM images obtained at the end of this measurement, where the presence of far more electrocatalyst was observed than was found for the other measurements. The effect assumed to be responsible for the enhanced stability observed for the oxidized GCEs (be it by plasma treatment or due to an accidental electrochemical oxidation) is the surface roughening of the GC substrate that accompanies its oxidation.(129) This surface roughening may cause stronger interactions between electrocatalyst and substrate due to a potentially larger contact area between the two. Furthermore, it has been shown that graphitized

carbons show better corrosion resistance than non-graphitized substrates(137) and it is feasible that the accidental oxidation of the GCE and the subsequent potential cycling lead to a graphitization that incorporated the electrocatalyst in its structure thus stabilizing it. This explanation may, in an alleviated form, also hold for the enhanced stability of the plasma treated GCEs as compared to the untreated ones.

Last but not least, an investigation of multiple sets of the aforementioned comparable nanoparticles was. For this purpose, untreated, Nafion-coated GCEs of the respective nanoparticles were prepared in order to retain the particulate structure of the electrocatalyst as much as possible by suppressing agglomeration. To ascertain the order of magnitude to be expected for the deviations between particle batches comparable in regard to size and composition, in a first experiment three particle sets that were comparable in both properties in question were examined. One of this three sets, however, consisted of nanoparticles exhibiting a different shape (non-spherical) as the other two. From the performed CV experiments a similar specific activity (deviation of 15 %) for the nanoparticle batches that were comparable in size, composition, and shape was observed, whereas for the non-spherical particles a much lower specific activity (deviation of approx. 80 % compared to the other two batches) was found, indicating the importance of particle morphology on catalytic activity. Next, an array of spherical nanoparticles that were comparable in one of the two properties, size or composition, but differed in the other, were examined. Nanoparticles were declared to be comparable in the respective property if the deviation of the respective values was smaller than 7.5 % of the lower value. A sufficient difference with respect to the second property was defined to be reached at a deviation of 22.5 % of the larger value. The specific activities determined in this investigation were all found within a surprisingly small range (approx. 100 to 600 $\mu A\,cm^{-2}$), which was even exceeded by the value found for the non-spherical particles mentioned above. This result agrees well with the report of an investigation into PtNi nanoparticles in regard to their composition-dependent catalytic activity for the oxygen reduction reaction (ORR),(94) the cathode reaction of a DMFC. Nonetheless, a clear trend could be deduced from the experiments conducted in this work, namely an increase in catalytic activity with particle size and nickel content. The highest catalytic activity was thus observed for nanoparticles with a diameter of 7.3 nm and a nickel content of 52 %.

Summarizing the results of the different investigations performed in this work leads to the realization of how important it is to closely follow changes in the electrocatalyst during its electrochemical examination. A nanostructured electrocatalyst constitute a very dynamic system that can greatly change with respect to shape and size (agglomeration), composition (Ni-leaching), and structure (formation of platinum skeleton

structure) under electrochemical conditions. In order to attribute certain parameters, such as catalytic activity, specificity, or stability to a nanostructured catalyst it is therefore necessary to determine the modifications this catalyst underwent in context with the performed electrochemical measurements. In addition, pretreatments, which are commonly applied to particles from solution synthesis to free active sites on the particle surface from ligands, may induce changes in the electrocatalyst as well. The flat electrode developed in this work to examine PtNi nanoparticles electrochemically is excellently suited to this task, since it allows the performance of SEM measurements at different stages of the electrochemical experiment, thus providing insight into the phenomenon of agglomeration. As could be shown in this work, agglomeration of particles is a very important process in connection with many factors determining an electrocatalytic system and might effectively lead to positive results in regard to catalytic activity.

Bibliography

[1] Verne, J. *The Mysterious Island*, 1874. 1

[2] Grove, W. *The London, Edinburgh and Dublin Phylosophical Magazine and Journal os Science* **1842**, *21*, 417–420. 1

[3] Kurzweil, P. *Brennstoffzellentechnik - Grundlagen, Komponenten, Systeme, Anwendungen*; Springer: Wiesbaden, 2013. 1

[4] Porter, N. S.; Wu, H.; Quan, Z.; Fang, J. *Accounts of Chemical Research* **2013**, *46*, 1867–1877. 1

[5] Liu, H.; Song, C.; Zhang, L.; Zhang, J.; Wang, H.; Wilkinson, D. P. *Journal of Power Sources* **2006**, *155*, 95–110. 1, 2, 29, 30, 31, 32

[6] Antolini, E.; Salgado, J. R.; Gonzalez, E. R. *Applied Catalysis B: Environmental* **2006**, *63*, 137–149. 1, 24, 28, 29, 31, 33

[7] Bandarenka, A. S.; Ventosa, E.; Maljusch, A.; Masa, J.; Schuhmann, W. *The Analyst* **2014**, *139*, 1274–91. 1, 28

[8] Zhong, C.-J.; Luo, J.; Njoki, P. N.; Mott, D.; Wanjala, B.; Loukrakpam, R.; Lim, S.; Wang, L.; Fang, B.; Xu, Z. *Energy & Environmental Science* **2008**, *1*, 454–466. 2, 32, 33

[9] Antolini, E. *Materials Chemistry and Physics* **2003**, *78*, PII S0254–0584(02)00389–9. 2, 32, 33

[10] Peng, Z.; Yang, H. *Nano Today* **2009**, *4*, 143–164. 2, 33, 35, 160

[11] Li, D.; Wang, C.; Tripkovic, D.; Sun, S.; Markovic, N. M.; Stamenkovic, V. R. *ACS Catal.* **2012**, *2*, 1358–1362. 2, 33, 41, 66, 150, 160

[12] Park, K.-W.; Choi, J.-H.; Kwon, B.-K.; Lee, S.-A.; Sung, Y.-E. *J. Phys. Chem. B* **2002**, *106*, 1869–1877. 2, 28, 30, 41, 98, 126

[13] Maillard, F.; Schreier, S.; Hanzlik, M.; Savinova, E. R.; Weinkauf, S.; Stimming, U. *Physical Chemistry Chemical Physics* **2005**, *7*, 385–393. 2, 34, 54, 161

BIBLIOGRAPHY

[14] Zhong, C.-J.; Luo, J.; Fang, B.; Wanjala, B. N.; Njoki, P. N.; Loukrakpam, R.; Yin, J. *Nanotechnology* **2010**, *21*, 1–20. 2, 32, 33, 34, 41

[15] Sawyer, D. T.; Sobkowiak, A.; Roberts Jr., J. L. *Electrochemistry for Chemists*, 2nd ed.; John Wiley and Sons, Inc.: New York, 1995. 3

[16] Kissinger, P. T. In *Laboratory Techniques in Electroanalytical Chemistry*, 2nd ed.; Kissinger, P. T.; Heineman, W. R., Eds.; Dekker: New York, 1996; Chapter 1, p 4. 3

[17] Kirubakaran, a.; Jain, S.; Nema, R. K. *Renewable and Sustainable Energy Reviews* **2009**, *13*, 2430–2440. 4, 31

[18] Bard, A. J.; Faulkner, L. R. *Electrochemical Methods - Fundamentals and Applications*, 2nd ed.; Harris, D.; Swain, E.; Aiello, E., Eds.; John Wiley and Sons, Inc.: New York, 2001. 4, 10, 11, 14, 16, 18

[19] Hamann, C. H.; Vielstich, W. *Elektrochemie*, 4th ed.; Wiley-VCH: Weinheim, 2005. 4, 11

[20] Faraday, M. *Trans. Roy. Soc. London* **1833**, *123*, 39. 4

[21] Ehl, R. G.; Ihde, A. J. *Journal of Chemical Education* **1954**, *31*, 226. 5

[22] Bagotsky, V. S. *Fundamentals of Electrochemistry*, 2nd ed.; John Wiley and Sons, Inc.: New York, 2006. 7, 18, 19, 27

[23] von Helmholtz, H. L. F. *Ann. Physik* **1879**, *7*, 337. 8

[24] EDLC-simplified-principle, http://commons.wikimedia.org/wiki/File:EDLC-simplified-principle.png, accessed January 14, 2015. 9

[25] Gouy, G. *Compt. Rend.* **1910**, *149*, 654. 8

[26] Chapman, D. L. *Phil. Mag.* **1913**, *25*, 475. 8

[27] Stern, O. *Z. Elecktrochem.* **1924**, *30*, 508. 8

[28] Grahame, D. C. *Chem. Rev.* **1947**, *41*, 441. 8

[29] Bockris, J. O.; Devanthan, M. A. V.; Müller, K. *Proc. R. Soc.* **1963**, *A274*, 55. 8

[30] Damaskin, B. B.; Frumkin, A. N. *Electrochim. Acta* **1974**, *19*, 173. 9

[31] Damaskin, B. B.; Palm, U. V.; Salve, M. A. *Soviet Electrochemistry* **1976**, *12*, 232. 9

[32] Damaskin, B. B. *J. Electroanal. Chem.* **1977**, *75*, 359. 9

[33] Trasatti, S. In *Proceedings of NATO ASI (1984)*; Reidel: Dordrecht; pp 25–48. 9

[34] Parsons, R. *Chem. Rev.* **1990**, *90*, 813. 9

[35] Brett, C. M. A.; Brett, A. M. O. *Electrochemistry: Principles, Methods, and Applications*; Oxford University Press: Oxford, 1994. 9, 15, 16, 17, 18

[36] Maloy, J. T. *Journal of Chemical Education* **1983**, *60*, 285–289. 11

[37] Faulkner, L. R. *Journal of Chemical Education* **1983**, *60*, 262. 11, 28

[38] G. Huttner; *Cyclovoltammetrie im Rahmen des Anorganisch-Chemischen Fortgeschrittenenpraktikums - Universität Heidelberg.* 13, 14

[39] Randles, J. E. B. *Trans. Faraday Soc.* **1948**, *44*, 327. 16

[40] Sevcik, A. *Coll. Czech. Chem. Commun.* **1948**, *13*, 349. 16

[41] Matsuda, H.; Ayabe, Y. *Z. Electrochem.* **1955**, *59*, 494. 17

[42] Markovic, N.; Ross, P. N. *Journal of Electroanalytical Chemistry* **1992**, *330*, 499–520. 19

[43] Kita, H.; Gao, Y.; Nakato, T.; Hattori, H. *Journal of Electroanalytical Chemistry* **1994**, *373*, 177–183. 19

[44] Batista, E. a.; Malpass, G. R. P.; Motheo, a. J.; Iwasita, T. *Journal of Electroanalytical Chemistry* **2004**, *571*, 273–282. 19

[45] Bagotzky, V.; Vassiliev, Y.; Pyshnograeva, I. *Electrochimica Acta* **1971**, *16*, 2141–2167. 19

[46] Clavilier, J.; Lamy, C.; Leger, J. *Journal of Electroanalytical Chemistry and Interfacial Electrochemistry* **1981**, *125*, 249–254. 19

[47] Nart, F.; Iwasita, T.; Weber, M. *Electrochimica Acta* **1994**, *39*, 961–968. 19

[48] Bai, L.; Gao, L.; Conway, B. E. *J. Chem. Soc. FARADAY TRANS.* **1993**, *89*, 235–242. 20

[49] Christensen, P. A.; Hamnett, A. *Techniques and Mechanisms in Electrochemistry*, 1st ed.; Blackie Academic and Professional: London, 1994. 19, 21, 23, 27

[50] Trasatti, S.; Petrii, O. A. *Journal of Electroanalytical Chemistry* **1992**, *327*, 353–376. 20

[51] Angerstein-Kozlowska, H.; Conway, B. E.; Sharp, W. B. A. *Electroanalytical Chemistry and lnterfacial Electrochemistry* **1973**, *43*, 9–36. 21

[52] Iwasita, T. *Electrochimica Acta* **2002**, *47*, 3663–3674. 21, 23, 27

[53] Manoharan, R.; Goodenough, J. B. *J. Mater. Chem.* **1992**, *2*, 875–887. 22, 23, 25, 26

[54] Cao, D.; Lu, G. Q.; Wieckowski, A.; Wasileski, S. a.; Neurock, M. *Journal of Physical Chemistry B* **2005**, *109*, 11622–11633. 21

[55] Samjeské, G.; Miki, A.; Osawa, M. *Journal of Physical Chemistry C* **2007**, *111*, 15074–15083. 22

[56] Braunchweig, B.; Hibbitts, D.; Neurock, M.; Wieckowski, A. *Catalysis Today* **2013**, *202*, 197–209. 22

[57] Chen, W.; Sun, S.-g.; Zhou, Z.-y.; Chen, S.-p. *J. Phys. Chem. B* **2003**, *107*, 9808–9812. 22

[58] Wang, H.; Löffler, T.; Baltruschat, H. *Journal of Applied Electrochemistry* **2001**, *31*, 759–765. 22

[59] Mattsson, T. R.; Paddison, S. J. *Surface Science* **2003**, *544*, L697–L702. 23

[60] Okamoto, Y.; Sugino, O.; Mochizuki, Y.; Ikeshoji, T.; Morikawa, Y. *Chemical Physics Letters* **2003**, *377*, 236–242. 23

[61] Neurock, M.; Wasileski, S.; Mei, D. *Chemical Engineering Science* **2004**, *59*, 4703–4714. 23

[62] Hofstead-Duffy, A. M.; Chen, D.-J.; Sun, S.-G.; Tong, Y. J. *J. Mater. Chem.* **2012**, *22*, 5205–5208. 23

[63] Aricò, A. S., Baglio, V. and Antonucci, V. In *Electrocatalysis of Direct Methanol Fuel Cells: From Fundamentals to Applications Electrocatalysis of Direct Methanol Fuel Cells: From Fundamentals to Applications*; Zhang, H. L.; J., Eds.; Wiley-VCH Verlag GmbH & Co. KGaA: Weinheim, 2009. 24, 30

[64] Pletcher, D.; Solis, V. *Electrochimica Acta* **1982**, *27*, 775–782. 24

[65] Christensen, P.; Hamnett, a.; Troughton, G. *Journal of Electroanalytical Chemistry* **1993**, *362*, 207–218. 24

[66] Stamenkovic, V. R.; Mun, B. S.; Mayrhofer, K. J. J.; Ross, P. N.; Markovic, N. M. *Journal of the American Chemical Society* **2006**, *128*, 8813–8819. 24, 25

[67] Stamenkovic, V. R.; Mun, B. S.; Arenz, M.; Mayrhofer, K. J. J.; Lucas, C. A.; Wang, G.; Ross, P. N.; Markovic, N. M. *Nat. Mater.* **2007**, *6*, 241–247. 24, 25, 81

[68] Wang, G.; Hove, M. A. V.; Ross, P. N.; Baskes, M. I. *Progress in Surface Science* **2005**, *79*, 28–45. 24

[69] Fowler, B.; Lucas, C. A.; Omer, A.; Wang, G.; Stamenkovic, V. R.; Markovic, N. M. *Electrochimica Acta* **2008**, *53*, 6076–6080. 24, 30

[70] Medway, S.; Lucas, C.; Kowal, A.; Nichols, R.; Johnson, D. *Journal of Electroanalytical Chemistry* **2006**, *587*, 172–181. 25

[71] Miao, Y.; Ouyang, L.; Zhou, S.; Xu, L.; Yang, Z.; Xiao, M.; Ouyang, R. *Biosensors and Bioelectronics* **2014**, *53*, 428–439. 26

[72] Prieto, P.; Nistor, V.; Nouneh, K.; Oyama, M.; Abd-lefdil, M.; Díaz, R. *Applied Surface Science* **2012**, *258*, 8807–8813. 26

[73] Atkins, P. *Physical Chemistry*, 3rd ed.; Wiley-VCH, 2001. 26

[74] Guerrini, E.; Trasatti, S. *Russian Journal of Electrochemistry* **2006**, *42*, 1017–1025. 26

[75] Jaksic, M. M. *J. New Mat. Electrochem. Systems* **2000**, *3*, 167–182. 27

[76] Aricò, A. S.; Srinivasan, S.; Antonucci, V. *Fuel Cells* **2001**, *1*, 133–161. 27, 28

[77] Bockris, J. O. M. *Journal of the Serbian Chemical Society* **2005**, *70*, 475–487. 27

[78] Wieckowski, A.; Neurock, M. *Advances in Physical Chemistry* **2011**, *2011*. 27

[79] Munichandraiah, N. *Journal of the Indian Institute of Science* **2010**, *90 (2)*, 261–270. 28

[80] Vielstich, W. In *Handbook of Fuel Cells*; John Wiley \& Sons, 2010. 28

[81] Qi, Z. In *PEM fuel cell electrocatalysts and catalyst layers*, 2008th ed.; Zhang, J., Ed.; Springer: London, 2008; Chapter 11, pp 547–607. 28

[82] Tritsaris, G. A.; Rossmeisl, J. *J. Phys. Chem. C* **2012**, *116*, 11980–11986. 28

[83] Lee, S.-A.; Park, K.-W.; Choi, J.-H.; Kwon, B.-K.; Sung, Y.-E. *Journal of The Electrochemical Society* **2002**, *149*, A1299. 28, 30

[84] Park, K.-W.; Choi, J.-H.; Sung, Y.-E. *J. Phys. Chem. B* **2003**, *107*, 5851–5856. 28, 30, 41

[85] Igarashi, H.; Fujino, T.; Zhu, Y.; Uchida, H.; Watanabe, M. *Phys. Chem. Chem. Phys.* **2001**, *3*, 306–314. 28, 29

[86] Toda, T.; Igarashi, H.; Uchida, H.; Watanabe, M. *Journal of The Electrochemical Society* **1999**, *146*, 3750–3756. 28

[87] Goodenough, J. B.; Manoharan, R.; Shukla, a. K.; Ramesh, K. V. *Chemistry of Materials* **1989**, *1*, 391–398. 28

[88] Wang, X.; Wang, H.; Wang, R.; Wang, Q.; Lei, Z. *Journal of Solid State Electrochemistry* **2012**, *16*, 1049–1054. 29, 31

[89] Prinz, J.; Gaspari, R.; Sto, Q. S.; Gille, P.; Armbru, M.; Brune, H.; Gro, O.; Pignedoli, C. A.; Passerone, D.; Widmer, R. *The Journal of Physical Chemistry C* **2014**, *118*, 12260–12265. 29

[90] Hernandez-Fernandez, P.; Lund, P. B.; Kallesø e, C.; Clausen, H. F.; Christensen, L. H. *International Journal of Hydrogen Energy* **2015**, *40*, 284–291. 30, 159

[91] Jusys, Z.; Kaiser, J.; Behm, R. J. *Langmuir* **2003**, *19*, 6759–6769. 30, 55

[92] Batista, E.; Hoster, H.; Iwasita, T. *Journal of Electroanalytical Chemistry* **2003**, *554-555*, 265–271. 30

[93] Seidel, Y. E.; Schneider, A.; Jusys, Z.; Wickman, B.; Kasemo, B.; Behm, R. J. *Langmuir* **2010**, *26*, 3569–3578. 30, 55

[94] Wang, C.; Chi, M.; Wang, G.; Van Der Vliet, D.; Li, D.; More, K.; Wang, H. H.; Schlueter, J. A.; Markovic, N. M.; Stamenkovic, V. R. *Advanced Functional Materials* **2011**, *21*, 147–152. 30, 126, 132, 161, 163

[95] Liu, F.; Lee, J. Y.; Zhou, W. *Journal of Physical Chemistry B* **2004**, *108*, 17959–17963. 31

[96] Liu, F.; Lee, J. Y.; Zhou, W. J. *Small* **2006**, *2*, 121–128. 31

[97] Hu, Y.; Wu, P.; Yin, Y.; Zhang, H.; Cai, C. *Applied Catalysis B: Environmental* **2012**, *111-112*, 208–217. 31

[98] Hsieh, C.-T.; Lin, J.-Y. *Journal of Power Sources* **2009**, *188*, 347–352. 31

[99] Zhao, Y.; E, Y.; Fan, L.; Qiu, Y.; Yang, S. *Electrochimica Acta* **2007**, *52*, 5873–5878. 31

[100] Tiwari, J. N.; Tiwari, R. N.; Singh, G.; Kim, K. S. *Nano Energy* **2013**, *2*, 553–578. 31

[101] Cohen, J. L.; Volpe, D. J.; Abruña, H. D. *Physical chemistry chemical physics : PCCP* **2007**, *9*, 49–77. 31, 32

[102] Hamnett, A. *Catalysis Today* **1997**, *38*, 445–457. 32

[103] Nichols, G.; Byard, S.; Bloxham, M. J.; Botterill, J.; Dawson, N. J.; Dennis, A.; Diart, V.; North, N. C.; Sherwood, J. D. *Journal of Pharmaceutical Sciences* **2002**, *91*, 2103–2109. 34

[104] Koper, M. T. M. *Nanoscale* **2011**, *3*, 2054–2073. 34, 42, 54, 161

[105] Cherstiouk, O. V.; Gavrilov, a. N.; Plyasova, L. M.; Molina, I. Y.; Tsirlina, G. a.; Savinova, E. R. *Journal of Solid State Electrochemistry* **2008**, *12*, 497–509. 34

[106] Somorjai, G. A. *The Journal of Physical Chemistry B* **2002**, *106*, 9201–9213. 34

[107] Kleijn, S. E. F.; Lai, S. C. S.; Koper, M. T. M.; Unwin, P. R. *Angewandte Chemie - International Edition* **2014**, *53*, 3558–3586. 34, 127

[108] Sun, C. Q.; Tay, B. K.; Zeng, X. T.; Li, S.; Chen, T. P.; Zhou, J.; L.Bai, H.; Jiang, E. Y. *Journal of Physics: Condensed Matter* **2002**, *14*, 7781 – 7795. 34

[109] Zhang, W.; Lu, X. *Nanotechnology Reviews* **2013**, *2*, 487–514. 35

[110] Kwon, S. G.; Hyeon, T. *Small* **2011**, *7*, 2685–2702. 35, 36, 37, 38, 39, 40

[111] Klabunde, K. J. *Nanoscale Materials in Chemistry*, 2nd ed.; Wiley-Interscience: New York, 2009. 36, 37, 40

[112] Peng, X.; Wickham, J.; Alivisatos, a. P. *Journal of the American Chemical Society* **1998**, *120*, 5343–5344. 38

[113] Sugimoto, T. *Advances in Colloid and Interface Science* **1987**, *28*, 65–108. 38

[114] LaMer, V. K.; Dinegar, R. H. *Journal of the American Chemical Society* **1950**, *72*, 4847–4854. 38

[115] Oxtoby, D. W. *Acc. Chem. Res.* **1998**, *31*, 91–97. 38

[116] Oxtoby, D. W. *Journal of Physics: Condensed Matter* **1992**, *4*, 7627–7650. 39

[117] Ahrenstorf, K.; Albrecht, O.; Heller, H.; Kornowski, A.; Görlitz, D.; Weller, H. *small* **2007**, *3*, 271–274. 42, 43, 57, 125, 141, 159

[118] Ahrenstorf, K.; Heller, H.; Kornowski, A.; Broekaert, J. A. C.; Weller, H. *Adv. Funct. Mater.* **2008**, *18*, 3850–3856. 42, 43, 50, 53, 104, 141, 159

[119] K. Ahrenstorf; Ph.D. thesis; Universität Hamburg; 2007. 44, 45, 46, 47, 48, 49, 50, 51, 52, 56, 108

[120] Mayrhofer, K. J. J.; Hanzlik, M.; Arenz, M. *Electrochimica Acta* **2009**, *54*, 5018–5022. 54

[121] McCreery, R. L.; Kline, K. K. In *Laboratory Techniques in Electroanalytical Chemistry*, 2nd ed.; Kissinger, P. T.; Heineman, W. R., Eds.; Dekker: New York, 1996; Chapter 10, pp 317–319. 55, 144

[122] Deegan, R. D.; Bakajin, O.; Dupont, T. F.; Huber, G.; Nagel, S. R.; Witten, T. a. *Nature* **1997**, *389*, 827–829. 55

[123] Nguyen, T. A. H.; Hampton, M. A.; Nguyen, A. V. *Journal of Physical Chemistry C* **2013**, *117*, 4707–4716. 55

[124] Aleksandrovic, V. T.; Ph.D. thesis; University of Hamburg; 2006. 55

[125] Ramirez, E.; Eradès, L.; Philippot, K.; Lecante, P.; Chaudret, B. *Adv. Funct. Mater.* **2007**, *17*, 2219–2228. 56

[126] Lau, C. Y.; Duan, H.; Wang, F.; He, C. B.; Low, H. Y.; Yang, J. K. W. *Langmuir* **2011**, *27*, 3355–3360. 59

[127] Scheele, M.; Engel, J. H.; Ferry, V. E.; Hanifi, D.; Liu, Y.; Alivisatos, a. P. *ACS nano* **2013**, *7*, 6774–81. 66, 150

[128] Barbero, C.; Silber, J. J.; Sereno, L. *Journal of Electroanalytical Chemistry and Interfacial Electrochemistry* **1988**, *248*, 321–340. 70

[129] Maruyama, J.; Abe, I. *Electrochimica Acta* **2001**, *46*, 3381–3386. 70, 116, 117, 162

[130] Agrawal, A. K.; Rangarajan, J. *International Journal of Scientific & Engineering Research* **2014**, *5*, 1544–1551. 98, 127, 133

[131] Ertl, G.; Küppers, J. *Low Energy Electrons and Surface Chemistry*, 2nd ed.; Wiley-VCH, 1985. 103

[132] Wang, G.; Van Hove, M. a.; Ross, P. N.; Baskes, M. I. *Journal of Chemical Physics* **2005**, *122*. 104, 161

[133] Strohl, J.; King, T. S. *Journal of Catalysis* **1989**, *116*, 540–555. 104

[134] Yoda, T.; Uchida, H.; Watanabe, M. *Electrochimica Acta* **2007**, *52*, 5997–6005. 110

[135] Mayrhofer, K. J. J.; Strmcnik, D.; Blizanac, B. B.; Stamenkovic, V.; Arenz, M.; Markovic, N. M. *Electrochimica Acta* **2008**, *53*, 3181–3188. 110

[136] Mayrhofer, K. J. J.; Ashton, S. J.; Meier, J. C.; Wiberg, G. K. H.; Hanzlik, M.; Arenz, M. *Journal of Power Sources* **2008**, *185*, 734–739. 110, 111, 122

[137] Borup, R.; et al. *Chem. Rev.* **2007**, *107*, 3904–3951. 116, 163

[138] Bandarenka, A. S.; Koper, M. T. M. *Journal of Catalysis* **2013**, *308*, 11–24. 124

[139] Deivaraj, T. C.; Chen, W. X.; Lee, J. Y. *Journal of Materials Chemistry* **2003**, *13*, 2555–2560. 126

[140] Scherrer, P. *Nachrichten von der königlichen Gesellschaft der Wissenschaften zu Göttingen - Mathematisch-physikalische Klasse* **1918**, *2*, 98–100. 142

[141] Holzwarth, U.; Gibson, N. *Nature nanotechnology* **2011**, *6*, 534. 143

[142] Klug, H. P.; Alexander, L. E. *X-Ray Diffraction Procedures*, 2nd ed.; John Wiley \& Sons: New York, 1974. 143

[143] *SumMet - Die Summe unserer Erfahrung*; 2013. 151

[144] Sharma, S.; Pollet, B. G. *Journal of Power Sources* **2012**, *208*, 96–119. 159

[145] GESTIS-Stoffdatenbank (IFA), http://www.dguv.de/ifa/Gefahrstoffdatenbanken/GESTIS-Stoffdatenbank/index.jsp, accessed June 14, 2015. 176

[146] Sigma-Aldrich, http://www.sigmaaldrich.com/germany.html, accessed June 14, 2015. 176

Appendix A

Chemicals and Samples

A.1 List of Hazardous Substances

Table A.1: GHS information on hazardous substances used in this work.(145)(146)

chemical	pictogram	H statements	P statements
Acetone		225-319-336 EUH: 066	210-233-305+351 +338
Ammonia		221-280-331-314-400 EUH: 071	210-260-280-273 -304+340-303 +361+353-305 +351+338-315 -377-381-405 -403
Chloroform		351-361d-331-302 -372-319-315	302+352-314
1,2-Dichlor-benzene		302-315-319-335 -410	261-273-305+351 +338-501
Diphenylether		319-411	-
Ethanol		225	210
n-Hexane		225-361f-304-373 -315-336-411	210-240-273-301 +310-331-302 +352-403+235
Hydrochloric acid		314-335-290	234-260-305+351 +338-303+361 +353-304+340 -309+311-501

continues on the following page

chemical	pictogram	H statements	P statements
Hydrogen peroxide		272-302-314-335	210-280-303+361 +353-304+340 +310-305+351 +338-370+378
Methanol		225-331-311-301 -370	210-233-280-302 +352-309+310
Nafion		225-318-336	210-261-280- 305+351+338
Nickel(II)- acetate		302+332-317-334 -341-350i-360D -372-410	260-285-302+352 -321-405-501
Nitric acid		272-314-290	210-260-280-301 +330+331-305 +351+338-308 +310
Oleic acid		315	-
Oleylamine		314-400	273-280-305+351 +338-310
Platinum(II)- acetylacetonate		302+312+332-315 -319-335-361	261-280-305+351 +338
Sulfuric acid		314-290	280-301+330+331 -305+351+338 -309+310
Tetrabutyl- ammonium hydroxide		314	280-301-305+351 +338-309
Toluene		225-361d-304-373 -315-336	210-301+310-331 -302+352

A.2 Sample Directory

Table A.2: Characteristics of PtNi nanoparticles synthesized in this work.

name	size (TEM) [nm]	size (XRD) [nm]	Ni (EDX) [at%]	Ni (XRD) [at%]
PtNi-a	2.6	2.1	19	14
PtNi-b	2.8	2.1	15	9
PtNi-c	2.3	2.1	11	6
PtNi-d	4.7	3.7	31	24
PtNi-e	5.4	4.2	45	35
PtNi-f	18.0	4.9	91	80
PtNi-g	3.8	3.2	10	4
PtNi-h	3.9	3.5	24	21
PtNi-1	2.4	2.1	7	1
PtNi-2	7.3	5.0	52	42
PtNi-3	2.3	2.0	-	8
PtNi-4	7.2	5.2	59	45
PtNi-5	2.3	-	8	-
PtNi-6	7.7	5.6	51	40
PtNi-7	2.3	2.2	18	10
PtNi-8	7.6	4.8	54	44
PtNi-9	2.3	2.3	22	22
PtNi-10	4.1	3.6	33	24
PtNi-11	4.3	3.6	46	30
PtNi-12	5.8	4.3	43	37

Appendix B

Additional Data
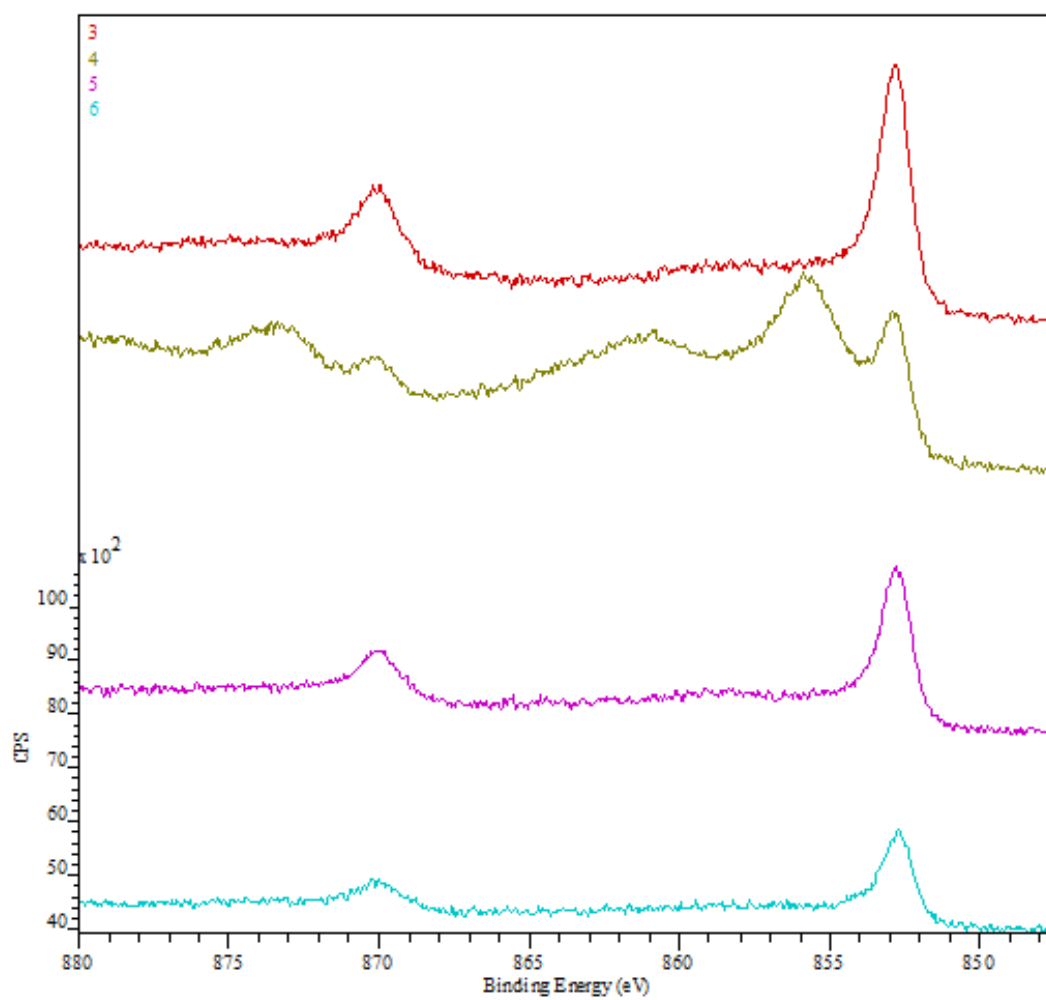
Figure B.1: XPS spectra of PtNi-2 (GCEs 3 - 6), Ni2p.
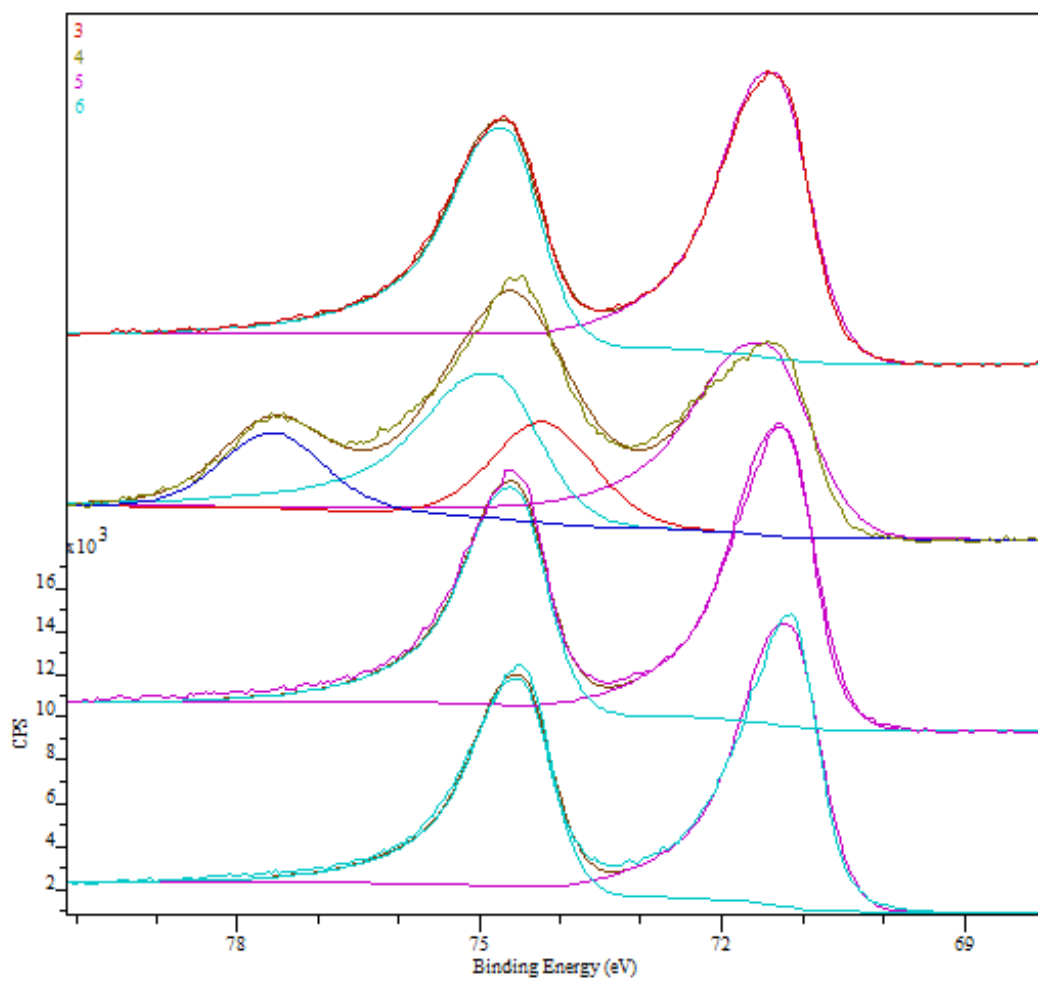
Figure B.2: XPS spectra of PtNi-2 (GCEs 3 - 6), Pt4f.
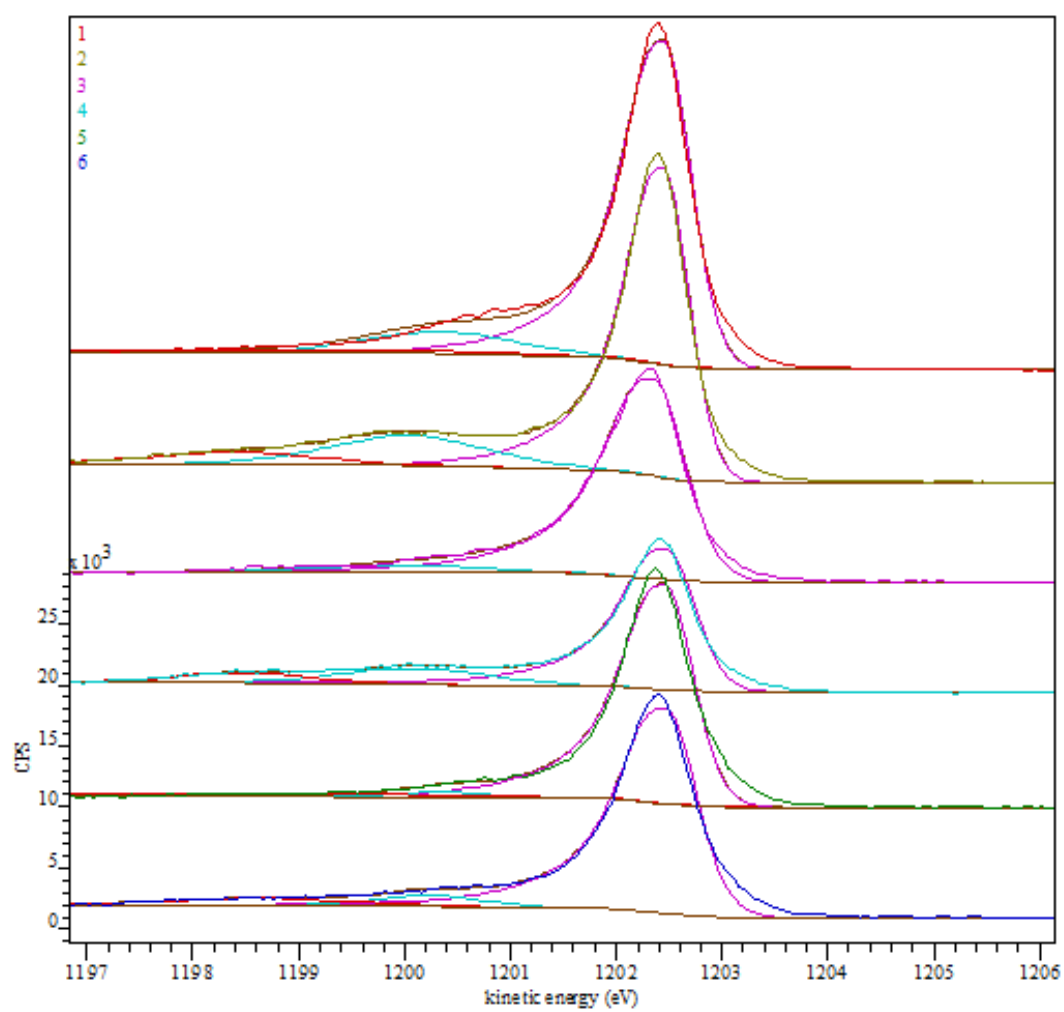
Figure B.3: XPS spectra of GCEs 1 - 6, C1s.
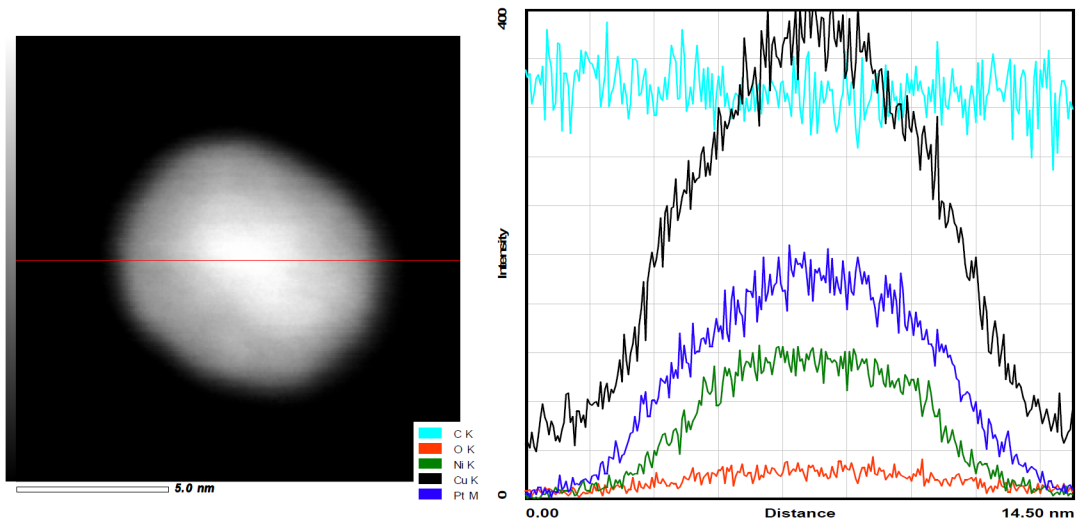
Figure B.4: Line scan (EDX) of PtNi-2, untreated.
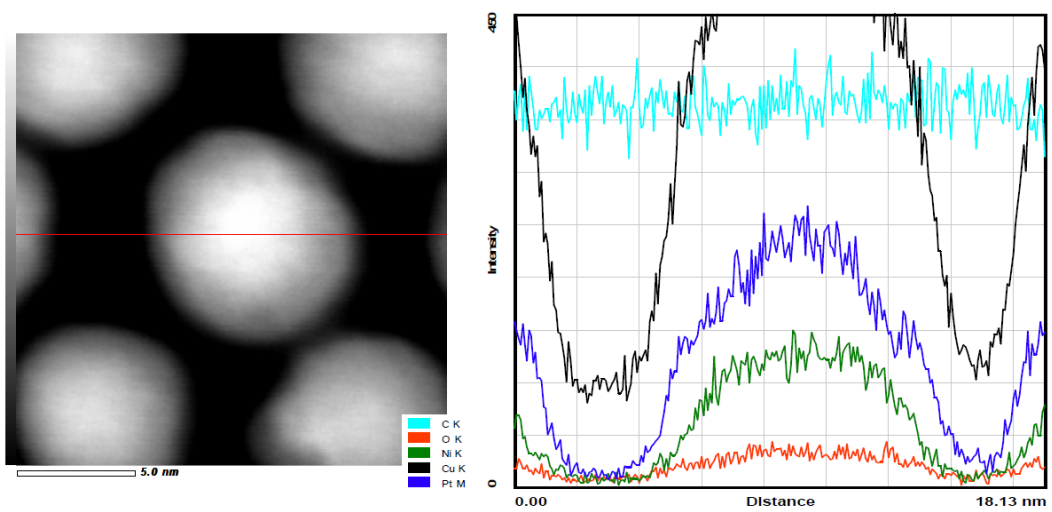
Figure B.5: Line scan (EDX) of PtNi-2, plasma treated.

Acknowledgements

Eidesstattliche Erklärung

Hiermit erkläre ich an Eides statt, die vorliegende Arbeit selbst verfasst und keine anderen als die angegebenen Hilfsmittel benutzt zu haben. Ich versichere, dass diese Dissertation nicht in einem früheren Promotionsverfahren eingereicht wurde.

Hamburg, den 14.06.2015

_____
Lena Wittern